A Thermodynamic Study of Layering and Capillary Condensation of Methane Adsorbed on Graphite Foam

Thesis by
Mark Joseph Lysek

In Partial Fulfillment of the Requirements
for the Degree of
Doctor of Philosophy

California Institute of Technology
Pasadena, California

1992

(Submitted October 9, 1991)

Acknowledgements

First, I must acknowledge the support of my wife, Katia. Without her help, this work would not have been possible. Joseph and Theresa Lysek, my parents, have also greatly aided my progress through undergraduate and graduate school.

My advisor, Professor David Goodstein, has given much to this experiment. This thesis is a direct descendant of on his PhD thesis. But I owe him a greater debt, because he has made my graduate career more than a pursuit of scientific knowledge. It was a practical education in the methods of science that can only be gained from a patient and skilled teacher.

This experiment was a continuation of Jeffrey Hamilton's heat capacity measurements. He contributed a large fraction of the intellectual content of this thesis and provided the framework on which this experiment was built. I have also enjoyed conversations with Professors M.H.W. Chan, J.G. Dash, and G.B. Hess.

Nils Asplund constructed and designed much of the apparatus and provided practical knowledge on how to actually accomplish the mechanical designs. Likewise, John Dick, Don Strayer, Jean Delayen and Edward Boud provided an education in cryogenic instrument design. Furthermore, all the staff at caltech deserve credit; a successful research project depends on the effort of many people.

Randy Pollack, Margie Pollack, and Marissa LaMadrid constructed a large part of the apparatus, as did Peter Day, who is cursed to live with my mistakes as he continues this work. There are many others that have contributed in one way or another, including Robert Housley, Franco Scaramuzzi, Michael Pettersen, Michael Weimer, Carlo Carraro, and Roya Maboudian.

The custom low noise resistance bridge input transformers were fabricated by Roger of Zenith Enterprises, who is a veteran of the times when huge 1 million volt transformers inhabited Sloan Laboratory. This work was made possible by support from Department of Energy contract No. DE-FG03-85ER45192.

Abstract

Multilayer films of methane adsorbed on graphite foam have been studied using heat capacity and vapor pressure measurements. An automated, high resolution differential calorimeter was designed and constructed that yielded far better data in much less time. It was found that capillary condensate in the pores of the graphite foam coexists with uniform films as thin as 1.1 layers. Heat capacity features near the triple point previously thought to be the melting of the uniform film are identified as the melting of the capillary condensate. The latent heat of melting of the capillary condensate was measured to be as small as half the bulk value when it was confined inside the smallest pores. The melting temperature of the capillary condensate confirms a simple model for the melting of bulk matter in cylindrical pores. This model explains why the melting temperature is the same for systems with the same chemical potential but on different branches of the hysteresis curve. The model indicates that the capillary condensate may undergo surface melting if the solid does not wet graphite and the condensate undergoes substrate freezing. The phase diagram of the layer closest to the substrate is altered slightly by the finding that this layer melts from the commensurate phase when the uniform film is thicker than 1.1 layers. Heat capacity signals from phase transitions in the uniform films map out complicated phase diagrams in the second, third and fourth layers, including a 2-D triple point and liquid vapor coexistence region for each layer. The layering critical temperatures indicate that the bulk solid-vapor interface may roughen at about 81 K.

Contents

List of Figures

List of Tables

Chapter 1

Introduction

The study of films on solid surfaces began in 1773 when C. W. Scheele[1] heated a chamber filled with charcoal. The gas pressure in the chamber was high when warm, but when sealed and cooled the pressure dropped greatly. Clearly, the gas was absorbed into the charcoal, which possesses a great internal surface area. In the following years, three mechanisms were found responsible for the adsorption of gas into porous solids.

- Chemisorption: Certain gases are chemically bonded to reactive surfaces; when heated, the bonds are broken.
- Physisorption: The solid surface attracts the gas via the van der Waals electrostatic interaction. Although this is a weaker force, it is applicable to all gases and surfaces.
- Capillary Condensation: The surface tension of the liquid or solid phase is large enough to cause the gas to condense in the small cracks of the adsorbate.

There are many practical applications of these phenomena. Chemisorption is important for understanding catalysis and corrosion. Physisorption and capillary condensation are relevant to cryopumping, and frost damage to porous building materials (cement and brick). Also, physadsorbed gases on uniform surfaces can model two dimensional matter, because the molecules lose the freedom to move perpendicular to the surface. This last reason has stimulated much study. Two

[1] Also discovered independently in 1777 by Abbé F. Fontana [3, page 5-98].

dimensional solids, liquids, and gases have been experimentally detected and theoretically explained. Because solving the theoretical problems in two dimensions is far easier than in three, we understand more about two dimensional phase transitions than three dimensional phase transitions, even though the melting of crystals in three dimensions is a very important problem, for example. Our study was motivated by an interest in studying how the melting of two dimensional films gradually changes into three dimensional melting as the film becomes thicker.

It has been proposed that for some adsorbates on graphite, the melting temperatures of the layers should decrease as we approach the upper layers of the film. This phenomenon may be evidence that the outer surface of bulk crystals melt before the inside, called surface melting. Surface melting is of great interest for the growth of crystals.

The physical system consists of a clean porous graphite surface immersed in methane gas. The gas molecules are attracted to the surface by the van der Waals force. This force is strong enough to hold a fraction of the methane molecules on the surface where they move only in the plane of the surface. The variables that determine the nature of the film are the temperature and the pressure of the methane gas above the substrate.

You can imagine a box filled with methane gas, whose temperature and pressure can be manipulated. For sufficiently high temperature, the kinetic energy of the gas molecules prevents them from being trapped on the surface (figure 1.1A). As the temperature is reduced, and the pressure is increased, the molecules are drawn out of the gas and onto the surface, as in figure 1.1B. At very low temperatures (possibly cryogenic), practically all of the gas molecules are in the film (figure 1.1C). Since the van der Waals force prevents them from moving in the Z direction, the system behaves as if it were two dimensional. Two dimensional solids, liquids and gases have been observed using heat capacity, vapor pressure, and neutron scattering experiments.

As the gas pressure is increased, the surface becomes more densely covered and a second layer forms on top of the first, as in figure 1.1D. The two layer film also can exist in 2-D solid, liquid, and gaseous phases. As we further increase the gas pressure more and more layers may form as the pressure approaches the bulk saturated vapor pressure.

Consider the bulk phase diagram of ordinary matter (figure 1.2). Depending on the pressure and temperature, either solid, liquid, or gas may be the equilibrium phase. Our film begins to form in the gaseous region of the phase diagram. As

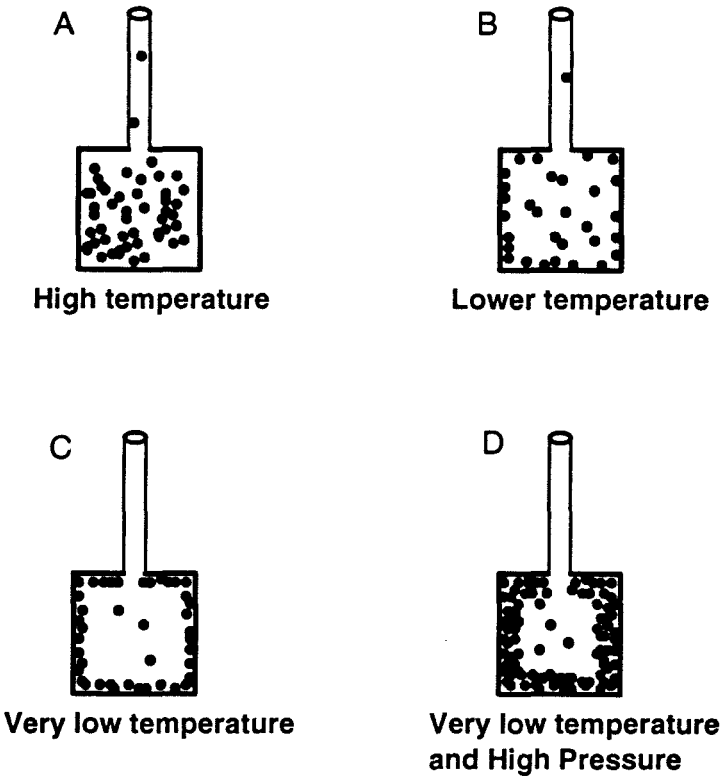

Figure 1.1: Boxes filed with gas with some adsorbed on walls, temperature is highest in A, lowest in C. D has higher pressure than C.

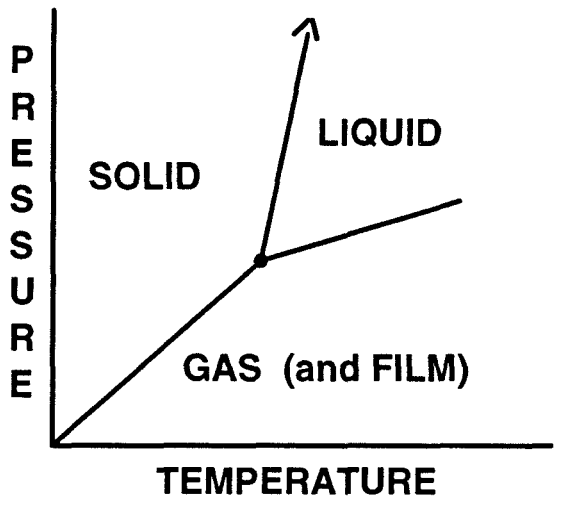

Figure 1.2: Bulk pressure vs. temperature phase diagram.

the pressure, P, increases, more and more layers may form until P reaches the line where bulk solid or liquid forms. Or, only a certain fixed number of layers may form as P approaches the bulk vapor pressure. In either case, the entire box must begin to fill with bulk matter when the pressure reaches the bulk saturated vapor pressure. At that point our box must fill with the proper bulk phase.

The most basic measurement to make on a film is its vapor pressure isotherm. At constant temperature, gas is added in small increments while recording the pressure. The isotherm is a plot of the number of atoms in the film (or its thickness) as a function of the vapor pressure from zero pressure to the bulk saturated vapor pressure. Since the films are just a few molecular layers thick, the measurement can be difficult. Three methods have been used:

- Measure the amount of gas adsorbed by a porous, high surface area substance (like activated charcoal).
- Measure the weight of the adsorbed gas on a porous, high surface area substance with a sensitive microbalance.
- Measure the thickness of the layer on a homogeneous crystal of highly oriented pyrolytic graphite (HOPG) with a small surface area using optical ellipsometry, or a vibrating wire microbalance [4].

With large surface area measurements, the substrate has a much larger area than the plumbing, so the vast majority of the molecules not in the vapor are on the substrate. Then the amount adsorbed can be found by measuring the number of molecules drawn from the gas or by weighing the film. For small surface areas, a large fraction of the molecules may be adsorbed on the cold walls of the apparatus, so other means must be used to know the film thickness. For example, optical ellipsometry has been used [5].

Early attempts to measure vapor pressure isotherms resulted in a curve with an initial steep rise as the first molecular layer was formed. Then, as the pressure increases, the average film thickness increases smoothly until it saturates when the pores of the adsorbent are filled. However, there should be more steep "steps" in the isotherm as additional layers form like the first. The surfaces studied were not uniform, and while a second or third layer was forming on some sites, there was only one layer at others. Despite this, a reasonable theory was made to explain most results and determine the surface area of the porous substrate, the Brunauer-Emmett-Teller (BET) equation [6].

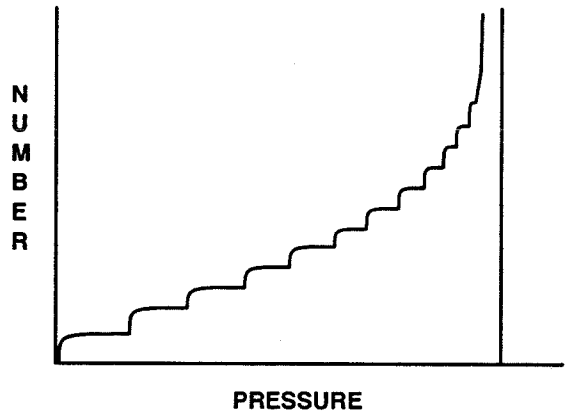

Figure 1.3: Example of a vapor pressure isotherm with steps.

The BET theory still finds application when the surface area of a porous material must be measured. Over time, better and better substrates were made, and now optical ellipsometry can see as many as ten sharp isotherm steps.

Examining the isotherms, we find that the film sometimes forms each new layer at constant pressure (figure 1.3). The rising edge of the steps are vertical. During layer formation, when a small dose of gas is added to the system, the pressure doesn't change. At this time the uppermost layer of the film is in two phase coexistence, as when a liquid is condensing from low density gas at constant temperature and pressure. In the film, the two phases are 2-D gas and 2-D solid or liquid. On top of the uppermost completed layer there are islands of 2-D solid or liquid surrounded by 2-D gas. As more molecules are added to the film, the solid or liquid islands become larger and eventually fill up the layer. Then, the pressure must increase to induce the formation of a solid or liquid in the next layer.

Just as in the three dimensional case, there may be a critical point in the 2-D phase diagram. Above the critical temperature, there is no longer a distinction between the 2-D liquid and gas. In that case the pressure increases smoothly as the layer becomes more dense. Then, the steps are rounded on the vapor pressure isotherm. Layering critical points have been observed in a number of systems [7].

However, it is usually a bad approximation to assume each layer in the film is unaffected by the others. For very thick films, the middle layers must begin to behave like three dimensional matter. Also, the force on each molecule in the film is not simply a function of the distance between the planar surface and the

molecule. If an orthogonal coordinate system is defined with the z axis perpendicular to the surface and the x and y axes parallel to the surface, the force on each molecule is a function of x and y as well as z because of the order in the layers above and below it in the substrate. The layers may grow epitaxially with the other layers, and the first layer may be in registry with the substrate. This is especially evident for nonspherical atoms that may orient themselves with respect to the surface in variety of patterns and phases. It is common to find registered solids, modulated fluids, incommensurate phases, and phase transitions as the pressure or temperature changes.

Most of the time, the state of ordinary 3-D substances can be described by two variables, temperature, T, and pressure, P. For example, consider a bag filled with liquid, solid, or gas. The atmospheric pressure keeps the pressure in the bag constant, the number of gas molecules is constant, but the volume of the bag is free to change. Locating the point on the P vs. T phase diagram will tell us whether the bag is filled with solid, liquid or gas. However, when the matter is melting, subliming, or evaporating, the state of the system lies on one of the phase boundaries, and P and T no longer totally define the state of the system. Imagine starting at low temperature, then warming the bag. As the temperature increases (at constant pressure) nothing exciting happens until the temperature reaches the melting temperature. At that point the temperature remains fixed until all the solid is melted. So while the solid is melting, P and T are fixed, but there is clearly something changing. Another variable is needed to completely describe the system: the density or volume of the matter in the container. As the solid melts, the density changes (usually decreases), so the density will tell us the fraction that has melted[2].

It is also instructive to draw the density vs. temperature phase diagram for ordinary matter, figure 1.4. At low temperature our bag is filled with bulk solid. As the temperature increases, the density decreases slowly due to thermal expansion, until it reaches the melting line. On the melting line, some of the solid melts to reduce the density further, but most of the bag is still filled with solid. The system state enters the "coexistence" region. There are two different phases present at the same time in the bag, when the system state is in the coexistence region. The upper boundary of the region represents the density of the solid state and the lower boundary represents the density of the liquid. It is not possible to make

[2]Ignoring the case where the solid and liquid densities are exactly equal.

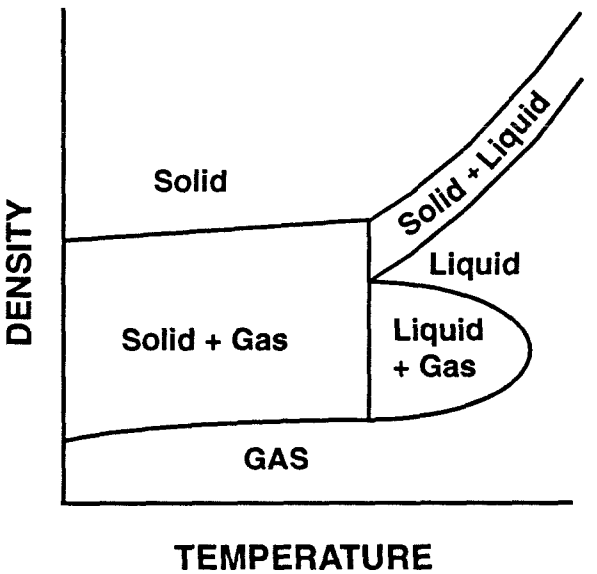

Figure 1.4: Bulk density vs. temperature phase diagram.

solid less dense than the value on the upper boundary or liquid less dense than on the lower boundary. During melting, the vertical distance traveled through the coexistence region represents the fraction of the matter that remains solid. At the lower boundary, the entire bag is filled with liquid.

Two dimensional film density vs. temperature phase diagrams are useful to consider for adsorbed films because they tell what the system state will be, given the number of molecules in the film and the surface area of the substrate. The number of molecules in the film divided by the surface area can define a film density[3]. Since the substrate area is constant, the film density vs. temperature phase diagram is usually just plotted as the number of molecules in the film verses the temperature (N vs. T). Since the surface area is fixed, the density is usually calibrated by the height of the first step on the N vs. P isotherm. This is called the monolayer capacity, and is approximately where the second layer begins to form.

As with 3-D matter, there are coexistence regions where two film phases exist simultaneously, and triple points where three phases coexist. For example, the first layer phase diagram for methane on graphite, figure 1.5, looks just like the 3-D bulk phase diagram except that there are 3 different solid phases. Since there

[3]It is also possible to define a separate density for each layer in the film. But since there is no well defined division between the layers, and the layers interact with each other, this density is not a proper thermodynamic variable.

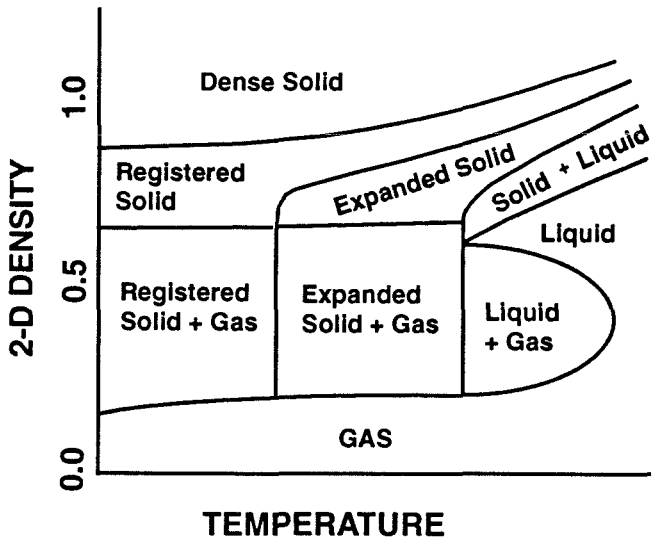

Figure 1.5: Monolayer methane first layer phase diagram; 2-D density units are monolayers adsorbed (approx.).

is only one layer, the number in the film divided by the area is equal to the 2-D density, completely analogous to the 3-D density. This phase diagram has been determined from heat capacity [8, 2], vapor pressure [9, 10, 11, 7, 12, 13], neutron scattering, [14, 15, 16, 17, 18, 19], and nuclear magnetic resonance (NMR) [20, 21, 22] measurements. At low temperatures and densities, islands of commensurate (registered) solid coexist with 2-D gas. Increasing the 2-D density, at constant temperature, causes the registered monolayer to fill the surface, and molecules begin to enter the second layer. At even higher densities, the monolayer breaks away from the substrates lattice and forms the dense solid phase.

Beginning at low temperatures and pressures, and moving to higher temperature, the solid registered phase initially coexists with 2-D gas. At about 48 K the first layer solid becomes incommensurate (unregistered) with the substrate and forms an expanded (lower 2-D density) phase. This happens because the kinetic energy of the atoms becomes large enough to break the molecules off the lattice imposed by the substrate. Many laboratories have studied this second order phase transition. Then at about 56 K, the expanded incommensurate solid phase melts in a first order phase transition. Just as in three dimensions, there is a coexistence region between 2-D liquid and gas. Above the critical point there is no distinction between the liquid and gas phases.

An explanation for the rounded shape of the coexistence regions is that starting below the lower boundary in the 2-D density vs. T plane and moving up in coverage, the gas becomes denser until the liquid is nucleated. This point marks the lower boundary of the coexistence region. Then, the liquid fraction grows at constant pressure until there is no longer any gas remaining. This point marks the upper boundary of the coexistence region. Above this point, the liquid may become denser as another layer forms on top. As the temperature is raised, the 2-D gas must become more dense before the liquid is nucleated, so the lower boundary moves upward in the phase diagram. Likewise at higher temperature, thermal expansion of the 2-D liquid reduces its density, so the upper boundary slopes downward. When the upper and lower boundaries meet, the 2-D liquid and gas densities are equal and there is just a smooth increase in density as the layer forms.

When the first solid layer is completed and the 2-D gas in the first layer disappears, the monolayer melting transition temperature rapidly increases. This happens because when the first layer 2-D solid melts, it expands and takes up a larger area on the substrate. While the 2-D solid coexists with a 2-D gas (before layer completion), the extra surface area comes from promoting a small number of molecules in the first layer 2-D gas to the second layer. But for films thicker than one layer, a much larger number of molecules from the 2-D solid must be promoted to make room for the expansion. Moving the molecules up from the first to second layers costs a large amount of energy, so the latent heat of melting and the melting temperature increases when the first layer is completed. The monolayer melting temperature changes from 57 K at .7 layers to about 100 K for 1.0 layers. This argument was first used by Elgin and Goodstein to explain the heat capacity of helium films on Grafoil [23].

The monolayer phase diagram of methane is identical to the ordinary 3-D bulk phase diagram except for the three different solid phases. These phases are caused by the variation of the attraction between the adsorbed molecules and the surface in the x-y direction. The basal plane graphite surface is composed of a regular hexagonal lattice of carbon atoms. When the adsorbed molecule is located in the center of a hexagon, the (repulsive) force is weaker than when it is directly above one of the carbon atoms (at the same height above the substrate). On a perfectly smooth substrate, the film would have a natural lattice constant that depends on the temperature, 2-D density and the size of the molecules. The periodicity of the substrate potential is different from the natural film lattice constant, so

under certain conditions either the registered, unregistered, or partially registered phases exist on the surface.

Since the phase diagram of monolayer methane is well understood, one asks what happens when the pressure is increased and thicker films form? In the simplest case, the second layer forms an ideal 2-D system on the first layer in the same way that the first layer forms an ideal 2-D system on the substrate. It has been stated that the first layer may be a more perfect substrate than the graphite [24]. The substrate potential and periodicity will be different from the first layer, so the phase diagram will not be the same. One could imagine a multilayer film comprised of many noninteracting 2-D layers.

As the film grows at constant temperature, each layer forms on the surface at nearly constant pressure. This implies that during layer formation there are two phases in coexistence, regions of the film with N layers and regions with N+1 layers.

Another contrasting view of the same phenomenon is to consider the uppermost layer of the film as a 2-D system, as discussed above. Then the two phases in coexistence are patches of 2-D liquid and the surrounding 2-D gas; there could be 2-D solid, liquid, and gas phases. The coexistence region ends above the critical temperature, the pressure then increasing smoothly as the film grows[4].

These two ways of explaining layer formation differ mainly in terminology. Where the film is N+1 layers thick there is a condensed 2-D phase on top of N layers. Where the film is only N layers thick, there may be a 2-D gas on top of the film because the 2-D density of the gas phase is low compared to the condensed phase. It is also strictly improper to think of the individual layers as noninteracting, so the first explanation is somewhat more accurate. The data for multilayer methane, from this study, seems to point somewhere in the middle: the film phases are somewhat like individual 2-D layers, but some of the features cannot be explained without invoking the whole film approach.

This study began as an attempt to understand the phase diagram for films thicker than two layers, and to examine the transition from two to three dimensional film behavior. However, for thicker films, capillary condensation compli-

[4]As the film grows, the uppermost layer usually forms while the other layers remain unchanged. Then the film density during layer formation equals the (fixed) density of the lower layers plus the two dimensional density of the newly forming layer. If no phase transition occurs in the lower layers, the section of the N vs. T phase diagram where the layer is forming shows the 2-D density vs. temperature phase diagram for the uppermost layer.

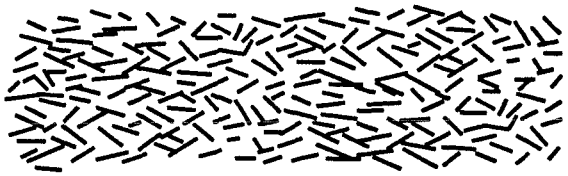

Figure 1.6: Cross section of graphite foam substrate.

cates the data interpretation.

Capillary Condensation

As mentioned above, high surface area substrates make it easier to take vapor pressure isotherms. The same is true for measurements of the film heat capacity. To measure the heat capacity, the temperature must be measured with an accurate thermometer while a heater warms the sample. If a small amount of heat, δQ, causes a small temperature change, δT, then the heat capacity is

$$C = \lim_{\delta T \to 0} \frac{\delta Q}{\delta T}.$$

Even the smallest thermometer has a heat capacity several thousand times that of a one layer film on a small surface area. Our porous substrate, graphite foam, has such a large internal surface area (20 m^2/g) that the film heat capacity is large enough to measure.

But there is a price to be paid for this convenience. Although the vast majority of the surface area is homogeneous basal plane graphite, there are small cracks and corners where the 3 μm wide by 100 Å thick platelets interconnect. Graphite foam is comprised of a random array of platelets, as shown in figure 1.6.

Just as liquid is drawn up a fine capillary tube, the gas is drawn into the cracks and corners of the pores. This is called capillary condensation because the bulk phase is "condensed" from the gas into the "capillaries," even when the vapor pressure is below the bulk saturated vapor pressure, as shown in figure 1.7. Whenever there is a crack in the surface, the Kelvin equation [3, 25] states that the vapor pressure of bulk matter in the crack, P, with a meniscus of radius R, is reduced:

$$P - P_o = -\frac{2\sigma}{R} \tag{1.1}$$

where σ is the surface tension of the bulk phase and P_o is the bulk saturated vapor pressure. Then the bulk matter can exist in the pores along with the film

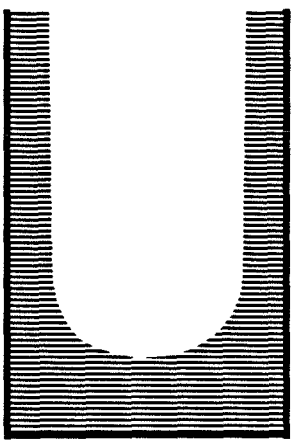

Figure 1.7: Capillary condensation in a closed pore coexisting with a thin film.

on the surface. For methane films on Grafoam that are thinner than one layer, no appreciable amount of matter is drawn into the corners. But for thicker films, two states of matter may coexist inside the porous substrate, film and capillary condensed bulk. Thick film data are much more difficult to interpret.

Just as when any two phases coexist, the fraction of the matter in the film compared to that in the bulk phase may vary continuously from zero to one, and another variable must be introduced to completely describe the state of the system. In the early isotherm measurements it was discovered that a different curve was followed for an isotherm when gas is added to the system compared to while gas is removed from the system. The amount of gas condensed in the porous substrate is lower as the pressure is ramped up than while it is ramping down. At first this hysteresis was explained as caused by dirt on the surface. As cleaner surfaces became available, it became clear that the hysteresis was a property of the gas/substrate interactions [26]. Although sometimes other causes exist, most often, capillary condensation causes the hysteresis.

The existence of capillary condensation still does not explain the hysteresis, because the molecules should condense spontaneously in the simple corners of the porous substrate. However, for certain pore geometries, there is a barrier to the formation of the capillary condensate. Consider an open tube, as we first build a film on the surface. The radius of the tube causes the vapor pressure of the capillary condensed bulk to be reduced by σ/R, as in figure 1.8 view A. But when the film reaches a certain thickness, it realizes that it can lower its energy by forming a meniscus across the cylinder, as in view B. The vapor pressure shift

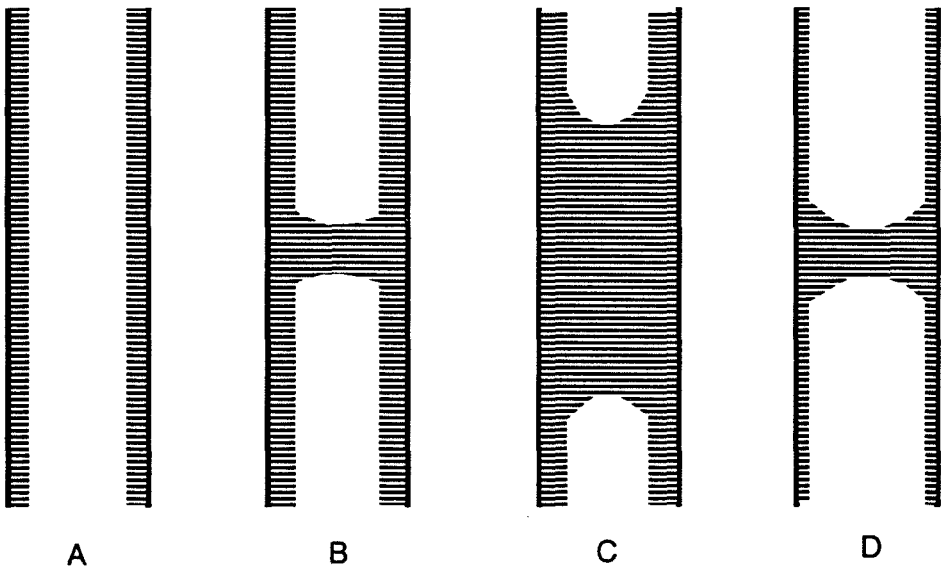

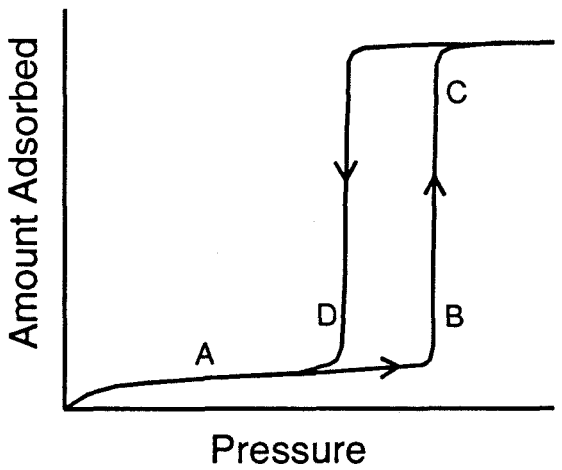

Figure 1.8: Capillary condensation in a tube.

for this configuration is $2\sigma/R$. The vapor pressure isotherm for this situation is also shown in figure 1.8. As the pressure is increased, the film grows thicker until it spontaneously fills the cylinder (view C). While gas is withdrawn, the pressure is constant until there is no longer enough bulk matter to form a meniscus across the cylinder (view D). Note that the pore fills and empties at constant pressure, but the two pressures are not the same [27, 28]. In most physical systems there is a distribution of interconnected pores of different sizes and shapes, so the curves smooth out, but the hysteresis remains. Our porous substrate consists of 2000 Å high caverns connected by channels that could be as narrow as 100 Å. It is in these channels that capillary condensation is delayed, and the hysteresis occurs. The extra variable needed to describe the film is the number of micro-capillaries in which capillary condensation has been nucleated. This variable will be a complicated function of the precise history of the film. The dominant contribution to this variable is the maximum amount adsorbed on the surface during the film's history.

A very elegant experiment was performed by Carman and Raal [29] that proved that the hysteresis is caused by the small pores. An isotherm on a loose carbon powder was performed that showed no hysteresis. When the same powder was compressed, hysteresis appeared, and for low pressure there was slightly less gas adsorbed by the powder. This is presumably because the compression reduced the surface area. However, for high pressures, even while adding gas to the system (adsorption branch), more gas was adsorbed on the compressed substrate. This indicates that there is some capillary condensation even on the upward-going isotherm.

Another common feature in the hysteresis curves is that a low pressures, usually at .2 to .3 times the bulk saturated vapor pressure, the curves close together. This pressure is relatively independent of the substrate used. This is explained as due to the fact that capillary condensation cannot occur in cracks that are smaller than a few molecular diameters, because surface tension is not present for just a few molecules in the crack. It is commonly accepted that equation 1.1 is strictly applicable for pores larger than many molecular radii, but it typically works well for smaller pores. There are many good reviews of capillary condensation and hysteresis; for example, see references [30, 31, 32, 33].

Project History

The original motivation of this project was to understand the properties of films as they take on the properties of the bulk. The first study of the heat capacity of multilayer methane on graphite by Hamilton [34], in this laboratory, uncovered two features: small peaks near 78 K related to layering and bulk surface roughening, and larger peaks close to 90 K where the film was presumed to melt. The films were from one to six layers thick. Capillary condensation was thought to occur in films thicker than about five layers (as calculated by the Kelvin equation), so was not considered to be present in the data. A more detailed study using the same apparatus showed the shapes of the melting peaks more clearly [35] for films as thick as 18.3 layers. These peaks were said to be caused by "triple point dewetting", a complicated but thermodynamically sound theory. The evidence in favor of triple point dewetting was thought so strong that capillary condensation was ruled out. Following this, an NMR study of the methane films on graphite corroborated the previous results and showed that capillary condensation did not occur in films as thick as 50 layers [36]. In other laboratories, similar studies were progressing with thick films. In a study of argon films on Grafoam, the shape of the thick film triple point melting peak was used to prove the existence of surface melting [37]. Capillary condensation was not thought to occur in this case either.

Meanwhile Kim, Zhang, and Chan [2] extended the earlier heat capacity and vapor pressure studies [8] of monolayer and submonolayer methane. Instead of the first layer melting heat capacity peak disappearing as the coverage increased toward a complete monolayer, as seen previously by Marx [8], they saw the peak reappear after shifting about thirty degrees higher in temperature. The monolayer phases for films just over a single layer progress from dense incommensurate solid, to registered solid, to expanded solid and finally to liquid, as the temperature increases at constant coverage (figure 1.5).

Simultaneously, Morrison[5] and coworkers studied the heats of adsorption of methane on Grafoam [39]. The results agreed well, but later data found hysteresis in both the vapor pressure isotherms and the heats of adsorption [40]. The cause was not clearly identified because the shapes of the hysteresis curves was not similar to that typically observed for capillary condensation [41].

Along with the vapor pressure hysteresis, Inaba, Koga, and Morrison also

[5]Morrison made the earliest heat capacity measurements of the film triple point melting peak and studied hysteresis curves for many adsorption systems [38].

found a wetting transition at 75.5 K (also for krypton and xenon [42]). Since other vapor pressure studies of methane on graphite did not find a wetting transition in this temperature range [7], both the wetting transition and the hysteresis were not believed at first. Later, Larher et al. [43] reexamined whether a wetting transition is present in xenon and argon, and argued that Inaba and Morrison's results were caused by capillary condensation; there is no wetting transition. Work stemming from Morrison's laboratory by Meichel et al. [44] came to the same conclusion. In 1990, a neutron scattering study found capillary condensation in argon films [45], invalidating the thick film results of Zhu and Dash [37]. While data was being collected for this study, very clear evidence that capillary condensation is present for xenon films on exfoliated graphite was found using x-ray scattering [46]. Morishige et al. studied the films on both the adsorption and desorption branches, and found there was capillary condensate coexisting with films as thin as one layer on the desorption branches. The authors report that the methane neutron scattering study by Larese et al. [47], that did not find a signal from the capillary condensate, was hindered because the reflection off the graphite substrate coincides with the bulk peak. As recently as 1990, a neutron study concluded that surface melting was present in thick methane films [48]. There was still some doubt about what exactly is happening in the methane-graphite system.

When this study was begun, it was clear that to understand the film behavior it was necessary to reproduce the hysteresis and determine its cause. The vapor pressure isotherms alone cannot determine the cause of the hysteresis. Heat capacity and structural data (neutron and x-ray scattering) could unravel the puzzle. There was already some neutron scattering evidence demonstrating the presence of bulk capillary condensate coexisting with the thick film for argon on graphite [45]. The obvious tasks were to reproduce the hysteresis curves and then try to take heat capacity data for films on the desorption branch as well as on the adsorption branch.

A feature in the heat capacity may be due either to phase transitions in the film or in the capillary condensate. Since the amount of bulk on the cracks of the substrate depends on the exact history of the system, the heat capacity data may be irreproducible unless the film is always formed by the same methods. But the hysteresis may be used as a tool to help decide which phase transitions are occurring in the film. Subtracting the distance between the upper and lower curves in the hysteresis curves gives the approximate amount of capillary condensate (at

low pressures). Then the amount of the adsorbed gas in the film can be computed. Most phase transitions in the film occur at a temperature that is a function of the film thickness. By studying films with varying amount of capillary condensation and film thickness, it can be deduced whether the phase transition is in the film or capillary condensate.

The chapters that follow will contain discussions of the experimental method, the new instrument, the experimental procedures, the data reduction, and an overview of the data from over 75 runs for methane films from .75 to eight layers thick on the adsorption and desorption branches. The data will follow the first (bottom) layer melting to even the thickest films. For the thickest films, the first layer transforms from expanded solid to commensurate solid before it melts. The pressure of the film above the surface prevents the formation of the expanded solid phase before melting, as found in thinner films by Kim, Zhang and Chan [2]. Near the bulk triple point (90.685 K) there is a heat capacity signal clearly attributed to the melting of the capillary condensed solid. At lower temperatures, the new instrument finds that the low temperature peaks that were barely seen in the previous study map out a complicated series of phase transitions that are related to layering and melting in the individual layers. These results permit us to draw the multilayer phase diagrams, try to come to some general conclusions about the film behavior, and propose some new experiments.

Chapter 2

Experimental Method

2.1 Substrates

Physically adsorbed films may be studied with a wide array of experimental techniques. Regardless of the method, the substrate qualities usually dominate the results. The ideal substrate would be a perfect crystalline surface that is flat over a length scale of several thousand angstroms and without lattice defects or impurities. To enable use of many of the experimental probes, one form of the "ideal substrate" should have a great surface area per unit weight to give a greater signal to background ratio. But it should not have any cracks or crevices in which to form capillary condensed bulk. Gas and heat should permeate easily through the substrate to make vapor pressure isotherms and calorimetry experiments possible. The surfaces in the porous substrate should be aligned approximately to simplify certain experiments, neutron and X-ray scattering for example. Lastly, all these properties should be available for the same substrate so that the information from the many different experimental techniques can be combined.

Unfortunately, it is not possible to optimize all these characteristics at the same time. For a high specific surface area, the substrate should be made of a matrix of many wide, thin crystals. To give good thermal conductivity for heat capacity experiments, the platelets should be joined to each other. Therefore, there must be microscopic cracks and channels where the crystals join and capillary condensation may take place. In fact, for there to be sufficient surface area to give a large heat capacity signal, the average platelet separation must be less than about .5 μm. Then the entire adsorbent will fill with capillary condensate when there are as few as 10 molecular layers on the surface. There is much interesting physics to study for films from one to 10 layers, so this is not a serious limitation, but capillary

condensate in the very small cracks and channels of the adsorbate may coexist with much thinner films.

Until recently, there were not any surfaces uniform or reproducible enough to study monolayer films. It was not possible to use physisorbed films as model systems for thermodynamic and solid state physics studies because the substrates did not present a single crystal face surface for adsorption. Early studies of films on jewelers rouge, sintered copper and rutile showed that there were interesting phase transitions in monolayer films [49, 50], but the data were very sensitive to the exact preparation and history of the substrate. Graphite foam was first used for studying physisorbed films in 1964 [51], and is the first substrate to present a reproducible, uniform substrate for adsorption.

Grafoam [52] is formed by exposing graphite crystals to a gas, allowing the gas to diffuse in between the planes of the crystals. Then the crystals are heated rapidly, and they cleave into small interconnected platelets that expose only one crystal face. This produces a very uniform surface, that has a very large internal surface area. After exfoliation, the resulting graphite "worms" are recompressed to form a commercial product, Grafoil. This experiment uses an intermediate product, Grafoam, that is five times less dense than Grafoil and 8% the density of graphite crystals. The specific surface area is large enough that the film heat capacity is a few percent of the total cell heat capacity for a film several atomic layers thick. This substrate has several other advantages besides its high surface area. When heated to just below its melting temperature and recooled, the platelets heal themselves, and show only one crystal face to the gas. The surface coherence length is on the order of 1000Å [53]. Also, this heating process cleans the surface of all contaminants. Since graphite is a good electrical conductor, it also conducts heat well, so it is ideal for heat capacity experiments [54]. And because the platelets remain interconnected after exfoliation, the heat settles down quickly in the calorimeter cell. The platelets in Grafoil tape are aligned to be more or less parallel when it is formed by recompressing the exfoliated "worms".

Grafoil satisfies all of the qualities for the "ideal substrate" except that there are small cracks and crevices where the platelets join. Electron micrographs show that after the platelets are separated, they form hollow cavities that are connected by small channels. Also, some of the platelets only partially separate. Since the capillary condensation that forms in these cracks doesn't occur for monolayer films, early studies successfully examined the phases of 2-D matter in monolayer films [55]. Vapor pressure isotherms on Grafoil and Grafoam show sharp steps for

five layers or more, so it was assumed that capillary condensation does not occur. Many studies of multilayer films were made under this assumption [56, 57, 35, 37]. These studies were probably correct if the films were never thicker than a few layers, because capillary condensation on the adsorption branch of the hysteresis curve does not usually begin until there are several layers on the surface. The only phase transition likely to occur in the capillary condensate is melting. This study will give conclusive proof that the heat capacity peak near the triple point, in multilayer films, is caused by the melting of the capillary condensate. This signal was commonly believed to be caused by the melting of the uniform film.

2.2 Experimental Techniques

Several techniques are available to study physically adsorbed films. Vapor pressure isotherms, ellipsometry, heat capacity, nuclear magnetic resonance, neutron and X-ray scattering and vibrating wire microbalance measurements have been used, among others. A full picture of the phase diagram of the films requires the use of more than one of these methods.

2.2.1 Vapor Pressure Isotherms

The oldest method used to study physically adsorbed films is to measure the amount adsorbed as a function of the pressure of the 3-D gas above the film. If capillary condensation does not occur, and the surface area of the adsorbate is known, then the number of molecules per unit area can be calculated. The steps in the vapor pressure isotherms roughly indicate when each layer forms, so the number of layers on the surface is known. The experimental methods for performing vapor pressure isotherms depend on whether the substrate is a porous collection of crystallites, or a single flat crystal.

Vapor pressure isotherms on porous, high surface area substrates are simple to perform because the surface area of the substrate is far larger than the surface area of the cold walls in contact with the gas (plumbing). An adsorbed film will form on any surface that is exposed to the gas at low temperature. If the vast majority of the surface area is on the chosen substrate, then the number of molecules in the film is found by subtracting the number in the gas from the total number in the system. Our cell contains 28.9 grams of Grafoam with about 578 m^2 of surface area. The surface area of the inside of the heat capacity cell (1.315" diameter by

5" long) is $2.28 \times 10^{-4} m^2$. Clearly, the surface area of the plumbing is negligible compared to that of the Grafoam.

It is possible to obtain single crystal cleaved substrates that are more perfect than Grafoil. Highly oriented pyrolytic graphite (HOPG) substrates have a coherence length of several thousand angstroms but offer less than a square centimeter of surface area. For studies with these surfaces, the internal surface area of the chamber walls is far larger than the substrate surface area. Optical ellipsometry is able to measure the approximate film thickness by reflecting a beam of polarized light off the film. It is not possible to calibrate the ellipsometer and measure the film thickness exactly because the (complex) dielectric constant of the film is not known. But it is possible to see clearly defined, sharp steps in the thickness as the pressure is increased. Up to 10 sharp isotherm steps have been observed for ethane films using ellipsometry [58]. The substrate must be located in an ultra high vacuum chamber to prevent contamination of the small surface area. Experimenters have used other techniques to study films on flat substrates. Small single crystals have been instrumented with thin film heaters and thermometers to measure the heat capacity of the adsorbed film [59]. Thin graphite fibers made to vibrate in a magnetic field are sensitive to the thickness of the adsorbed film that lies on them. The frequency of oscillation can be measured to find the film thickness, in order to record vapor pressure isotherms [4]. These experiments lack the sensitivity needed to see the small heat capacity features found in the multilayer methane at high temperatures where the substrate heat capacity is large. The difficulty of measuring the properties of the small surface area film are compensated by the fact that there is no capillary condensation on the flat substrates. The ellipsometry experiments complement the large surface area experiments by helping to determine whether capillary condensation occurs in the porous substrates. The isotherms from the two methods can be compared to determine the approximate amount of capillary condensation.

The data from the vapor pressure isotherms can determine boundaries of the coexistence regions in the phase diagram. Whenever the film is in a two phase coexistence region, the pressure is constant but the film thickness may change. When there is coexistence between patches of N layer thick film and patches of N+1 layer thick film, there must be a vertical step in the vapor pressure isotherm. Likewise, when the film passes through a first order melting transition, there is a small vertical step in the isotherm as the film density changes suddenly. However, the substrate imperfections can limit how vertical the isotherm steps are when

two film phases are in coexistence, because there are some regions of the surface with higher binding energy than others. The islands of the denser phase cannot expand without a slight increase in pressure, since they first form in the regions with the highest binding energy.

Vapor pressure isotherms can determine the substrate surface area to calibrate the monolayer capacity of the film. Previous studies of helium on Grafoil have determined the vapor pressure isotherm at 4.2 K [60]. At a point in the isotherm a registered monolayer phase exists on the surface. If the number of molecules in the film is known, and the film is in a registered phase on the surface, then the area can be calculated. The previous study from this laboratory of methane on Grafoam, by Hamilton [34], performed a 4.2 K isotherm with helium and found the substrate area. In this study, the methane data are compared against the methane data taken by Hamilton to compute the substrate surface area. It is common to use the first layer inflection point in the vapor pressure isotherm to define the monolayer coverage. Following Hamilton, this defines one methane monolayer. Note that the definition of a monolayer is somewhat arbitrary and is best used as a standard for the comparison of data from different laboratories, rather than a measure of the actual film thickness.

2.2.2 Heat Capacity Measurements

Heat capacity measurements are probably the most sensitive means to identify when a substance changes phase. Most other experimental techniques measure a material property of the substance, for example, the lattice constant. When there is a phase transition, the material property will change either discontinuously or smoothly, but the heat capacity will rise sharply. It is far easier to locate a peak in real experimental data than a small discontinuity or change of slope on a smoothly changing background. For example, vapor pressure isotherms record a discontinuity in the number of molecules adsorbed as a function of pressure when the film enters a coexistence region, but the heat capacity records a well defined peak. Whenever a phase change occurs, there is a discontinuity in either the entropy or its Nth derivative with respect to temperature at constant pressure [61, page 133]. Since the heat capacity is proportional to the first derivative of the entropy, $C = TdS/dT$, it is especially sensitive to changes of phase.

For adsorbed films, the volume and surface area are constant while the heat capacity data are taken. Then a first order phase transition in the film will not

result in a delta function heat capacity spike because the system passes through the coexistence region over a finite temperature range. The heat capacity for a first order phase transition may be lambda shaped [61, page 134], but still easy to separate from the background signal.

The number of molecules in the film is also not constant as the heat capacity data are collected. As the temperature increases, molecules from the film escape into the 3-D gas. Part of the heat needed to raise the temperature will be used for overcoming the binding energy of the molecules that are expelled. A correction must be made to the heat capacity to correct for this effect, called the desorption correction. It is possible to calculate this correction with reasonable accuracy if vapor pressure isotherms are available.

Phase boundaries that are horizontal in the number adsorbed vs. temperature phase diagram are more difficult to find using heat capacity measurements. If the system's path as the temperature rises, $N_{ads}(T)$, lies nearly parallel with the phase boundary, the phase transition will occur over a wide range of temperatures. The heat capacity will show a very broad feature that will be difficult to identify. A comprehensive review of the calorimetry of monolayer films is given by Marx [62].

2.2.3 Other Experimental Methods

Heat capacity measurements are good at finding when phase transitions occur, but do not identify the nature of the different phases. Several experimental techniques yield information about the nature of the adsorbed phases:

- NMR measures the rate of diffusion of the molecules in the film to determine if the film is solid, liquid, or gas [63, 64, 65].
- Elastic neutron scattering [14, 45] and X-Ray scattering [66] find the structure and lattice constant of the adsorbed film and identify if a phase has crystalline order.
- Quasi-elastic neutron scattering measures the mobility of the atoms in the film [19, 48].

Many of the above methods are difficult to interpret because they rely on models to convert the raw data into the desired result. For example, neutron scattering requires fitting the lineshapes to model curves. Heat capacity and vapor pressure isotherms directly measure thermodynamic quantities. However,

these methods are necessary to complete the picture of the film structure and give information that is not readily available from the heat capacity or vapor pressure data.

2.2.4 The Thermodynamic Method

As stated by Hamilton [34] and Elgin [55], it is possible to obtain a complete thermodynamic description of the film from the combination of heat capacity and vapor pressure measurements. All properties of a thermodynamic system can be found if an energy function is known as a function of its proper variables. When equilibrium is established, the chemical potentials of the film phase(s) and the 3-D gas are equal. The chemical potential of a 3-D gas is trivial to compute from the formula given by Hamilton [34, page 27]:

$$\mu = k_b T \log\left(\frac{1}{k_b}\left(\frac{2\pi\hbar^2}{m k_b}\right)^{3/2}\frac{P}{T^{5/2}}\right) + B(T) + \mu_{rot}(T) \tag{2.1}$$

where B(T) is the second virial coefficient of methane, $\mu_{rot}(T)$ is the contribution from methane's rotational energy levels, and m is the mass of the methane molecule. The Gibbs-Bangham equation allows us to find the Landau potential of the film from the chemical potential [67]. At low temperatures, the vapor pressure is too low to measure, but the heat capacity can be used to extend the Landau potential to lower temperature [55, page 48]. If such an analysis can be carried out, any thermodynamic property of the film can be calculated. In practice, taking enough vapor pressure data to fully characterize the film is very time consuming, (one hour per point) and the desorption correction to the heat capacity is difficult to make accurately enough. Since the heat capacity data give most of the information about the phase changes, this study will not attempt to apply the thermodynamic method, but the heat capacity data will be corrected for desorption using the vapor pressure measurements [34, page 29].

The previous data by Hamilton for methane on Grafoam showed some interesting features, but were not accurate enough to resolve the onset of the triple point melting peak and the small peaks around 78 K clearly. Also, it took a very long time to collect the data manually. It is necessary to automate the calorimeter and use a more efficient calorimetry technique. The next two chapters describe the design and construction of the new calorimeter.

Chapter 3

Experimental Details: Calorimetry

In its simplest form, our calorimeter consists of a graphite foam sample enclosed in a vacuum tight can or "cell," connected to the sample gas by a thin tube. A known quantity of heat is injected into the cell while measuring the temperature. The heat flow to the cell's surroundings must be either known, or minimized to yield precise or at least reproducible results.

Calorimetry measures the temperature rise for a give heat input to the sample, $C = \Delta Q/\Delta T$. Three factors determine the accuracy of a calorimeter: errors in the measurement of ΔT, errors in the amount of heat injected into the sample, and stray heat flow between the sample and its environment. The size of ΔT is another important parameter. Since ΔT must be a finite quantity, a reported heat capacity point at a temperature T is actually an average of the heat capacity over the range from $T - \Delta T/2$ to $T + \Delta T/2$. Data taken with a larger ΔT will have improved accuracy, because the fractional noise in ΔT and ΔQ will be reduced. However, since the phase transitions that we want to study may produce narrow peaks in the heat capacity, we will want to make ΔT small compared to the width of these peaks.

Our calorimeter is designed to optimize sensitivity and temperature resolution. The previous techniques either had sufficient sensitivity but insufficient temperature resolution to determine the finer features in the data, or the noise in the data obscured those features when operated with smaller ΔT. The methane film contributes a small signal in comparison to the heat capacity of the Grafoam and the aluminum can that surrounds it. Each layer of film has a heat capacity of about 1% of the background. For 1% accuracy in the data from a one layer film,

the calorimetry must be .01% accurate. Since the previous data showed features in the data separated by .1 K, ΔT must be less than this value.

Given these requirements, one must choose among several calorimetric methods: discrete heat pulse, A.C. heat input, or steady heat input techniques. Careful calculations of the thermal behavior of the proposed calorimeter yields the requirements for the thermometry, thermal isolation and heater power control for each method.

In the sections below, we will describe the different methods and how to find the required accuracy with each.

3.1 Calorimetric Methods

All methods of calorimetry measure the temperature change of a sample given a known heat input in a controlled thermal environment. The environment must either not interact thermally with the sample, or the heat flow must be corrected for. First we will discuss the experimental limitations for thermal isolation and the measurements of ΔT and ΔQ. Then we can choose among the calorimetric techniques.

Temperature Measurement

In the temperature range we are interested in, around the triple point of methane, the temperature scale is determined by several fixed points (the triple points of argon, oxygen etc.) and a standardized interpolation procedure based on the resistance of strain free platinum resistance thermometers [68]. This procedure gives errors less than 1 mK relative to true thermodynamic temperature over our temperature range and should give results reproducible to within .1 mK for different laboratories. The difficulty of establishing one's own temperature scale based on this standard is considerable, so the only practical alternative is to purchase a thermometer that has a calibration traceable to this standard. Also, suitable strain free platinum thermometers are large and have a high heat capacity that would reduce our signal to noise ratio. Miniature platinum thermometers are made that are small enough, but these are only reproducible to within 10 mK over time and thermal cycling. For calorimetry, these thermometers are sufficient because they can measure very small changes in temperature over short periods of time, given that the derivative of the calibration curve is stable. The most

significant errors in the measurement of small temperature changes is the noise and nonlinearity in the thermometer resistance measurement. Johnson noise in the thermometer, for a typical (100 ohm at 0°C) sensor driven with 100 μA, is about 3 $\mu K/\sqrt{Hz}$ at 90 K. Resistance bridges constructed with typical decade resistors are accurate to .005% or 3 mK. A much more expensive alternative is a ratio transformer bridge that approaches .0001% linearity, yielding 60 μK errors. To achieve .05% accuracy in the calorimetry using such a bridge, ΔT should be greater than .12 K for discrete heat pulse calorimetry.

Stray Heat Leaks

The sources of the stray heat flow to the calorimeter cell in our temperature range (63 to 120 K) are:

- Thermal conduction through the cell supports and the gas supply line.
- Heat flow through the residual gas surrounding the cell.
- Radiative heat transfer between the cell and its radiation shields.

All of the above factors depend on the specific details of the design and method. It is necessary to control the radiation shield temperature and the temperatures at the end of the gas supply line to minimize the heat flow. For the discrete pulse method, the temperature changes rapidly during the heat pulse. It is difficult to control the isolation temperatures accurately during this pulse, so the stray heat flow for this method will be larger and less reproducible. In contrast, the stray heat flow will not affect A.C. calorimetry, under the right conditions.

To minimize the stray heat flow from thermal conduction through the cell mechanical connections, electrical leads and fill tube:

- The supports should be made of a low thermal conductivity material, nylon or stainless steel, for instance.
- The supports should have a low area to length ratio. For the fill tube this is difficult, because we need a large diameter tube to be able to produce a high vacuum in the cell to clean the substrate.
- The end of the supports should be tied to a temperature regulated at the same temperature as the sample cell.

- The supports should be made of a material with fast thermal response time. The ratio of the heat capacity to the thermal conductivity should be small, otherwise the heat flow into the support would depend on the thermal history of the support.

Heat flow between the sample cell and its radiation shields is caused by thermal radiation and gaseous heat conduction through the residual gas surrounding the cell. The heat flow through helium gas at low pressures is approximately $dQ/dt = 2.1 a_o P \Delta T$ where the result is in $Watts/m^2$, a_o is the accommodation coefficient (near $1/2$), and P is in Pascals. For thermal radiation, the heat flow between two plane surfaces of emissivity e_1 and e_2, for small ΔT is

$$\frac{dQ}{dt} = 4\sigma T^3 \frac{e_1 e_2}{e_1 + e_2 - e_1 e_2} \Delta T$$

where σ is Stefan's constant and the result is in W/m^2 [69, page 130]. For pressure equal to 1×10^{-6} torr and emissivities of .1, the two sources of heat flow are equal at the temperature $(P/.2\sigma)^{1/3} = 23K$. Therefore, radiation is the more important source of heat transfer for this experiment.

3.1.1 Three Methods of Calorimetry

The three methods commonly in use differ in the way the heat is introduced to the sample as a function of time.

Discrete Pulse Calorimetry

In the discrete pulse method a single heat pulse is injected into the sample for a short time and the temperature change is estimated from the discontinuity in the temperature. The advantage of this method is its simplicity. All that is required is a heater and a thermometer on the sample, and adequate thermal isolation. Stray heat flow before and after the heat pulse is partially eliminated by extrapolating the pre- and post-pulse temperature versus time drift curves to the center of the heat pulse. The difference between the two extrapolations gives ΔT. There are several significant disadvantages to this technique:

- The radiation shield and fill tube may not follow the cell through the stepwise change in temperature caused by the heater pulse. Sophisticated control algorithms and careful thermal design may minimize this effect.

- If the sample under study takes a long time to reach thermal or thermodynamic equilibrium, then the post-pulse extrapolation will be less inaccurate. This may be a problem near phase transitions in our films.

- The linearity of the resistance bridge used to measure the thermometer resistance directly affects the accuracy of ΔT. As mentioned above, for .05% accuracy with a resistance bridge that is linear to one ppm, the temperature steps must be greater than .12 K . This step size is too large for some of the fine details expected in the data.

- Each heat capacity point takes at least 20 minutes of time to complete. This includes five minutes of post-pulse dead time and 15 minutes of temperature measurement. Typical thermal equilibrium times for Grafoil/aluminum cells are one to two minutes. A scan from 65 K to 120 K, the desired range for this experiment, would take eight days of continuous operation. This is far too long, since at least 20 runs are needed to characterize the film's behavior.

These considerations make the discrete pulse method undesirable for our study, despite its simplicity.

A.C. Calorimetry

A.C. temperature calorimetry overcomes many of the difficulties of conventional discrete pulse calorimetry by eliminating the need for ideal thermal isolation between the sample and its surroundings, and by allowing the data for a single point to be averaged over time to improve the signal to noise ratio. The procedure is to provide a thermal link between the sample and another body held at a fixed temperature, T_b. The sample heater power is varied sinusoidally, so the heat flow into the sample is

$$Q_{sample} = A(1 + \sin \omega t) + K(T_b - T_a)$$

where t is time, A is the amplitude of the heater input, $\omega/(2\pi)$ is the frequency of the sinusoidal heat input, T_a is the sample temperature, and K is the thermal connection between the sample and the body at fixed temperature. The sample responds to the heat input by warming exponentially to a temperature A/K

degrees above T_b, along with a sinusoidal variation:

$$\frac{A}{(C\omega)^2 + K^2}(K \sin \omega t + C\omega \cos \omega t)$$

where C is the heat capacity of the sample. If the thermal relaxation time for the cell is much larger than the period of the heater input, $C/K << 2\pi/\omega$, then it is easy to find the heat capacity of the sample from the known power input and the measured amplitude of the sinusoidal temperature variation. Another condition must be met for this method to work: the thermometer response time and the times for internal thermal and thermodynamic equilibrium must be short compared to the period of the heater input. Small samples are used to give fast thermal response times, but it is difficult to estimate the time needed for thermodynamic equilibrium, especially near phase transitions. Once the sample temperature has stabilized, data can be averaged for a long time to reduce the effect of noise in the thermometer and in the temperature control of T_b. The noise in the heat capacity caused by the thermometer noise n is equal to $nC/(G\sqrt{t})$ where t is the measurement time, G is the amplitude of the temperature oscillations and n is measured in units of $K/\sqrt{Hz}$. If we allow .01 K oscillations, and use a platinum thermometer resistance bridge with 2 $nV/\sqrt{Hz}$ voltage noise and 100 μA excitation, then the measurement time to achieve .05% error is 100 seconds. Since the data should be taken for several periods of the heat input frequency, each data point may take much longer than 100 seconds. Also, the sample to environment time constant, K/C, must be long compared to the frequency of the heat input, so it may take several minutes for the D.C. sample temperature to stabilize before data are taken. Nevertheless, this technique is capable of yielding high accuracy data, without elaborate thermal isolation. (See for example reference [2]. For a more through analysis of this method, see reference [70].)

Differential Scanning Calorimetry

Differential scanning calorimetry is a technique that can solve the problems of the other methods, and produce data at a rate limited by the noise in the data. There are several variations on this method, but the most standard is to place two identical sample holders side by side in a radiation shield. One holder contains the sample to measure and the other contains a standard with known heat capacity. Thermometers monitor the sample temperature and the temperature difference between the two bodies. A constant heat input to the standard causes

its temperature to rise linearly with time. Meanwhile, the sample heat input is adjusted to keep the temperature difference zero. If $T_{std}(time) = T_{sample}(time)$, then

$$C(sample + holder) = C(std + holder)\frac{Q(sample)}{Q(std)}$$

ignoring all stray heat flow.

If the two bodies have the same heat leak to the environment and the same heat capacity, the stray heat flow will not affect the heat capacity ratio measurement. Also, since the temperature is rising smoothly with time, it is easier to maintain the environment at the same temperature as the sample. As we will discuss below, it is possible to obtain .01% error with this technique.

3.2 Differential Scanning Calorimetry

The configuration we will analyse below has two bodies. Similar methods were used by many experimenters, for example references [71] and [72]. The first body holds the sample, having heat capacity C_0, temperature T_0, heat input W_0, and unknown heat leak W_{o0}. The second has known heat capacity C_1, temperature T_1, heat input W_1, and unknown heat leak W_{o1}. The two cells are coupled together with thermal coupling K, so that $K(T_1 - T_0)$ watts flow into the sample cell. Then the first order differential equations for both bodies are

$$\frac{dT_0}{dt} = \frac{W_0 + K(T_1 - T_0) - W_{o0}}{C_0(T_0)}$$

$$\frac{dT_1}{dt} = \frac{W_1 - K(T_1 - T_0) - W_{o1}}{C_1(T_1)}.$$

We measure the temperature of the sample, T_0, and the temperature difference between the two cells, $\delta T = T_0 - T_1$. Substituting,

$$\frac{d\delta T}{dt} = \frac{W_0 - K\delta T - W_{o0}}{C_0(T_0)} - \frac{W_1 + K\delta T - W_{o1}}{C_1(T_1)}$$

Solving for the unknown $C_0(T_0)$ gives:

$$C_0(T_0) = \frac{C_1(T_1)(W_0 - K\delta T - W_{o0})}{C_1(T_1)\frac{d\delta T}{dt} + W_1 + K\delta T - W_{o1}}$$

To find the film heat capacity we must subtract the heat capacity measured during a background run without a film:

$$C_{film}(T_0) = C_0'(T_0) - C_0(T_0) =$$

$$\frac{C_1'(T_1')(W_0' - K'\delta T' - W_{o0}')}{C_1'(T_1')\frac{d\delta T'}{dt} + W_1' + K'\delta T' - W_{o1}'} - \frac{C_1(T_1)(W_0 - K\delta T - W_{o0})}{C_1(T_1)\frac{d\delta T}{dt} + W_1 + K\delta T - W_{o1}}$$

Note that T_1' is not necessarily equal to T_1. If we assume that there is no stray heat flow and that $K\delta T$ is negligible,

$$C_{film}(T_0) = \frac{C_1'(T_1')W_0'}{C_1'(T_1')\frac{d\delta T'}{dt} + W_1'} - C_{background}(T_0) \tag{3.1}$$

where C_{bgnd} is a previously measured background heat capacity. It is useful to linearize this with respect to the small quantities $C_1 d\delta T/dt$, $K\delta T$, W_{o0} and W_{o1}. To first order in these:

$$C_0 = C_1\left(\frac{W_0}{W_1} - \frac{K\delta T + W_{o0}}{W_1} - \frac{W_0}{W_1}\frac{C_1\frac{d\delta T}{dt} + K\delta T - W_{o1}}{W_1}\right) \quad .$$

But to find the film heat capacity we must subtract the background heat capacity. If we assume that the background run was taken with the same standard heat capacity and heater power, $C_1' = C_1$ and $W_1' = W_1$. Then the film heat capacity equals

$$C_{film} = C_0(T_0) - C_0'(T_0) = C_1\frac{W_0 - W_0'}{W_1} + \frac{1}{D^2}\left[W_0\frac{d\delta T}{dt} - W_0'\frac{d\delta T'}{dt}\right] +$$

$$\frac{1}{D}\left[\left(1 + \frac{W_0}{W_1}\right)K\delta T - \left(1 + \frac{W_0'}{W_1'}\right)K'\delta T' + \left(W_{o0} - W_{o1}\frac{W_0}{W_1}\right) - \left(W_{o0}' - W_{o1}'\frac{W_0'}{W_1'}\right)\right]$$

where $W_1/C_1 = W_1'/C_1' = D$, and where D is the standard drift rate per unit time. Let us examine each term.

$$C_1\frac{W_0' - W_0}{W_1}$$

This term is the ideal value for the film heat capacity assuming that the temperature control is perfect and there are no heat leaks.

$$\frac{1}{D^2}\left(W_0\frac{d\delta T}{dt} - W_0'\frac{d\delta T'}{dt}\right)$$

This term is the correction for the finite temperature difference between the sample cell and standard. As the cell temperature drifts through features in the heat capacity, there will be some small error in the temperature control. This can

be corrected for by numerically differentiating the δT data. The statistical and systematic errors in computing this derivative are significant and will be discussed below.

$$\frac{1}{D}\left[\left(1+\frac{W_0}{W_1}\right)K\delta T-\left(1+\frac{W_0'}{W_1'}\right)K'\delta T'\right]$$

This term represents the error caused by the finite thermal coupling between the two bodies and the errors in the sample temperature control. With accurate temperature control, and careful design to keep the coupling low, this term can be made small.

$$\frac{1}{D}\left[\left(W_{o0}-W_{o1}\frac{W_0}{W_1}\right)-\left(W_{o0}'-W_{o1}'\frac{W_0'}{W_1}\right)\right]$$

All the stray heat leaks into the cell and standard are lumped into this expression. There are two sources of such heat leaks. The first is thermal contact (gaseous heat conduction and thermal radiation) between each body and the radiation shield. The second is heat flow through the bodies' mechanical supports including the gas supply lines. Note that if the background run has similar heat leaks, there will be some cancelation in the above expression. A major purpose in the design of the calorimeter is to reduce the size of this term.

The size of the each term above determines the requirements for a part of the probe and associated instruments. We will first discuss the rough technical requirements for making each term's error contribution near the desired accuracy of .01%, then in the sections that follow we will describe the details of the instruments actually used.

Errors in the Ideal Film Heat Capacity

The primary contribution to the film heat capacity comes from the ratio of the cell/standard power inputs multiplied by the standard heat capacity

$$C_1\frac{W_0'-W_0}{W_1}.$$

The standard heat capacity is computed from the simple relationship:

$$C_{std}=W_{std}\Big/\frac{dT_{std}}{dt} \tag{3.2}$$

using data from a background heat capacity run. Since the standard heat capacity is smooth, the data may be fitted to a low order polynomial to reduce the large statistical errors caused by computing the derivative numerically. Systematic

errors in this measurement are caused by errors in the heater power and errors in the temperature scale for the thermometer.

The thermometry errors were made as small as practical by purchasing a miniature platinum thermometer calibrated against a secondary standard by Lake Shore Cryogenics. Strain free platinum thermometers and certain fixed temperature points define the temperature scale from 14 to 673 K according to IPTS-68. Although our thermometer is not strain free, the data for the entire temperature range from 14K to 320K were fit to a single function with 21 parameters as described in IPTS-68. This yields a temperature scale that may have some smooth errors, but should have no "bumps". The error in the standard heat capacity due to the temperature scale is hard to estimate since it is the derivative of the temperature scale error. Since the calibration data were originally accurate to 1 mK and a long term shift due to strain on the platinum wire is likely to give only a uniform shift to the temperature scale, the thermometry errors should be insignificant. In any case improving this technique would require a much larger strain free thermometer [73]. This is impossible because of the added heat capacity and longer thermal response time.

Typically, the thermometers exhibit less than 1 mK temperature shifts once cold, but can drift 10 mK upon thermal cycling to room temperature. Therefore it is necessary to remake the background heat capacity measurement every time the apparatus is warmed to room temperature. The cell platinum thermometer resistance is measured with an automated programmable ratio-transformer bridge that is linear to one part in 10^6 and has less than 1 $nV/\sqrt{Hz}$ noise. The resistance standards in the bridge are precision wirewound resistors, measured by a resistance bridge traceable to N.B.S., with better than 10 ppm/C temperature stability. They are maintained to within .1°C in a temperature controlled oven. Therefore our temperature scale should be limited only by the thermometer stability.

The fractional error in the film heat capacity due to the standard heat capacity error is simply $\delta C_1/C_1$. Because of the large background signal, we can only determine the heat capacity of a one layer film to about 1%. Therefore, we only need to know the standard heat capacity to better than 1%, provided that it is stable to .01% between the background and sample runs to allow an accurate background subtraction.

For .01% accuracy in the sample heat capacity we need to know the cell heater power to that accuracy. Since $P = V^2/R$, we need to make the voltage measurement to within .005% and the resistance measurement to within .01%. To meet

this goal, we have constructed a heater power source that continuously monitors the heater resistance while applying the desired voltage to the heater. The circuit is based on a 16 bit D-A converter (Analog Devices AD1147) that is linear to .00076%. This gives us .005% accuracy for outputs that are 15% of full scale, and allows full accuracy over a wide dynamic range. During operation, the heater is wired in a 4-wire D.C. Kelvin resistance bridge that compares the heater resistance to a decade resistance box accurate to .02% or better. The ratio arms of the bridge consist of a pair of .01% precision wirewound resistors. The bridge imbalance is measured with a P.M.I. AMP-01 instrument amplifier whose output is is digitized and recorded by the computer.

Errors Due to Cell and Standard Temperature Measurement and Control

The contribution to the heat capacity due to the temperature control error is

$$\frac{1}{D^2}\left(W_0\frac{d\delta T}{dt} - W_0'\frac{d\delta T'}{dt}\right)$$

where $D = W_1/C_1$. The main error contribution to this term is in the error in measuring $d\delta T/dt$, since W_1, W_0 and C_1 are known to .02%. It can be shown that for normally distributed random noise on a slowly varying signal, the best way to compute the derivative is to fit the data to a line by minimizing the sum of the squared deviations[1]. In this case the noise in the derivative is $n = e\,2\sqrt{3}\,t^{-3/2}$, where e is the noise per $\sqrt{Hz}$ in the input data, t is the measurement time in seconds. It is assumed that there are many points in the interval. To estimate the thermometry noise required for .01% error, we will choose reasonable valves for the parameters, and assume $W_1 = DC_0$. The cell heat capacity is about 15 J/K, and the drift rate is 2 K/hour. We expect the cell to come to thermal equilibrium in approximately 90 seconds, so we should allow 180 seconds or longer to compute each derivative point. Then the necessary thermometry noise is $40\mu K/\sqrt{Hz}$. The nominal sensitivity of platinum resistance thermometers is $40\mu V/K$ using sensor currents of .1 mA, so the desired noise in the resistance bridge is $1.6nV/\sqrt{Hz}$. This is well within the Johnson noise limit for the thermometer, and a transformer coupled bridge can typically give noise performance below 1 $nV/\sqrt{Hz}$. We use a

[1] If the data have significant curvature, as when the calorimeter passes through a heat capacity peak, a higher order curve should be used. The heat capacity data were analysed by fitting a cubic polynomial to δT.

four wire A.C. Kelvin resistance bridge with ratio transformer voltage dividers to measure δT. Its voltage noise is about $2nV/\sqrt{Hz}$.

Stray Heat Leaks and Thermal Design

The heat capacity error due to stray heat leaks is

$$\delta C = \frac{1}{D}\left[\left(W_{o0} - W_{o1}\frac{W_0}{W_1}\right) - \left(W'_{o0} - W'_{o1}\frac{W'_0}{W'_1}\right)\right] \quad .$$

Stray heat flow into the sample must be less than or known to within .01% of DC_0 and stray heat flow into the standard must be less or known to within .01% of DC_1W_1/W_0. If $C_0 \approx C_1$, $D = 2\ K/hour$, and $C_0 = 15\ J/K$, then the stray heat leaks should be less than or known to within .8 μW. The sources of heat transfer are due to heat flow through the cell mechanical supports and thermal radiation between the radiation shield and the bodies.

The heat flow through the gas fill line is caused by simple linear heat conduction, $W = K(A/L)\Delta T$. To give adequate pumping speed for eliminating contaminants from the large Grafoil surface, we decided to use a large, 1/4 inch diameter fill tube. A large fill tube also reduces the chance of forming plugs of bulk solid when filling the cell. The wall thickness needed for a 1/4 inch diameter stainless steel tube to withstand external pressure of two atmospheres is about .003 inches. A .005 inch thick wall is more mechanically stable and gives a reasonable safety margin. The longest practical length for the fill tube is two inches, because of the limited vertical space in our dewar. Using standard values for the stainless steel thermal conductivity at 100 K, we find the thermal conductivity of the fill tube is .5 mW/K. The twenty-eight 20 cm long, 37 gauge copper electrical leads connected to the standard provide .6 mW/K of additional thermal conductivity. Then, to limit the heat flow to below .8 μW, we must control the temperature of the stage above the standard to better than 1.3 mK. If the thermal connections between the sample and the environment and between the standard and the environment are matched to within 10%, then we can allow 13 mK error in the temperature and still achieve .01% error in the heat capacity ratio between the two bodies. Since it is possible to control temperatures to within 2 mK using platinum or silicon diode thermometers, heat transfer through the fill tubes may be controlled adequately.

A temperature controlled radiation shield must enclose the bodies to eliminate stray heat flow. The probe must be evacuated to isolate the bodies from the

radiation shields. The amount of thermal radiation is given approximately by assuming the two surfaces are parallel and of equal area, and that ΔT is small compared to T,

$$W = 5.67 \times 10^{-12} AT^3 \frac{e_1 e_2}{e_1 + e_2 - e_1 e_2} \Delta T$$

with W in watts, A in cm^2, e_1 and e_2 are the emissivity of the surfaces, and T is in Kelvins. To keep this heat flow below .8 μW at 100 K, the temperature control errors should be less than 12 mK for the following typical conditions: 2 K/hour drift rate, a sample cell 1.25 inches diameter by five inches long, and the cell and radiation shield emissivities one and .03 respectively. This is a reasonable requirement for the inexpensive and easy-to-interface diode thermometers.

What is the vacuum necessary to keep the heat transfer due to gaseous heat conduction between the radiation shield and the cell below that from thermal radiation? Helium gas is used for cooling down the cell, so we must assume that this is primary residual gas. The heat flow through helium gas is given by $2.1 a_o P \delta T$ where the result is in W/m^2, a_o is the accommodation coefficient (near 1/2), and P is in Pascals. This equation takes the thermomolecular correction into account. It is assumed that the pressure is low enough for the mean free path to be greater than the $\sim$1 cm spacing between the radiation shield and sample cell. Then to give heat flow less than .8 μW, with $\Delta T = 12mK$, the pressure should be less than 3×10^{-5} torr. We can easily achieve pressures less than 2×10^{-6} torr.

To maintain the radiation shield as an equithermal surface, it is necessary to add another radiation shield around it. Variations in heat flow along the surface caused by variations of emissivity, geometry and bath temperature may cause irreproducible thermal gradients in the shield. This problem is difficult to model, but it is clear that small changes in these parameters, when combined with the fact that the temperature shield may be as much as 60 K above the bath temperature make it clear that two radiation shields are necessary for temperature control to within 12 mK, for a radiation shield as long as is necessary for this experiment (12 inches).

Design Implementation

I have demonstrated that it is possible to achieve calorimetry that is accurate to .01% using a differential scanning technique with two nearly identical bodies, a sample and a standard. However, a practical problem stands in the way of this design. To make the bare Grafoil heat capacity large compared to the heat

capacity of the cell walls, the sample cell must have reasonably large dimensions, about 1.25" wide and 5" long. Two cells, surrounded by two concentric radiation shields spaced .25" apart make the total diameter equal to 4.25". A detachable vacuum joint must be made between the vacuum can and the probe, increasing the diameter about 1", to total 5.25". Since the available dewar flasks for this experiment were 4" and 12", and the 12" dewar is too costly to operate with liquid helium, it was necessary to consider a way to make the probe narrower. One possibility was to place two identical cells one above the other, but since the cells need to be about 5" long, this made the probe too long, as well as violating the symmetry that makes the heat input to both cells identical. The solution implemented was to give up matching the cells and make the standard cell of a heavy block of solid copper mounted directly above the sample cell. Then the lighter sample cell is not thermally connected to the fill tube support, and the high standard cell heat capacity reduces the temperature control requirement for the fill tube support. If the standard heat capacity is five times the sample cell heat capacity, the maximum error for the fill tube end temperature becomes 6.5 mK, a requirement that is easily achieved with inexpensive diode thermometers and electronics.

Figure 3.1 shows a schematic diagram of the calorimeter probe. During operation, the standard heat capacity receives a constant heat input from heater H1. The temperature difference between thermometers T2 and T1, δT, is input to a digital proportional-integral-derivative (P. I. D.) feedback control algorithm that controls the power to the sample cell heater H2. δT is typically below .001 K, even with rapid changes in the sample heat capacity. Silicon diode thermometers are located on the standard heat capacity, the isolation thermal mass, the upper thermal platform, and both radiation shields. The signals from these thermometers control the relative temperatures of these bodies to within .5 mK of their set-points, to prevent irreproducible stray heat flow to the standard or sample. During operation, the upper thermal platform and the isolation thermal mass set-points are .1 K warmer than the sample cell to eliminate the condensation of bulk solid or liquid inside the gas fill line. The heat flow coming from room temperature via the fill tube and electrical leads travels through the upper thermal platform and the helium gas heat switch, then to the liquid nitrogen or helium bath. By varying the pressure of the gas in this device, we can operate either close to the bath temperature or far above it without wasting the cryogenic bath surrounding the probe. Radiation baffle C and the inner radiation shield enclose

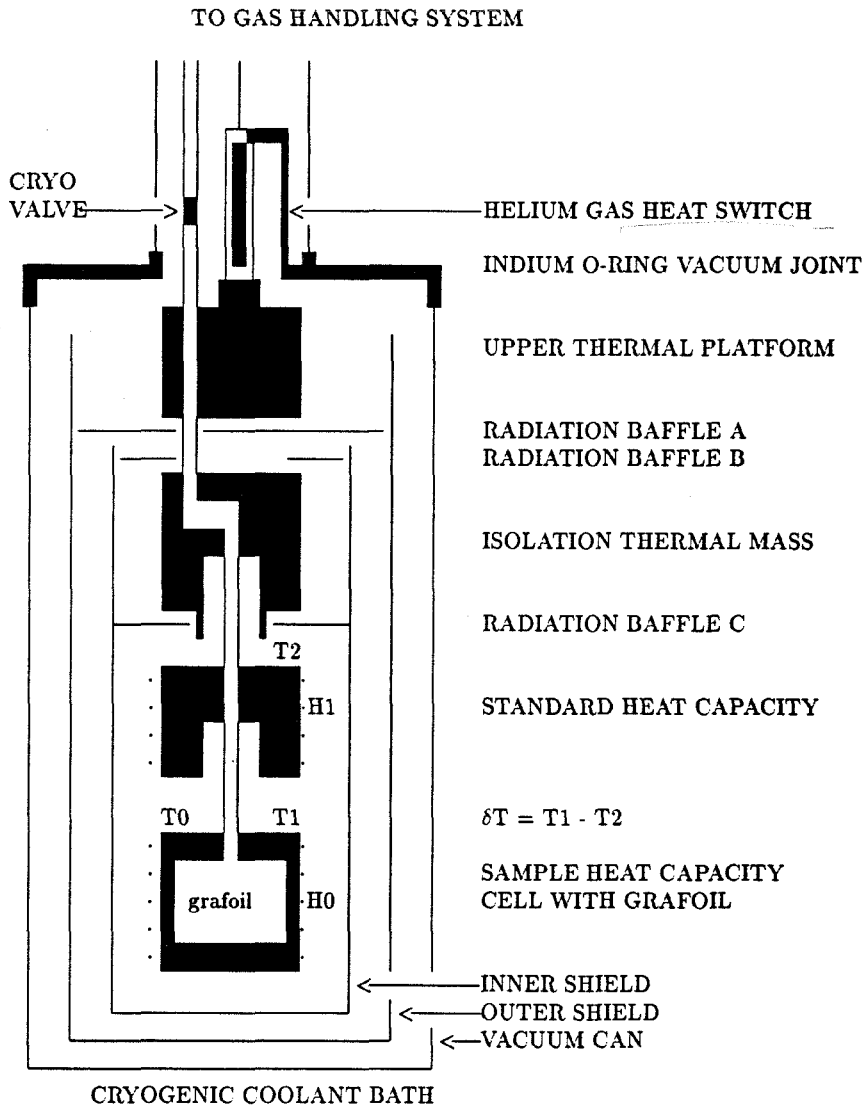

Figure 3.1: Calorimeter Schematic Detail.

the sample cell and standard heat capacity in a reproducible thermal radiation environment. The hot thermal radiation from room temperature is blocked by the outer radiation shield and radiation baffles A and B in order to allow accurate temperature control of the isolation thermal mass and the inner radiation shield. The cryogenic valve in the gas fill line may be closed to limit the volume of gas in the vapor phase in the system. Then the amount of sample gas in the film is more constant as the cell temperature and gas vapor pressure rise during calorimetry. The aluminum sample cell contains 28.9 grams of Union Carbide Grafoil Mat which has been outgased at 1000°C and 1×10^{-6} torr.

This design is much like the calorimeter used by Buckingham et al. [71] except that we cannot enclose the successive stages within each other. This is because the cell is cooled down by introducing helium gas into the vacuum can to increase the thermal conductivity between the cell, radiation shields and the cryogenic bath. At all times, the cell must be the coldest part of the system, to prevent the gas from condensing anywhere but on the graphite. There cannot be a large thermal contact between the radiation shields and the upper stages of the calorimeter, since the radiation shields must be colder than the cell in order to cool down. Therefore we need twice as many temperature regulated stages compared to Buckingham et al. , and it is more difficult to prevent radiation leaks between the successive stages.

Another necessary feature of the calorimeter is computer control. During operation, four isolation temperatures are regulated, the cell heater power and the resistance bridge balance ratio must be changed, and the sample and standard heater power recorded. A manual system is impossible since a scan from 65 to 120 K takes 28 hours at a 2 K/hour drift rate. Several other modes of operation are necessary as well, because the apparatus must also be used for vapor pressure isotherms. Precooling before the heat capacity run must follow a reproducible temperature vs. time curve. With computer control, the setpoints of the temperature controllers and their control parameters can be reset with each different mode of operation. Also, computer control improves the reproducibility of the data. It was decided early on in the design of this apparatus to implement nearly total automation, instead of adding automation to a manual version of the apparatus. This saved time in two ways: all testing and debugging of the experimental methods and instruments took advantage of the computer control, and many of the instruments were more easily built with only digital interfaces without manual control panels. Furthermore, the low noise A.C. resistance bridges were so sen-

sitive to interference noise from the computer that they could be debugged only with the computer interface in place.

Chapter 4

Instrument Design

In the sections below we will describe each subsystem of the aparatus, following the outline below.

4.1 Graphite Foam Substrate

4.2 Calorimeter Design and Construction

4.3 Probe Plumbing Details, Heat Switch

4.4 Sample Gas Delivery and Pressure Measurement

4.5 Thermometry: Overview

4.6 Relative Resistance Bridge

4.7 Absolute Resistance Bridge

4.8 Silicon Diode Thermometer Interface

4.9 Heaters and Power Metering Circuits

4.10 Computer Control and Interface

4.1 Graphite Foam Substrate

The Grafoil Mat used in this experiment was acquired from the Union Carbide Corporation Electronics Division Specialty Products Group. As mentioned above, it is a precursor to Grafoil sheet. After exfoliation and recompression, the graphite was purified by heating to 1500°C in a chlorine atmosphere. Upon arrival in our

laboratory, the .1 inch thick sheets of foam were cut into 1.315 inch diameter disks with a brass "cookie cutter." The disks fit tightly to improve the thermal contact between the Grafoil and the cell. A .18 inch diameter hole was punched in the center of each disk, to improve the flow of gas through the cell. In our laboratory, the foam was outgassed at 1000°C in a quartz tube until the pressure was below 1×10^{-6} torr. The quartz tube was evacuated by a liquid nitrogen trapped turbo-pump, and the temperature was measured with a chromel-alumel thermocouple. The outgasing procedure was significantly improved from our previous experiments [34, 74], where the sample was surrounded by an electric heater within the vacuum chamber. In this experiment, the heater was outside of the vacuum, surrounding the quartz tube. This reduced contamination and allowed lower pressures to be attained.

Without exposing the Grafoil to air, the sealed tube was transferred to a glove box filled with dry nitrogen gas. In the glove box, the graphite disks were pressed into the cell. The cell was bored to a slightly larger inside diameter at the opening to ease fitting the disks into the cell. Then the cell was sealed off and attached to the calorimeter.

4.2 Calorimeter Construction and Design

The minimum requirements to implement the differential scanning calorimeter as described above are:

- Sample cell
- Standard heat capacity
- Dual radiation shields
- Isolation thermal mass on gas fill line attached to the standard.

Also, there must be an extra stage located above the isolation thermal mass. This is because there will be a large amount of room temperature heat conducted through the electrical leads and gas fill tube to the first stage at low temperature. The heat flow will generate large temperature gradients in the first stage, making its temperature difficult to control accurately. Since the first stage will need to have a direct thermal connection to the bath to be maintained at constant temperature, the heat flow from the bath will vary as the bath temperature fluctuates.

That makes it much harder to achieve the ~7 mK temperature control needed to isolate the standard heat capacity thermally. Adding another temperature regulated stage, isolated from the "isolation thermal mass," solves this problem.

4.2.1 Sample Cell

The most important part of the calorimeter design is the sample cell. Its properties affect the design of all other parts of the calorimeter. The sample cell is simply a gas-tight container filled with Grafoil and connected to the gas fill line. It must have an electric heater and one or more thermometers. The design criteria for the sample cell are:

1. The Grafoil foam heat capacity should be the largest fraction of the cell heat capacity.

2. Heat applied to the cell should be distributed through the cell and Grafoil rapidly to minimize the cell's thermal time constant.

3. The cell should be able to withstand an external pressure of two atm while evacuated, and an internal pressure of two atm while surrounded by vacuum.

4. The cell should not contain any internal parts with vapor pressures above 1×10^{-6} torr, to avoid contaminating the Grafoil surface. The Grafoil should not be contaminated while the cell is sealed off.

5. A reliable cryogenic vacuum seal must be made between the cell and the low thermal conductivity stainless steel gas fill tube.

6. The cell heater must have low heat capacity, be electrically isolated from the cell, and thermally anchored to it.

7. There must be locations for mounting thermometers on the cell and for tempering the thermometer leads to the cell.

A cell design that does not satisfy the third requirement would rupture or collapse, so we will consider this requirement first. As anyone who has ever crushed a beer can will attest, the collapsing pressure of a vessel is much lower than its

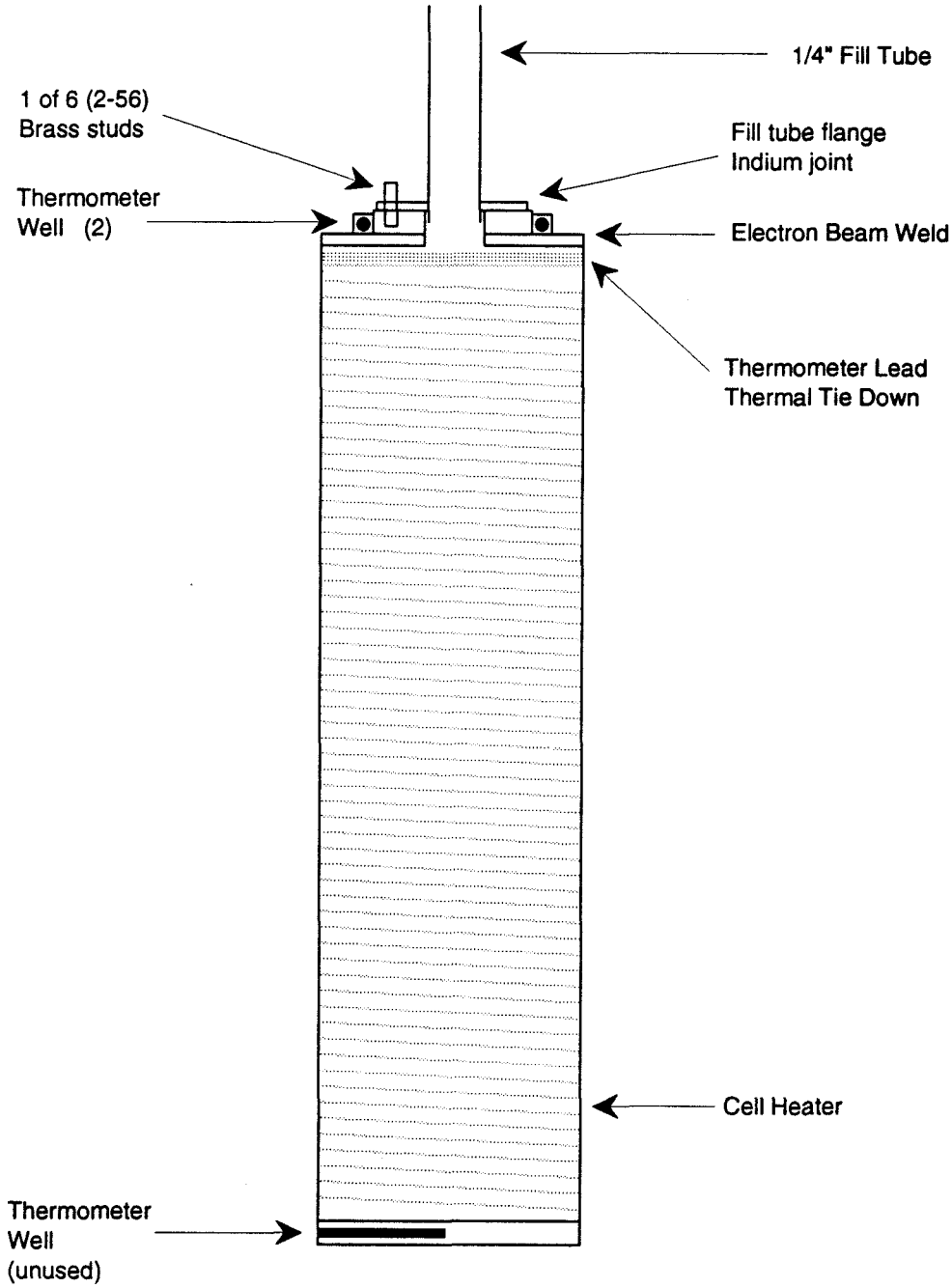

Figure 4.1: Calorimeter Sample Cell.

bursting pressure, so the cell wall thickness is fixed by the maximum external pressure. The collapsing pressure for an infinitely long tube is

$$P = \frac{2E}{1-\sigma}(\frac{t}{D})^3$$

where E is Young's modulus, σ is Poisson's ratio (about .37), t and D are the wall thickness and diameter respectively, and P is given in pounds per square inch. Then the thickness of the cell wall is

$$\frac{t}{D} = \sqrt[3]{P(\frac{1-\sigma}{2E})} \quad .$$

The wall thickness then scales linearly with the diameter of the vessel, and as the cube root of the material property. Young's modulus for copper is about 16×10^6 lbs/in^2 and for steel it is 30×10^6 lbs/in^2. Therefore, the wall thickness does not depend strongly on which metal we use. For 2 atm of pressure outside a copper cell, t/D equals .011. If the Grafoil is tightly packed, it will provide considerable stiffness to resist collapse, so a large safety factor is unnecessary. Our cell has an outside diameter of 1.32 inches, with .010 inch wall thickness, see figure 4.1. For more information about vessels under external pressure with internal supports (submarines) see references [75, 76, 77, 78].

Because the mechanical properties do not determine the cell's dimensions, we are free to choose a material that optimizes the thermal properties. The cell can be thermally modeled as two bodies joined by a weak thermal link, the cell wall and Grafoam. Each has an individual heat capacity and a time for internal thermal equilibrium. The thermal contact between the cell and the Grafoam is usually poor, the heat flow occurring through the sample gas and the direct points of contact. For low sample gas pressure, this thermal boundary will be the limiting factor for the cell's thermal equilibrium. The time constant for thermal equilibrium between the two bodies is proportional to

$$\frac{K(C_{gr} + C_{cell})}{C_{gr}C_{cell}}$$

where K is the thermal conductivity of the weak link. In this case the cell should be constructed of a material with low ρC to minimize the background heat capacity, in order to increase the signal to noise ratio as well as reduce the time for thermal equilibrium. Table 4.1 shows the thermal properties of copper, aluminum, magnesium, and Grafoil foam with densities of 8.96, 2.70, 1.74, .172 g/cm^2 respectively [79, 54].

	Temperature (Kelvins)								
Property/material	20	40	60	80	100	140	200	250	300
Thermal conducitivity K, (W/K cm)									
OFHC Cu	>10	>10	7.0	5.0	4.5	4.5	4.5	4.5	4.5
6063 Al	1.8	2.8	2.8	2.3	2.1	2.0	2.0	2.0	2.0
Pure Mg	12	5.5	2.8	1.9	1.7	1.6	1.6	1.6	1.6
Grafoam $\parallel$	.003	.02	.05	.1	.15	.2	.2	.2	.2
Grafoam $\perp$	.0005	.003	.006	.01	.01	.009	.008	.007	.006
Thermal diffusivity, K/ρC (cm^2/seconds)									
OFHC Cu	160	18	6.0	2.8	2.0	1.6	1.4	1.4	1.3
6063 Al	73	17	7.8	2.3	1.6	1.1	.93	.86	82
Mg	46	24	4.7	2.1	1.5	1.1	.99	.94	.90
Grafoam $\parallel$	2.9	4.3	4.8	5.8	6.2	4.8	2.8	2.0	1.6
Grafoam $\perp$	.48	.64	.58	.58	.41	.21	.11	.07	.05
Thermal density ρC (J/K cm^3)									
Cu	.063	.54	1.2	1.8	2.3	2.8	3.2	3.3	3.5
Al	.024	.21	.58	.96	1.3	1.8	2.2	2.3	2.4
Mg	.026	.23	.58	.89	1.1	1.4	1.6	1.7	1.8
Grafoam	.001	.005	.01	.017	.024	.041	.071	.098	.124

Table 4.1: Calorimeter cell wall materials

The thermal conductivity gives the heat flux through a 1 cm cube for 1 K temperature difference across opposing faces. The thermal diffusivity is proportional to the inverse of the time constant for thermal equilibrium within the material. The thermal density gives the heat capacity of a 1 cm^3 cube. The thermal density of aluminum is almost half that of copper, but aluminum has roughly half the thermal conductivity of copper. If the thermal contact between the Grafoam and the cell wall limits the thermal equilibrium time, then aluminum is better. We decided to make the cell out of aluminum to minimize the cell time constant when there is no sample gas, and because it reduces the background heat capacity, which increases the signal to noise ratio. Magnesium was not used because it is more difficult to work with (being quite combustible), and would yield only a slight reduction in background heat capacity. Calorimeters are not usually made of aluminum because it is not easily soldered or brazed, and because it is difficult to make leak tight detachable joints between aluminum and stainless steel.

Another problem to be solved in designing the cell is how to seal the Grafoam in the cell without contaminating it. It is undesirable to solder or braze the cell after inserting the Grafoam, because soldering flux would contaminate the foam. An indium wire seal can be used to seal the cell top, but this increases the diameter

of the cell, and adds to its heat capacity [34]. Instead the cell was joined together with an electron beam weld. Because electron beam welding is done in a vacuum, without any flux, the grafoam is not significantly contaminated. Also, these welds are very reliable and leak tight when thermally cycled.

The cell must be attached to the sample gas stainless steel fill tube with a leak-tight joint. It is easier to construct the calorimeter if this joint is detachable. Since aluminum and stainless steel cannot be welded or soldered together [80], an indium wire joint was made between the cell top and a miniature flange that was silver soldered to the sample gas fill tube. The joint was held together by six (2-56) brass studs, nuts, and hardened beryllium copper cup-shaped spring washers. Since aluminum contracts much more than stainless steel when cooled to cryogenic temperatures, this joint tends to leak an insignificant amount of gas whenever rapidly cooled or warmed. The stainless steel flange was later replaced with a brass one, because brass matches the thermal expansion of aluminum three times better than stainless steel.

The cell heater should provide power to the cell that is known to $\pm.01\%$. To improve the response time of the cell's feedback control, the heater must be thermally anchored to the cell, and it must have low heat capacity. Also, the heater wire resistance should be constant over the temperature range of the experiment, and the heat should be applied evenly to the surface of the cell. A 6-wire heater mounted on the cell satisfies these requirements and also allows four different resistance choices to match the maximum power to the desired experiment. Two strands of heater wire and one copper wire wind together around the cell in a spiral groove. They are glued to the cell using Stycast 2850 epoxy (catalyst 24LV)[1]. This glue was used for all of the wires on the apparatus and proved very reliable. The heater wires were 12.6 and 82.5 Ohm/foot Evanohm[2] wire, which have temperature coefficients of resistance less than 10 ppm/C. The three wires are soldered[3] together on the bottom of the cell. On the top of the cell, each of the

[1]Trademark, Emerson & Cuming Inc. The standard calorimetry cement, G.E. 7031 varnish, could not be used because it does not adhere to aluminum. Stycast epoxy also provides better thermal contact and may be removed later with a special stripper. This and all other heaters in the apparatus were wound on a special motor driven wire winder. The three wires were wound in parallel onto the form. Just before they contacted the form, their undersides were coated with epoxy from a hypodermic syringe. Compressed air drove the thick epoxy out of the syringe.

[2]Trademark, Wilbur B. Driver Co.

[3]The evanohm wire was soldered using acid flux and lead solder. After a through cleaning, the joints were glued to the cell with an insulating layer of cigarette paper to prevent an electrical short.

two heater wires are soldered to two copper wires, a voltage and a current lead. The copper wire extends to the standard heat capacity where it joins current and voltage leads also[4]. The currents in the adjacent heater wires cancel to prevent generating a magnetic field that would interfere with the thermometers. Coupled with the heater control circuit to be described below, the cell heater was accurate and reliable.

There are two platinum thermometers on the cell, one to read the absolute temperature, and the other as one of a pair of thermometers that read the temperature difference between the cell and the standard. They were coated with type 'L' Apiezion[5] grease and inserted into tight fitting holes on the top of the sample cell. It is important to temper the electrical leads of any thermometer, so the copper thermometer leads were wound once around the cell and glued down with epoxy.

Two modifications were made to the cell after its initial testing. To reduce the emissivity of the cell, it was wrapped with aluminized mylar that was tied down with dental floss and thermally anchored with vacuum grease. The second modification was to mount a separator that prevents the cell from touching the inner radiation shield. The separator consists of a very light stainless steel ring with four lengths of .007 inch diameter music wire tightly strung inside it to form a square that the cell fits inside. The separator is tied in place around the cell with several strands of extra fine unwaxed dental floss.

4.2.2 Standard Heat Capacity

In contrast with the cell design, the standard heat capacity was made as heavy as possible. (See figure 4.2.) That way the stray heat flow through the fill tube and electrical leads have a smaller affect on the standard's temperature. It is also necessary for the standard to come to thermal equilibrium quickly, so it was made of solid O.F.H.C. copper. Its heat capacity is typically five times the sample cell background heat capacity. A six lead heater, nearly identical to the cell heater, was wound in a spiral groove around the standard. All the electrical leads that are tied to the standard and sample are thermally anchored in grooves above and below the heater. This body also holds two thermometers, one of

[4]Extending one heater lead to the next body before it splits into I and V leads corrects for the heat generated in the section of the heater leads between the standard and the cell.

[5]Trademark, Apiezon Products Limited.

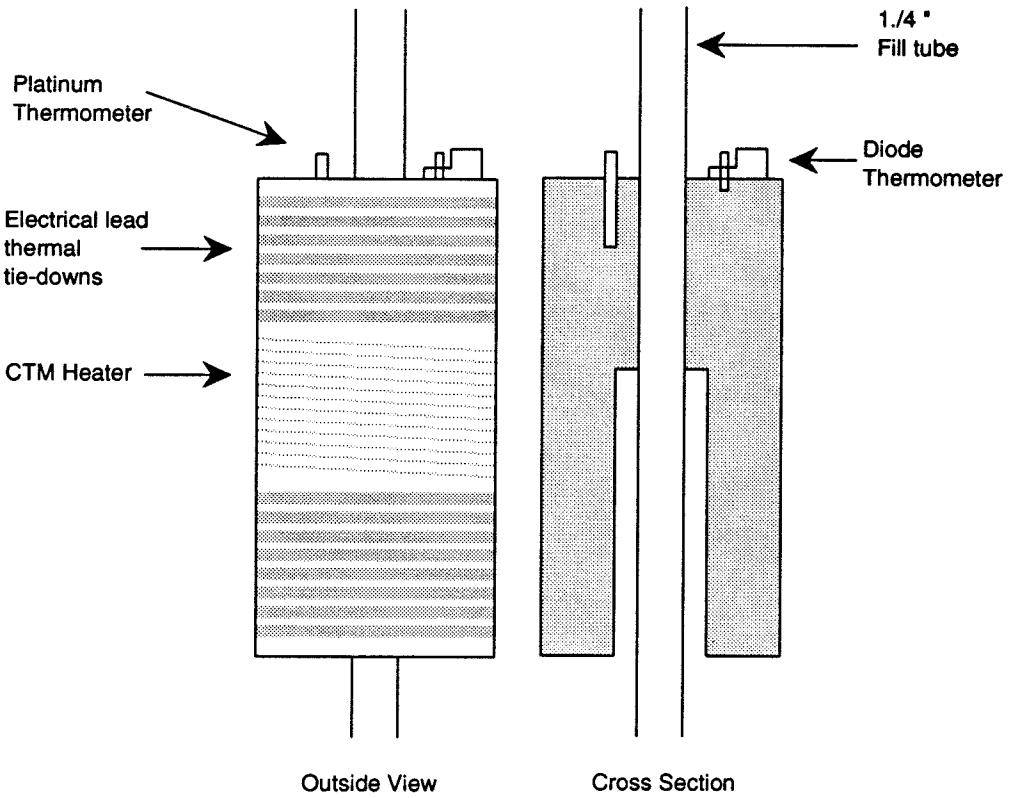

Figure 4.2: Standard Heat Capacity.

a pair of thermometers that measure δT, and a silicon diode thermometer that determines the temperature setpoint for thermal isolation. The output voltages from the diode thermometers on the radiation shields, isolation thermal mass, and upper thermal platform are electronically subtracted against the output voltage of this "master" diode thermometer. Each difference signal is digitized, added to a temperature dependant setpoint, and then used as a feedback signal for temperature control. Because of the low noise and accuracy of the platinum thermometers, δT will always be less than .5 mK, so it is sufficient to use only the standard's temperature to determine the isolation thermal regulation setpoint for both the sample and the standard. To reduce the thermal conductivity between the sample cell and the standard, the fill tube was made longer by making the the standard reenterant. This minimized the overall length of the calorimeter and also shielded the sample gas fill tube from the cold helium heat exchange gas used while cooling down. Since the fill tube is very thin stainless steel (.004

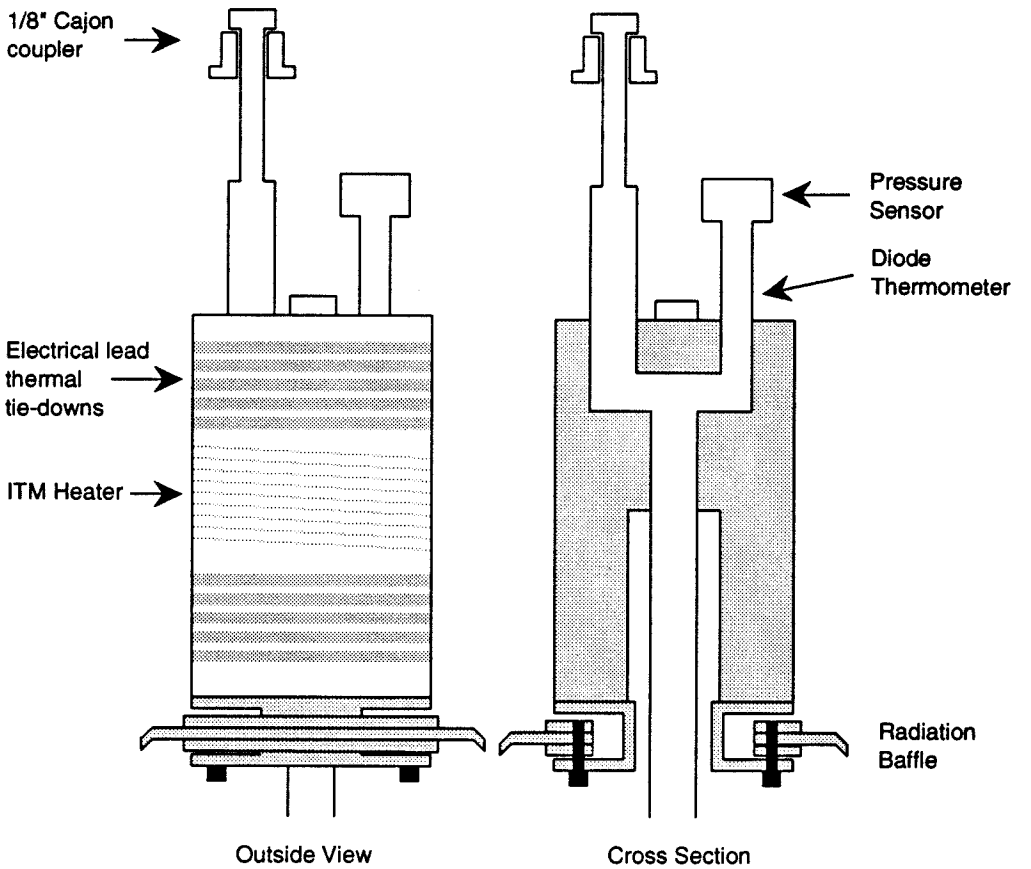

Figure 4.3: Isolation Thermal Mass.

inches thick), the exchange gas could cool it below the cell temperature. Then the sample gas would condense in the fill tube, instead of on the graphite surface. The fill tube is soft-soldered in a tight fitting hole in the standard to provide a good thermal joint.

4.2.3 Isolation Thermal Mass

The isolation thermal mass (ITM) is located on the fill tube, directly above the standard, see figure 4.3. To reduce its temperature control noise, the ITM heat capacity should be large. There is a direct analogy between a simple R-C filter and these thermal circuits. In this case, the (noisy) temperature source is the upper thermal platform (UTP); the thermal resistance is the sample gas fill tube and electrical leads. By making the R-C time constant large enough, the high

frequency fluctuations in the UTP temperature will not effect the ITM temperature. Active temperature control easily compensates for the low frequency heat flow. The output from the digital temperature control algorithm is converted to a bipolar analog voltage then applied to a two wire bifilar Evanhom wire heater that is glued around the middle of the ITM with Stycast epoxy. Capacitive and magnetic coupling between the heater and the sensitive electrical leads is minimized by using a bifilar heater driven from a bipolar (+V, -V) voltage source. This technique was used for all the heaters except the cell and standard heaters. All the electrical leads that connect to the standard and sample are thermally anchored to the ITM in grooves adjacent to the heater. As with the standard, the ITM has a reenterant shape to minimize the length of the calorimeter. An inexpensive silicon diaphragm strain gauge pressure sensor is mounted to the top of the ITM. This device failed after a few thermal cycles. It could be replaced in the future as miniature cryogenic pressure sensors become commercially available[6]. In order to simplify the calorimeter's construction, a detachable vacuum joint[7] couples the UTP to the ITM. To facilitate brazing the vacuum joint from inside the recessed lower section of the ITM to the fill tube, the ITM was made in two sections. After the joint was brazed, the ITM was joined together with soft solder. Silver solder was used for brazing nearly all of the vacuum joints on this apparatus because of the poor reliability of lead-tin soldered stainless steel joints.

A thermal radiation baffle is located on the bottom of the ITM. Because the inner shield must be cooler than the ITM while cooling down, these bodies cannot have a large thermal connection. But it is necessary to isolate the sample cell and standard from any external thermal radiation. Unlike the usual cryogenic apparatus, we need to shield against radiation from bodies colder than the sample cell as well as warmer than it. Therefore a leak tight baffle is glued[8] to the bottom of the ITM. A teflon washer seals the inner radiation shield to the baffle, without allowing a large thermal contact. The electrical leads going to the standard travel through the baffle, protected against abrasion by mylar tape. The inside of the

[6]The device tested was an Omega PX82-01GV. Strain gauge pressure sensors are not accurate enough for our work, but the literature mentions several miniature capacitive and optical sensors that might be suitable [81, 82].

[7]The coupler, a 1/8 inch Cajon coupler used with copper washers, was 100% reliable, even after several thermal cycles.

[8]Glued with Emerson & Cuming Inc. Ecobond 285 with catalyst 23LV, which is equivalent to Stycast 2850 except that it is optimized for use as an adhesive rather than as a potting agent.

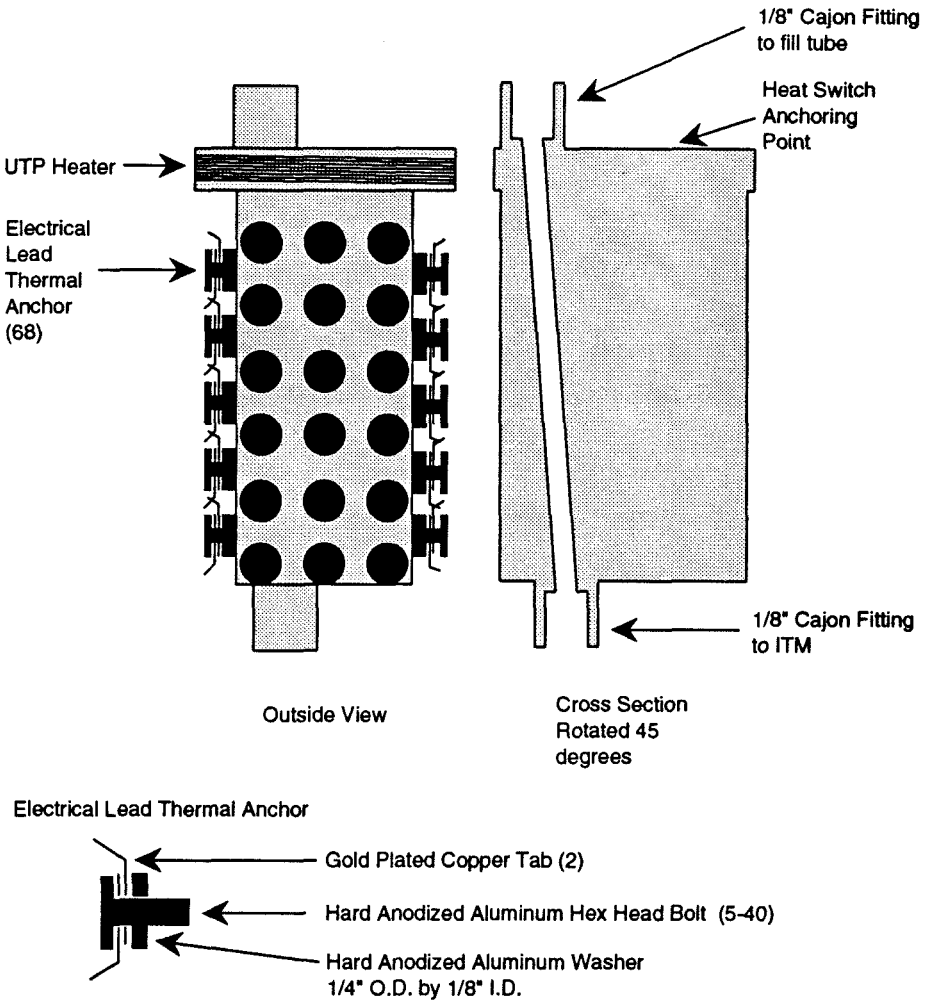

Figure 4.4: Upper Thermal Platform.

baffle and the upper section of the inner radiation shield are painted with colloidal graphite[9] to prevent any radiation from bouncing through.

4.2.4 Upper Thermal Platform

The upper thermal platform (UTP) is located above the isolation thermal mass, suspended from the heat switch and the fill tube (figure 4.4). The heat flow from room temperature down the fill tube and electrical leads travels through the upper section of the UTP and into the bath via the heat switch. To minimize the

[9]Ted Pella, Inc., Catalog number 16053.

temperature gradient in any part with a large thermal current, the path for the heat flow should be as short as possible, and the part should have high thermal conductivity. All sources and sinks of heat should be close together to localize the thermal gradients. Therefore the major heat sources and sinks, the fill tube, the heat switch connections and the heater, are located in the upper section of the UTP. The diode thermometer is located close to the heater to improve the temperature control stability. On the top and bottom of the UTP are female 1/8 inch Cajon connectors to couple to the fill tube and the ITM respectively. These are joined together by a diagonal passage through the UTP. Stainless steel allen-head screws join the heat switch to the top of the UTP.

The 60 or so electrical leads must be thermally anchored to, but electrically isolated from, the UTP. Many methods were experimented with, for example mica washers, or brass strips glued down with epoxy. The most satisfactory design was to compress two gold plated tabs, connected to the incoming and outgoing electrical leads, against the UTP with hard anodized aluminum washers providing electrical isolation. Each stack consisting of the tabs and washers was held down with a hex-head, hard anodized aluminum screw. Hard anodization produces a layer of aluminum oxide that is several thousandths of an inch thick, virtually impossible to scratch through, a good electrical insulator, and a good thermal conductor. The tabs and washer were coated with type 'L' Apiezion grease to improve the thermal conductivity. A disadvantage of this design is that it is ineffective at temperatures below the superconducting transition of aluminum, far below the temperature range for this apparatus. The design allowed us to disconnect the entire lower section of the calorimeter for servicing, and to interchange it with a specially designed lower unit used to calibrate the thermometers against each other and against the methane bulk vapor pressure and triple point. This calibration lower section is nearly identical to the calorimetry lower section except that a massive copper triple point cell replaces the sample cell. The copper triple point cell holds 13 ml of bulk liquid or solid, eight silicon diode sensors and three platinum resistance thermometers.

4.3 Probe Plumbing Details

In this section, we will discuss the calorimeter probe that houses the sample cell, standard heat capacity and thermal isolation masses. The probe is immersed in the cryogenic bath contained within a stainless steel dewar flask. A thin wall

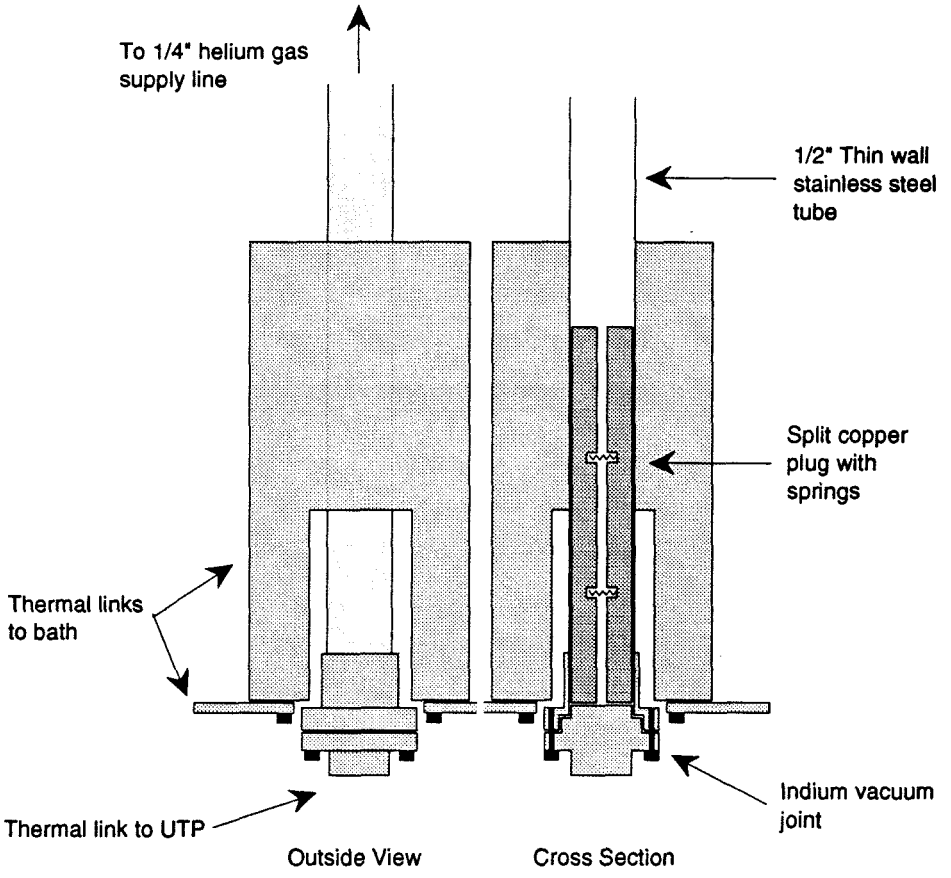

Figure 4.5: Heat Switch.

stainless steel pump line hangs from the top plate that is bolted to the top of the dewar. The vacuum can is attached to the end of the pump line, at the bottom of the dewar.

4.3.1 Heat Switch

The heat coming from room temperature down the sample gas fill tube and electrical leads must be delivered to the cryogenic bath; otherwise, the first calorimeter thermal stage (the upper thermal platform) will not cool down. The simplest design would be to include a fixed thermal resistance between the UTP and the bath. However, if the thermal resistance is small enough to enable the UTP to cool to within a few degrees of the bath temperature, then there will be too much heat sent into the bath when the calorimeter is operating 50 K above the bath

temperature. The heat leak from the fill tube (3/8" diameter, .010" wall thickness, 36" long) plus the 50 electrical leads (37 gauge copper) is about 76 mW from 300 to 70 K. To operate within one degree of the bath temperature requires a 76 mW/K thermal resistance. When there is a 50 K temperature difference across the thermal resistance, the heat leak would be 3.8 W. For comparison, the inevitable heat leak coming from thermal conduction through the stainless steel pump line (1.75" diameter, .025" wall thickness, 36" long) is .27 watts (from 300 to 70 K). To operate over a wide temperature range, we need to vary the thermal resistance.

In place of a fixed thermal resistance, we use a heat switch that conducts heat through helium gas (figure 4.5). The thermal resistance is controlled by changing the gas pressure. A 1/2 inch diameter stainless steel tube links the bath to the upper thermal platform. The tube inside walls were honed to be round and parallel to within .0001 inch. A split copper plug inside the tube has the same diameter as the inside of the tube to within .0001 inch. Weak springs between the halves of the plug force it against the walls of the tube. When there is no helium gas in the tube, there is little heat conducted because the stainless steel tube has low thermal conductivity. Little heat travels through the plug because it makes low pressure contact with the tube at isolated points. When the tube is filled with helium gas, heat flows through the copper plug, which acts as a thermal short across the thermal resistance of the tube. The amount of heat conducted through helium gas between parallel surfaces is proportional to the gas pressure only as long as the mean free path of the atoms is longer than the spacing between the surfaces. When the gas pressure is so high that the mean free path of the atoms is less than or equal to the spacing, additional pressure does not increase the thermal conductivity. To decrease the thermal resistance, it is necessary to reduce the spacing between the surfaces, and increase the pressure. In our design, the spacing is as small as .0002 inches over a large fraction of the copper plug's area. The maximum heat flow occurs for pressures above $\sim$200 torr. When the switch is on, it conducts about 180 mW/K, but when it is off, it conducts only 30 mW/K (for operation near liquid nitrogen temperatures). A 1/4 inch tube from a two liter reservoir at room temperature supplies gas to the heat switch. The gas pressure in the reservoir is controlled by opening or closing two computer interfaced 110 VAC solenoid valves that connect to a mechanical vacuum pump and to 10 PSI helium gas. Besides minimizing the heat leak into the bath, the heat switch also helps improve the upper thermal platform temperature control

by thermally isolating it from the bath temperature fluctuations. While cooling down, the heat switch is filled with helium gas, but during calorimetry the switch is evacuated.

4.3.2 Radiation Shields

As described above, the sample cell and standard heat capacity must be isolated from thermal radiation from any colder or warmer surfaces (figure 4.6). Two concentric temperature controlled radiation shields surround the sample cell and standard heat capacity. The inner shield temperature needs to be reproducible to within 12 mK over its entire surface. Because the calorimeter may operate as far as 50 K above the bath temperature, any variation in position or emissivity of the shield would cause irreproducible temperature gradients. Surrounding the inner shield by a temperature regulated outer shield solves this problem. The inner shield is made of copper to eliminate temperature gradients and is gold plated to reduce its thermal emissivity. The outer shield is made of aluminum to improve the thermal response time and to reduce the heat capacity. The sections of the shields above the radiation baffles are painted with colloidal graphite to absorb any external radiation. Shallow spiral groves around the outside of the shields hold the bifilar evanohm heater wires, glued with stycast epoxy. The inner shield has a bottom plate that was soft soldered in place before it was plated. The outer shield bottom was joined by a heli-arc weld. Both shields have silicon diode thermometers mounted on their bottom plates. The leads for these thermometers are thermally anchored with epoxy for one turn around each shield. The thermometer and heater leads run up through the space between the two shields to thermal tie-downs on the upper thermal platform. The shields are centered within each other and within the vacuum can with short teflon pins. Three pins are held in threaded holes on the top and bottom of each shield (12 pins total). During installation, the shields are suspended from stainless steel wire from the top of the vacuum can. When the vacuum can is in place, each shield rests on a low thermal conductivity support. Each support is made of a stack of two hundred and fifty .001 inch thick stainless steel disks that are 3/8" diameter, with a 1/8" hole in the center. To reduce the thermal contact between disks, they are coated with fine manganese dioxide powder [69, page 149]. The disks are tied to a stainless steel screw threaded into the bottom of each shield. This method insures the accurate and reproducible positioning of the shields within the vacuum

can.

4.3.3 Vacuum Can

A vacuum better than 1×10^{-6} torr is required to isolate the cell from the radiation shields, so the lower unit and radiation shields are enclosed in an evacuated chamber. The vacuum can that surrounds the shields is made of 3" diameter, 1/8" wall thickness copper tubing, with a copper bottom silver soldered in place. The can was gold plated to reduce corrosion and thermal emissivity. To allow the calorimeter to be serviced, a detachable indium wire joint seals the top and bottom of the can together. This joint is made of two stainless steel flanges, one welded to the vacuum can bottom, and the other welded to the pump line. Mating .1 inch wide double steps trap the 1/16 inch indium wire between the flanges, compressed by eight (8-32) bolts (with two extra threaded holes to allow the flanges to be separated). The flanges fit inside each other with .001 inch clearance to produce high pressures on the o-ring without the indium running through the cracks. The joint is leak tight at cryogenic temperatures if it is retightend after a preliminary cooling with liquid nitrogen[10].

4.3.4 Probe Pump Line and Diffusion Pump

A pump line connects the vacuum can to a room temperature diffusion pump. The pump line is as thin as possible to reduce the heat leak to the bath, while still thick enough to prevent collapse (.025 inches wall thickness). Reducing its diameter would also reduce the heat leak, but it must have a large diameter to ensure adequate pumping speed to the vacuum can. The conductance of the various components of the room temperature diffusion pump station are approximated using standard methods [83, page 91].

- 170 l/s Edwards model E02 diffusion pump plus water cooled chevron baffle.

- 400 l/s liquid nitrogen cold trap plus butterfly valve.

[10]Leak testing the joint was difficult because the 68 electrical lead thermal tie-downs form a large virtual leak. These should have had a fine hole drilled through their center before anodization. Also, it is necessary to remove all grease and oil from the flanges before sealing, since indium does not adhere strongly to stainless steel.

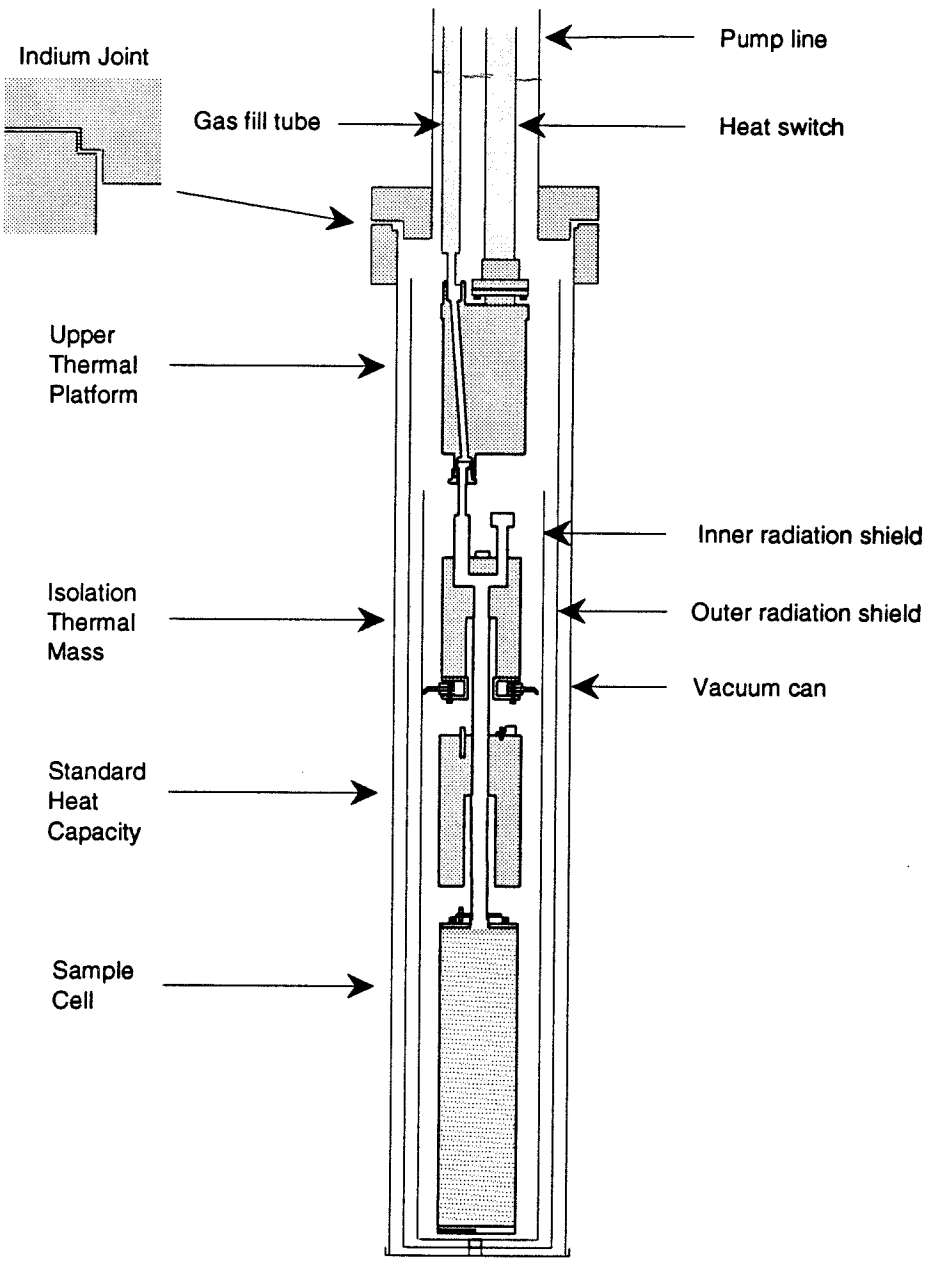

Figure 4.6: Vacuum can and calorimeter.

- 60 l/s approximately 3 feet of 3 inch diameter from the vacuum can to the top flange.

- 85 l/s air actuated bellows sealed right valve.

The total pumping speed to the top plate is found by summing the impedances, 27 l/s. The probe pump line is 1.75 inches in diameter, and about 30 inches long. Its pumping speed for helium at 200 K is about 11 l/s. From experience, this size pumping line is sufficient because the low temperature probe does not outgas, and a larger tube would increase the heat leak. There are five gold plated baffles in the tube that prevent room temperature radiation from reaching the calorimeter and hold the electrical leads and gas supply fill tube.

The electrical leads, the sample gas fill tube and the heat switch gas supply line travel up from the vacuum can top, through the pump line, to the probe top plate. The wires are divided into groups to prevent crosstalk:

1. Sample cell platinum thermometer leads

2. Sample cell / standard heat capacity ΔT thermometer leads

3. Silicon diode thermometer leads

4. Sample cell and standard heat capacity heater leads

5. Bipolar D.C. heater leads.

Each group is enclosed in teflon tubing inside a 3/16 inch stainless steel tube that is separately grounded. The tubes fit in holes in the radiation baffles; all but number 5 are electrically insulated with heat-shrinkable teflon tubing. Tube number 5 is soldered to the radiation baffles for mechanical stability. The tubes and the radiation baffles are thermally connected to the bath temperature with copper wires. The heat switch gas supply line also fits in holes in the radiation baffles. Teflon spacers on the baffles insulate the sample gas fill tube from cold spots that would condense the gas. Also, to prevent the sample gas from condensing, an electrical heater wraps around the fill tube. It is only used when there is heat exchange gas in the probe.

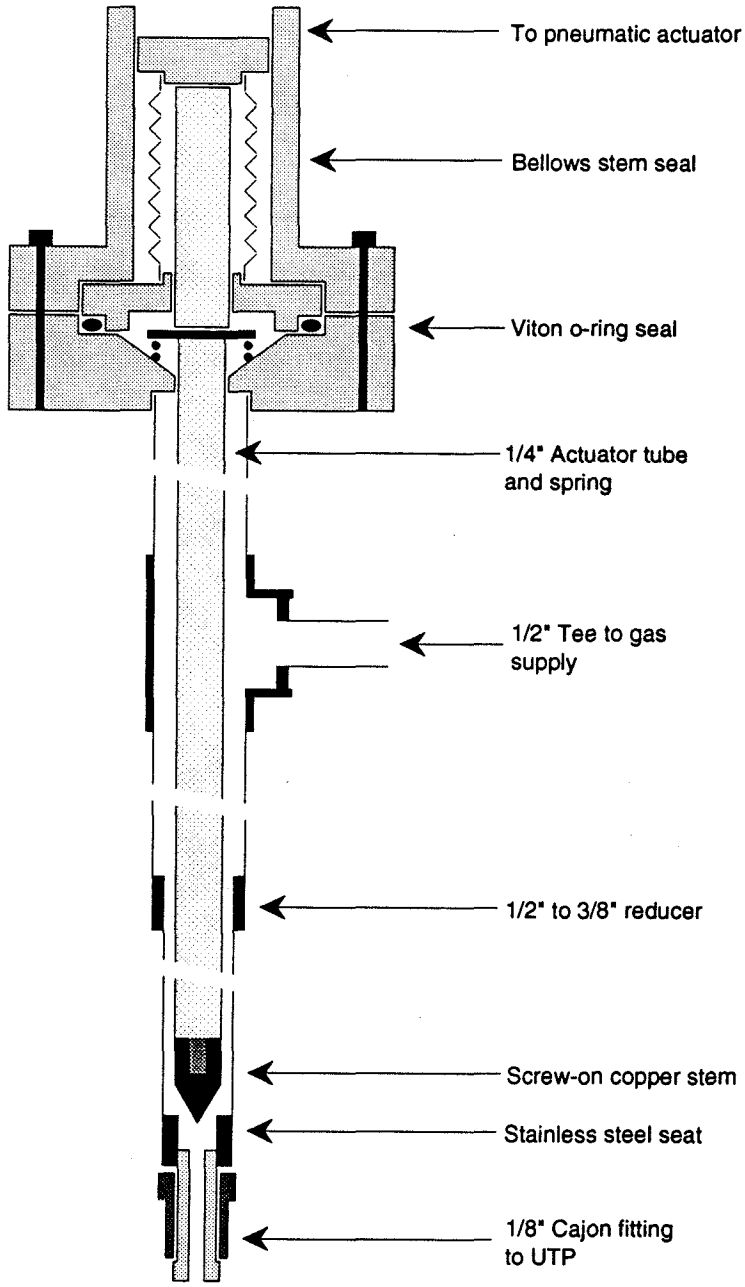

Figure 4.7: Fill tube and cryogenic valve.

4.3.5 Fill Tube and Cryogenic Valve

A cryogenic valve is located at the bottom of the sample fill tube to minimize the volume of gas outside the cell (figure 4.7). As the sample cell warms, the sample gas pressure increases. To increase the pressure, heat is needed to desorb the gas molecules. This heat, added to the film heat capacity, is recorded by the calorimeter. Closing the cryogenic valve eliminates half of the molecules in the gas phase, and reduces the desorption term in the heat capacity signal. Several valve designs were investigated. A teflon ball on a conical seat was found to seal at low temperatures, but leaked badly whenever the temperature was changed. The final design uses a conical copper stem that seals in a stainless steel seat. Copper was used because it has nearly the same thermal expansion as stainless steel at cryogenic temperatures. The valve seat is a hole with polished corners. The copper stem is screwed onto a 1/4 inch actuator tube that fits within the 3/8 inch fill tube. A small brass bellows acts as a movable seal at the top of the valve. Pressure to close the valve comes from a compressed air actuator[11] at room temperature that presses the top of the bellows. The force travels down the actuator rod to drive the stem against the seat. The valve is leak tight except during sudden changes in temperature, when it leaks an insignificant amount (.1 stpcc of gas or .0005 layers). The leak is caused by thermal expansion when the valve seat changes temperature suddenly.

4.3.6 Probe Top Plate

The top plate mates to the inner dewar upper flange and to the probe pump line, connects the probe pump line to the diffusion pump and holds the electrical wire feed-throughs. A tow inch welded stainless steel tee is soft soldered into the eight inch diameter, 1/2 inch thick brass top flange (figure 4.8). The horizontal leg of the tee is connected to the diffusion pump station that evacuates the probe. The downward leg goes through the top flange to a gold wire sealed joint that mates with the probe pump line. The upward leg has a viton rubber o-ring flange welded to it that connects to a 2-3/4 inch diameter, 1/2 inch thick brass flange. This small flange has two viton rubber quick disconnects hard soldered to it that seal to the sample gas fill tube and the heat switch gas line. It also has two 1/2 inch diameter stainless steel tubes hard soldered to it that connect to assemblies

[11] Hoke part number 0477A4H.

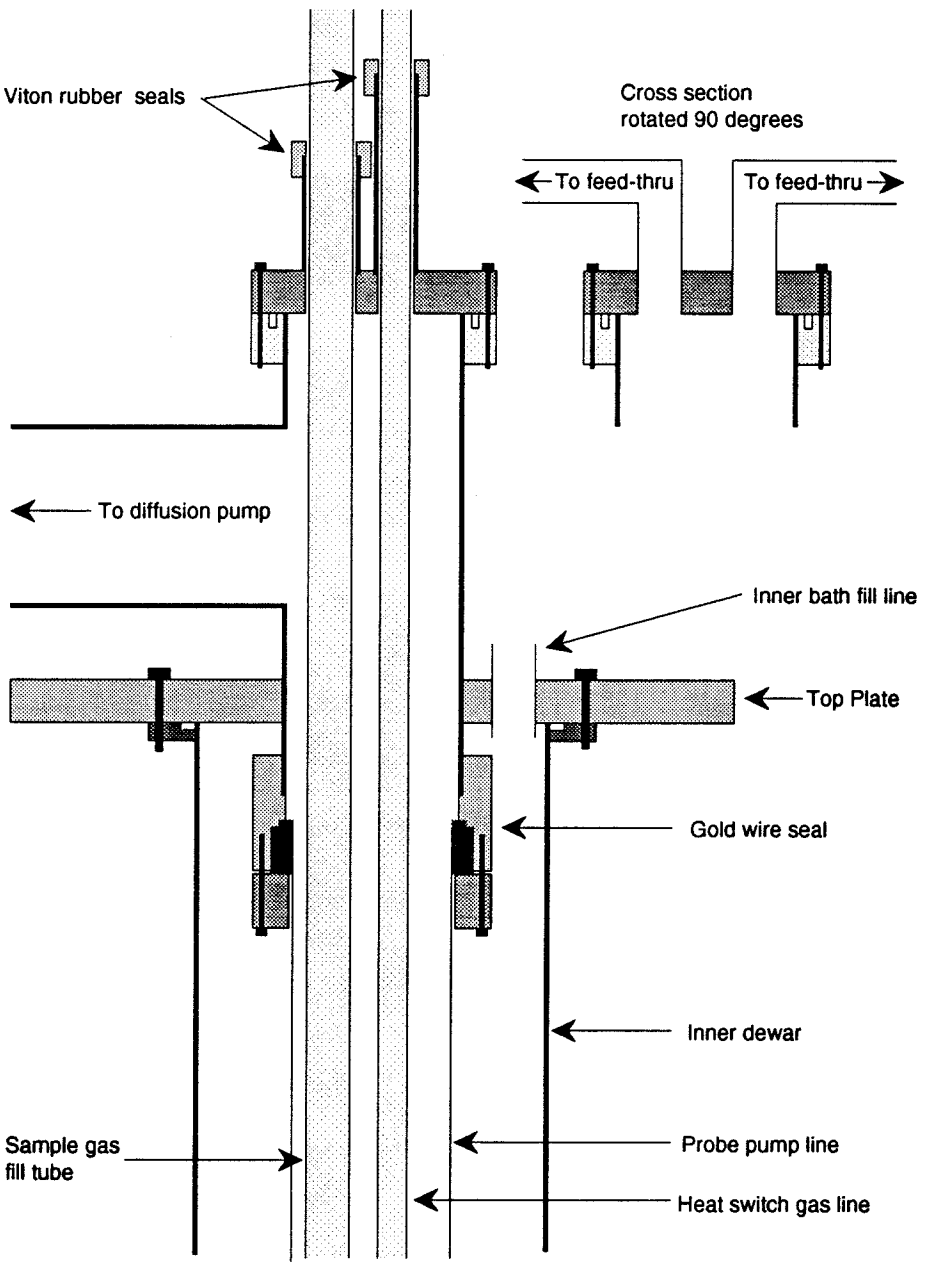

Figure 4.8: Top plate.

containing the electrical feed-throughs.

The first feed-through has four 25 pin 'D' connectors potted in stycast epoxy. The connectors are mounted so that the male pins are on the vacuum side of the feed-through and can be serviced by removing an access plate. Each wire from the probe is soldered to individual female gold plated connectors and plugged into the D connector. This makes a electrical switchboard that allows any wire or connection to be changed without altering the feed-through. Four more 25 pin 'D' connectors mate back to back with those in vacuum, and connect to cables from the electrical instruments.

A second electrical feed-through is used for the silicon diode thermometer leads. Voltages generated by the thermoelectric effect from the dissimilar metals used in electrical connectors can be as large as 5 μV/K, which can cause temperature errors as large as a few miliKelvin (the thermometer sensitivity is about 2.5 mV/K). Therefore the silicon diode leads consist of unbroken copper wires that travel from the upper thermal platform, through the probe pump line, and finally through a poured stycast epoxy feed-through to connectors away from the dewar. All the wires for the diode's thermometers were soldered with low thermal EMF cadmium alloy solder.

Connections for servicing the inner cryogenic bath are on the probe top plate. One hole through the top plate connects to the inner bath fill tube that runs down to the bottom of the dewar. Another hole connects to the inner bath to sense its pressure. The lead for a capacitive fluid level sensor that monitors the inner bath level goes through a rubber stopper in the final hole on the top plate. The inner bath level sensor is constructed of coaxial stainless steel tubes separated with fishing line, as described by White [69, page 52]. The sensor's capacitance sets the frequency of a relaxation oscillator [84, page 162], that drives a 16 bit counter interfaced to the computer through an optical coupler.

4.3.7 Dewars and Cryogenic Baths

According to standard practice, there are two cryogenic baths, an inner bath filled with liquid nitrogen or helium, and an outer bath filled with liquid nitrogen (figure 4.9). The temperature range for this experiment was above 63 K, so liquid nitrogen was used in the inner dewar. At first, we attempted to maintain the inner bath at low temperature by reducing its vapor pressure with continuous pumping. The inner and outer baths were isolated by a vacuum chamber on the inner dewar. The

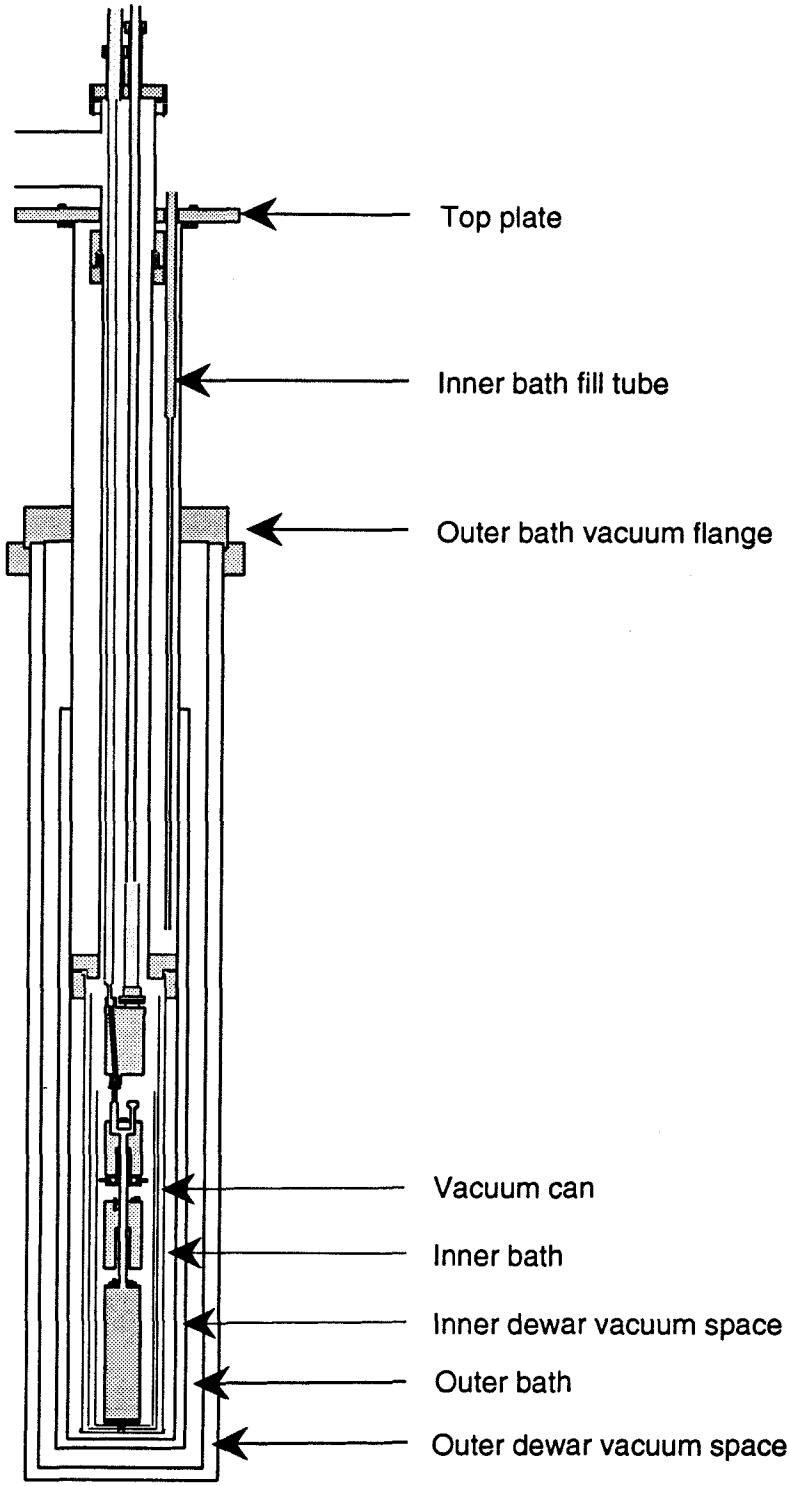

Figure 4.9: Dewars and probe.

outer bath was at atmospheric pressure. Using this method, the inner bath would only last about eight hours before it needed to be refilled. Since refilling the inner bath caused a large thermal disturbance to the calorimeter, the apparatus needed to be stopped, recooled a few degrees, and restarted. Fortunately we found a way to operate the probe continuously at any temperature above the liquid nitrogen triple point, 63 K. A flange was made that sealed off the outer bath, which was pumped continuously to cool below 60 K. The vacuum chamber that previously isolated the two baths was filled with a few microns of helium gas to form a weak thermal link. Then the inner bath was filled with liquid nitrogen and sealed off. The heat that leaked into the inner bath is carried off through the weak thermal link to the colder outer bath. When the outer bath is refilled, the inner bath temperature only changes by a few degrees because the inner bath thermal time constant is very large. This method maintained the inner bath at or below 63 K during 28 hour heat capacity runs. The outer bath was automatically refilled every 1.5 hours from a computer interfaced cryogenic solenoid valve connected to a 160 liter pressurized LN_2 storage dewar. A zener diode temperature sensor, mounted at the top of the outer bath, indicates when the outer bath filling is complete. The diode dissipates 1/4 watt during operation so that the sensor is able to distinguish between liquid nitrogen and cold vapor. The diode is wired as one arm of a Wheatstone bridge, and the sign of the bridge's imbalance is interfaced to the computer.

Two liquid nitrogen traps on the probe vacuum diffusion pump station and the sample gas handling system are also filled automatically. A separate storage dewar is pressurized with dry nitrogen gas to fill the traps by activating an interfaced three-way solenoid valve. When the traps are filled, the excess liquid nitrogen is piped to a dewar that holds a second zener diode level sensor. When this level sensor is submerged, the dewar is vented to atmospheric pressure to stop the filling.

The vacuum can and probe were evacuated by a diffusion pump connected to a water cooled baffle, liquid nitrogen trap, butterfly valve and the three inch main pump line. At the top of the main pump line is a short section of brass tubing that has an ion gauge tube, exchange gas ports and a thermocouple gauge mounted on it. This tube is mounted to the main pump line and to an air actuated bellows valve with QF-50 flanges. A 12 inch long, QF-50 stainless steel bellows connects to the probe. This and all other pump lines are electrically isolated from the probe with nylon bushings or teflon seals as required, to prevent ground loops

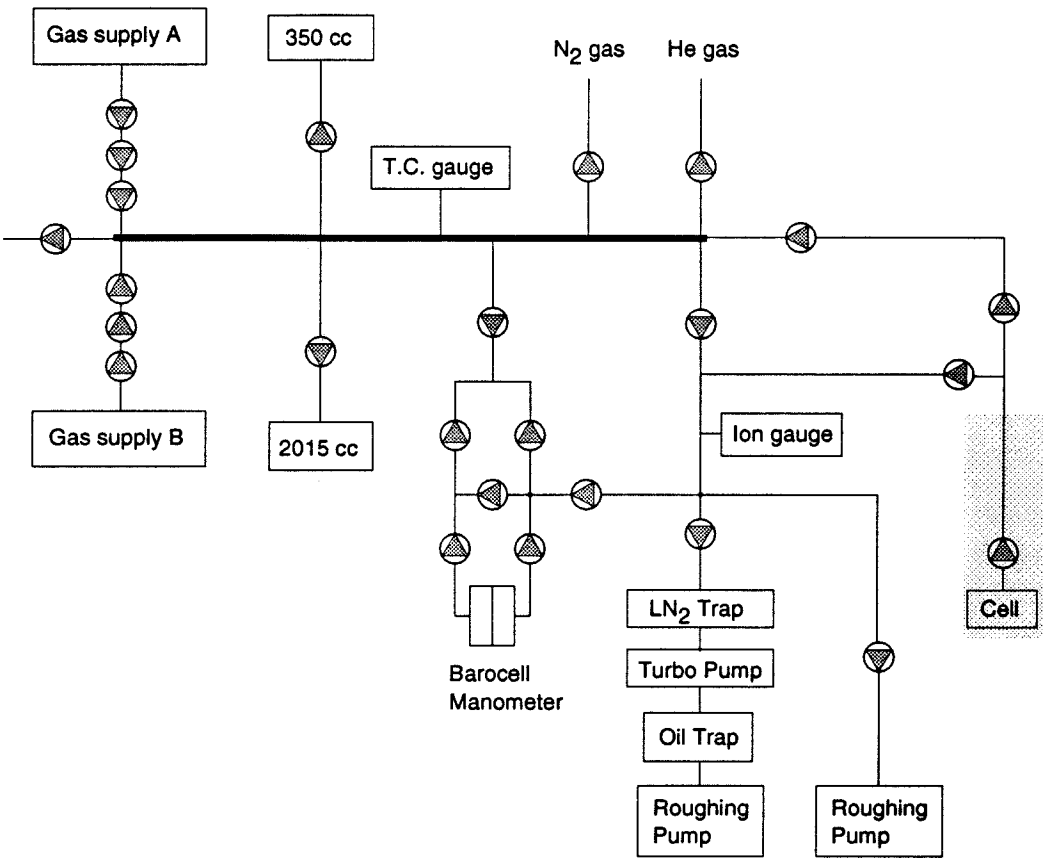

Figure 4.10: Gas Handling System

that would interfere with the electronics.

To cool down the experiment, it was necessary to inject a metered pressure of helium gas into the vacuum can under computer control. Since pneumatic or electrically actuated leak valves are expensive, another solution was necessary. We used a commercial variable leak valve as well as a home-made fixed leak that were each connected to a three way 110 VAC solenoid valve. When no gas was to leak, the valves were connected to a rough vacuum and an insignificant amount of gas leaked through. When the valves were meant to leak, the valves were connected to a 10 PSI helium gas supply to raise the pressure in the vacuum can to the desired amount. The leaks were calibrated so that the pressure was about five microns of mercury while the diffusion pump was still pumping out the system.

4.4 Sample Gas Delivery and Pressure Measurement

The methane films are formed by condensing gas on the Grafoam surface. To make a film with a certain thickness we must measure the total number of gas molecules in the cell and plumbing and know the substrate surface area. Accurate vapor pressure measurements enable us to determine the chemical potential of the film to obtain a complete thermodynamic description. The gas should not be contaminated by molecules outgassing from the surfaces of the plumbing, otherwise the vapor pressure readings will be inaccurate, or the film may be contaminated.

The gas handling system, figure 4.10, provides a known amount of pure sample gas to form the films. To know the number of molecules in the gas handling system, we measure the pressure of a known volume of gas. A two liter stainless steel beaker was calibrated by measuring its weight when filled with water. This beaker is connected through a bellows sealed valve to the main manifold. Nine valves[12] connect the manifold to the turbo-pump, dry nitrogen and helium gas, two sample gas supplies, a 350 ml volume, the manometer, and the cell. The connection to the probe is made with a 1/4 inch copper tube from the manifold valve to another valve[13] mounted on the fill tube. The sample gas is removed from the high pressure cylinders by withdrawing small doses of gas that is trapped between the cylinder valve and a diaphragm valve[14] mounted on the cylinder. The gas handling system was automated by using several air operated valves, and by converting certain manual valves with air actuators[15].

To form a film for calorimetry, the gas was drawn from the calibrated volume to condense on the surface. When the desired amount of gas was in the cell, the valve on the calibrated volume closed. During upward and downward vapor pressure isotherms small doses of gas must be added or subtracted from the cell. When gas was to be removed from the cell, the fill line valve was closed, and the gas in the manifold was pumped out by the turbo-pump. Then the fill line valve was reopened to pull gas out of the cell into the manifold. In order to add a small dose of gas, the air actuated valve on the fill line was closed and a dose of

[12]The turbo pump valve is a Nupro SS10BK normally closed air actuated valve, the remaining valves are all Hoke part number M482.

[13]Nupro 10BK normally open air actuated valve.

[14]Matheson part numbers 4351-350 and 4351-580, no pressure regulators were used to improve the system cleanliness.

[15]Hoke part number 0477A4H used with valves part number M482, catalog number 4551.

gas was leaked into the manifold from gas stored in the calibrated volume. Then the fill line valve was reopened to introduce the gas into the cell. To convert the calibrated volume valve into an air operated leak valve, a special actuator was designed that was modeled after the commercial actuators, except that the valve opening was limited by a micrometer and the actuator shaft traveled within precision bearings[16].

A 1000 torr capacitance manometer[17] reads the pressure in the gas handling system manifold. To enable the computer to change the range setting of the pressure readout electronics, two relays were wired as an alternative to the manual range switch. The relays were interfaced to the computer through two stages of optical isolation to avoid interfering with the electronics. The readout provides a digital optically isolated output that was interfaced to the computer. The signal was double-buffered to prevent the reading of data in transition because the readout updating and the system clock are asynchronous. The manometer is typically linear to $\pm.05\%$ of full scale, as calibrated by the factory.

The ultra-low pressures used for most surface physics studies are not necessary for films on high surface area substrates because a tremendous amount of gas is required to form a monolayer of film. Pressures of 1×10^{-7} torr are low enough to keep the contamination far less than a monolayer. It is more important to have a low outgassing rate in the room temperature plumbing. During operation, if the room temperature plumbing outgasses high boiling point vapors, then they would accumulate on the surface. Low boiling point vapor may not condense on the surface, but it would cause the pressure readings to be erroneously high. Producing a low outgassing gas handling system is just as challenging as an ultra-high vacuum system. Ideally the system should be constructed of all metal components, but such a system is expensive and difficult to design. Small quantities of viton rubber, Kel-F, and teflon were used for seals and valve stems. The ultimate limit of the vacuum in the gas handling system is 1×10^{-7} torr; caused by the vapor pressure of the cadmium and zinc alloys. Besides using the proper components, the cleaning of the gas handling system is critical to achieve low outgassing rates. Flux residues, corrosion, and shop dirt cause very high outgassing rates. When

[16]This worked well enough except that the Kel-F stem seal on the Hoke valves was found to have a memory. The plastic would compress when the valve was closed, and then expand a minute after the valve was opened. This made it difficult to get reproducible flow rates. A copper stem seal valve would work better.

[17]Datametrics model 538H-12 sensor, 1174 readout.

our plumbing was first installed after a superficial cleaning with solvents, the outgassing rates were very high, 10 μm Hg per day. Then the plumbing was cleaned by pumping the heated solvents simultaneously through all the orifices, which reduced the outgassing rate to below the drift of the barocell pressure gauge, 1 μm Hg per day. The ougassing rate of the probe plumbing probably is somewhat greater than this because of the large viton o-ring that seals the bellows on the cryogenic valve[18].

To reduce the contamination further, the gas handling system and sample were evacuated with a liquid nitrogen trapped turbo-pump with a base pressure typically below 1×10^{-7} torr. Because the pumping speed through the gas handling system manifold was very slow due to the long lengths of 1/4 inch O.D. copper tubing, a separate one inch pump line goes from the turbo-pump to a manual valve on the sample gas fill tube. Because the gas handling system ion gauge tube is mounted just above the turbo-pump, the measured pressures are unusually low when pumping the sample through the manifold. The apparent pump down time is only a few hours if the cell is pumped out with only the 1/4 inch line because the ion gauge reading is inaccurate. But with the one inch line it increases to 36 hours. During the experiments, the cell was pumped out every few weeks to prevent contamination.

4.5 Thermometers and Resistance Bridges

To implement the calorimeter as described above we need to measure the absolute temperature of the heat capacity cell, the temperature difference between the sample cell and the standard heat capacity, and the temperatures of all the bodies that provide thermal isolation for the cell and standard. A temperature measurement is characterized by the noise in the reading, the absolute precision of the measurement relative to true thermodynamic temperature, and the reproducibility. The requirements for each thermometer readout will be calculated below.

Sample Absolute Temperature Measurement

The cell temperature reading is used for several purposes. Initially these data are used to calibrate all the thermometers to each other to establish an accurate relative temperature scale in order to thermally isolate the calorimeter. To give

[18]This seal was later replaced with a cleaner teflon washer seal.

T(K)	C_{bknd} (J/K)	dC/dT (J/K^2)	$\delta C/(C_{bknd}\delta T)$ (1/K)	δT for .01%, mK
70	12.758	0.2879	0.0319	3.13
80	15.542	0.2688	0.0245	4.08
90	18.133	0.2495	0.0195	5.12
100	20.531	0.2301	0.0159	6.29
110	22.734	0.2104	0.0131	7.63
120	24.738	0.1905	0.0109	9.17

Table 4.2: Allowed absolute temperature measurement error.

adequate isolation, this calibration should be more accurate than ±1 mK. During the heat capacity runs, the background heat capacity must be subtracted from the data. Noise in the absolute temperature will enter the film heat capacity as:

$$C_{film}(T) = C_{film+bknd}(T) - C_{bknd}(T)$$

$$\delta C_{film} = \frac{dC_{film+bknd}}{dT}\delta T_{samplerun} + \frac{dC_{bknd}}{dT}\delta T_{bkndrun} \quad .$$

In the case where the film signal is small compared to the background and the errors during both measurements are uncorrelated, the fractional error (relative to the background) will be:

$$\frac{\delta C}{C_{bknd}} = \frac{\sqrt{2}}{C_{bknd}}\frac{dC_{bknd}}{dT}\delta T \quad .$$

If the random noise in the cell temperature measurement is larger than this value, or if the thermometry is not reproducible between the background run and the film heat capacity measurement, then the error will be significant. The allowed errors are shown in table 4.2.

The temperature measurement should also be reproducible and agree with true thermodynamic temperature. In previous measurements there were features in the data close to the bulk triple point, so the temperature scale must be calibrated accurately relative to T_3. The resistance bridge should be at least as reproducible as the thermometers, 10 mK[19]. We purchased a calibrated thermometer with a calibration traceable to NBS standards to within ±10 mK.

The accuracy of the calibration slope affects the heat capacity because it determines δT, given the change in the thermometer output. In the differential

[19]Our platinum thermometers are reproducible to ±10 mK when thermally cycled to room temperature. When held at low temperatures, they should be reproducible to ±1 mK or better.

scanning calorimeter, the calibration affects the data through the initial measurement of the standard's heat capacity. This error will be smooth, so it should not limit our ability to find peaks in the data, but it will affect any thermodynamic calculations based on the data, and it will limit our ability to compare our data with other laboratories. However, since the overall noise in the film heat capacity should be larger than the the error caused by the inaccurate temperature scale, this will not be a serious problem. The film heat capacity is typically .5 J/K per layer and the noise varies from .003 J/K at 70 K to .015 J/K at 120 K. This represents fractional errors in the film heat capacity of .6% to 3% for a monolayer film. It is difficult to estimate the errors in the derivative of the temperature scale because the scale is derived from a fit to many data points over a wide temperature range. However, it should be much less than 1%. Primary calibrations are performed by measuring the known saturated vapor pressure of a gas versus the sensor output. Unfortunately, the vapor pressures of only a few gases have been measured with sufficient accuracy; these measurements only yield continuous data over a narrow region of temperature, and the pressure measurements need to be very precise and traceable to absolute standards. We measured the vapor pressure of methane versus temperature, as well as the triple point temperature. But the vapor pressure of methane is not tabulated with sufficient accuracy for us to calibrate our thermometers. However, we did shift the temperature to read correctly at the triple point and the normal boiling point.

Relative Temperature Measurement

The relative temperature between the cell and the standard heat capacity must be measured with even greater precision, since the calorimetric accuracy depends on this measurement. During operation, a constant heat input is injected into the standard heat capacity, and the relative temperature, δT, is maintained at zero by feedback from the relative bridge. An error in the relative temperature measurement, E(time), causes an error in the heat capacity equal to

$$\Delta C = \frac{W_0}{D^2}\frac{dE(t)}{dt} + \frac{1}{D}\left(1 + \frac{W_0}{W_1}\right)KE(t)$$

where $W_1/C_1 = W_1'/C_1' = D$, D is the standard drift rate per unit time, K is the thermal coupling between the standard and sample. The first term is caused by error in the measurement of the drift rates of the standard and sample. Ideally, both bodies should be drifting upward at the same rate. The second term is

caused by the heat flow between the sample cell and the standard heat capacity, caused by the two bodies not being at the same temperature. To achieve .01% error, the derivative of the relative temperature error should be less than

$$\frac{dE(t)}{dt} < \frac{C_{bknd}D^2}{W_0 10^4} \sim \frac{D}{10^4} \quad .$$

The noise in the derivative of a signal with white noise is $n = 2e\sqrt{3}\,t^{-3/2}$, where e is the noise per $\sqrt{Hz}$ in the input data, and t is the measurement time (in seconds). It is assumed that there are many points in the interval. For three minute measurement times, and 2 K/hour drift rates, there should be less than $.12\ mK/\sqrt{Hz}$ noise. There may also be nonrandom contributions to $E(t)$ caused by shifts in the thermometer calibration and electronics.

The error caused by heat flow between the sample and standard is approximately $\Delta C = KE(t)/D$, since $W_0 << W_1$. A thin walled stainless steel tube (2" long, 1/4" diameter, .004" wall thickness) and 13 copper wires (37 gauge) connect the sample cell and standard. At 80 K the thermal coupling is about .9 mW/K. Then the allowed temperature error for .01% error is about 1 mK for 2 K per hour drift rates, using the cell background heat capacity mentioned above.

Isolation Temperature Measurement

Finally, the sample and standard must be located in an adiabatic environment. The temperatures of the radiation shields, upper thermal platform, and the isolation thermal mass must be regulated. We have demonstrated above that we require temperature control better than 4 mK to provide thermal isolation for .01% errors at 2 K/hour drift rates.

4.5.1 Three Types of Thermometers

What type of thermometers and readout electronics satisfy these requirements? There are three commonly used electrical thermometers in our temperature range: thermocouples, silicon diodes, and platinum resistance thermometers.

Thermocouples are not useful as accurate absolute standards, but are good for determining the relative temperature between two bodies. The highest sensitivity thermocouple in our temperature range is the chromel-constantan pair (30 μV/K at 100 K). A high quality nanovoltmeter has about 30 nV_{pp} noise for a .3 Hz bandwidth, or at best 6 $nV/\sqrt{Hz}$ noise density. The resulting thermometry noise

is .2 $mK/\sqrt{Hz}$. But it is very difficult to reduce the noise generated by stray thermal voltages in the thermocouple leads to anywhere near 30 nV_{pp}. Typically, the noise will be 10 times this value. It is possible to use multiple junctions (a thermopile) to amplify the thermocouple sensitivity, but working with so many junctions is difficult. This technique was successfully used by Loram [72], but at much higher drift rates. Differential thermocouples have the advantage that they have zero output when the two bodies are at exactly the same temperature, but they still require calibration to accurately measure the differential sensitivity.

Both silicon diodes and platinum thermometers are usually reproducible to better than 10 mK when thermally cycled to room temperature. Silicon diodes give a large D.C. voltage change in response to temperature changes, about -2 mV/K; but it is very difficult to measure small D.C. voltages generated from devices inside a cryostat, because of stray thermal voltages generated from the large temperature gradients along the sensor lead wires. Stray voltages less than a .2 μV (corresponding to a .1 mK temperature error) are very difficult to achieve. This accuracy is sufficient for the isolation thermometry, and possibly the absolute temperature measurement, but is is not good enough for measuring the relative temperature between the sample and standard. The frequency spectrum of the noise generated by stray thermoelectric voltages is not uniform, it is distributed according to the frequency and size of fluctuations in the room and cryostat temperatures. Then there would be nonrandom noise in the heat capacity data if a thermocouple or silicon diode thermometer were used to measure δT. The stray voltages may be less than .2 μV, but to measure the absolute temperature the diode voltage must be compared to a reference. Precision voltage references typically exhibit 1 μV_{pp} of noise (for a two volt full scale output). Therefore it will be difficult to achieve low noise with a D.C. voltage measurement.

Platinum resistance thermometers have smaller sensitivity (40 $\mu V/K$ at .1 ma current) than silicon diodes, but they may be used with A.C. excitation to eliminate the effect of stray thermal voltages. With transformer input coupling, the effective input voltage noise for A.C. voltage measurements can be as low as 1 $nV/\sqrt{Hz}$, yielding about 25 $\mu K/\sqrt{Hz}$ temperature noise.

Noise is not the only consideration in measuring temperatures. Linearity and reproducibility are also important. It is easy to measure D.C. voltages linear to within $\pm$.004% of full scale range, which would correspond to a 40 mK error for the silicon diode sensor (zero to two volts range). It is possible to achieve another

decade of linearity with considerable effort. The amplitude of A.C. voltages can be measured with much greater linearity using inductive voltage dividers.

Platinum resistance thermometers are customarily measured using an A.C. Wheatstone bridge and a decade resistance box. Resistance boxes are usually accurate to only $\pm.01\%$ (leading to a 25 mK error for a 100 ohm decade resistor), and their reactance varies with the resistance setting. A better alternative is the ratiotransormer bridge. A ratiotransformer is an inductive A.C. voltage divider that is accurate to better than 10 ppm. The ratiotransformer is simply a precision autotransformer, with its windings around a toroidal core. The input voltage is applied across the windings, and the output voltage is taken from an adjustable tap. The output is simply the input voltage times the fraction of the turns between the tap and ground. Because the windings present little D.C. resistance, there is no significant Johnson noise generated in the ratiotransformer. Several kinds of resistance bridges can be made with ratiotransformers. Most designs compare the unknown resistance to a fixed standard resistance, nulling the bridge by changing the ratiotransformer tap. A version of the Kelvin bridge (a 4-wire version of the classic Wheatstone bridge) can be made using two ratiotransformers. Because this bridge symmetrically compares two resistors, it is used in this apparatus to compare two platinum thermometers that read the temperature difference between the cell and the sample. A.C. Anderson [85, 86, 87] conceived a bridge that provides 4-wire measurement with only one ratiotransformer and only one active component (an op-amp). Because the Anderson bridge can eliminate the effect of noise in the standard resistor (under certain conditions), and because it requires only a single computer controlled ratiotransformer, we used it to measure the resistance of a platinum thermometer on the sample to give the absolute temperature.

Silicon diode thermometers on the remaining bodies are use to control the temperatures of the calorimeter's environment. To eliminate the errors due to the linearity of the A to D conversion, the diodes' voltages were measured with a unique bridge circuit that compared the voltages against each other and to a reference voltage. In the next three sections we will describe the design and performance of each instrument.

4.6 Relative Resistance Bridge

The *relative resistance bridge* measures the temperature difference between the standard and the sample by comparing the resistances of two platinum thermometers, one on the sample and the other on the standard. Because the two thermometers have different calibration curves, δT is not simply proportional to the difference between the sensors' resistances. Since the sample temperature is independently measured, and the two platinum thermometers on the sample are at the same temperature, the sample differential thermometer resistance can be calculated from its calibration curve. Given the sample differential thermometer resistance, the relative resistance bridge finds the standard differential thermometer resistance. The standard temperature is calculated from a calibration function, and δT can be found by subtraction.

Because the thermometers are made from very pure platinum wire, the only differences between them are the wire length and thickness[20]. Then the resistance of the sensors should be nearly proportional over a wide range of temperatures. Since resistance bridges are nulled when the two sensors have a certain resistance ratio, we can select the balance point to be where δT is zero. The relative resistance bridge balance adjustment can be constant though each calorimetry run from 65 to 120 K. Then the bridge can be made with manually operated ratiotransformers (programmable ratiotransformers are much more expensive, and not more accurate).

The standard instrument for comparing two resistances is the Wheatstone bridge. The Wheatstone bridge allows a four wire measurement of the resistance of only one of the sensors, and a three wire measurement of the other. Typical lead wire resistances are a few ohms, and the sensor resistance at 100 K is about 20 ohms, so a four wire measurement is necessary for both the sensors. William Thompson, Lord Kelvin, solved this problem by including another arm in the bridge that compensates for the extra voltage across the lead between the two sensors [87, page 285]. The Kelvin bridge balances when the resistance ratio of the primary and secondary arms equal the resistance ratio of the two sensors. By replacing the resistive voltage dividers with ratiotransformers, the A.C. Kelvin bridge becomes very accurate and quiet. Below we will describe the construction of

[20]The wire in our thermometers is subject to mechanical strain, so there are resistance shifts between different thermometers as a function of temperature and as the thermometers are cycled. Strain free thermometers are too large and heavy for our application.

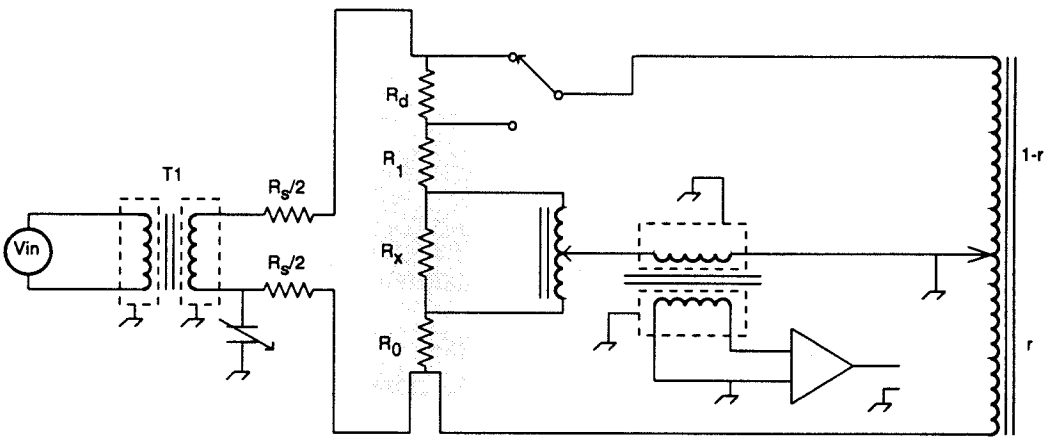

Figure 4.11: Relative resistance bridge.

our resistance bridge which typically exhibits 1 to 2 $nV/\sqrt{Hz}$ noise, repeatability better than 1 ppm and linearity better than 10 ppm.

4.6.1 Bridge Design

Figure 4.11 shows a schematic diagram of the A.C. Kelvin bridge. The thermometers are labeled R_0 and R_1. They are connected by a short length of copper wire, resistance R_x. The circuit is grounded at the center tap of the primary ratiotransformer, and the output is taken across the ground and the output of the secondary ratiotransformer. The detector input impedance is taken as Z_o, and r is the number of turns below the voltage tap of the ratiotranformers, divided by the total number of turns in each transformer. The excitation is coupled into the bridge through a homemade double shielded toroidal transformer[21]. The sensor current is injected into the thermometers through a resistance that is much higher than the sensor resistance (75 KΩ = $R_s/2$) to make the current relatively constant. It is a good approximation to model each ratiotransformer as an ideal voltage divider (infinite input impedance and zero output impedance), with a resistor, Z_{rat}, in parallel with the input, and a resistance, Z_{ro}, in series with the output. Then the output voltage is exactly

$$\frac{V_o}{V_s} = \frac{(rR_1 - (1-r)R_0)\frac{R_s \| Z_{rat}}{R_s}\frac{Z_o}{Z_o+2Z_{ro}}}{R_0+R_1+R_s\|Z_{rat}+R_x\|Z_{rat}+\frac{(R_s\|Z_{rat}+R_x\|Z_{rat})(R_1r^2+R_0(1-r)^2)+R_0R_1(1+r(1-r))}{(Z_o+2Z_{ro})(1-r)}}$$

[21] 100 turn primary, 200 turns secondary, on a Magnetics Inc. tape wound core, part number 54103-4K, each winding progressively wound in one section.

where the "$\|$" operator finds the resistance of two resistors in parallel. The output is nulled when $R_0/R_1 = r/(1-r)$. For platinum sensors at and below room temperature,

$$R_s \parallel Z_{rat} >> (R_0 \sim R_1) > R_x \parallel Z_{rat} \quad .$$

We can therefore approximate the output as

$$\frac{V_o}{V_s} \sim \frac{(rR_1 - (1-r)R_0)\frac{Z_o}{Z_o+2Z_{ro}}}{R_s(1+\frac{R_1r^2+R_0(1-r)^2}{(Z_o+2Z_{ro})(1-r)})} \quad . \tag{4.1}$$

Ideally the detector input impedance, Z_o, should be much larger than R_0, R_1 or Z_{ro}, but this is not always the case for our bridge. Therefore the bridge sensitivity is dependent on the approximate values of the sensor resistances, and the bridge output is nonlinear when the output is large. The latter is not a serious problem because the full scale output of the bridge and lock-in amplifier is well below the point where the nonlinearity is significant. But it is necessary to recalibrate the bridge sensitivity periodically as the temperature changes. The sensitivity must be known accurately because the derivative of the bridge output with respect to time is a significant correction term in the heat capacity.

A unique method to calibrate the bridge sensitivity to small resistance changes was implemented. An extra 10.0 $m\Omega$ precision resistor (R_d) was fabricated and included in series with the thermometer on the standard heat capacity. An extra lead came out of the cryostat so that a relay could be wired to select between two configurations, with and without the extra resistance. Periodically during the bridge operation, the relay is energized for a short time. It is then possible to calculate the bridge sensitivity from the shift in the bridge output when the sensor resistance changes. The resistance value and the bridge gain were chosen to make the jump about half of the full scale output.

The sensitivity calibration resistor must have a constant resistance over the entire range of operation, and we must be able to measure its resistance. Evanohm[22] wire has constant resistance within a few ppm per degree centigrade, so it was used to form the resistance element. A very short section of heavy gauge resistance wire was spot welded between two thinner pieces of resistance wire to form an "H." Six fine constantan wires were spot welded to the ends of the thinner resistance wire to provide contacts to the resistor that could be soldered to. This design insured that all of the current that generated the voltage across the resistor

[22]T. M. Wilbur B. Driver Co., Newark N.J.

passed through resistance wire, with none through the contacts. The resistor was potted in Stycast epoxy on a copper tab and screwed down on the standard heat capacity with grease to improve the thermal contact.

This resistor, R_d, measures the bridge gain to determine the magnitude of the derivative of δT, a correction to the heat capacity. Since R_d is in series with the thermometer on the standard, R_1, it determines the bridge sensitivity to small changes of R_1, dV/dR_1. The magnitude of $d\delta T/dt$ is proportional to the value of R_d,

$$\frac{d\delta T}{dt} = \frac{R_d}{\Delta V}\frac{dT}{dR}\frac{dV_{out}}{dt}$$

where ΔV is the change in the bridge output, V_{out}, when R_d is included in R_1. dT/dR is computed from the thermometer calibration curves. If we believe R_d is larger than it actually is, then the calculated value of δT will be too large also. $d\delta T/dt$ is used to correct the heat capacity for times when the sample temperature control is inexact (equation 3.1). It is difficult to measure the value of R_d directly, but easy to measure the effect when R_d is incorrect. The measured heat capacity will show an error proportional to the magnitude of $d\delta T/dT$. R_d was measured by varying the sample temperature control setpoint sinusoidally during a background run, causing a sinusoidal deviation from the smooth background when an incorrect value for R_d was used to analyse the data. Using trial and error, a value for R_d was discovered that eliminated the sinusoidal contribution to the heat capacity[23].

Every five to ten minutes, during each heat capacity run, the relay was activated and the shift in the bridge output was calculated by subtracting the average of the output with R_d in place from a least squares line fit to the output without the relay on. To analyse the data later, all the sensitivity calibrations during a heat capacity run were fit to the predicted functional form, simplified because the ratiotransformer settings were constant and the bridge is always very close to balance,

$$\frac{dV_{out}}{dR_1} = \frac{A}{1 + BR_1} \tag{4.2}$$

where A and B are complex constants. The calculated value for the bridge sensitivity as a function of R_1 was used to compute δT and then the heat capacity. Although δT was calculated in real time, it was not used to control the sample heater power because it was not available whenever the absolute resistance bridge changed its ratiotransformer setting to follow the drifting temperature. Instead,

[23] Actually a small sinusoidal component 90 degrees out of phase with $d\delta T/dT$ always remains. It is caused by heat flow between the sample cell and standard heat capacity.

the relative bridge output, δR, was used as feedback to the sample temperature regulation, eliminating jumps in the control when the absolute bridge changed its ratio. The sample temperature was controlled to zero the bridge output, not to keep δT zero. A small correction was added to the heat capacity to compensate for the smooth but nonzero value of $d\delta T/dt$.

One way to calculate $d\delta T/dt$ is to differentiate the calculated value for $\delta T = T_1(R_1) - T_0(R_0)$, with the T_0 measured by the separate platinum thermometer on the sample, and T_1 derived from the relative bridge output. However, when the computer changes the balance setpoint on the sample thermometer resistance bridge to follow the drifting temperature, the sample temperature is unknown for a short time and we cannot compute δT directly. Since the majority of the information about δT comes from the relative bridge output, this wastes the data taken during this time. Most of the information about δT comes directly from the relative resistance bridge output. The absolute temperature only sets the thermometer sensitivity (which varies slowly with temperature). We need an expression for $d\delta T/dt$ that is a function of the thermometer calibrations, the sensor calibration curve slopes, and the time derivative of the bridge output for small deviations from balance. The bridge imbalance can be written as

$$\delta R_1(T0, T1) = \frac{V_o}{G} = R_1(T_1) - kR_0(T_0)$$

where $k = (1-r)/r$, and we can measure G directly from the discontinuity in the bridge output when we switch in R_d, $G = \delta V_o/R_d$. G is a slowly varying function of R_0 and R_1. Then we can write δT as

$$\delta T = T_1(R_1) - T_0(R_0) = T_1(\delta R_1 + kR_0) - T_0 \quad .$$

Differentiating and rearranging yields

$$\frac{d\delta T}{dt} = \frac{dT_1}{dR_1}\bigg|_{R_1} \frac{d\delta R_1}{dt} + \left(k\frac{dT_1}{dR_1}\bigg|_{R_1} - \frac{dT_0}{dR_0}\bigg|_{R_0}\right)\frac{dR_0}{dt}. \tag{4.3}$$

The coefficient of the second term is about 400 times smaller than the coefficient of the first because the thermometer calibration curves are nearly universal, if k is chosen to balance the bridge when $\delta T = 0$. Another advantage of the method described above is that the noise contributed by the sample temperature measurement is nearly eliminated because dR_0/dt does not contribute much to δT. $d\delta R_1/dt$ is found by calculating the slope of the least squares line that fits the

δR_1 data over a narrow interval (usually three minutes long). Using the average values over the chosen interval of R_0 and R_1 and the slope of the sensor calibration curves at these resistances we can evaluate equation 3.1 to find the heat capacity.

4.6.2 Bridge Implementation

Figure 4.11 shows a schematic diagram of the double differential thermometer and resistance bridge. The components in the shaded box are mounted within the cryostat. Thermometer R_0 is on the cell. R_1 and the sensitivity calibration resistor mount on the standard. A total of eight leads emerge from the sensor. The extra leads that parallel the primary ratiotransformer input leads are used to measure and compensate for the small error caused by the finite resistance of the leads to the ratiotransformer. Since the input impedance of the ratiotransformer is about 150 $K\Omega$, a few ohms of lead resistance could cause one part in 10^5 error in the ratiotransformer ratio. A rotary switch in the bridge circuit allows the input to the detector to be one of several sources. Selecting one of the spare ratiotransformer input leads allows us to measure the voltage drop across the ratiotransformer input lead and compensate for the error. Another rotary switch sets the input to the primary ratiotransformer. The bridge circuit is quite simple, but the excitation source and detector were difficult to construct because they must interface with the computer, and they must not add any noise to the bridge.

Excitation Source

An excitation source provides a 330 Hz, 10 VAC signal to the primary of the input transformer. The input transformer couples the signal into the bridge, eliminating any common-mode voltage on the excitation signal. If there were more than one path to ground in the bridge, a ground loop would be formed that would pick up interference noise. Also a high frequency ground loop would be created if the bridge were capacitively coupled to a wire with a second path to ground. Therefore, both the input and the output transformer must have two electrostatic shields, one totally enclosing the primary and another around the secondary. A single electrostatic shield is not sufficient because a shield connected to ground through a wire with nonzero impedance will not be at ground potential. Then a high frequency ground loop could be formed that includes the primary and secondary windings. Two or more electrostatic shields reduce the coupling because much less current flows through the second shield's ground wire.

The excitation source must have constant frequency and amplitude to make the bridge output stable when it is off balance. The detector is a lock-in amplifier that needs two accurate reference signals phase locked to the excitation source. The "frequency/phase" circuit generates the excitation frequency and lock-in reference signals by dividing down a 6 MHz clock. Each reference signal is generated by delaying the excitation signal by a fixed number of 6 MHz clock periods. The circuit contains several Intel 8254 counter-timer chips interfaced to the metrabus computer interface. These counters are programmed with the excitation frequency divisor and the time delay for each reference signal. Because the resistance bridges easily pick up any signal at the excitation frequency, the frequency/phase circuit generates signals at twice the desired frequency. The signals are divided by two when received by the lock-in amplifier and the "resistance bridge excitation circuit."

The resistance bridge excitation circuit converts its input, a 660 Hz square wave, to a 10 V_{pp}, 330 Hz sine wave. The input signal drives the input of a optocoupler, to prevent a ground loop between the frequency/phase board and the excitation circuit. The input frequency is divided by two with an edge triggered flip-flop. Besides reducing the interference noise to the bridge, inputting twice the desired frequency also insures that the excitation circuit input is an exact square wave. The amplitude of the square wave is multiplied by the output from a Burr-Brown VFC-100 voltage to frequency converter operating in frequency to voltage mode. The input frequency for the F/V converter is taken from an eight channel rate multiplier circuit that is interfaced to the metrabus. This frequency and a 2^{18} Hz reference frequency is coupled in the excitation circuit with high speed optocouplers to eliminate ground loops. The resulting variable amplitude square wave, at the desired frequency, is transformed into a pure sine wave with a "biquad" bandpass filter with $Q = 10$. The biquad filter is used here rather than simpler designs, a VCVS filter for example, because it is more stable with respect to the drift of component values and because its center frequency can be tuned with a single trimmer without affecting the Q of the circuit. The sine wave output of the filter drives a unity gain, A.C. coupled output stage consisting of an op-amp driving a discrete transistor push-pull current buffer within the op-amp's feedback loop. High frequency noise is isolated from the output by an L-C filter in the output. The excitation amplitude was measured to be stable to within .02% over a 24 hour test period.

During construction, it was discovered that if there was a large loop area

through the circuit connecting the bridge ground, excitation circuit ground, excitation signal output, and bridge excitation input, then the bridge would pick up interference noise from the computer, even though the input transformer has a double electrostatic shield. This problem was solved by routing all the signal and power lines for the rack containing the lock-in amplifier and excitation board through a three inch copper pipe that served as the ground line for the rack. Furthermore, it was found useful to double shield the bridge input and output 50 Ω coaxial cables by stuffing each through 3/8" copper refrigeration tubing that was grounded to the bridge chassis. The precise wiring arrangement for all the shield ground lines was determined by trial and error. It would be best to tie all the ground wires to a single point as close to the resistance bridge as possible. But there are significant currents passing through some of the ground lines; these lines should be connected to the main experiment ground to prevent bridge ground noise [88].

An external capacitance was mounted on the output of the bridge input transformer to balance the quadrature signal. Because the voltage level of the bridge at the output of the excitation transformer is 8000 times the voltage across the sensors, an unsymmetrical capacitance in the input transformer windings is equal to a capacitive imbalance 8000 times greater across the thermometers. A variable capacitor to ground at one of the transformer output terminals corrects for any imbalance in the winding capacitance. The output transformer is mounted in its own chassis and located a distance from the bridge to prevent interference. The current source resistors are mounted in this chassis because all the high voltage wiring from the output transformer should be mounted rigidly to keep the quadrature signal constant.

Output Detector

The relative resistance bridge detector measures the amplitude and phase of the bridge output, without contributing any noise. The Johnson noise generated by a 20 Ω thermometer at 90 K is .3 $nV/\sqrt{Hz}$. Typical transistor circuits have about 2 $nV/\sqrt{Hz}$ input noise voltage, optimum for a 2 KΩ source resistance. A transformer can be used to match the bridge output resistance to the optimum source for the detector input while also isolating the bridge from the detector circuit. To prevent a ground loop with the detector circuit, the transformer has two electrostatic shields, as mentioned above. To prevent magnetic pickup by

the transformer's windings, the transformer core is made of tape-wound, high initial permeability magnetic material and the transformer is surrounded with mu-metal shields[24]. If the core permeability is larger, fewer turns are required in the transformer primary to give a certain primary self-inductance. The primary self-inductance must be high enough to prevent loading the source voltage. Fewer turns in the primary reduces the number of turns in the secondary, for a given turns ratio, which reduces the stray magnetic pick-up. A design trade-off must be made between increasing the total number of turns in the transformer, to reduce its input impedance, and reducing the number of turns in the secondary, to reduce the stray pick-up. The transformer we used had a 15:1 voltage gain and a 300 turn primary. The input impedance at 300 Hz is about 100 Ω. More primary turns would be necessary for higher source impedances[25].

The signal from the bridge output transformer secondary was amplified and filtered with a preamplifier located in the bridge chassis before it was input to the lock-in amplifier. The preamplifier input stage consisted of a pair of 50× gain noninverting amplifiers made with PMI OP-37 operational amplifiers. The amplifier outputs were summed at the input of a VCVS bandpass filter that was tuned to the bridge frequency. More stable and complicated filter circuits were tried, but the circuit with the lowest noise was the simple single op-amp VCVS circuit. A filter is necessary in the preamplifier because even though we have taken great precautions to eliminate interference noise pickup, there is a lot of 60 Hz noise present on the preamplifier input. The bridge excitation frequency is chosen to be far from any power line frequency harmonic. The filter is also necessary because our lock in amplifier design is sensitive to odd harmonics of the

[24]The transformer core is made of Supermalloy, Magnetics Inc. core number 54103-2F. The core was wound by Roger at Zenith Enterprises, Northridge, CA. The primary consisted of 300 turns of two #21 wires in parallel, the secondary 4500 turns of #31 wire. There were two electrostatic shields between the windings, and both windings were wound in two separate equal sections to reduce the interwinding capacitance.

[25]We tried several commercial instrument transformers to try to improve the bridge performance (Triad-Utrad G-4, UTC LS-12X). These transformers did not perform as well as our own design because they are not toroidal, they do not use double electrostatic shields, and they do not use high initial permeability tape-wound cores. The commercial transformers are designed for smooth frequency response and low average noise over a broad bandwidth. Our design is optimized for very low noise over a very narrow bandwidth and frequency range. These designs are derived from standard microphone input transformers, where high signal levels and a wide frequency range are encountered. Note that commercial low-Z lock-in amplifier preamplifiers are made with this type of transformer, and cannot produce optimum performance in this specialized application.

excitation frequency. The Q of the filter was set to reduce the power line noise to a low enough level to prevent overloading the lock-in amplifier input stage. The power source for the preamplifier is a ± 15 volt regulated supply that has its input voltage isolated with two shielded isolation transformers[26]. A capacitor to ground was inserted to balance the capacitance between the two isolation transformer windings to improve the shielding.

The preamplifier output is detected by the lock-in (phase sensitive detector). An instrumentation amplifier (PMI AMP-01) isolates and amplifies the preamp output. Any connection between the grounds of the bridge and lock-in would create a ground loop. The instrumentation amplifier output is limited (± 10 V) and inverted by a precision inverting circuit. Both the signal and its inverse are fed into a two channel, two input CMOS multiplexer (4066). Each multiplexer output is either equal to the instrumentation amplifier output or its inverse, depending on the state of a control signal. The control signals are the reference outputs from the frequency/phase circuit that have been opto-isolated and buffered. Therefore the multiplexer output will take the absolute value of the input signal when it has the proper frequency and phase. The computer can vary the phase of the reference signals by reprogramming the counter chips on the frequency/phase board to make one channel in phase with the bridge output, and the other 90 degrees out of phase. four pole butterworth VCVS low-pass active filters ($F_{3db} = 5Hz$) average the multiplexor outputs for each channel. The lock-in outputs are digitized by Burr-Brown VFC-100 frequency to voltage converters whose optoisolated outputs are counted by a 16 channel 16 bit counter board that is interfaced to the metrabus isolated computer interface.

All the instruments use the same V/F converter scheme to convert analog signals to digital and interface them with the computer. Then to isolate the different instruments from the metrabus ground level requires only two optoisolators, one for the V/F output and another for the VFC-100's reference frequency. A standard cable and connector to all the V/F outputs allows quick modification of the set-up to suit the desired experiment. The V/F converters are stable and linear to .02% in V/F and F/V modes. In V/F mode, the converter outputs are a true integral of the input signal over the time period over which the output is counted. Then it is not necessary to use an anti-aliasing filter before the input to the converters and the output responds quickly to changes in the input. This scheme

[26]Double-shielded power transformers are no longer available except by special order.

proved an economical and convenient alternative to separate conventional 14 bit D-A and A-D converters in each instrument for low speed data acquisition and control.

The metrabus instrument interface simply provides an external 8-bit parallel data path between the computer and each instrument, controlled by a card in the IBM P.C. AT. The data transfer is under complete computer control and the frequency counter and computer are synchronized by a 2 Hz clock that triggers an interrupt service routine in the PC. During operation, every half second the computer reads the output from the two counter channels and records it in a file. Every five to ten minutes, the PC energizes a relay that switches in the small resistor in series with the standard differential thermometer to calibrate the sensitivity. The computer corrects the output for the ratiotransformer lead wire imbalance, calculates the sensitivity, and computes the resistance imbalance in real time. The imbalance is fed into a proportional-integral-derivative control algorithm that sets the sample's heating rate.

4.7 Absolute Resistance Bridge

The absolute resistance bridge measures the resistance of the platinum thermometer on the sample cell, and calibrates the platinum thermometers with each other and to the isolation diode thermometers. A.C. excitation is used in order to eliminate the effect of thermoelectric voltages and to use a transformer coupled detector. For suitable accuracy, the measurement should not be affected by the lead resistances of either sensor, so a 4-wire bridge is necessary. The relative resistance bridge described in section 4.6 above uses two ratiotransformers to compare two resistances that are always nearly equal. However, the absolute bridge must compare the thermometer resistance to that of a known standard. If programmable decade resistance boxes were accurate and linear to one part in 10^6, then a Kelvin bridge with fixed ratiotransformer ratios and a variable standard resistance would work. But programmable resistance boxes are usually ten times less accurate than ratiotransformers, so the circuit should use a fixed standard resistance and vary the ratiotransformer setting. Computer controlled ratiotransformers are the best solution, but since they cost about \$10K each, and two would be required for a Kelvin bridge, we searched for an accurate resistance bridge using a single ratiotransformer. Commercial resistance bridges of suitable accuracy cost as much as \$40K, and may not give extremely low noise. Other researchers have employed

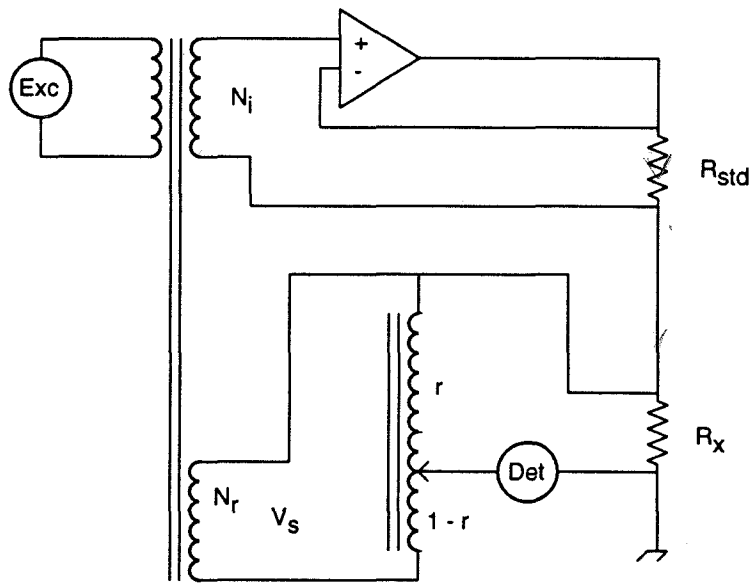

Figure 4.12: A.C. Anderson resistance bridge.

switches in the bridge circuit to periodically measure and compensate for the lead resistance for Wheatstone style ratiotransformer bridges [89], but this experiment needs continuous automatic operation over a wide temperature range.

A.C. Anderson devised a 4-wire A.C. resistance bridge that uses one ratiotransformer and only one active component (op-amp), see figure 4.12. A.C. voltage applied to the primary of the input transformer generates a voltage, $V_s N_r$, on the lower secondary, and $V_s N_i$ on the upper secondary winding. The upper circuit generates a current equal to $V_s N_i / R_{std}$, which all passes through the unknown resistor (if the detector has infinite input impedance). The voltage across the sensor is then $R_x V_s N_i / R_{std}$. The ratiotransformer divides $V_s N_r$ by the ratiotransformer ratio, r, which is compared to the voltage across the unknown by the detector circuit. The detector input will be:

$$V_{detector} = \frac{R_x V_s N_i}{R_{std}} - r V_s N_r$$

and the bridge will balance when $r N_r / N_i = R_x / R_{std}$.

In the sections below we will discuss the noise in the resistance bridge, effects of nonideal op-amp performance, finite ratiotransformer input impedance, and other corrections to the absolute resistance bridge. Then we will describe how the bridge was constructed.

4.7.1 Noise in the Absolute Resistance Bridge

The Johnson noise voltage across the platinum thermometer is .3 $nV/\sqrt{Hz}$ at 90 K. With the bridge frequency at about 300 Hz, there is little 1/f noise generated by the sensor. Our goal in designing the absolute resistance bridge is to make the source resistor noise the dominant noise source. There are several sources of noise in the relative bridge. All resistors in the bridge circuit generate noise, including the resistance in the windings of the transformers. The operational amplifier has a certain amount of current and voltage noise across its input terminals.

The RMS Johnson noise voltage across a resistor with resistance R, at absolute temperature T and measured in the bandwidth B Hz, is $\sqrt{4K_bTRB}$. Following the notation in reference [85], a noise source can be characterized by the resistance of a resistor at room temperature (300 K) that generates the same noise voltage over the same bandwidth, $R_n = e_n^2/(4K_b300B)$ or, if the source is a resistor at temperature T, $R_n = R(T/300)$. This is called the "noise resistance" of the noise source. When there are several sources of noise adding together in a circuit the noise resistances should be summed to find the total noise. The inevitable noise caused by the thermometer resistance at 90 K (26 Ω) has a noise resistance of about 7.7 ohms. It was originally claimed that the Johnson noise voltage across the standard resistor would not cause noise in the bridge output, because the op-amp output impedance is low, but it was later argued that there would be noise current in the unknown resistor's excitation [90]. Johnson noise across the standard resistor will cause a noise current to flow in the unknown, e_{std}/R_{std}. Then the noise voltage across the unknown is $e_{std}R_x/R_{std}$, equivalent to an extra noise resistance in series with the unknown, R_x^2/R_{std}.

Also the op-amp input voltage noise (e_{op}) will cause a noise current through the unknown (e_{op}/R_{std}) that causes a noise voltage across the sensor, $e_{op}R_x/R_{std}$. Low noise op-amps usually have about 3 $nV/\sqrt{Hz}$ of input voltage noise that can be characterized by an additional noise resistance in series with the sensor, $R_n = 543(R_x/R_{std})^2$. The current noise in the op-amp will cause a noise current in the sensor that equals i_nR_x, contributing an insignificant $1.5 \times 10^{-5}R_x^2$ ohms of noise resistance. If $R_x \sim R_{std}$, the op-amp input voltage noise will be much too large. To reduce this effect, instead of using the same number of turns in the two secondary windings of the input transformer, our resistance bridge has about 20 times more turns on the secondary that drives the current source than on the secondary that drives the ratiotransformer. Then the bridge will balance

when $r/20 = R_x/R_{std}$. If the ratiotransformer ratio is near one when the bridge is balanced, the noise resistance contributed by the op-amp and the Johnson noise across the standard resistor will be $R_x/20 + 543/400$ ohms.

Additional noise comes from the detector preamplifier input voltage and current noise, and the transformer winding resistances. A noise voltage at the input of the detector preamplifier, e_{det}, is equal to a noise voltage, $e_{det}N_p/N_s$, in series with the sensor. The first stage has two noninverting amplifiers in parallel to reduce the noise voltage to 1.7 $nV/\sqrt{Hz}$ at the preamplifier input. The output transformer turns ratio is $N_p/N_s = 300/4500 = 15$, so the additional noise resistance is .8 ohms. Current noise is also generated by the detector op-amps, .5 $pA/\sqrt{Hz}$ per op-amp stage, that adds another $R_x^2/74$ ohms of noise resistance in series with the sensor. When R_x is above 22 ohms, the current noise contributes at least as much noise as the unknown resistor[27].

The noise resistance of the input and output transformer winding resistances are made very small by using heavy gauge wire and the smallest number of turns possible, but the ratiotransformer windings may contribute as much as four ohms of noise resistance when the ratio is near 1/2. The calculations above greatly overestimate the noise performance of the bridge because it is difficult to shield the bridge from sources of high frequency interference noise. And, since the ratiotransformer is at best linear to one part in 10^6, noise below $R_xI_x/10^6$ averaged over the measurement period is insignificant. With .1 mA sensor current, the noise should average less than 2 nV over the measurement period. The noise generated by a 10 ohm noise resistance averages to less than 2 nV after only .2 seconds, if a lock-in detector is used. We have demonstrated that this bridge design can yield excellent noise performance, well below the linearity of the bridge, with noise comparable to the Johnson noise in the thermometer.

4.7.2 Sources of Bridge Inaccuracy

The balance equation for the absolute resistance bridge, $rN_r/N_i = R_x/R_{std}$, assumes that all the bridge components are ideal. However the transformers are only approximately ideal: the op-amp has finite open loop gain, and the standard resistance has a reactive component. In this section we will discuss the effect of

[27] In this case it would be useful to use only a single preamplifier op-amp input stage. For even higher source resistances, another output transformer should be wound with a smaller turns ratio (N_s/N_p) to better match the optimum op-amp source impedance and to increase the input transformer input impedance.

these errors.

The operational amplifier that drives the current source is far from ideal. It has finite input impedance, nonzero output impedance, finite open loop gain, and nonzero common mode gain. The fractional current source error due to finite open loop gain and nonzero common mode gain is given by $(A_v \pm A_{cm})/(1 + A_v) - 1$ where A_v is the open loop gain and A_{cm} is the common mode gain at the excitation frequency. A_v is about 90 db for the PMI OP-27 at 300 Hz, A_{cm} is about -36 db, so the current source error is about .003%[28]. The op-amp input impedance, R_d, is about 5 MΩ, which causes a relative error in the current $(R_x + R_{std})/(AvRd)$ or about one part in 10^{14} for $R_{std} = 1K\Omega$.

The bridge input, output and ratio transformers are not ideal; they have finite input and output impedances. No errors are caused by the input transformer secondaries' winding resistance or impedance since the number of turns are small, and the ratiotransformer and current source op-amp input impedances are large. The ratiotransformer linearity is quoted at .001%; this is the second largest source of error. The ratiotransformer output impedance is $(4\ \Omega + 75\ \mu H)$, which reduces the output when the bridge is off balance but doesn't affect the balance point. Likewise, the output transformer input impedance only reduces the bridge output when out of balance and makes the output slightly nonlinear. In order to calibrate the output gain, the discontinuity when the ratiotransformer ratio is changed can be used to find the sensitivity.

The standard resistor(s) have significant series inductance at the bridge frequency, $\sim$ 300 Hz. Then the sensor current will be complex and equal to

$$V_s \frac{R_{std} - jwL_{std}}{R_{std}^2 + (wL_{std})^2} \quad .$$

A variable capacitor is located effectively in parallel with the standard resistor to balance the inductance, but the real part of the resistance is still reduced by .0004% for a R_{std} with 1 KΩ ohms resistance and 1 mH inductance.

In this section we have shown the dominant sources of error in the absolute resistance bridge to be caused by the finite open loop gain of the current source and the ratiotransformer nonlinearity. Since the voltage at the current source output is nearly constant ($R_x < R_{std}/20$), the current source error should be constant as R_x changes. Then it should be possible to remove the current source

[28]Given that $R_{std} + R_x >> R_o$, where R_o is the op-amp open loop output impedance, 70 ohms. With lower R_{std} values, the current source error will be larger.

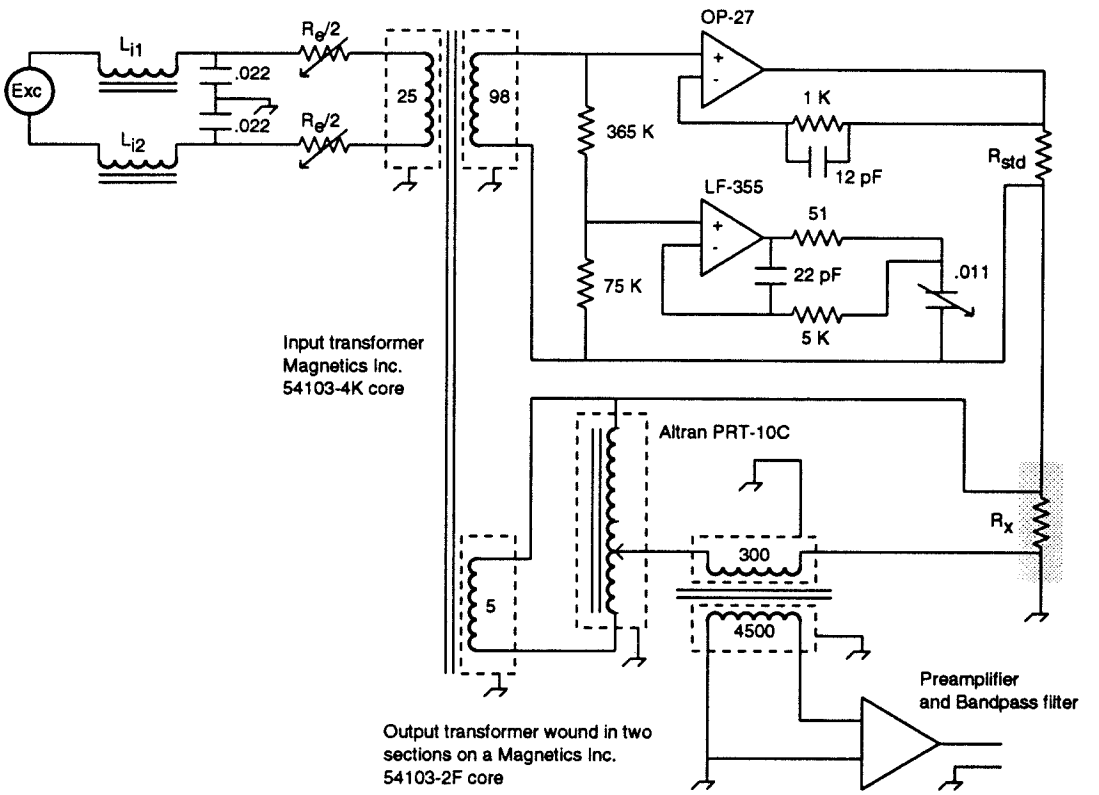

Figure 4.13: Absolute Resistance Bridge.

error by calibrating the bridge with resistance standards. In the next section we will discuss the resistance bridge construction details.

4.7.3 Absolute Resistance Bridge Implementation

Figure 4.13 shows the circuit used for the bridge. Great care was taken in constructing the bridge to eliminate interference noise, ground loops and room temperature sensitivity. The input excitation comes from a circuit identical to that used for the relative bridge described above. High frequency differential and common mode noise is attenuated by the L-C filter[29] at the input to the bridge. The excitation is varied by changing the resistance in series with the input transformer primary (R_e). The flux through the core is controlled by varying the amplitude of

[29]Each inductor, L_{i1} and L_{i2}, is 100 turns on a Arnold Co. A4-1060-440-E core, about 1.3 mH, and the capacitors are .022 μF.

the A.C. current through the primary winding[30]. The voltage across the current source secondary on the input transformer drives the input of a P.M.I. OP-27 op-amp that supplies the current for the standard resistor (selected by a four pole, six position rotary switch with R_{std} between 100 and 2400 ohms). The resistor and capacitor in the amplifier feedback loop help stabilize the circuit. Another current source provides variable amplitude current that is 90 degrees out of phase to balance the standard resistor inductance. The current source primary voltage is attenuated by a resistive voltage divider to enable finer adjustment. A National LF-355 op-amp provides the current passing through the variable capacitance box. Components in the feedback loop of this amplifier prevent the quadrature current source from oscillating because of the capacitive load. The output from the current source generates a voltage across the sensor, R_x, that is compared with the voltage across the other input transformer secondary attenuated by the ratiotransformer. There are only five turns in this secondary winding, so the output impedance of this secondary is very low. Therefore the secondary voltage is not affected by the ratiotransformer input impedance, 150 KΩ.

The detector, consisting of the output transformer, preamplifier, and bandpass filter compares the voltage across the ratiotransformer output to the voltage across the unknown resistance, R_x. The output transformer is identical to that used in the relative bridge and was designed to match the source resistance, R_x, to the noise performance of the preamplifier, to isolate the preamplifier from the bridge, and to minimize the pick-up of stray magnetic fields. Also, the same preamplifier and lock in amplifier design was used as in the relative bridge, two P.M.I. OP-37 noninverting amplifiers that feed into a bandpass filter, then into the lock-in amplifier.

To minimize the sensitivity to room temperature fluctuations, the entire circuit is mounted within a copper box that is within a styrofoam box inside a aluminum chassis. The copper box is heated by a homemade analog temperature control circuit that uses integral and proportional control to regulate the temperature to

[30]The input transformer core was a Magnetics Inc. core number 54103-4K in a homemade plexiglas box. The primary winding is a single layer of #28 copper magnet wire that was box shielded with copper tape. Another box shield and a corrugated rubber spacer was then formed over the core. The 98 turn current source secondary was progressively wound with #26 plastic insulated stranded wire. Another corrugated rubber spacer, layers of polypropylene cloth and a box shield were taped to the core. Then five turns of Belden #7221 75Ω coaxial cable were wound to form the secondary that drives the ratiotransformer. The coaxial cable's shield was used as a box shield. The corrugated spacers reduce the distributed capacitance of the secondary windings.

$\pm.1$ K. Precision wirewound resistors typically have temperature coefficients of 5 ppm/C or less, so the standard resistors should change by less than .5 ppm. One of three test resistors may be selected as R_x, instead of the thermometer, in order to test the bridge performance. These resistors must be located inside the temperature controlled oven in order to have a resistance standard stable enough to test the bridge.

The bridge was also wired with careful attention to ground loops and shielding. Shield and signal lines take the same path to the common ground to prevent ground loops. The power supply for the ratiotransformer was removed from the ratiotransformer chassis and mounted away from the bridge. Both the ratiotransformer and the bridge power supplies are isolated by a common Ultra-Isolation transformer[31] and each is further isolated by a pair of back to back shielded isolation transformers. Most of the ground lines join a common grounding block at the back of the bridge, which is grounded by a #4 copper wire to the main system ground bus. When initially constructed, the bridge was very sensitive to noise from the computer. It was discovered that two or more opto-isolation stages were necessary to shield the bridge from modulated high frequency noise. Because the capacitance across opto-couplers is nonzero (20 pF), two stages of opto-isolation equal one electrostatic shield, with the intermediate circuit as the ground. At least two electrostatic shields (or equivalent) are used in all connections between the computer and the bridge. When properly grounded, there is no measurable interference between the computer and the bridge, the noise is below 1 $nV/\sqrt{Hz}$, and the data are linear to about 1 ppm.

The bridge is completely controlled by a computer program written in the 'C' language. During initialization, the lock-in phases are set, an initial balance is found, the quadrature signal is set, and a starting gain is calculated. Then during normal operation the computer adjusts the ratiotran ratio to stay in balance. Every five to ten minutes the ratiotran ratio is changed and the output sensitivity is calculated and averaged with the last three sensitivity calculations to reduce the statistical noise in the sensitivity. The sensitivity is used to calculate the unknown resistance when the bridge is not exactly in balance. To calculate the sensitivity, the complex bridge output data are fit to a least squares line, including the discontinuity when the ratiotran ratio, R, changes

$$V_{out} = S_r R + A + Bt$$

[31] Topaz Inc.

where S_r is the ratio sensitivity, t is time, and all the constants are complex numbers. The least squares fit to the data is calculated in real time using the data from 20 seconds before and after the ratio is changed. If the resistance is drifting rapidly and causes the output to go nearly off scale, the ratiotran ratio is not set to rebalance the bridge exactly, but to oppose the drift rate in order to maximize the time until the output is again off scale.

Under certain conditions the cell temperature may jump up or down, for example, when a large dose of gas is added to the cell. In this case the sensitivity calculation can be fooled and generate incorrect results. Three features help prevent this. First, if the bridge goes off scale suddenly, all the previous output data are not used for the future sensitivity calibrations and the output is put back in range by a binary search. Second, if gas is to be removed from the cell and it is known that the temperature will jump, a variable can be set to order the bridge to forget the previous sensitivity data after the jump occurs. Third, if a sensitivity calculation is much different from the average of the last three calculations, it is ignored[32]. The bridge has operated successfully for as long as sixty days without being reinitialized.

4.8 Silicon Diode Thermometer Interface

Four bodies in the calorimeter provide an adiabatic environment for the sample cell and the standard: the isolation thermal mass, upper thermal platform, and the inner and outer shields. The temperatures of these bodies need to be regulated to equal the standard temperature to within about one miliKelvin. Diode thermometers are a good alternative to platinum thermometers because they are inexpensive and have very high sensitivity. However, two problems must be solved. First, reading the diodes to within 1 mK over the range from 10 to 300 K requires voltage measurement accurate to within .0001% or 20 bits (0 to 2V range, 2.5 mV/K sensitivity). There are no inexpensive D-A converters that are this accurate. Second, thermally generated voltages in the cryogenic lead wires can easily cause temperature errors greater than one miliKelvin.

[32]If data are encountered where there is significant curvature over short times (40 seconds), the sensitivity calculation should be changed to use a quadratic fit to the bridge output, otherwise the sensitivity data will be incorrect. During the heat capacity data the drift was linear, so a linear fit was sufficient. It would probably be best to examine the sum of the squared errors for each sensitivity calculation.

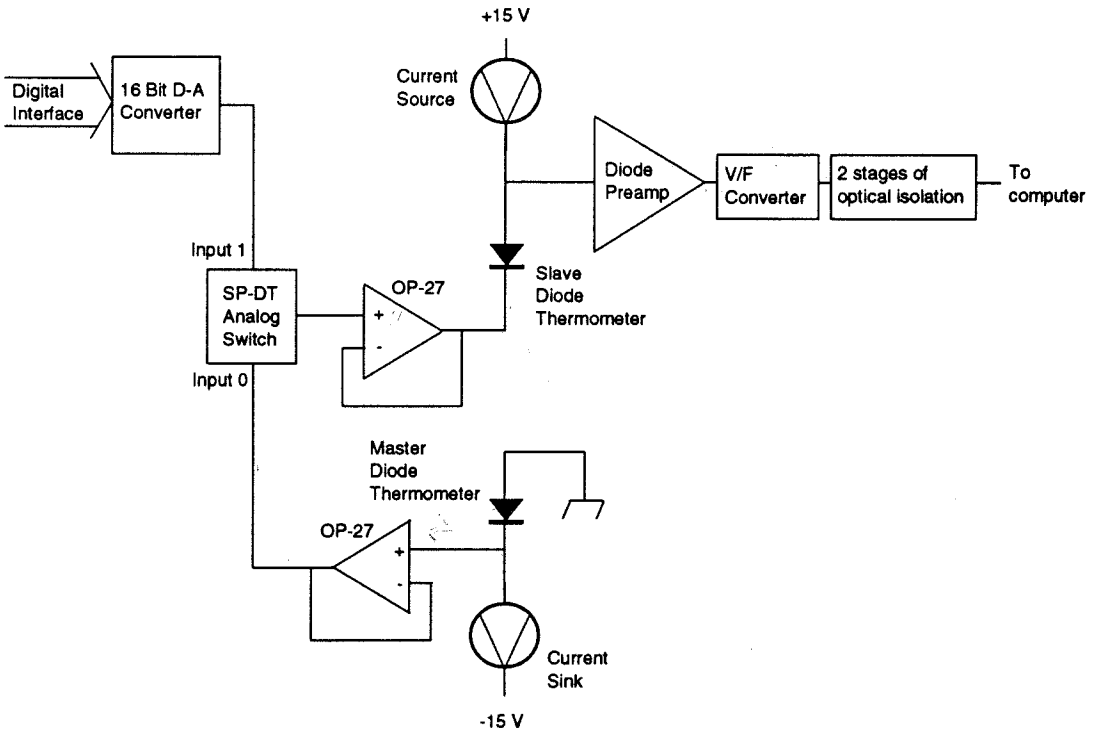

Figure 4.14: Diode Interface Circuit.

The solution to the first problem lies in realizing that only the relative temperature measurement needs to be accurate, not the absolute temperature reading. Another diode thermometer, the "master diode," is located on the standard heat capacity and the other four diodes' voltages are compared with its output or the output of a reference voltage V_{ref}. It is much easier to measure the small voltage difference between the thermometers by subtracting the voltage across the diodes in the hardware than to measure the voltage to within 20 bits and then subtract. Figure 4.14 shows the block diagram for the diode interface. The $10\mu A$ current sink excites the master diode that has its positive terminal grounded. Then the voltage across the master diode is read on the negative terminal and buffered with an OP-27. An analog switch is interfaced to the digital input so the computer program can select either the master diode output or a D-A converter output to compare to all the slave diodes' outputs. The slave diode's negative terminal is fixed at the voltage on the output of the analog switch, so that the difference between the slave diode voltage and the comparison voltage can be read on the slave diode's positive terminal. The difference voltage is amplified, digitized by

the V/F converter, and sent to the frequency counter board on the metrabus interface to the computer. Two stages of optical isolation, one inside the diode interface chassis, and another outside the diode interface prevent high frequency noise from entering the circuit. There are seven identical slave diode channels[33], each consisting of a $10\mu A$ current source, a 1200 times gain preamp, a V/F converter and two stages of optical isolation. The computer program sets the 16 bit D-A converter output close to the (negative) voltage across the master diode. The master diode absolute voltage is measured with an AMP-01 instrumentation amplifier that compares the D-A converter output to the (buffered) master diode output, which is digitized with the same V/F circuit as used by the slave diodes.

An important consideration in interfacing to silicon diode thermometers is their source resistance. The diode voltage vs. current curve is [84, page 65]:

$$I_d = I_o(T)(e^{qVd/kT} - 1)$$

$$V_d = \frac{K_b T}{q} \ln\left(\frac{I_d - I_o(T)}{I_o(T)}\right)$$

for temperatures above 30 K, where q is the charge on the electron, and K_b is Boltzmann's constant. For constant current, the output voltage is roughly proportional to $1/T$. The dynamic output impedance of the sensors is

$$\frac{dV_d}{dI} = \frac{k_b T}{q I_d}$$

which equals 560 ohms at 90 K for our diodes[34]. Then, although the diodes' effective resistance is about 100 $K\Omega$ (1 volt / 10^{-5} A), the voltage vs. current curve is very flat and they should be treated as a low resistance and low noise signal source. Therefore bipolar op-amps rather than FET input op-amps should be used to amplify the diode outputs, because they match the diodes' dynamic resistance.

Figure 4.15 shows a detailed circuit diagram for the current source and sink, and the preamplifier. The current source is made by fixing the voltage across a

[33]The extra channels are needed because four diode thermometers are used to provide an isothermal environment when the diodes are calibrated against the platinum thermometer. Then three channels are left to use for measuring the thermometers to be calibrated.

[34]We used commonly available 1N914 diodes glued into machined copper holders. Thin copper leads were glued to a rounded part of the holder to heat sink the leads. The holders were screwed down with 2-56 stainless steel screws. Commercial diode thermometers may be more reproducible, but our thermometers were stable upon thermal cycling to about 1 mK and were much less expensive. The diodes were repeatedly cycled from 300 to 77K before they were used in the calorimeter.

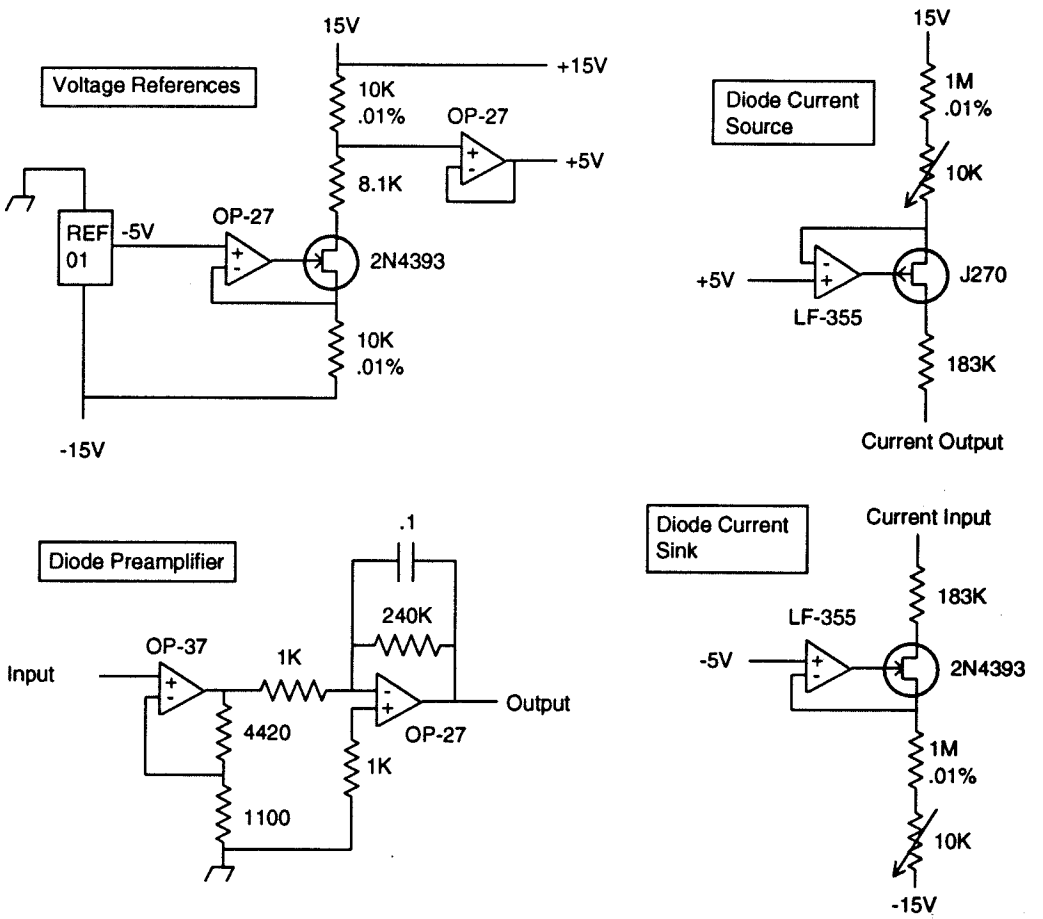

Figure 4.15: Diode Interface Circuit Components.

known resistance, then the current through the resistance is known from Ohm's law. The voltage across the known resistance must be stable, so it is derived from a precision 10 volt reference integrated circuit. This chip is connected to deliver a voltage 10V above the -15V supply. A second reference voltage 10V below the +15V supply is derived from the first reference. In the current source a one megohm resistor is connected to the +15V supply. Feedback from the operational amplifier adjusts the current through the JFET transistor to set the voltage at the other side of the resistor at the same level as the 5V reference voltage. Then the voltage across the resistor is 10V, and the current is $10\mu A$. Since the current through the op-amp inputs and through the JFET gate terminal is negligible, $10\mu A$ flows through the output. The 183 $K\Omega$ resistor limits the current through the sensor in case the transistor should fail, and reduces the voltage across the

JFET to reduce the gate current leakage. The current sink circuit is identical to the current source circuit reflected about ground.

The diode preamplifier circuit is simply a five times noninverting amplifier followed by a 240 times gain inverting amplifier. Two stages are used because if the comparison voltage were far from the diode voltage, the first amplifier would saturate. If this amplifier had high gain, there would no longer be zero voltage across the op-amp's input terminals and current would flow through the protection diodes built into the op-amp. A large current could easily destroy the diode thermometer. The low gain first stage amplifier is never saturated, preventing this problem. The .1 μF capacitor across the second stage feedback resistor limits the amplifier's high frequency response.

Reducing the stray EMF's in the diode leads requires careful attention to the cryostat wiring. Each diode lead is made of a continuous #37 copper wire from outside of the probe, through the vacuum feed-through, to the upper thermal platform. At the upper thermal platform, the leads are attached to gold plated OFHC copper tabs that are squeezed between hard anodized aluminum washers to anchor them thermally at low temperature. The wires are thermally anchored on the other bodies by gluing several inches of wire in groves with high thermal conductivity epoxy. All the junctions are made with low thermal EMF cadmium alloy solder. Tests have shown that the stray EMF's are at or below 1 μV.

The computer controls the diode interface by adjusting the D-A output and by setting the control signal for the analog switch to select the source for the comparison voltage. There are two modes of operation for the interface. While the bridge operates in the first mode, the slave diodes are compared against the master diode output. In the second mode the slave diodes are compared with the D-A output. In the first mode, the D-A converter is set to keep the master diode preamplifier output in range; the master diode voltage can be computed from this output, the D-A output voltage and the preamplifier gain. The slave diode preamplifier outputs report the difference between the voltage across each slave diode and the master diode, so the slave diodes' voltages can be computed from each channel's gain, the master diode voltage and the preamplifier output. During the second mode of operation the D-A converter is adjusted to keep as many of the channel's preamplifier outputs in range as possible, with some of the channels having higher priority than others. Each diode output voltage can be computed from the preamplifier output and gain. In either mode, the diode interface reports the voltages across whichever diodes are in range and another

section of the program converts the voltage to a temperature using a calibration curve (4th order Chebyshev polynomial over the temperature range from 65 to 120 K). A large number of diodes were tested at 77 K to find a set of eight that had nearly the same calibration curve. Then these were calibrated against the platinum thermometer.

During calorimetry, while the diodes are used in a feedback loop to keep all the bodies at the same temperature, all the diode voltages are nearly identical. If the interface is using the first mode, the slave diode preamplifier outputs will be nearly zero and the temperature error due to inaccuracies in the channel gain data will not greatly affect the temperature measurement. Therefore the first mode of operation is more precise for relative temperature control, compared to the second mode where the errors caused by uncertainty in the gain will be large when the preamplifier output is nearly full scale. Mode two is useful when the diodes are at different temperatures and the D-A output can be adjusted to bring more of them into range, since the full scale range of the preamplifiers is only $\pm 3.5K$.

The diode interface is a unique instrument that is less expensive and more accurate than commercial temperature controllers for comparing the temperatures of several bodies when they are near to each other. Although the commercial circuits may give better absolute accuracy[35], this circuit will provide much better isolation for the calorimeter. The noise on the relative temperature readings is about .3 mK and the long term stability is about 1 mK.

4.9 Heater Power Circuits

Precisely metered, computer controlled electrical power needs to be provided for the sample cell and the standard heaters. Heaters on the upper thermal platform, isolation thermal mass, inner shield, outer shield, and fill tube are also controlled by the computer. To collect heat capacity data accurate to .01%, the sample and standard heater voltages must be known to within .005% and the heater resistances must be known to within .01%. During operation, the heat input to the standard heat capacity is constant, so we only need to know the heater resistance to set the voltage. Feedback control is used to set the heat input to the sample in order to maintain the sample at the same temperature as the standard. Analog control circuitry would be able to maintain δT near zero but

[35] Probably because their D-A or A-D converters are more linear than the Burr Brown DAC-703KP used in this circuit.

makes it difficult to measure the power input to the sample. Digital feedback will not control the cell temperature as well as analog control but will easily and accurately measure the sample power. The cell heater power source must also measure the cell heater resistance during operation, so the heater is part of a D.C. Kelvin resistance bridge. Power for the heaters on the other parts of the cryostat is provided from the scaled output of V/F converters.

The standard method of feedback control is to feed the error signal into an analog circuit that sums the output of three analog circuit functions, a multiplier (amplifier), an integrator, and a differentiater [91]. The heater power is proportional to the sum of the output from these circuits. But to measure the power delivered by a heater, either the power must be constant, or the voltage and resistance must be recorded as a function of time. Invariably, each voltage and resistance measurement represents an average over a time period. If the heater voltage changes significantly over the time of the measurement, then the power computed from the data as $< V >^2 /R$ will not equal the true power, $< V^2/R >$, where $< V >$ denotes an average over the measurement time, δt. The error in the power is

$$\frac{< V^2 > - < V >^2}{R} = \frac{1}{\delta t}\int_{-\delta t/2}^{\delta t/2} \frac{V(t)^2}{R} dt - \frac{1}{R}\left(\frac{1}{\delta t}\int_{-\delta t/2}^{\delta t/2} V(t) dt\right)^2 \quad .$$

given that the heater resistance is constant. If the voltage is rising linearly with time, the fractional error in the power is

$$\frac{< V^2 > - < V >^2}{< V^2 >} = \frac{\dot{V}^2}{4 < V^2 >}\delta t^2$$

As the cell is drifting up in temperature, the heat capacity and the heater power are changing. The error in the measured sample heater power can be written in terms of the rate of change in the sample heat capacity, with the sample drifting upward in temperature at a constant rate,

$$\frac{< V^2 > - < V >^2}{< V^2 >} = \left(\frac{1}{4C}\frac{dC}{dT}\frac{dT}{dt}\right)^2 \delta t^2 \quad .$$

Although in principle dC/dT can be infinitely large when going through sharp phase transitions, in practice the error due to this affect is negligible for even the sharpest phase transitions in our films.

Digital control eliminates the above problem, simplifies the computer interface, and only slightly degrades the control accuracy. A fast, precise D-A converter is

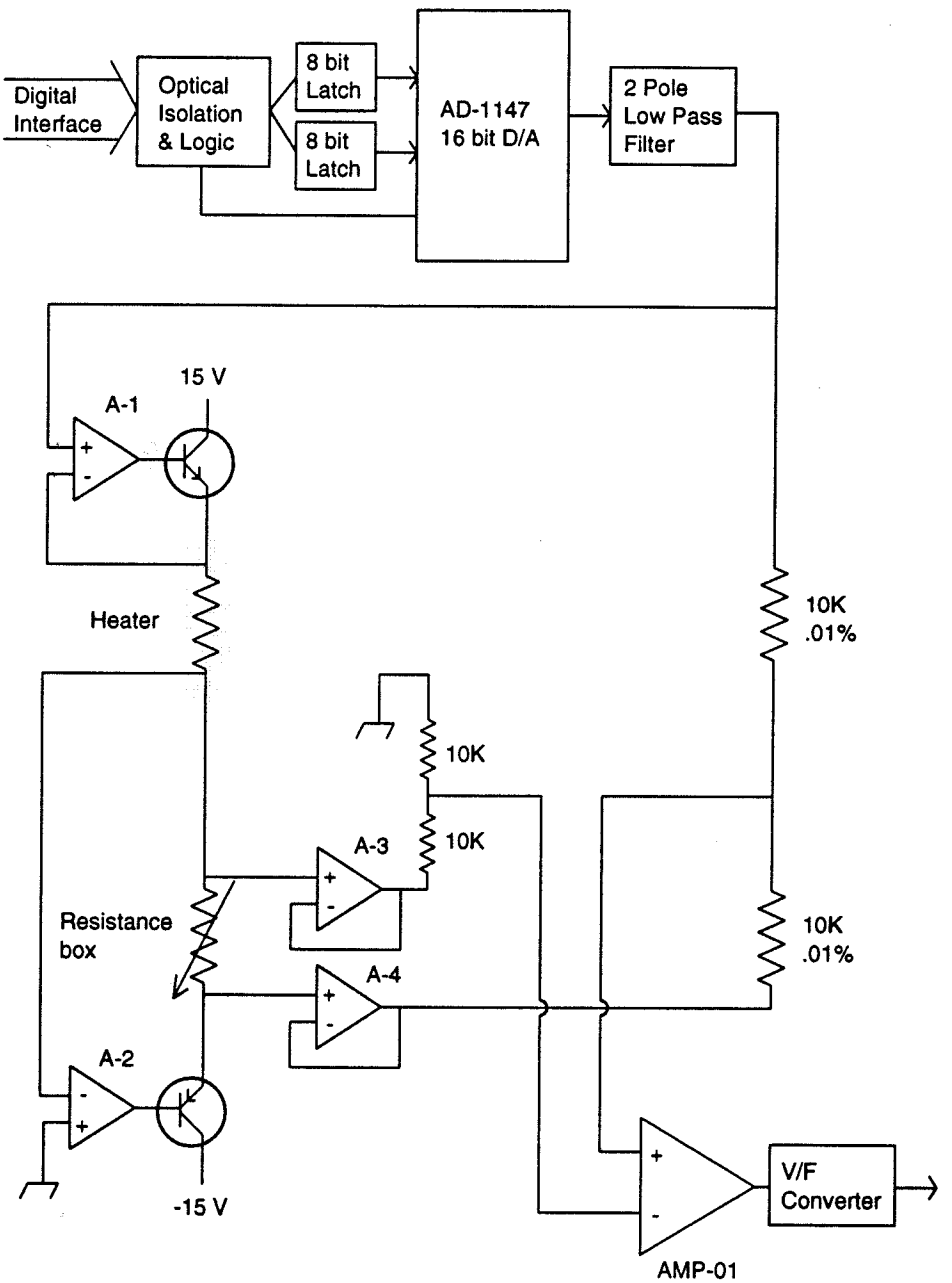

Figure 4.16: Sample and Standard Heater Source

used to set the cell heater power, so the voltage will be constant except during the short time just after it is changed. The sample power can be computed exactly, including a small correction for the finite time it takes for the voltage to settle to each new value. A computer algorithm sets the heater voltage; therefore it is easy to alter the control parameters and to choose which thermometer controls each heater. For example, when taking isotherm data, the standard heater is controlled by the relative bridge in order to isolate the sample. But during heat capacity runs, the relative bridge controls the sample heater. With total software control of the heater outputs, the program can easily change the control parameters to suit the particular mode of operation. An analog control circuit with this flexibility would be very complicated. Analog control is somewhat better when high frequency noise is present, but digital control was sufficient and easier to implement for this experiment.

Figure 4.16 shows the circuit used to power the sample and standard heaters. Separate, identical circuits (sharing the optical isolation and digital logic sections) control each heater. A digital interface allows the computer to set the output voltage for the next 1/2 second time period. The 2 Hz clock, that synchronizes the entire apparatus, strobes the data into the D/A converter. The Analog Devices AD-1147 D/A converter is linear to $\pm.00076\%$ over a zero to 10V range and has programmable zero and full scale output adjustment. A two pole low pass filter smooths the voltage applied to the heater to prevent high frequency interference with the thermometers. The filter's response to a step input was calculated and squared to find the small correction due to the filter time constant. Software that controlled the D-A converter applies this correction in real time.

The filter output voltage is applied to the heater while it is in a four wire D.C. Kelvin resistance bridge. Op-amp A-1 fixes the voltage on the positive heater input at the filter output voltage. The negative heater input is held at ground by op-amp A-2. Transistors on the outputs of A-1 and A-2 allow the op-amps to output a larger current (100 mA). All the current passing through the heater also passes through the resistance box because the op-amps have very high input impedances. Amplifier A-3 and two 10 KΩ 1% resistors divide the voltage across the stray resistance in the wire between the heater and the resistance box in two. The filter output voltage is halved by a pair of precision wirewound resistors (10KΩ .01%). When the resistance box and heater resistances are equal the input to the AMP-01 instrumentation amplifier is zero. If there is a slight difference between the two resistances, it is measured by the output of the instrumentation

amplifier, digitized by the V/F converter and recorded by the computer.

The computer finds the new output voltage using the desired heater power and the resistance calculated from the previous 1/2 second time slice. Since the heater resistance may change between time slices, the true power is computed using the heater voltage and resistance for each time slice, which may be different from the desired power.

Since the power output range is fixed from zero to 10 volts, and different experiments demand different amounts of heater power, a quad resistance heater was used for all but the upper thermal platform and fill tube heaters. Two evanohm heater wires and a single copper wire were soldered together, wound, and glued down. This forms two separate heater resistances R_1, R_2 that can be used singly, in series, or parallel to give four 4-wire heater resistances (R_1, R_2, R_1+R_2, $R_1||R_2$). Three relays under digital control select the desired configuration and there are two identical positive voltage drivers (op-amp A-1) to provide 4-wire operation when using the $R_1||R_2$ mode. By selecting the configuration with the largest resistance heater that still supplies enough power, it is insured that the sample and standard heater voltages are known to at least $\pm.005\%$.

It is not necessary to know the exact power dissipated by the heaters on the bodies providing thermal isolation to the calorimeter, but the power should be a monotonic and smooth function of the desired output. Frequency to voltage converters are ideal for generating the output voltage from the digital input because they are linear to $\pm.02\%$ and guaranteed to be monotonic. Figure 4.17 shows the circuit used. The computer inputs the desired output voltage to the rate multiplier frequency source. Instead of generating a periodic waveform at the desired frequency, the rate multiplier outputs a symmetric pattern of pulses that has the correct average frequency. Generating a pure frequency would require a complex frequency synthesizer, but most of the rate multiplier circuit is contained in three integrated circuits (7497 TTL, six bits per IC). The VFC-100AG is a V/F or F/V converter, depending on the external connections to the IC. It is designed to receive pulses that are synchronous with an input clock, as generated by the rate multiplier circuit. This circuit used an input frequency range from zero to 2^{17} Hz. The two pole, low pass filter removes the high frequency components of the F/V converter output. A digitally controlled range switch chooses among one, two, 4.5, and 10V full scale output ranges to insure that fine control is available for all circumstances. The bipolar output driver applies the output voltage to the positive heater input and the negative of the output voltage to the negative

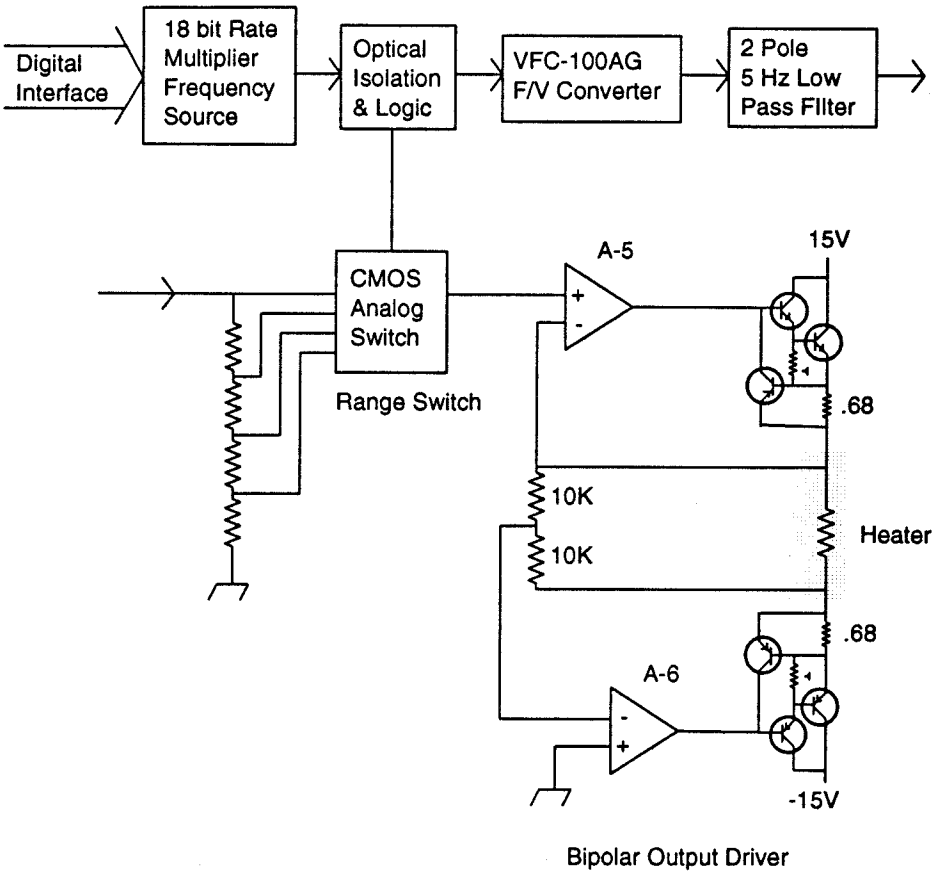

Figure 4.17: Bipolar Heater Source.

terminal. This quadruples the available power and reduces capacitively coupled interference noise with the thermometers. A fast acting current limiting circuit limits the output current through either positive or negative terminal to 1 A in order to protect the circuit and probe wiring. Six identical bipolar output heater voltage sources provide power to the isolation thermal mass, the upper thermal platform, both shields, and the fill tube.

It was not unusual for the computer to crash while controlling the apparatus during initial software debugging; therefore precautions had to be taken to protect the apparatus. A "dead man" circuit disables the current to all the heaters and to the gas handling system valves if the computer fails for longer than a few minutes. All the valves move to safe positions whenever the power is removed. In an emergency situation, the valves open the cell plumbing to the large calibrated volume to prevent high pressure from rupturing the cell.

4.10 Computer Interface and Software

This apparatus was interfaced to an IBM P.C. that totally controlled the more commonly performed experiments. Computer control is necessary for this apparatus, since each data run takes about 26 hours with the calorimeter drifting at 2 K per hour. To study the multilayer phase diagram from one to six layers, at least 24 runs are necessary to see heat capacity features due to the formation of each new layer. Then it is clearly necessary to interface the apparatus to a computer to collect such a large volume of data. To date, this apparatus has made 77 runs, collecting 300 megabytes of raw data or 33,000 separate heat capacity data points. Differential scanning calorimetry was selected partially because it is well suited for computer control, as data is collected continuously. Previous techniques, using about 1/2 hour per data point, would require 3.6 years of continuous operation to obtain the data this apparatus collected in five months. As the design was refined, it was also clear that this apparatus is not reliable without total computer control. The probability of human error during the complicated procedures needed to form the films and measure their heat capacity is too great.

4.10.1 Computer Interface

Automated scientific apparatus are usually composed of a central homemade assembly that includes several devices, each capable of either measuring some physical quantity, or changing the current state of the instrument. Usually these devices are connected to commercially produced instruments that input or output data either directly on the computer's internal data bus, or through a standard external interface (IEEE-488). Recently, commercial computer software has become available to simplify the instrument interfacing and to perform data analysis in real time. This type of apparatus often offers the best possible performance for a small time investment. However, there are several problems implementing this scheme for the differential calorimeter:

- Commercial instruments are often not available that perform the required measurement.
- It is difficult to interface homemade instruments to the standard data busses.

- When available, the computer interfaced instruments are often much more expensive than their manually operated equivalents.

- Instruments that mount within the computer chassis are much cheaper than external ones. However, these are only available with limited functions and are often affected by high frequency noise from inside the computer.

- External computer data busses are often bad sources of high frequency interference noise and ground loops, depending on the precautions taken by each instrument manufacturer.

- Commercial data acquisition software is easy to use but often cannot perform the operations that actual experimental apparatus require.

For example, this experiment requires two low noise, high precision resistance bridges. The equivalent instrument that replaces our absolute resistance bridge costs $30K. There is no commercially available instrument that replaces the relative resistance bridge. The alternative design strategy is to purchase whatever instruments are suitable and within budget and to make the rest in the laboratory.

It is challenging to interface low noise electronics to a computer. The computer is a powerful source of modulated high frequency noise that is emitted as electromagnetic radiation or transmitted through the computer's ground and signal lines. The main way that the instruments pick up the computer noise is through ground loops. To prevent ground loops, the instrument racks must be electrically isolated from each other. Isolation is provided by optical isolators, shielded transformer coupling, or high input impedance instrumentation amplifiers. To limit the number of optical isolators and the inevitable capacitive noise coupling through them, most of the analog or digital signals are converted to a frequency signal between zero and 2^{17} Hz. Then only a single optical coupler is required to transfer 16 or 18 bits of information twice per second.

The general design of each instrument was to use F/V converters to generate analog control signals, and V/F converters to record the value of analog outputs. A 16 channel, 16-bit frequency counter, interfaced to the computer, measured the optically isolated frequency output of each V/F converter. An eight channel, 18-bit rate multiplier circuit, also interfaced to the computer, generated the frequency inputs for the F/V converters. Individual V/F or F/V converters were

used for each signal, rather than using single, central multiplexed fast D-A or A-D converters in order to more easily isolate the ground levels between signal sources and receivers using a single optical coupler. One data line per bit would need to be optically isolated if expensive, high accuracy (16-bit .01%) D-A or A-D converters were used for analog input and output within the instruments. V/F converters also do not require anti-aliasing filters because they respond to the integral of the input signal. Because the time scale of the physical processes within the probe is always longer than a few seconds, the V/F and F/V converters respond quickly enough with two 16 bit measurements per second. Separate optically isolated digital data lines also input and output data to several special function circuits. This apparatus required interfacing many complex but slow instruments to the computer, rather than only a few simple and fast instruments.

Ground isolation was very important to allow the absolute and relative resistance bridges to achieve subnanovolt noise performance [88]. When a signal passes from one instrument to another, and each instrument is grounded via a separate wire to earth ground, then magnetic flux passes through the loop formed by the signal and ground lines. Changes in the flux generates a voltage around the loop that causes a current to flow in the ground and signal lines. This current generates a voltage across the impedance in the wires that interferes with the operation of the instruments. For extremely low noise instrumentation, a ground loop may be significant even if it is broken by a small capacitance, especially at high frequencies. If the high frequency noise is modulated at low frequencies then the electronics demodulate the noise to generate low frequency interference.

Figure 4.18 shows the standard resistance bridge circuit diagram, with the excitation circuit omitted for clarity. The resistance bridge contains only passive components, and the low level bridge output is read by a commercial lock-in amplifier with a single shielded input transformer and a digital output to the computer. There are two potential ground loops in this circuit, one formed by the path labeled as G-A-B-H-G, where the capacitance between the lock-in input transformer primary and shield couples B and H. Depending on the isolation of the lock-in's digital output, another ground loop can be formed through path G-H-D-E-F-G. Either ground loop can introduce a great deal of noise into the resistance bridge.

Figure 4.19 shows the improved circuit used for the relative resistance bridge. In this design the impedance matching transformer is located in the bridge chassis and there are two shields between the primary and secondary windings. The effect

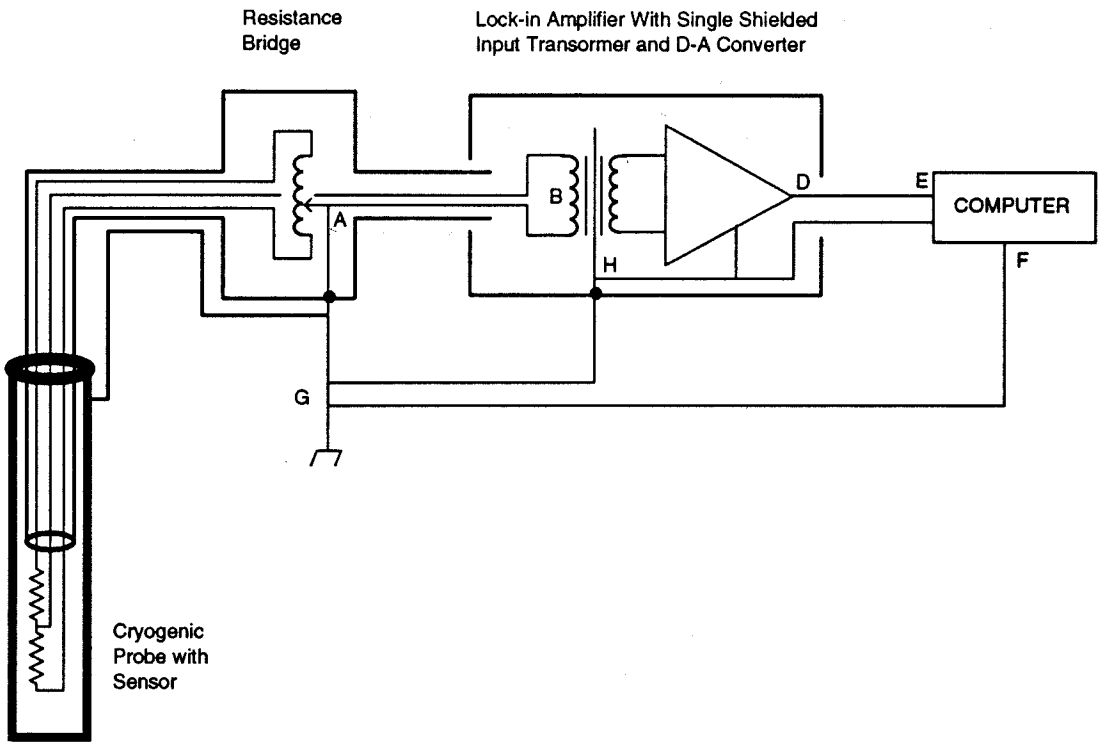

Figure 4.18: Standard resistance bridge circuit.

of the inevitable ground loop around path G-A-B-H-G is reduced because the double shields isolate the low level bridge signals from the bridge output circuit. Here the coupling between B and H is caused by the finite input impedance of the lock-in's input differential amplifier, about 10 GΩ and ~50 pF. Since the transformer and bridge preamplifier together have about 1000 times gain, the voltages generated by the current flowing through the ground loop cause 1000 times less interference. Two stages of optical isolation between the lock-in output and the computer prevent the high frequency noise generated by the computer from reaching the resistance bridge. The ground lines to the lock-in amplifier, the 16-bit counter and the computer are heavy gauge copper pipe to reduce the impedance to ground. The power and signal lines to each component pass through the copper pipes to prevent noise pick-up or radiation. The bridge input and output signals are conducted through a homemade triaxial cable consisting of standard coaxial cable stuffed through 3/8" copper tube that is insulated by a nylon sleeve. Similar grounding procedures were used for the absolute resistance bridge, including optical isolation between the ratiotransformer BCD digital input

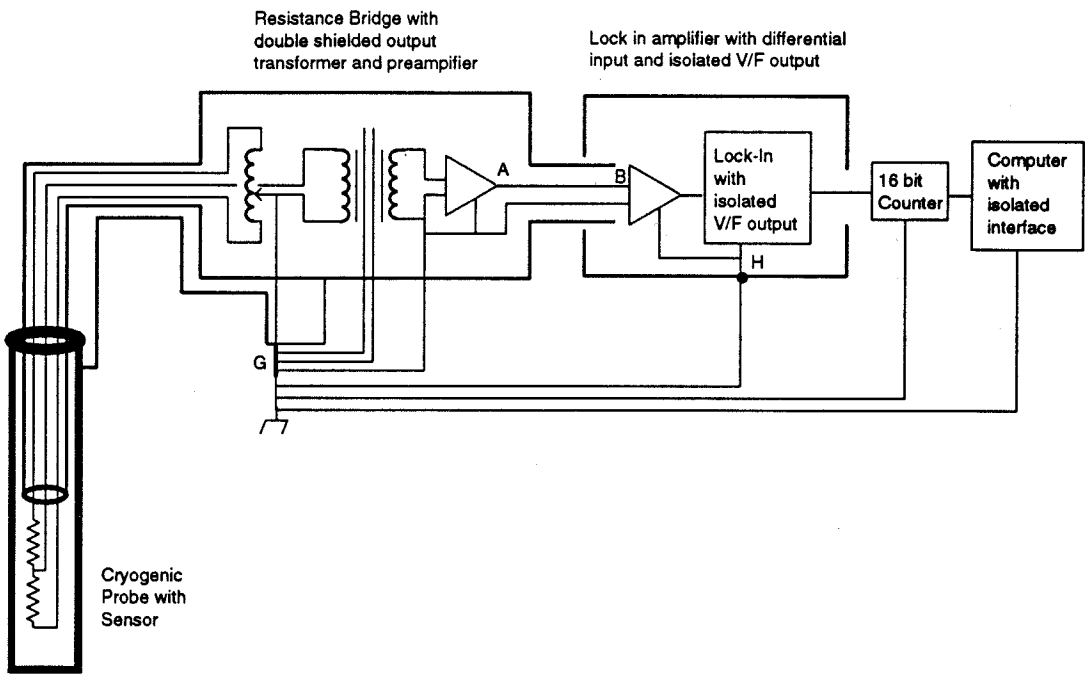

Figure 4.19: Improved resistance bridge circuit.

and the computer BCD output.

An optically isolated Metrabus computer interface interfaces the computer to the many digital signals from the instruments. A card in the P.C. mediates the transfer of data between the digital electronics connected to the Metrabus and the computer. The Metrabus cable connects to each instrument and caries eight bits of data, six address lines, read/write control and power lines. Computer subroutines set the address lines and send or receive data from the selected port. Compared to the IEEE-488 interface, the Metrabus is very easy to connect to and enables us to construct our own instruments. Data can be transferred at about 100 Kilobytes per second across the bus[36].

Figure 4.20 is a schematic diagram of the calorimeter heater and thermometer interface. The absolute resistance bridge measures the resistance of thermometer T0 on the sample cell. The Metrabus sets the output of the rate multiplier frequency generators and the frequency/phase inputs for the A.C. excitation sources that provide the drive signal for the resistance bridges. The output of the absolute

[36]The standard Metrabus was modified to improved reliability by changing the power supply from five to eight volts and including a five volt power supply regulator on each circuit that connects to the bus.

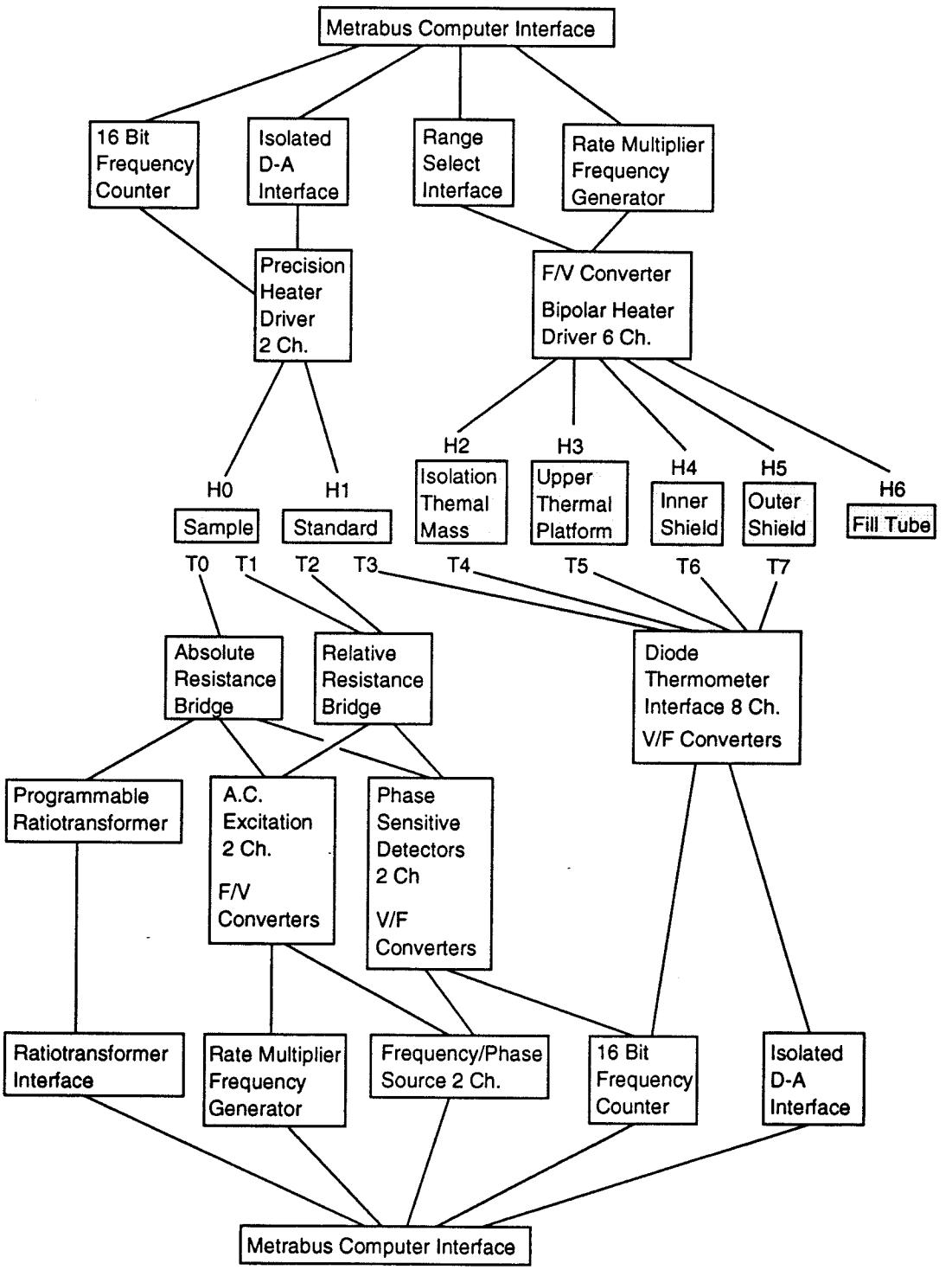

Figure 4.20: Calorimeter heater and thermometer interface.

resistance bridge is detected by a dual channel phase sensitive detector that generates an output frequency proportional to the signal amplitude. This frequency is counted by a 16 bit frequency counter that is read by the Metrabus. The relative resistance bridge reports the ratio of the resistances of thermometers T1 and T2 in order to find the temperature difference between the sample and the standard. The input and output circuits for the relative resistance bridge is identical to that for the absolute bridge.

The voltages across diode thermometers T4 through T7 are compared against the voltage across thermometer T3 and the output of a D/A converter by the diode thermometer interface. V/F converters in the diode interface generate a frequency proportional to the difference between each thermometer voltage and the reference voltage. A 16 bit frequency counter reads each frequency.

The sample and standard heaters are driven with zero to 10 volts D.C. as their resistances are measured to proved a known power input. Each heater is in a four wire D.C. kelvin resistance bridge during operation. The bridge imbalance is converted to a frequency signal by F/V converters that is recorded by the 16 bit counter and Metrabus interface.

Heaters H2 through H6 are driven by a bipolar heater driver circuit that generates zero to 20 volts across each heater. The Metrabus selects the frequency output from the rate multiplier circuit that sets the analog voltage output of the F/V converters. This output is multiplied by the computer controlled range setting, and then delivered to the heaters.

Figure 4.21 is a schematic diagram of the computer interface to the auxiliary instrumentation. The gas handling system room temperature thermometer records the temperature of the manifold and calibrated volume in order to know the number of sample gas molecules in the system. The barocell pressure sensor and readout electronics provide a digital BCD output that is recorded by the computer. The barocell range is selected by relays added to the interface, that are driven by an optoisolated interface. Several air pressure actuated valves on the gas handling system are activated from a set of 24 VDC solenoid valves mounted on a 60 psi air supply and ballast tank. The 24 VDC solenoids are fed from an eight channel control panel that allows either computer or manual operation.

The isolation vacuum pumping station evacuates the probe to reduce the heat flow between the sample and its environment. Several valves on the pumping station are operated by air pressure or 110 VAC electrical power. An eight channel 110 VAC computer controlled control panel provides power for these valves.

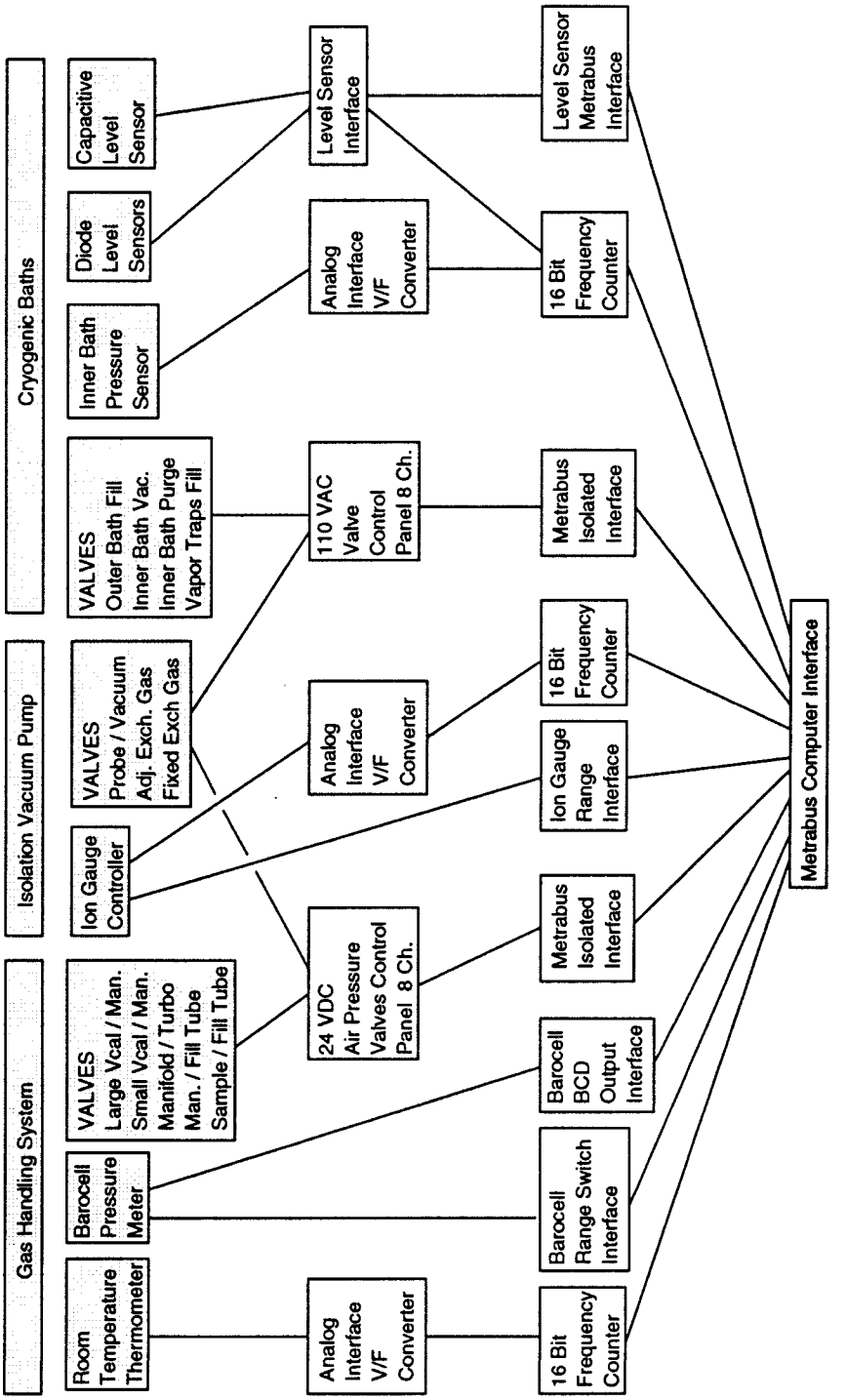

Figure 4.21: Auxiliary instrument interface.

Optically isolated, zero voltage and current electronic relays switch the power without generating electrical noise. The control panel also allows either computer or manual control. An interfaced ion gauge controller can be interfaced either to the gas handling system turbo pump gauge or to the isolation vacuum diffusion pump gauge.

Several 110 VAC valves control the cryogenic bath pumping and filling to maintain a constant sample temperature and to keep the liquid nitrogen vapor traps on the pumping stations filled. A homemade coaxial capacitor level sensor in the inner bath sets the frequency of a relaxation oscillator. The output frequency is recorded by a 16 bit frequency counter channel to monitor the inner bath level. Two homemade zener diode cryogenic level sensors within 1/4" tubes are located within the outer bath and the overflow from the liquid nitrogen vapor traps. The zener diodes are excited by a 1/4 watt power input so that they are more sensitive to the difference between the cold vapor and the liquid nitrogen. These sensors are used to indicate when to stop filling the baths, which are filled every few hours.

4.10.2 Computer Software

As with the computer interface, this program places unusual demands on the computer software. Instead of just controlling the higher level functions of commercial instruments, this software must also manage all the low level details of several complicated homemade instruments. For the sake of simplicity, the computer program should hide the low level details of each instrument. For efficiency, the computer code that controls each instrument should be written in a compiled computer language. Therefore, one section of the computer code is devoted to a real time compiled 'C' language program that controls the operation of the instruments, making them simple to operate. Figure 4.22 shows the major components of the computer software. The two Hz clock triggers the activation of a real time interrupt handler on the IBM P.C. The interrupt handler runs code to control each instrument in turn using a nonpreemptive multitasking kernel [37]. There are several instrument handler tasks:

- Absolute resistance bridge
- Relative resistance bridge

[37]The nonpreemptive multitasking kernel was a much expanded version of a multitasking system taken from reference [92].

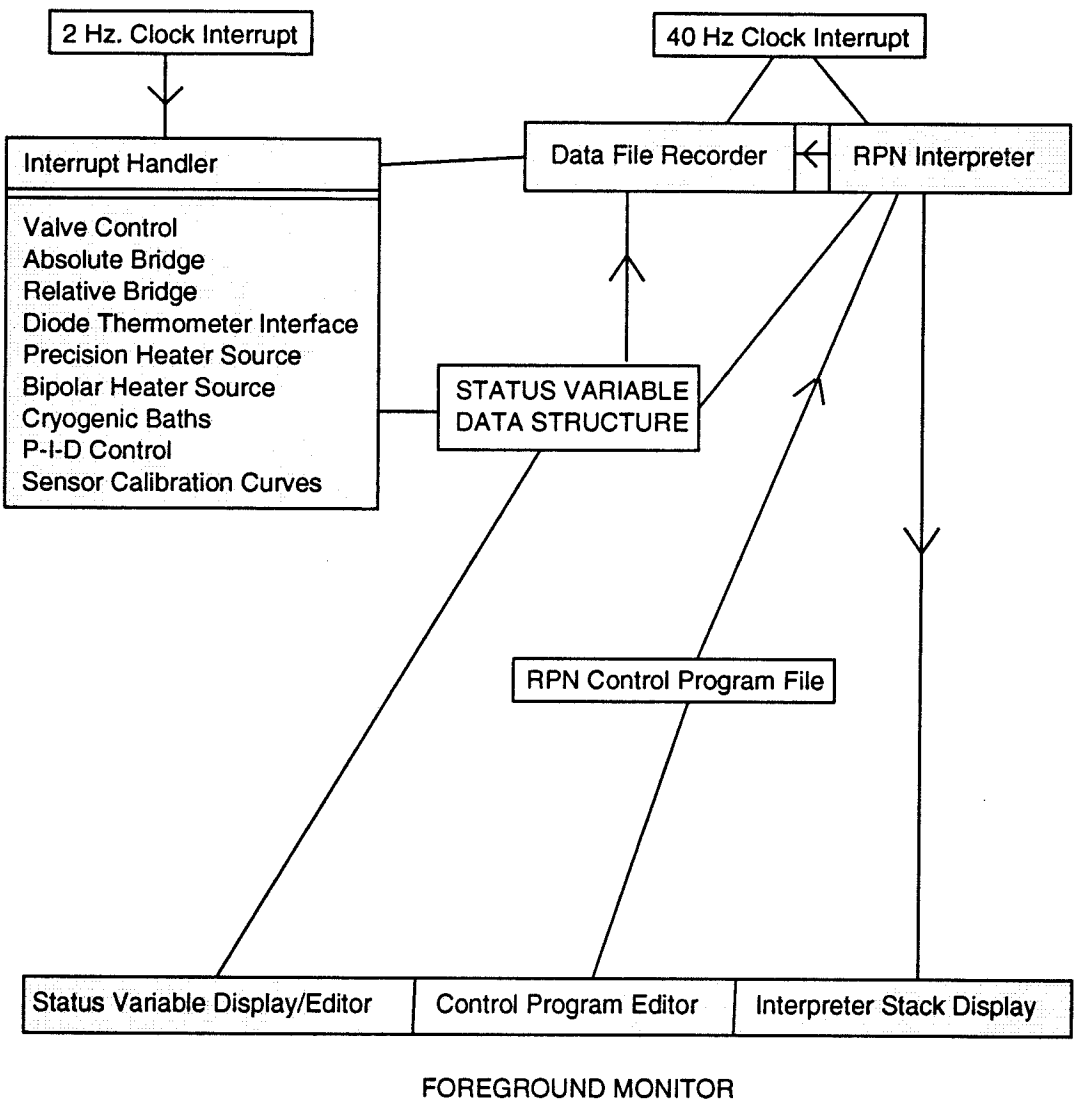

Figure 4.22: Control software block diagram.

- Diode thermometer interface
- Precision heater source interface
- Bipolar heater source
- Cryogenic bath filling and valve control
- Proportional, integral, derivative feedback controller (software only)
- Chebyshev polynomial evaluator (software only).

Each of the above instrument handlers run until finished performing the necessary duties for each time slice, then call a subroutine that turns over control to the next instrument handler task. When all the tasks are finished, the interrupt handler waits until the next interrupt to activate again. The PID feedback controller has several channels that may take input from any thermometer output (optionally subtracted from any other thermometer output or fixed value), and it may be set to output to any heater channel. The Chebyshev polynomial evaluator also has several identical channels that each take any data output as input. The input is transformed using a polynomial function whose coefficients are set during runtime.

If a compiled language were used to control higher level functions, then the software that controls each instrument would need to be restarted whenever a new experiment was needed, or all the possible experiments would need to be included in the compiled code. If a problem were found with the compiled program, the entire experiment would need to be restarted. Since the apparatus will be used for many different experiments, an interpreted language should be used to schedule the the different states of each instrument. But most interpreted languages do not allow the program to be modified while it is running, also requiring the program to be restarted whenever a problem was encountered. To control the experiment sequencing, a special purpose reverse polish notation (RPN) interpreted language interpreter was created that allows the code below the currently executing line to be modified. While the instrument handler tasks are not running, the interpreter reads commands from a buffer in memory that contains the contents of the current experiment control command file. A special full screen editor can enter and change the commands in the buffer. The commands take their operands off of a typed stack of values (floating point, integer, and variable length character string

types), and the results are returned on the same stack. Commands are available for mathematical manipulations as well as structured conditional branching and looping. A macro facility allows nested command substitutions and floating point, integer and character string variables. A more complicated subroutine call command makes it possible to run a section of another command file that receives and returns arguments off the stack, then returns to the caller. The interpreter can perform most of the functions of a compiled language, but allows the user to change the direction of an experiment instantly. An example of the RPN program code is included in appendix A.

Because the interpreter is used to set-up the modes of the instruments, the interpreter can access a block of memory shared with the instrument handlers. The "Status variable data structure" resides in this memory block and holds the input and output variables that are used as input and output for the instrument handlers. Interpreter commands are available that read and write to these variables in order to communicate with the instruments.

To record the data collected by the apparatus, another section of the interrupt handler calls a function within the interpreter at the end of each time slice. This function writes selected variables to a FIFO buffer that the interpreter copies to a disk file and empties whenever it is more than half full. Commands run by the interpreter select which variables are to be written to the data file. Because the amount of data collected by recording the state of the experiment every half second for a 24 hour data run can amount to more that 10 megabytes, the data are stored in binary format and it is possible to bin (average) the data from any odd number of time slices before they are recorded to the data file[38]. All of the data reported in this study were averaged over three time slices or 1.5 seconds. Since the thermal response time of the cell is 90 seconds or longer, this has no effect on the results and greatly reduces the data file size.

Along with the data file, a log file is written that indicates the contents of each record in the data file and associates an ASCII name with each variable recorded. A subroutine library was written for data analysis programs to access the variables stored in each record of a data file according to the ASCII name. Then, the data analysis programs can operate on data files written with any combination of data items. General purpose data manipulation programs were created that operate

[38]While most of the data items may be binned, it is possible to mark any of the items so that they are not. These are stored as a vector of the unaveraged data from each 2 Hz clock tic in the output record.

on any data item to compute integrals, averages, derivatives, and polynomial functions of the data. A plotting program was written that will display any data items in the raw binary data files. The library also buffers the data file so that files larger than the available computer memory can be read.

Because the experiment can collect data continuously for as long as 26 hours, only the features programmed into the data collection program computer are available for long periods of time unless a multitasking operating system is used. Unfortunately the standard operating system for the IBM P.C. AT computer (the only computer we could afford), MS-DOS, is not multitasking. Another operating system that runs on the IBM P.C., XENIX, is multitasking, but has very unpredictable real time response[39]. Luckily, the officially undocumented features of the internal workings of MS-DOS have been discovered by trial and error and published [93, 94]. Since the internal operation of MS-DOS is very simple and the designers themselves have had to use multitasking in certain system utilities, it is possible to add multitasking to the MS-DOS operating system by using certain "secret" hooks in the operating system. As long as the OS system calls are not used while in use by another task, several tasks can coexist. In fact, Microsoft Windows, a successful commercial program, takes advantage of these undocumented features to build a multitasking OS around MS-DOS. Since the time critical tasks in this experiment (the instrument handlers) do not use the OS functions, it is possible to interrupt almost any other task to run the interrupt handler. Then the real time response of this MS-DOS based program can be far better than a XENIX based system, and even better than some true real time operating systems. Since the interrupt handler program and the RPN interpreter must constantly be running, they are loaded permanently into memory as "TSR"[40] programs. The programs that provide the human interface to the apparatus can be called up from the command line when needed, or other programs can be run in the foreground while the apparatus is running. Not including unnecessary functions in the background code frees more memory for the different foreground tasks. For example, since the data can be examined while they are generated by running the standard plotting utility, a plotting program did not need to be built

[39] More recently, expensive real time versions of UNIX have appeared and another operating system, QNX, claims to provide good real time response, but very little software is available for this OS and it is expensive.

[40] A "Terminate and Stay Resident" program is able to return control of the computer to the operating system yet retain the memory it was loaded into. Then, it can be activated by an external event such as a clock interrupt.

into the interface. It is also possible to use debugging utilities to work on one part of the program while the other resident programs are loaded and running. Until a widely used, efficient real time operating system is in place for a personal computer, MS-DOS is still the best solution[41].

This apparatus requires four simultaneous tasks to function:

- Interrupt handler running several instrument handlers
- Data file recorder
- RPN intrepeter
- Foreground user interface program.

Since the second and third tasks both use operating system functions from the background, they are combined into a single resident program that is activated by the 40 Hz system clock interrupt. If certain critical tasks are not running when the interrupt occurs, the program checks to see if the data file buffer is more than half full and the interrupted task is not executing an OS function call. If so, the data file recorder is activated to clear out the buffer. When this task finishes, control is returned to the interrupted task. If the buffer is less that half full, the interpreter is activated to run for a certain fixed time period (or until it demands an OS function call if the interrupted program is using an OS function). When finished, the interrupted task is restarted.

The foreground user interface program is called up from the regular OS command line. There are three subprograms in the user interface–the RPN command file editor, the interpreter stack display, and the status variable display/editor. Because it is often necessary to use more than one of these subprograms at once, the user interface program runs the same non-preemptive multitasking kernel as the interrupt handler program. Also, the user interface display is organized into two tiled windows, so that the user can display two of the three subprograms simultaneously, or the full screen can be devoted to a single subprogram. A function key is devoted to switching the keyboard input among one or two active subprograms and a control task that starts the desired subprograms. This simple system provides the essential functions of a complicated windowing system, but was much easier to program.

[41]The AMIGA personal computer is supposed to have a good real time operating system, but it doesn't have the broad array of tools for programming and it is not widely supported. The NeXT UNIX workstation/PC may soon have good real time performance.

The RPN command file editor is a full screen editor that allows the user to modify the command files even if they are currently being executed by the interpreter[42]. The command files are limited in length to 16 K bytes long and lines are limited to 80 characters wide to simplify the file buffering. A 64 K byte buffer contains four file buffers and is located in EMS 4.0 expanded memory (if available). This buffer holds the running command file, and the two command files that may be edited at once in each of the two windows. Special editor features allow the editor to follow the operation of the interpreter, insert and delete breakpoints, and to single step the interpreter through the command files.

The interpreter stack display shows the contents of the interpreter stack variables, which may be either floating point or integer numbers, or variable length character strings. By opening the editor display in one window, and the stack display in the other, it is easy to debug the somewhat cryptic RPN command files by single stepping through the programs.

The status variable display/editor is a way to view directly and modify the variables in the status variable data structure. This subprogram allows a character based display of these variables with notation describing the function of each variable. If a variable has not been marked as "write protected," it may be modified by moving the cursor to the field and entering a new number. In this way the user can directly communicate with the instruments for setup and debugging. Some of the instruments will respond with character string messages to talk the user through setup procedures or to indicate the current mode of operation. The status variable display provides a "control panel" for the apparatus, and the RPN interpreter automates its operation by scheduling the different modes of the various instruments.

[42]However, only the lines below the executing line may be edited.

Chapter 5

Data and Discussion

To map out the phase diagram of methane on Grafoil, 75 heat capacity scans were performed on films nominally[1] from .8 to 13 layers thick on both the adsorption and desorption branches. Upward and downward vapor pressure isotherms were collected at 95 K. First, this chapter will discuss the calorimetric accuracy of the apparatus, found from the noise and repeatability of the background runs. Then the vapor pressure measurements will be shown. These were made to find the monolayer capacity of our Grafoam sample and to determine whether hysteresis is present. After displaying all of the heat capacity data, each feature will be examined. Finally, a tentative phase diagram for the first four layers can be drawn.

5.1 Background Heat Capacity Scans, Calorimetric Accuracy and Precision

Before data could be collected, several background runs were made so that the film heat capacity could be computed. Whenever the calorimeter was warmed up to room temperature, the background and relative resistance bridge calibration runs were redone. The accuracy of the calorimeter can be determined by comparing two background runs. The calorimetric precision can be found by looking at the noise on the smooth background curve. Figure 5.1 shows the background heat capacity of the sample cell. All the data were taken at approximately 2 K/hour drift rates unless otherwise indicated. The data from each background run were

[1] "Nominally" means that the number listed is the number of molecules in the entire system, including the 3-D gas at room temperature and the molecules that are capillary condensed. This number is often scaled to the number of atoms in a uniform film one layer thick.

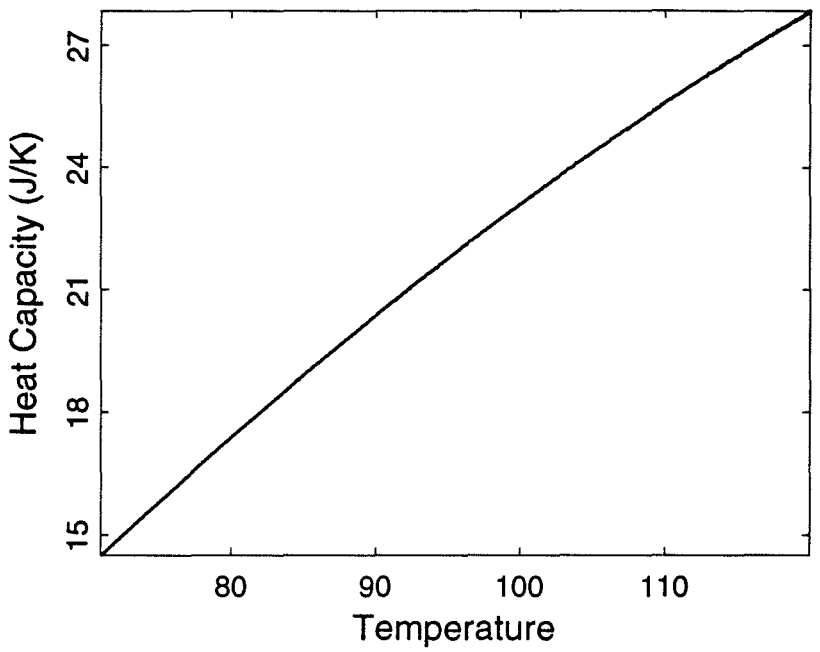

Figure 5.1: Bare Sample Cell Heat Capacity.

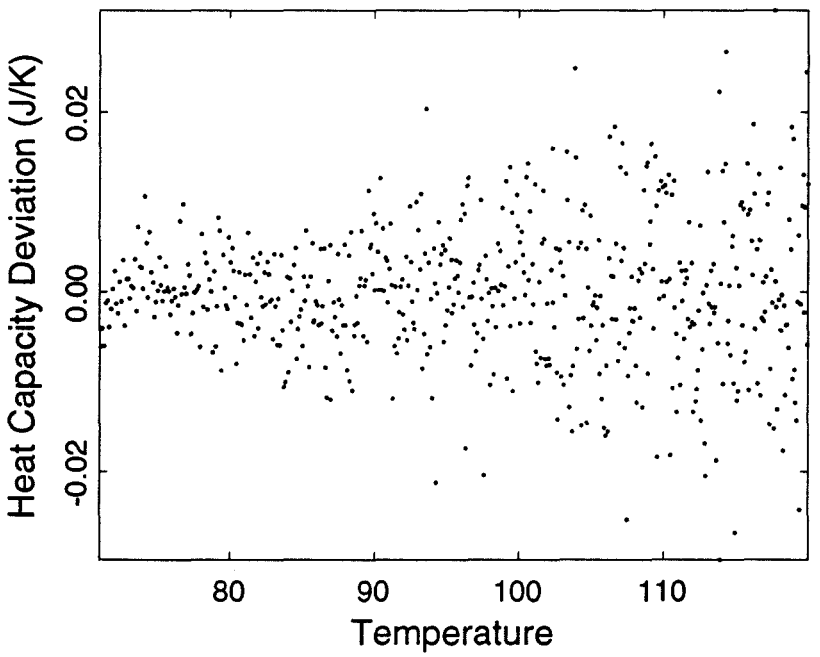

Figure 5.2: Noise on the background data.

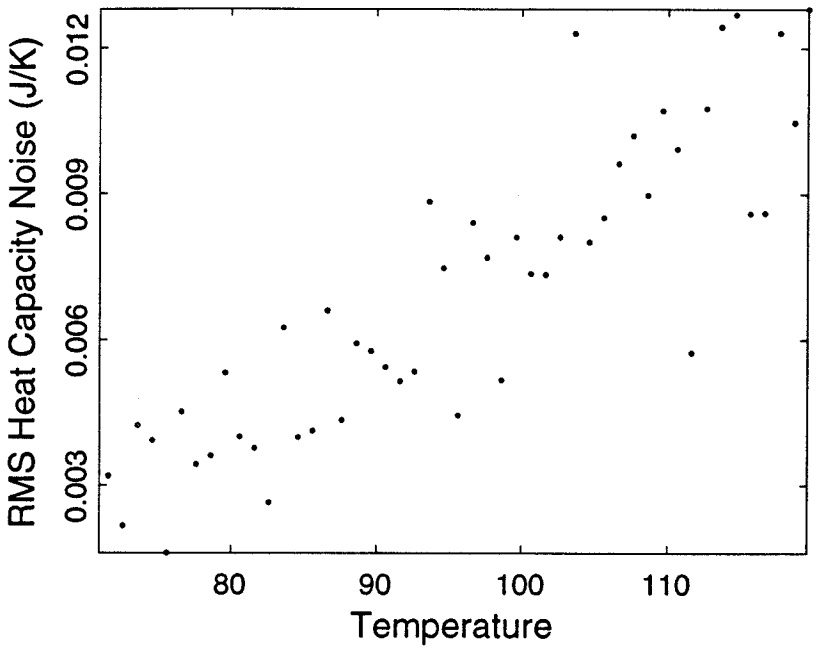

Figure 5.3: RMS noise on the background data for 1 K intervals.

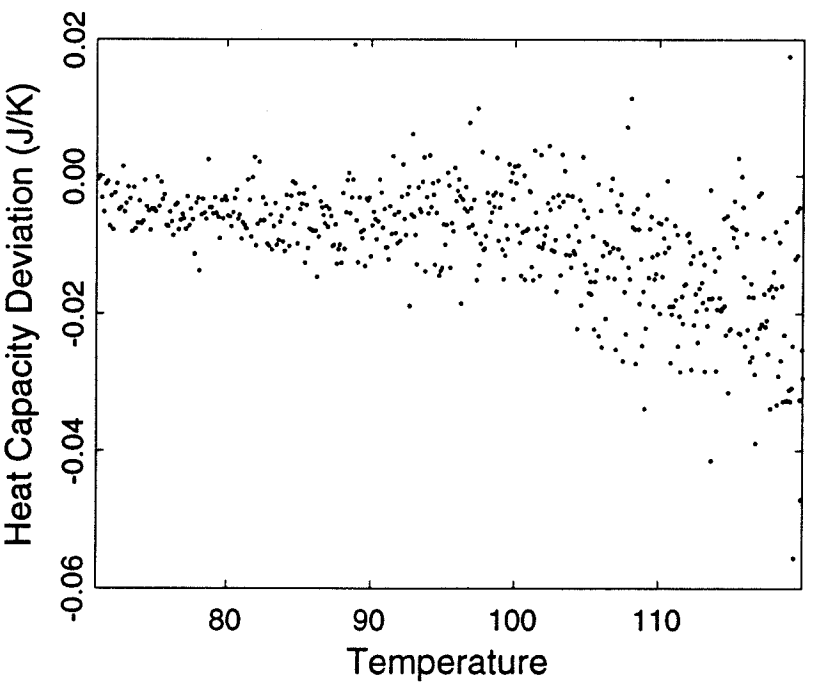

Figure 5.4: Comparison of the smoothed background data from figure 5.1 with another unsmoothed background run.

fitted to a third order Chebyshev polynomial as a function of temperature to find a smoothed background. The smoothed background was subtracted from the heat capacity data to find the film heat capacity. The deviation of the unsmoothed background heat capacity from the smoothed curve is an indication of the noise in the data, shown in figure 5.2. The RMS amplitude of the deviation, computed over 1 K intervals, is shown in figure 5.3. The calorimetric noise relative to the background heat capacity goes from about $\pm.015\%$ at 72 K to $\pm.045\%$ at 120 K. This noise is a measure of the precision of the heat capacity data. Figure 5.4 compares the smoothed background data from figure 5.1 and the data from another (unsmoothed) background run, to assess the accuracy and repeatability of the data. Note that there is some systematic error in the data, but it is about as large as the random noise. Occasionally, larger noise spikes can be seen in the data. Since each point is statistically independent of the others, any feature identified by more than a few points is not due to the noise.

Another noise source is not represented in the above discussion. When there is a film on the substrate, the cell cryogenic valve is open, and there is gas in the room temperature plumbing, room temperature fluctuations change the number of molecules in the 3-D gas phase. While the room temperature is drifting, the number of molecules in the film is changing and there is an error in the heat capacity caused by the heat of desorption, q_d, of these molecules. The desorption correction (calculated in section B.3.3) should correct for this error, but the correction term is not always accurate because of the problems mentioned above. Also, the gas handling system temperature may not be uniform. Features were identified in the high temperature/high coverage data that were correlated with the outer cryogenic bath filling, the largest room temperature disturbance. These features were considerably larger than the random noise in the data, but were only seen for data taken above 100 K in the thicker films[2], with the cryogenic valve open.

5.2 Vapor Pressure Isotherms

As discussed in section 2.2.1 on page 22, the inflection point of the first step on the isotherms is used to determine the monolayer capacity. Since Hamilton made

[2]This problem was only identified after the majority of the data were recorded. If greater care is taken to isolate the gas handling system from temperature fluctuations, this noise can easily be reduced by an order of magnitude.

a rigorous measurement of his surface area, the surface area for this experiment was found by comparing our vapor pressure isotherms with his data, to derive a scaling factor. The scaling factor times Hamilton's monolayer capacity gives the monolayer capacity. In order to minimize the effect of capillary condensation, an upward isotherm was performed, starting at zero coverage. It was found that the isotherms would overlay perfectly below 1.1 layers, but Hamilton's data had an extra upward step above 1.1 layers. The monolayer coverage of our substrate was 194 STPCC (Hamilton's monolayer coverage was 90.9 STPCC)[3].

The extra kink was the first hint that the vapor pressure hysteresis found by Inaba, Koga and Morrison [41] for methane on Grafoam and Grafoil were present in Hamilton's data also. Hamilton performed vapor pressure isotherms going downward in coverage because it is easier to achieve mass distribution and thermodynamic equilibrium at higher coverages than at lower coverages. The extra step marked the sharp closure of the hysteresis loop. This step was noticed in Hamilton's data and attributed to the first layer melting transition [57].

When a complete series of upward and downward isotherms was performed, it was clear that the hysteresis in our data is identical to the curves found by Inaba et al. The lower curve in figure 5.5 is the number in the system as a function of the pressure while gas is added to the system at 95 K. The upper curve is the downward vapor pressure isotherm[4] starting at 11 layers adsorbed. The typical cause for such hysteresis is capillary condensation, but Morrison was not certain of this explanation because the hysteresis curves were slightly different from the classical behavior usually attributed to capillary condensation [41, pages 1820-1826].

The literature contains much experience, and even a standard vocabulary for discussing vapor pressure isotherms when capillary condensation is present [30, 31, 33]. Figure 5.6 shows a typical hysteresis curve with boundary and scanning curves. Isotherm data taken by incrementally adding gas to the porous substrate, starting with no adsorbate, traces out the "lower boundary curve." The "upper boundary curve" is found by removing doses of gas, starting from a fully saturated system. The boundary curves may join at low coverage, where there is no capillary condensate, and at high coverage, where the pores in the adsorbent are completely

[3]One STPCC is the number of molecules in a cubic centimeter at standard temperature and pressure, 760 torr, 0°C, 2.686831×10^{19}.

[4]Hamilton's isotherm data (not shown) follow the upper curve after briefly traversing the scanning region.

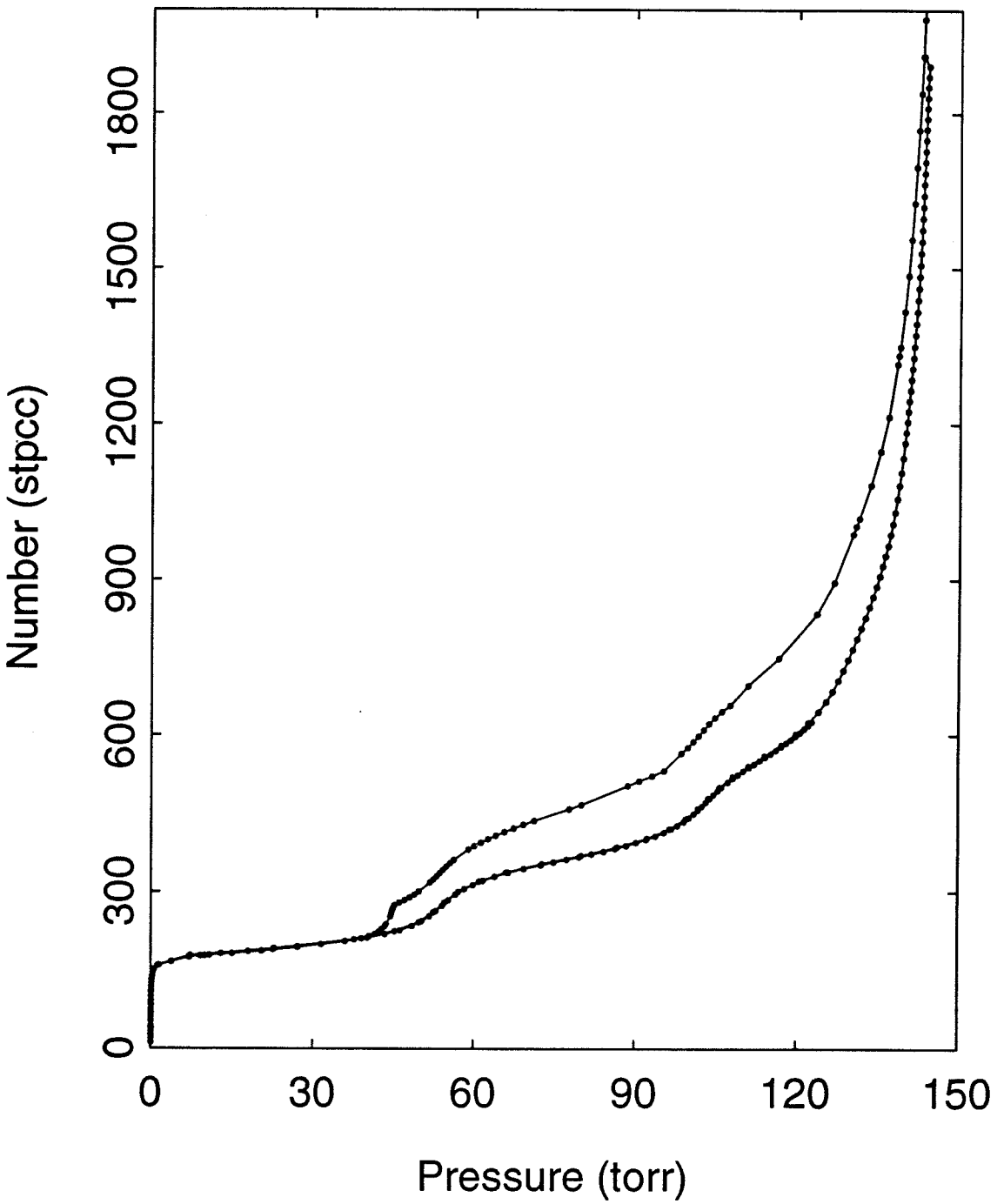

Figure 5.5: Vapor pressure isotherm at 95 K, upper desorption curve begins at 11 layers adsorbed. The first layer point of inflection occurs with 194 STPCC's adsorbed. The bulk saturated vapor pressure of methane as found using equation B.1 is 148.84 torr.

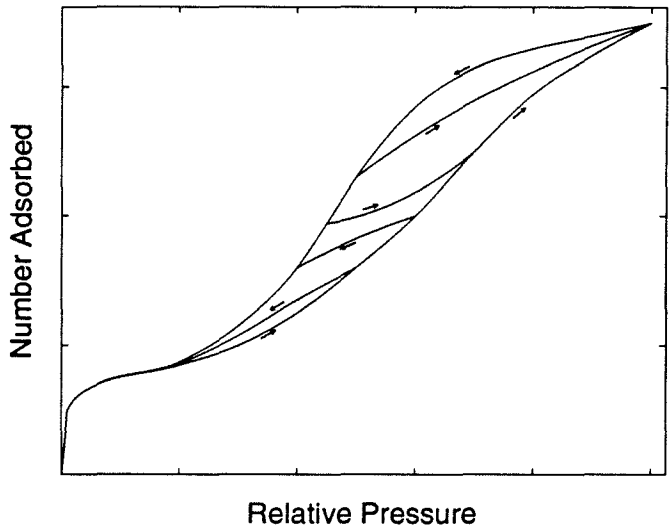

Figure 5.6: Typical boundary and scanning curves for adsorption on a porous substrate. Note that the scanning curves may or may not rejoin the boundary curves.

filled. A "scanning curve" is any isotherm curve that lies between the upper and lower boundary curves. Upward scanning curves are made by adding gas to the system when it is not on the lower boundary curve. Likewise, downward scanning curves come from withdrawing gas when the system is not on the upper boundary curve. A typical upward scanning curve might start on the upper boundary curve, pass into the region between the boundary curves, and may or may not join the lower boundary curve. Likewise, a typical downward scanning curve might start on the lower boundary curve, and may or may not join the upper boundary curve.

The most usual downward scanning curves join with the upper scanning curve above where the hysteresis loop closes [26]. However, in the methane/Grafoil system, another downward isotherm that started at 14 nominal layers adsorbed (not shown) demonstrates that the methane/Grafoam system differs from the classical boundary and scanning curve behavior, in that the downward scanning curves do not join the upper boundary curve until a large fraction of the film is desorbed. It is possible that the scanning curves do not join until the point where the boundary curves meet, as found by Inaba and Morrison from their vapor pressure isotherms. This lead Inaba and Morrison to doubt that capillary condensation was the cause of the hysteresis. However, Everett [30] and de Boer

[95] show a wide variety of shapes for boundary and scanning curves caused by capillary condensation, with some similar to those for methane on Grafoam.

The adsorption and desorption isotherms in figure 5.5 do not join at the high coverage limit because no coverages larger than 14 nominal layers were examined. The bounding curves would presumably join again at a much higher coverage, when the 2000 Å average spacing between the Grafoil platelets is filled. Continuing the isotherms to higher coverages or lower temperatures was impractical, because that would require very long times to establish equilibrium for such a large Grafoam sample[5].

Hysteresis at temperatures below the bulk triple point is not well understood. The literature contains examples where the lower point of closure of the hysteresis loop increases as the temperature drops far below the triple point [30, page 1064], but a variety of other behaviors have also been reported. It is certainly difficult to establish true thermodynamic equilibrium at low temperature when capillary condensation is present. The behavior of the vapor pressure isotherms as a function of temperature in the methane graphite system lead Inaba et al. to conclude at first that there was a wetting transition near 75.5 K. Then, below this temperature, the film only forms a few uniform layers as the pressure reaches the bulk vapor pressure. Similar conclusions were found for krypton and xenon on Grafoam [42]. But further work by Larher [43] and later by Miechel et al. (originating in Morrison's laboratory) examines the interplay between vapor pressure hysteresis, capillary condensation and the possible wetting transition [44]. Both studies suggest that it is possible that there may be only temperature dependent capillary condensation, instead of a wetting transition. Furthermore, Nham and Hess have made optical ellipsometry measurements [5], on a flat graphite substrate where capillary condensation is not present, that clearly show a maximum of 8.5±0.9 layers in the temperature range from 57 to 72 K, 8.8±0.4 layers from 68 to 73 K, and 10.4±1.0 layers from 71 to 76 K. Therefore, it should be possible to form uniform films at least ten layers thick in our temperature range, but the uniform film must coexist with the capillary condensate. A simple calculation shows that the spaces between the graphite platelets will fill completely with capillary condensate when the uniform film is greater than about ten layers thick. But capillary condensation begins in the smaller pores of the adsorbate when the

[5]Vapor pressure isotherm studies typically use very small samples to decrease the time required for equilibrium. Heat capacity studies often use a larger sample to optimize the signal to noise ratio.

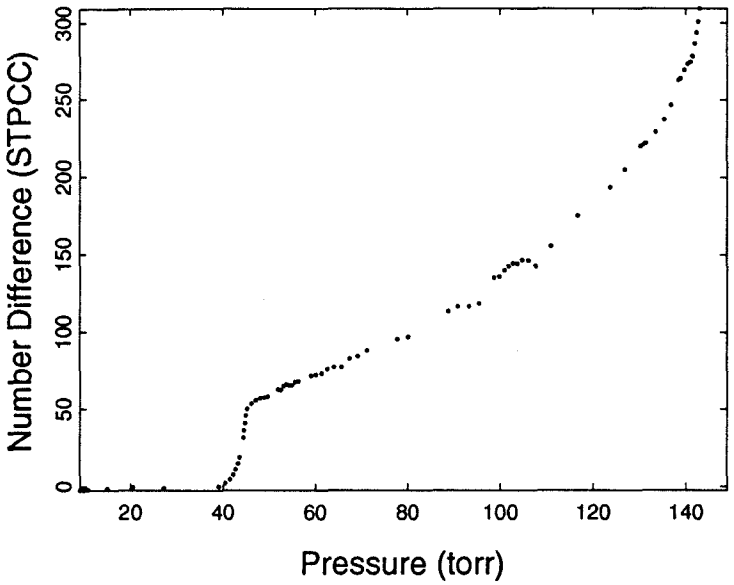

Figure 5.7: Distance between the upper and lower curves in figure 5.5 as a function of the pressure. P_o = 148.84 torr at 95 K.

uniform film is much thinner. Some theoretical calculations [96, 97] have shown that the capillary condensate grows very rapidly once it begins to form. The rapid formation of capillary condensate would distort the vapor pressure isotherms and could make it appear that thick uniform methane films cannot form on graphite.

Most recently, Larese et al. [45] and Morishige et al. [46] have found neutron and x-ray scattering evidence for capillary condensation of argon and xenon on graphite, respectively. In particular, Morishige et al. examined the films on both the adsorption and desorption branches and found capillary condensation coexisting with films as thin as a monolayer.

To further examine the isotherm measurements in figure 5.5, the distance between the two isotherm branches has been computed and plotted as a function of pressure, in figure 5.7, and as a function of the number adsorbed on the adsorption branch, in figure 5.8. For low coverages, the distance between these branches is very close to the number of molecules capillary condensed on the surface, since little capillary condensation is expected on the adsorption branch. But when more molecules are adsorbed, there is likely to be a considerable amount of capillary condensation on the adsorption branch, as demonstrated by the classic experiment by Carman and Raal [29]. In this case, there should be considerably more cap-

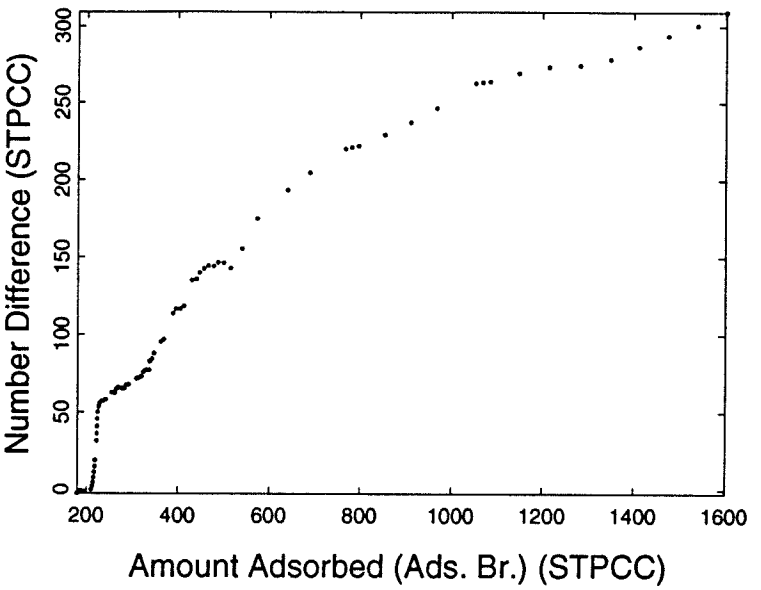

Figure 5.8: Distance between the upper and lower curves in figure 5.5 as a function of the number adsorbed on the lower curve (adsorption branch).

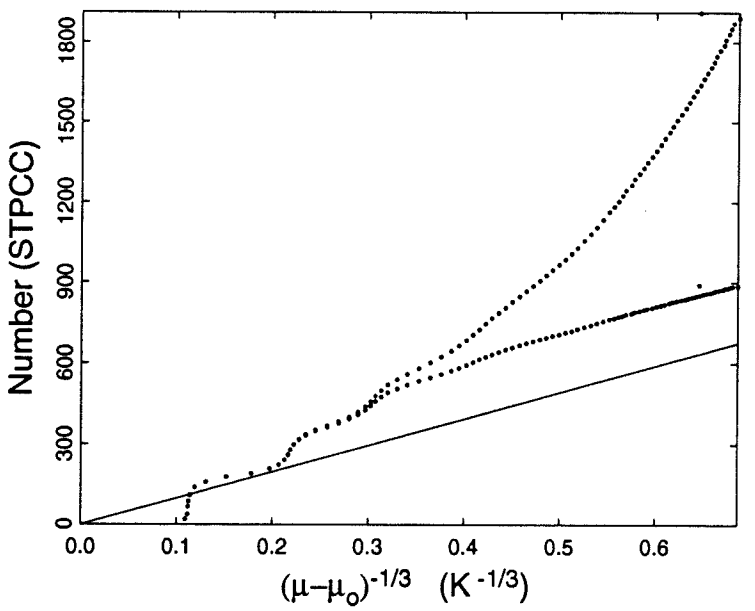

Figure 5.9: 95 K adsorption branch isotherm plotted against $(\mu - \mu_0)^{-1/3}$. This should be a straight line if equation B.5 is followed. Shown are the data uncorrected for capillary condensation (upper points) and corrected for capillary condensation (lower points) using the thick film limit of the model in reference [96] as discussed on page 198. The line is the prediction of the FHH equation for $\Delta C_3^{lv} = 1.25 \times 10^4$ K Å^3 [36, page 94].

illary condensation than indicated by the distance between the upper and lower boundary curves. These plots will be useful for understanding the heat capacity data.

Finally, it is instructive to plot the vapor pressure isotherms as N vs. $(\mu - \mu_o)^{-1/3}$ as done by Hamilton [34, page 57]; see figure 5.9. In the thick film limit, the films should follow the Frenkel-Halsey-Hill isotherm, equation B.5, if no capillary condensation is present. This curve should be a straight line at higher coverages when the isotherm steps can no longer be observed. There is clearly more gas adsorbed into the porous substrate than would be indicated by the simple theory. This is more indirect evidence that capillary condensation causes the vapor pressure hysteresis and that it occurs on both branches of the hysteresis loop. Figure 5.9 also shows the data after being corrected for capillary condensation. The corrected data will be discussed later, in section 5.3.5.

5.3 Heat Capacity Data

The heat capacity data may be split into two types, those taken on the adsorption branch (from 70 to 120 K) and those on the desorption branch (70 to 95 K)[6]. All the data for films on the adsorption branch were recorded twice, first with the cryogenic valve closed and then again with it open. All the runs on the desorption branch were made with the cryogenic valve open. All plots of the data are shown with points connected by straight lines. These lines are only meant to assist the reader in following the curves, and do not indicate the expected behavior between the data points.

5.3.1 Overview of the Features in the Data

Figures 5.10 and 5.11 show the adsorption branch heat capacity data, without the desorption correction, plotted together. There are four major features in the

[6]The films on the desorption branch could not be continued to higher temperatures because at high temperatures there is a significant amount of gas desorbed from the film into the 3-D vapor. The state of the system in the vapor pressure isotherm would move into the scanning region as the gas is readsorbed when the system is cooled down before performing the next heat capacity run. Then, each coverage studied on the desorption branch would require a large withdrawal of gas from the system to place it back on the desorption branch (if the downward scanning curves intersect the upper boundary curve; otherwise there is no way to get the film back on the desorption branch without reforming it). One run was continued to higher temperature to ensure that the high temperature features behaved as expected.

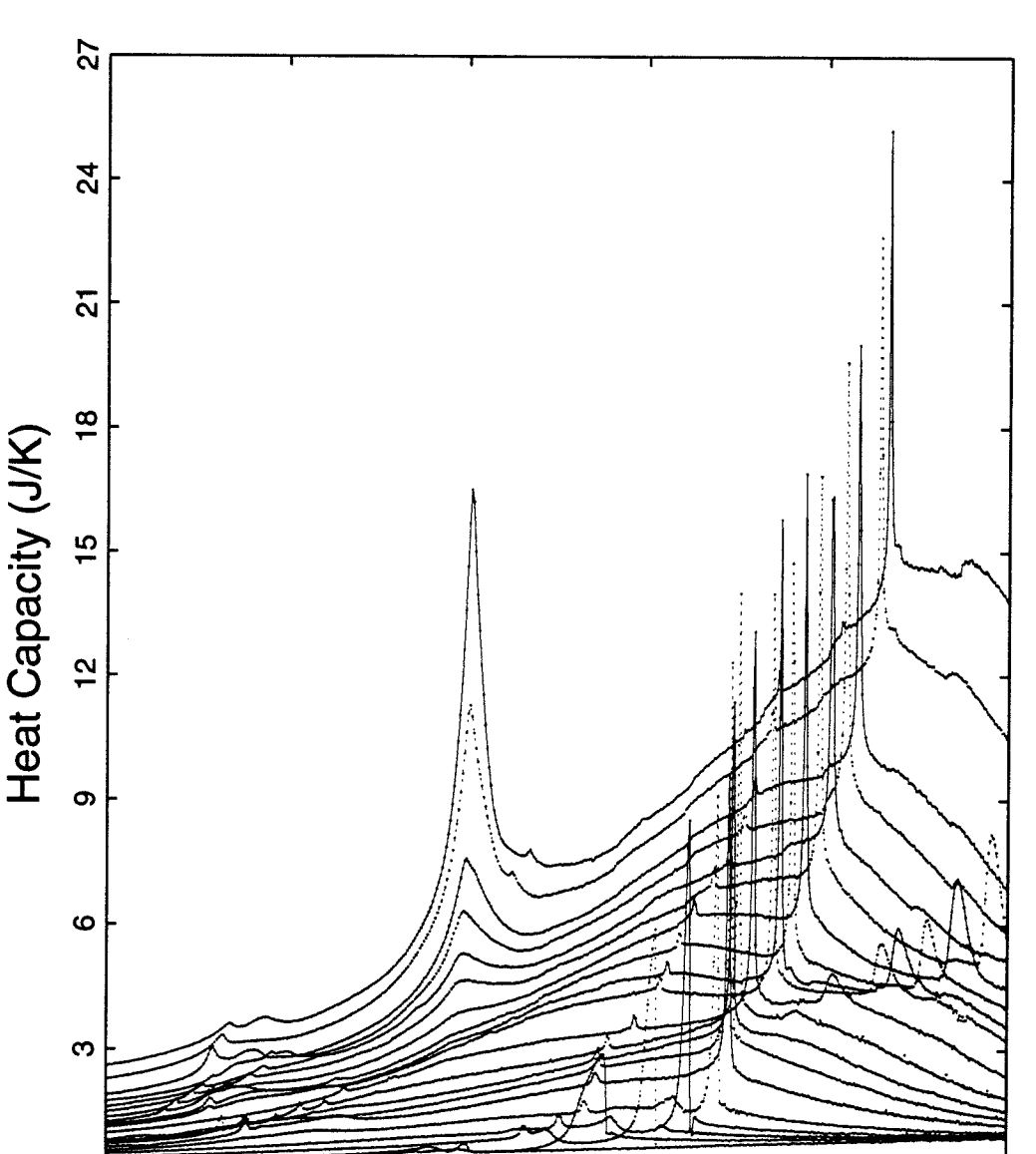

Figure 5.10: Heat capacity for films on the adsorption branch with the cryogenic valve open, uncorrected for desorption. Coverages are: 0.87, 0.94, 1.03, 1.12, 1.25, 1.55, 1.70, 1.85, 2.06, 2.44, 2.67, 2,84, 3.00, 3.30, 3.66, 4.00, 4.43, 4.87, 6.0, and 7.0 nominal layers in the system (gas, film and capillary condensate).

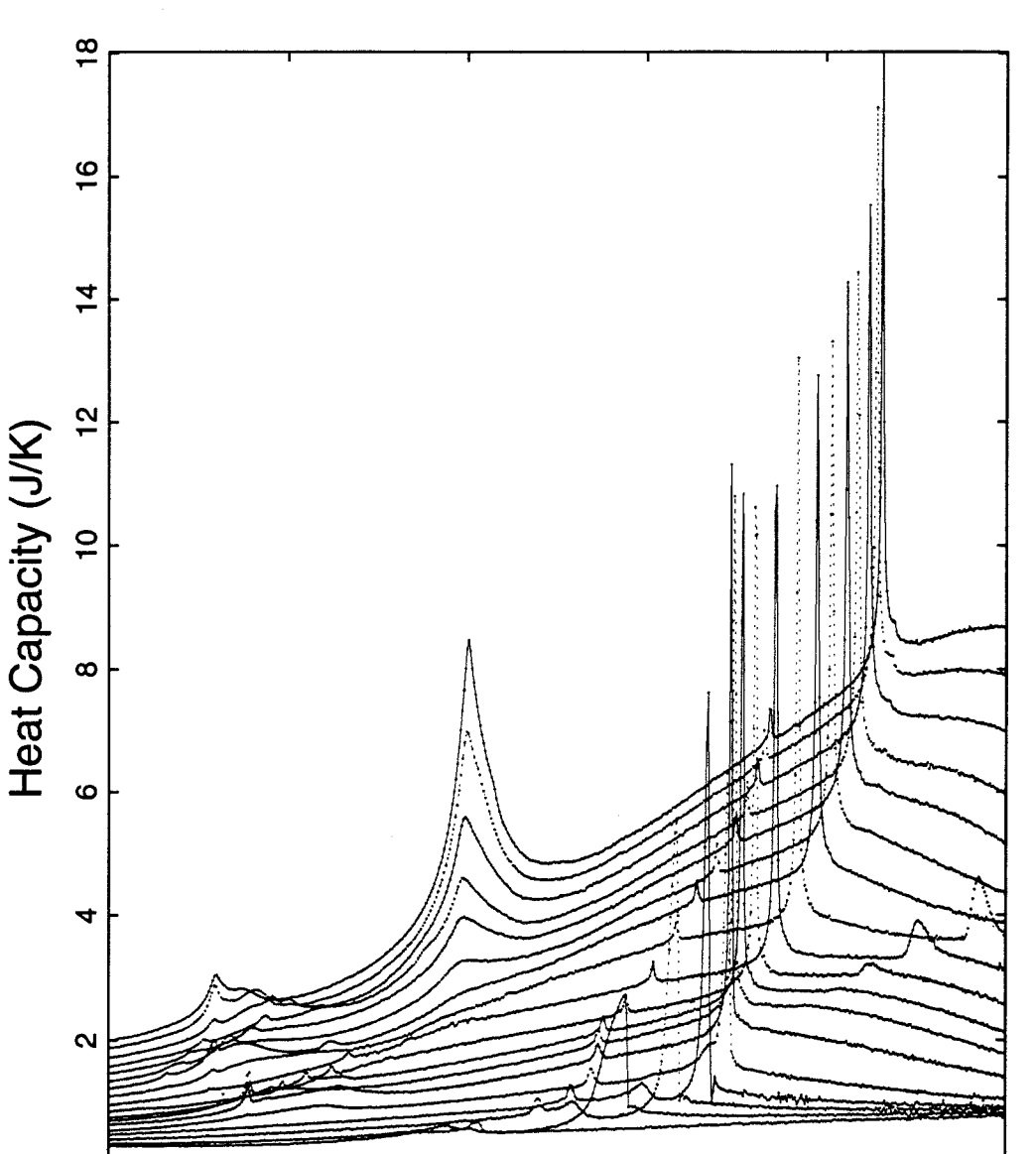

Figure 5.11: Heat capacity for films on the adsorption branch with the cryogenic valve closed, uncorrected for desorption. Coverages are: 0.87, 0.94, 1.03, 1.12, 1.25, 1.55, 1.70, 1.85, 2.06, 2.44, 2.67, 3.00, 3.30, 3.66, 4.00, 4.43, 4.87, and 5.27 nominal layers in the system (gas, film and capillary condensate).

data:

- Large peaks from 90 to 112 K attributed to the continuation of first layer melting and small peaks due to the commensurate to incommensurate phase transition at high coverages.

- Broad peaks from 112 to above 120 K that are likely due to the desorption of the film when the experimental path passes downward through the first step in the vapor pressure isotherm.

- Peaks near 90 K that will be shown to be the melting of the capillary condensate.

- Small peaks from 75 to 85 K that appear to be related to the 2-D phase diagram for the second, third and fourth uniform layers.

Figure 5.12 shows the results from two heat capacity runs from separate cell fillings, overlayed on top of each other. This comparison shows that even the finer details in the data are reproducible. Note that the low temperature features are barely recognizable on figure 5.11. These small features are not clearly resolved in Hamilton's data [34], due to the noise and the small number of points per degree in his data.

Figures 5.13 and 5.14 make the low temperature features in plots 5.10 and 5.11 clear by spreading the data runs apart.

The locations of all the peaks for the adsorption branch data in the N_{film} vs. T plane are shown in figure 5.15. The lines follow the peaks through the different coverages and represent possible phase boundaries. Figure 5.16 shows the $\mu - \mu_{solid}$ vs. T phase diagram, where the dashed lines represent the system's path as the temperature warmed.

5.3.2 First Layer Melting Peaks

In order to tie into the well documented first layer phase diagram of methane on Grafoam, figure 1.5, data were taken on the adsorption branch up to 120 K in order to see the first layer melting. The heat capacity data of Kim, Zhang and Chan [2] clearly map out the monolayer phase diagram up to 1.0 layers adsorbed,

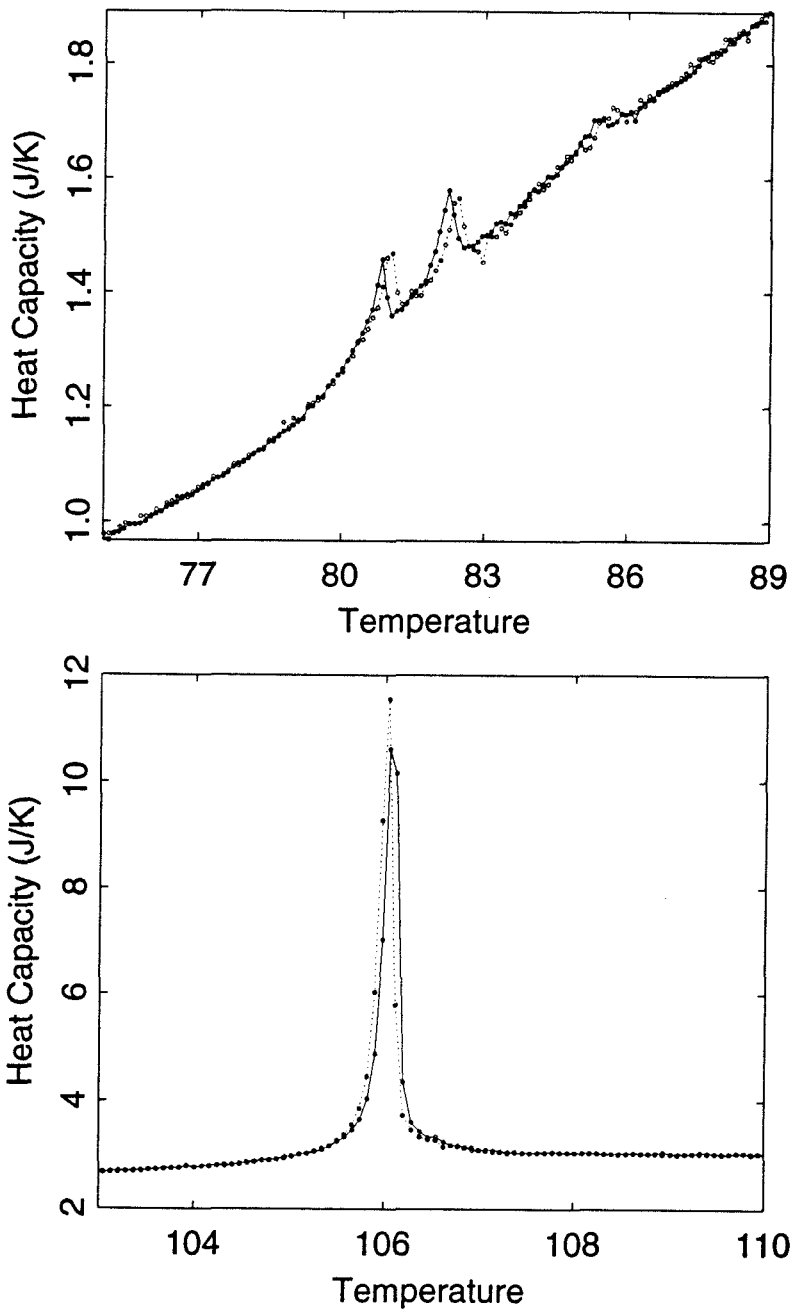

Figure 5.12: Comparison of the high and low temperature heat capacity features for two identical films on the adsorption branch from different fillings to demonstrate the reproducibility. Hollow and filled circles are from runs "nc07" and "nc15" respectively. Coverage is about two layers.

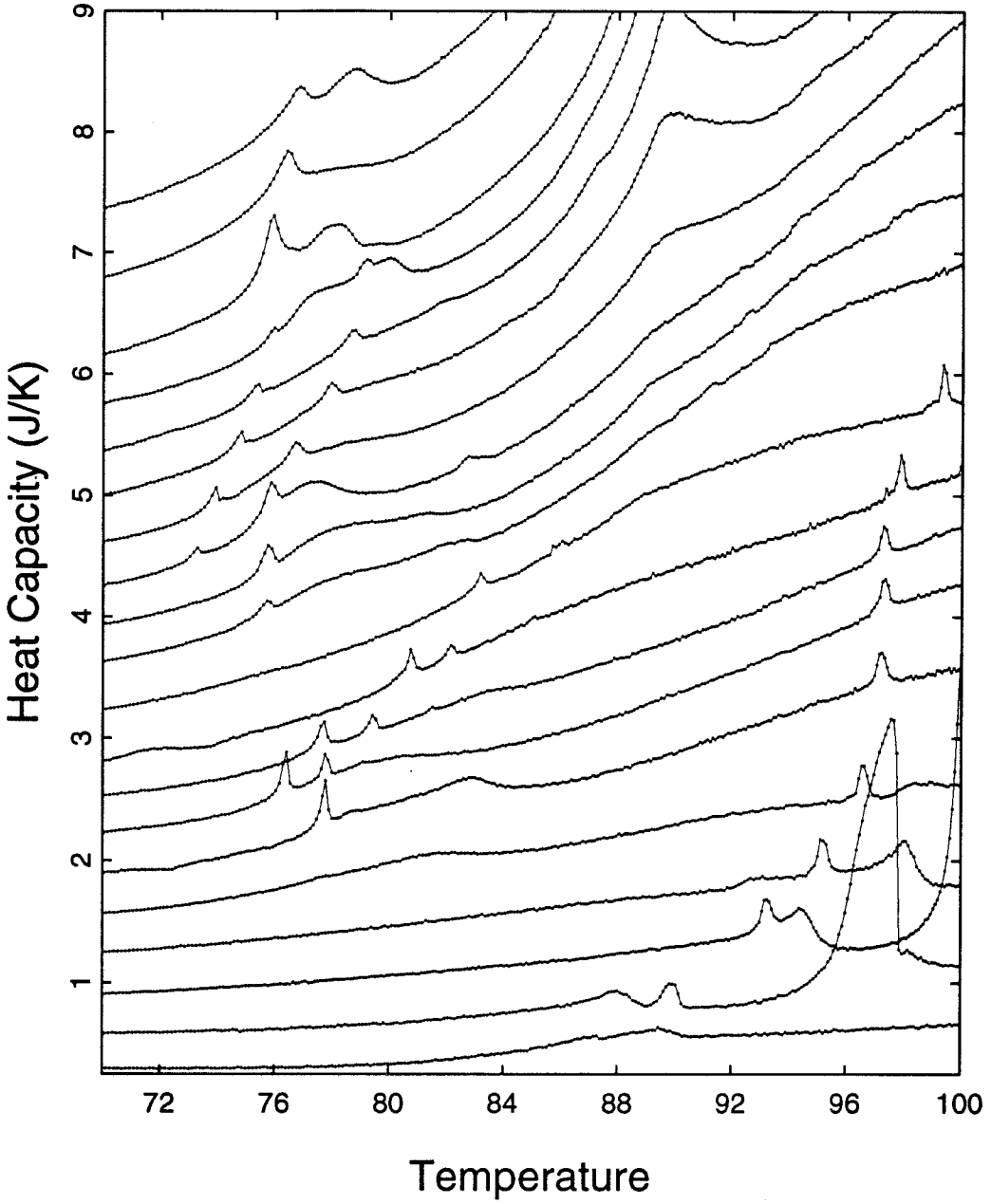

Figure 5.13: Heat capacity for films on the adsorption branch with the cryogenic valve open, uncorrected for desorption. Each scan was stepped upward by .25 J/K, with the highest coverage run at the top of the plot. Coverages are: 0.87, 0.94, 1.03, 1.12, 1.25, 1.55, 1.70, 1.85, 2.06, 2.44, 2.67, 2,84, 3.00, 3.30, 3.66, 4.00, 4.43, 4.87, 6.0, and 7.0 nominal layers in the system (gas, film and capillary condensate).

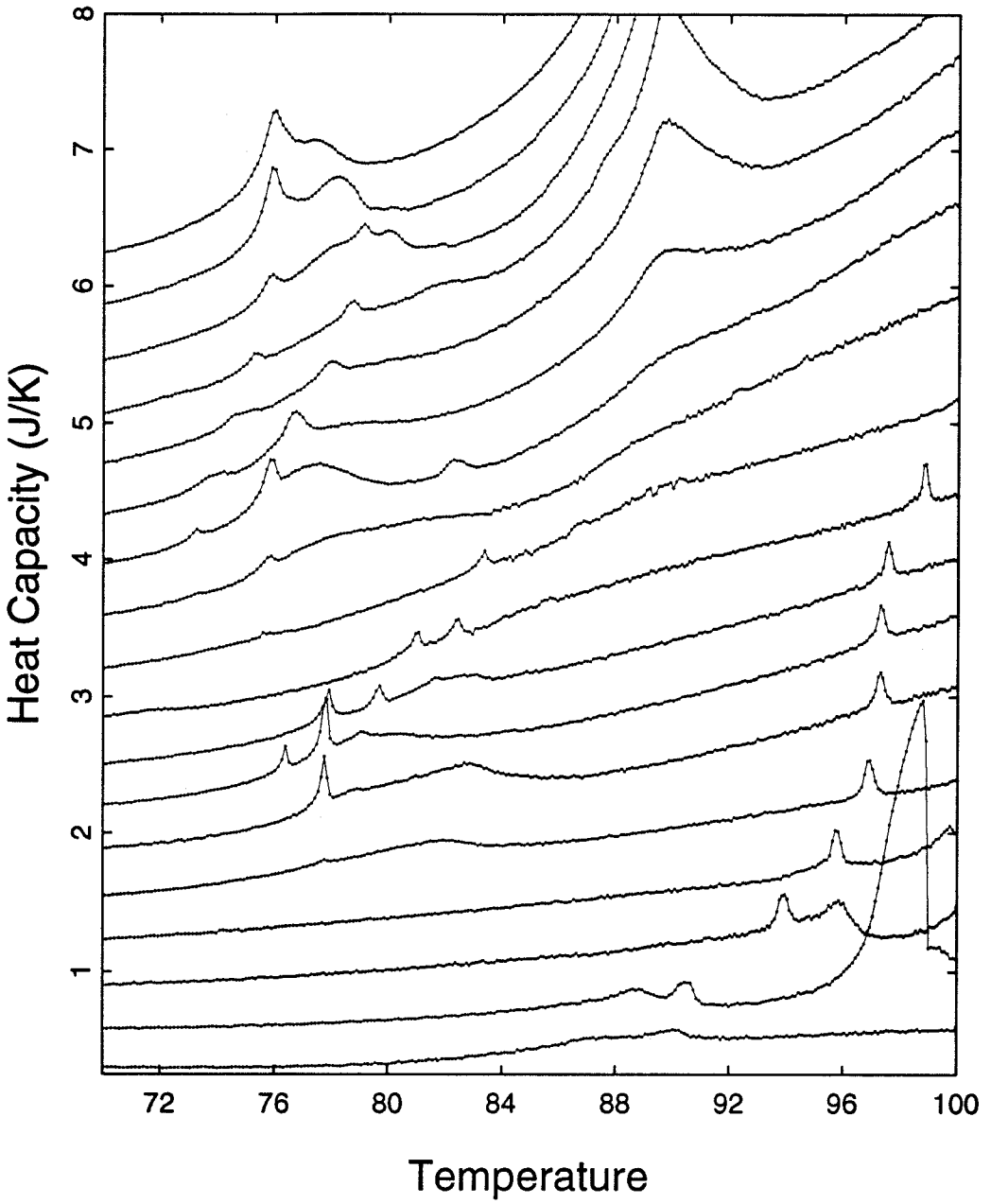

Figure 5.14: Heat capacity for films on the adsorption branch with the cryogenic valve closed, uncorrected for desorption. Each scan was stepped upward by .25 J/K, with the highest coverage run at the top of the plot. Coverages are: 0.87, 0.94, 1.03, 1.12, 1.25, 1.55, 1.70, 1.85, 2.06, 2.44, 2.67, 3.00, 3.30, 3.66, 4.00, 4.43, 4.87, and 5.27 nominal layers in the system (gas, film and capillary condensate).

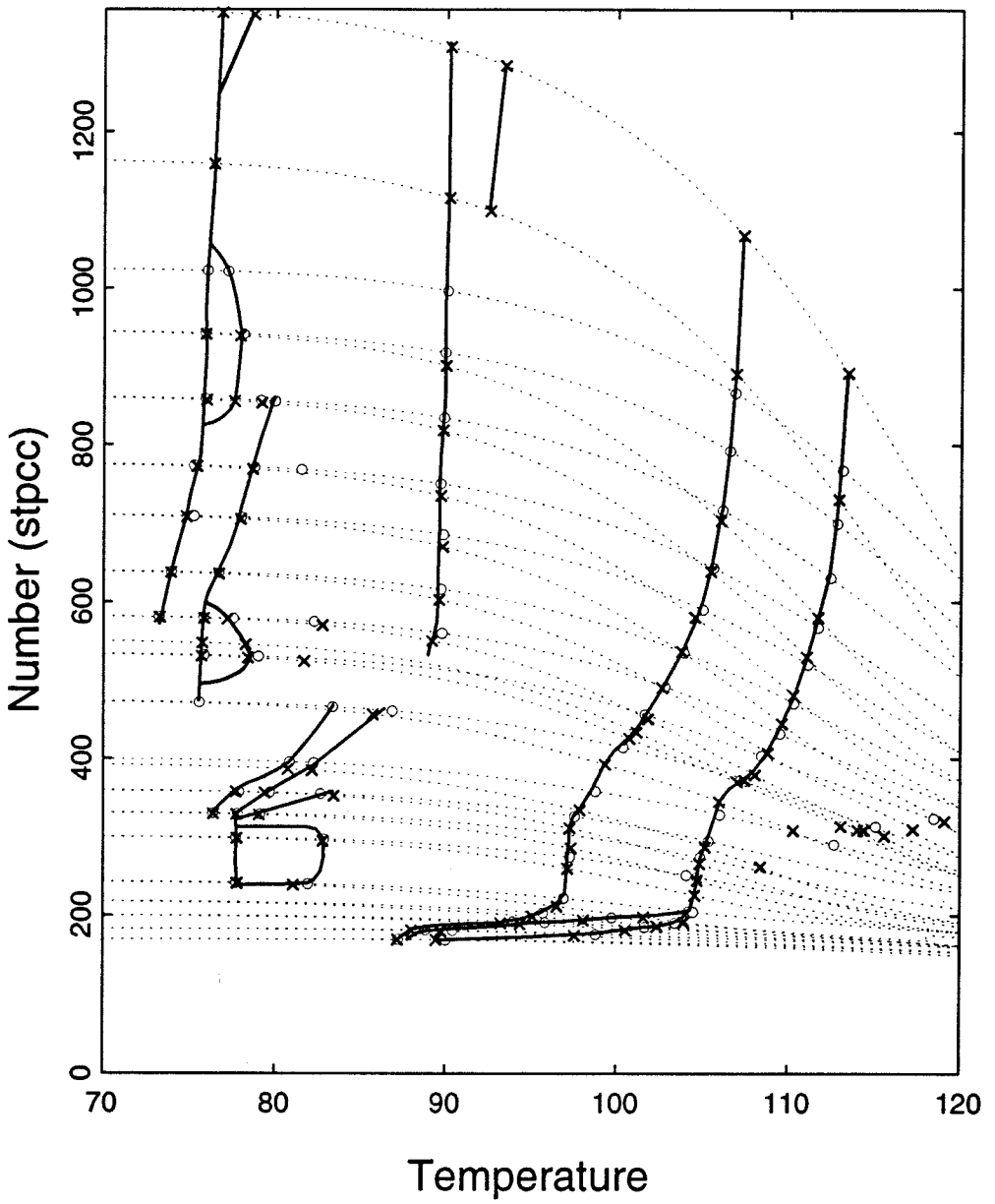

Figure 5.15: Locations of the peaks in the heat capacity for films on the adsorption branch in the N_{film} vs. temperature plane. Crosses are for data taken with the cryogenic valve open, circles are data taken with it closed. The dashed lines represent the path traveled by the system as the film was warmed. Heavy lines connect similar peaks together to form possible phase boundaries.

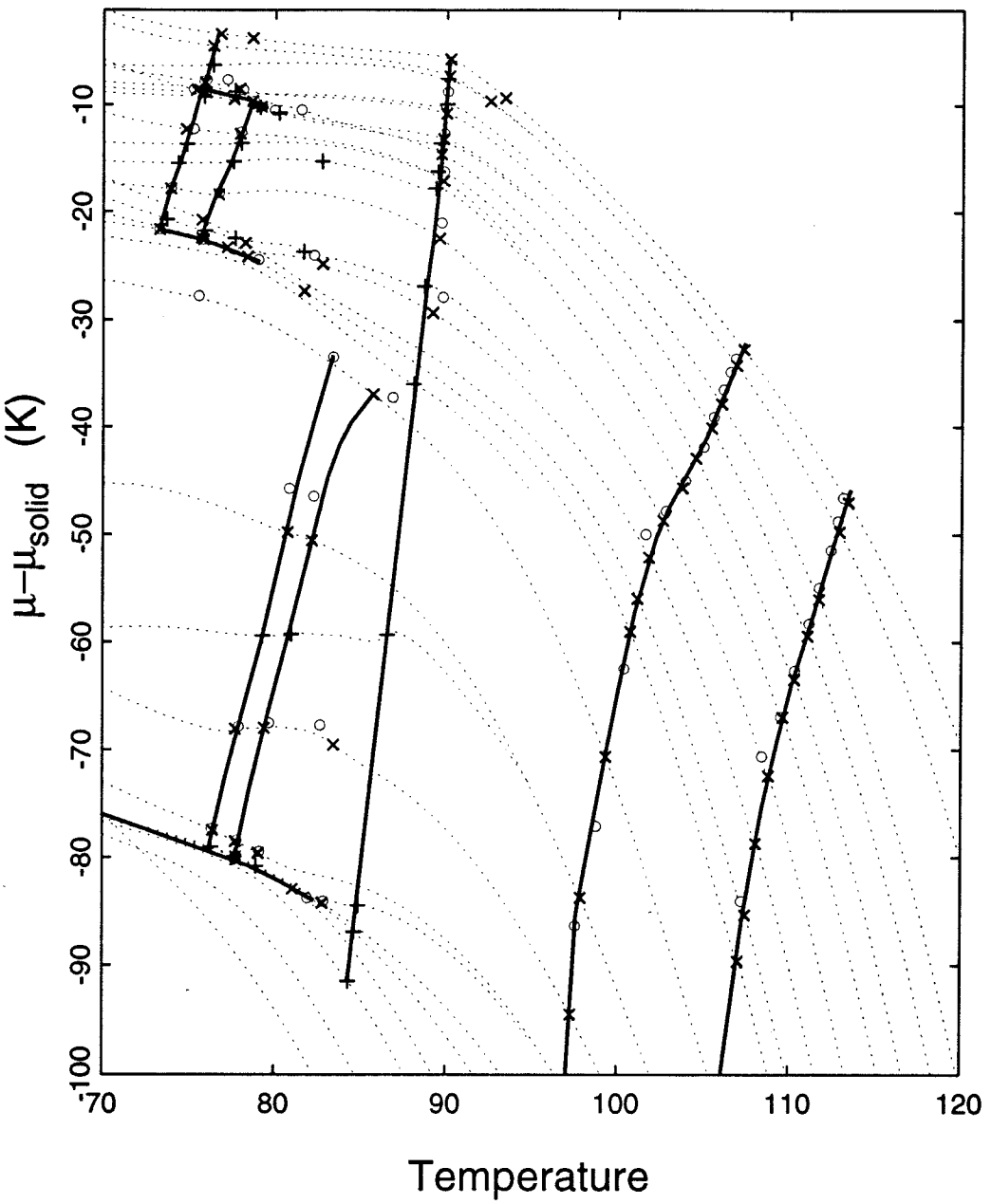

Figure 5.16: Locations of the peaks in the heat capacity in the $\mu - \mu_{solid}$ vs. T plane for the higher coverages. X(valve open) and O(valve closed) label points on the adsorption branch. Crosses label points on the desorption branch. The dashed lines represent the path traveled by the system as the film was warmed. Heavy lines connect similar peaks together to form possible phase boundaries.

from five to 100 K. Our apparatus is only able to record data[7] from 65 to 120 K, so it was only possible to catch the high temperature, high coverage part of the first layer melting curve reproduced in figures 6 and 9 of reference [2], or figure V-6 on pages 147–149 of reference [1]. However, there are interesting features in this part of the monolayer phase diagram, often called the "extended" monolayer regime.

Kim, Zhang and Chan found that the monolayer melting heat capacity peak does not disappear near monolayer completion, as concluded by early heat capacity studies [8], but continues to higher coverages and temperatures. This observation is not surprising, and has since been observed [98] and explained [99] for other systems. An explanation for the sudden elevation of the melting temperature near monolayer completion is given by Etters, Roth and Kuchta [99]:

> We postulate that the fundamental distinction between melting of partial and complete monolayers is that there are many vacancies between islands of the former that promote thermal fluctuations in the plane of the substrate which, in turn, facilitates self-diffusion, thermal expansion, and melting at T_M. For the latter case all lattice sites are occupied and thermal expansion in the plane is eliminated by the boundary of the experimental apparatus and/or possibly grain boundaries. Thus, only fluctuations in the $\hat{\mathbf{z}}$ direction can provide space sufficient to initiate 2D melting. This is important because forces impeding thermal expansion normal to the plane are about an order of magnitude larger than those in the plate. Melting therefore should occur at a higher temperature for monolayers than for partial monolayers.

The first layer melting peak also increases in size drastically and becomes much narrower when the monolayer completes. This can be explained by a similar argument given in Chapter 1 on page 9, due to Elgin and Goodstein [23, page 42], that offers another explanation for the sudden increase in the melting temperature.

Hamilton [34, page 67] also points out that while the monolayer is completing and T_M ranges from 78 to 98 K, T_M is a linear function of $\mu - \mu_o$. Computer simulations like that of Etters, Roth and Kuchta could be used to investigate this

[7]The calorimeter should work well at lower temperatures until the platinum thermometers lose sensitivity at about 20 K. The lack of an inexpensive cryogenic coolant for lower temperatures limits the temperature range of this apparatus to above about 60 K. The best solution for lower temperatures would be a closed cycle refrigerator.

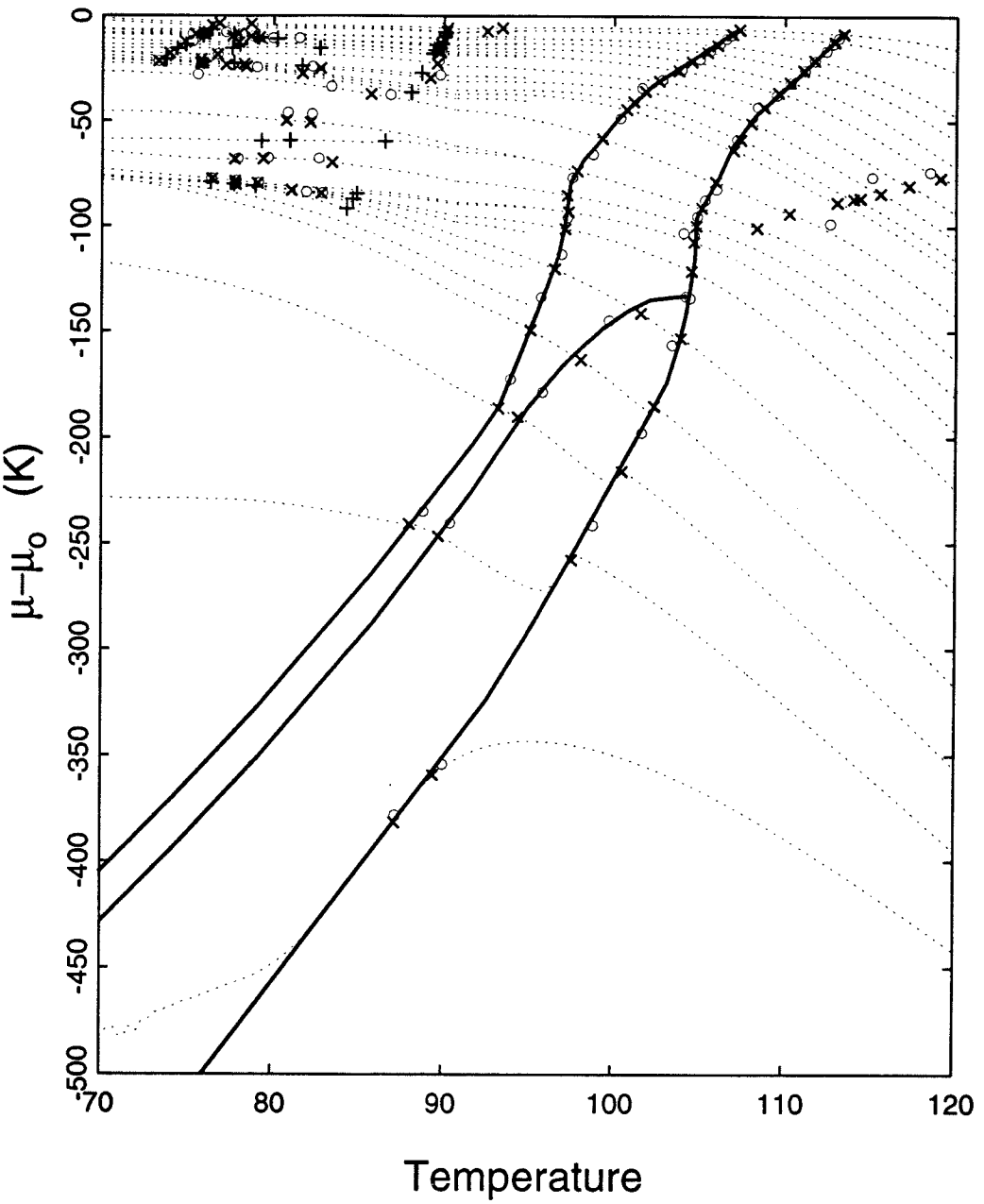

Figure 5.17: Locations of the peaks in the heat capacity in the $\mu - \mu_o$ vs. T plane. Crosses are for data taken with the cryogenic valve open on the desorption branch, X denotes the location of peaks on the adsorption branch with the valve open and circles are for data taken with this valve closed. The dashed lines represent the path traveled by the system as the system was warmed. Heavy lines show proposed phase boundaries in the first layer.

phenomenon. There are not enough data taken in this study for films with T_M in the linear range to add to this picture, except to say that this behavior does not seem to occur at higher coverages, as seen in figure 5.17.

Incommensurate to Commensurate Phase Transition Before Melting

Vora, Sinha and Crawford [14] identified all the phases and the approximate locations of the phase boundaries of monolayer methane using neutron diffraction in 1979. They identified six two dimensional phases: dense incommensurate solid (DS), commensurate solid (CS), expanded incommensurate solid (ES), supercritical fluid, gas, and liquid, as seen in figure 5.18. They ended the CS phase region in the high coverage/temperature part of the phase diagram and postulated that there was a phase transition from ES to DS phase at about .88 layers. The additional work by Kim, Zhang and Chan [2] described the shape of the boundaries between these phases and continued the CS phase region upward to higher temperatures and coverages. They still ended the CS phase region, implying that there is a phase transition between the two incommensurate phases, ES and DS.

Figure V-6 on pages 147–149 of reference [1] shows heat capacity scans for coverages from .82 to 1.0 layers that resolve two heat capacity features a few degrees below the first layer melting temperature. The first feature represents the phase transition between the DS to CS solid phases and the second is the signature of the CS to ES phase transition. At higher coverages, the two heat capacity peaks seemed to merge into one, so Kim et al. postulated that the CS phase disappeared, and a phase transition between the DS and ES phases occurs just before the first layer melts. The topology of the phase diagram proposed by Kim, Zhang and Chan is shown in figure 5.18.

From our data at much greater coverages and temperatures, it is clear that the first layer phase diagram needs further modification. Figure 5.19 displays the small features in the heat capacity just below the first layer melting from .87 to 1.33 monolayers coverage. In the two lowest coverage scans, the features are very broad and hard to see at the scale shown. The small bump in each of these runs is on the first layer melting curve shown in figure 5.17, so they can be identified as due to first layer melting. The DS to CS and the CS to ES phase transition heat capacity peaks are below 65 K and are not seen. Three phase transitions, DS to CS (A), CS to ES (B), and ES to liquid (C), are clearly visible in the runs from 0.930 up to and including 1.140 monolayers. The temperature distance

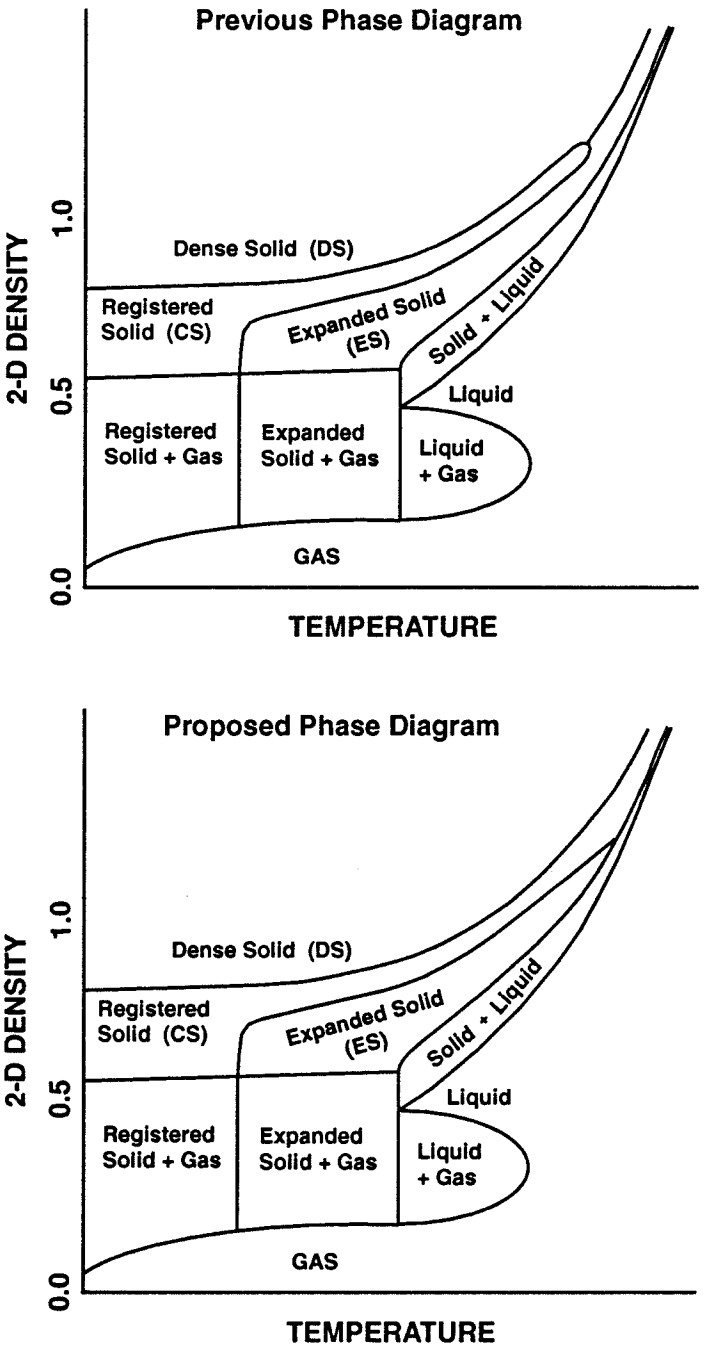

Figure 5.18: Upper: N_{film} vs. T phase diagram for monolayer methane on Grafoam proposed by Kim, Zhang, and Chan [1, 2]. Note that the CS phase region ends at high coverages, leaving the DS to ES phase transition. Lower: Proposed extended first layer phase diagram.

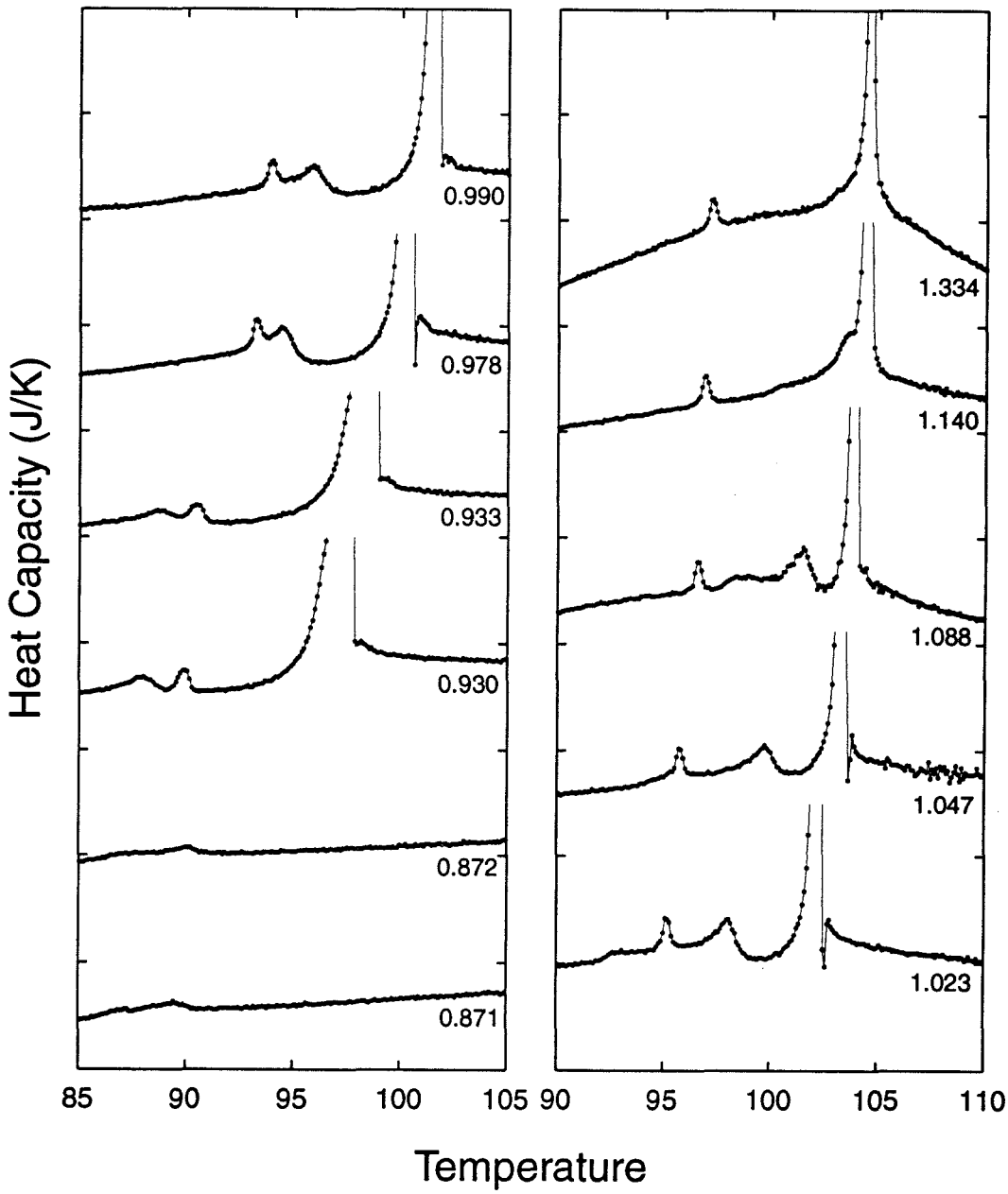

Figure 5.19: Heat capacity peaks for the first layer adsorption branch data. The number of monolayers in the film at the point of the DS to CS phase transition (lowest temperature feature) is indicated below each curve.

between feature A and C is approximately constant for all the plots above 0.930 monolayers, but peak B moves from just after A to just before C in the coverage range from 0.930 to 1.140 monolayers. At 1.334 monolayers, peak B is consumed by C. Since the phase boundary between the ES and CS phases (peak B) ends on the first layer melting line, the expanded solid region of the phase diagram ends between 1.140 and 1.334 monolayers. The location of these points in the $\mu - \mu_s$ plane is shown in figure 5.17. At high coverages, as the temperature is raised, the monolayer changes from DS to CS phase; then the CS phase melts.

Another argument in favor of this interpretation is that if the CS phase region of the phase diagram ends as Kim, Zhang and Chan propose, then the low temperature peak at 1.334 layers and above would represent a phase transition between two incommensurate phases with different densities. But since there is no difference in the symmetry or density between these two phases, the phase transition should be continuous, and the heat capacity peak should be very broad. Instead, it is quite sharp. Figure 5.19 shows that the single low temperature peak must represent the DS to CS phase transition. The resulting phase diagram is shown by figure 5.15.

5.3.3 Heat Capacity Above 110 K

In the heat capacity data that are not corrected for desorption (figure 5.11), there is a prominent set of peaks beginning a few degrees above first layer melting and extending to above 120 K. When the unapproximated desorption correction is included (figure 5.20), these peaks become "valleys" and even dip below zero. Since the film heat capacity can never be negative, the desorption correction must be wrong. The error comes from inaccuracies in the value of $[\frac{\partial \mu}{\partial T}]_N$, as discussed in section B.3.3. When the desorption correction is calculated using the approximation noted in section B.3.3 ($[\frac{\partial \mu}{\partial T}]_N = \frac{d\mu_\sigma}{dT}$) and subtracted from the data, the peaks are eliminated to within the scatter in the data (figure 5.21). The large nonrandom scatter in these data at high temperatures is correlated with the outer bath filling and is due to temperature fluctuations of the gas handling system as discussed in section 5.1. The noise in the desorption correction also adds to the scatter.

Unless the desorption correction is calculated accurately and without approximation, it is impossible to say whether the peaks are actually present in the heat capacity. The data with the approximate desorption correction hint that these

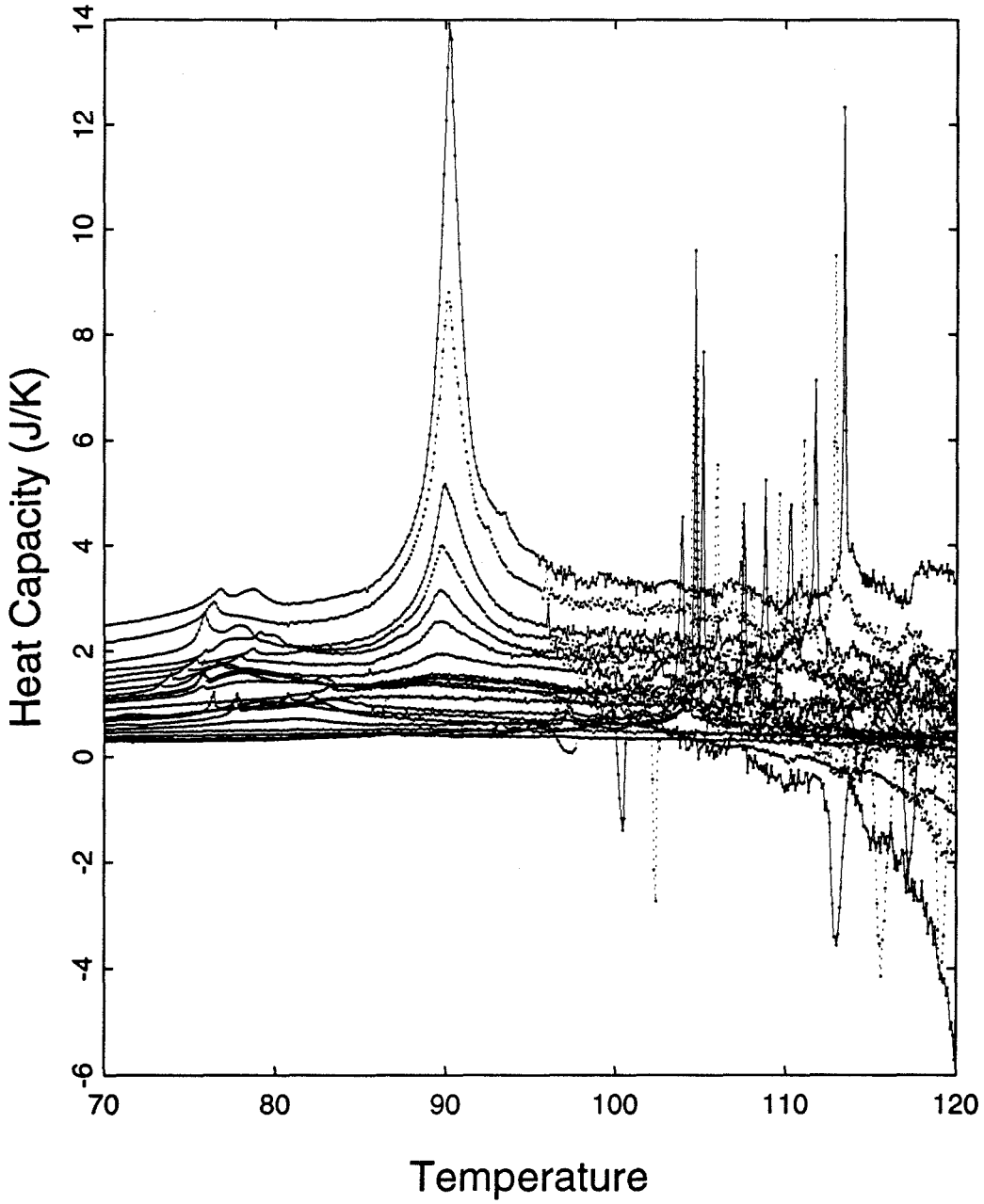

Figure 5.20: Film heat capacity for all runs on the adsorption branch with the cryogenic valve open, corrected for desorption without any approximations.

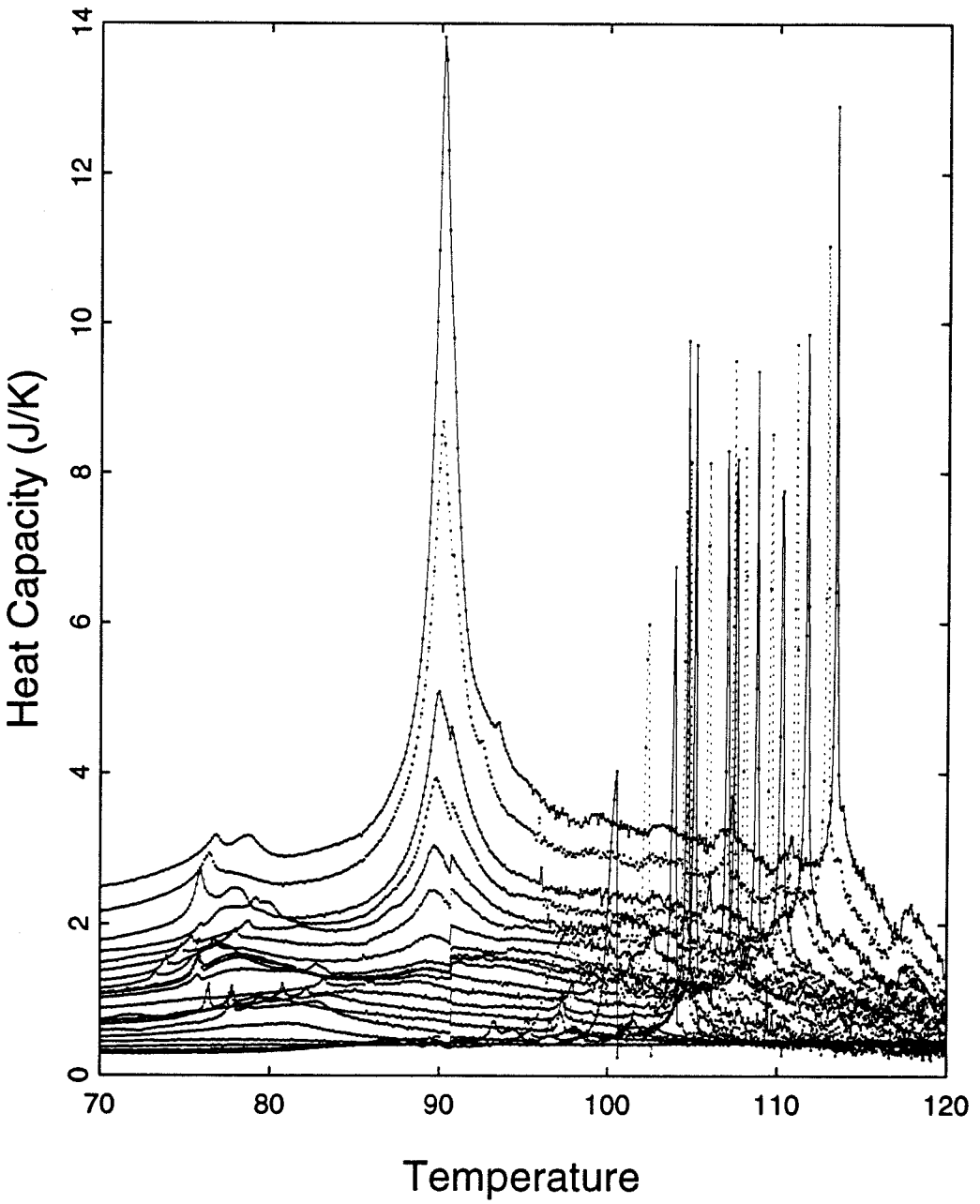

Figure 5.21: Film heat capacity for all runs on the adsorption branch with the cryogenic valve open, corrected for desorption assuming that $[\frac{\partial \mu}{\partial T}]_N = \frac{d\mu_o}{dT}$.

peaks may be caused by peaks in the amount of desorption, as the temperature rises. What could cause a sudden increase in the rate of desorption, or the heat of desorption? The desorption rate is equal to the slope of the experimental path in the N vs. T phase diagram, figure 5.15. At high temperatures the rate of desorption increases dramatically, and the film begins to lose thickness rapidly. The rate of desorption can be calculated assuming that the 3-D gas coexisting with the film is either in the heat capacity cell, or in the gas handling system at room temperature:

$$\left[\frac{dN}{dT}\right]_X = \left[\frac{dP}{dT}\right]_X \left(\frac{V_{room}}{k_b T_{room}} + \frac{V_{cell}}{k_b T}\right) + \frac{V_{cell}}{k_b T^2} \tag{5.1}$$

where N is the number in the film, X represents the experimental path ($N(T)$), P is the pressure, and V_{room} and V_{cell} are the volumes of the gas handling system manifold and the sample cell respectively. T and T_{room} are the temperatures of the sample cell and the gas handling system. Since the cell and room temperatures change little over the range of temperature of the heat capacity bumps, if there is a change in the rate of desorption, it should appear in the pressure data. When the raw pressure data are examined, there are features in the pressure vs. temperature curves exactly when the bumps occur in the heat capacity. One possible explanation is that $[\frac{dP}{dT}]_X$ can be written as the sum of two terms:

$$\left[\frac{dP}{dT}\right]_X = \left[\frac{\partial P}{\partial T}\right]_N + \left[\frac{\partial P}{\partial N}\right]_T \left[\frac{dN}{dT}\right]_X \quad . \tag{5.2}$$

The first term on the r. h. s. of equation 5.2 is usually smooth, but there are definite steps in $[\frac{\partial P}{\partial N}]_T$, as seen in the vapor pressure isotherm curve, figure 5.5. Solving equations 5.1 and 5.2 for the rate of desorption as a function of the derivatives of the pressure gives:

$$\left[\frac{dN}{dT}\right]_X = \frac{[\frac{\partial P}{\partial T}]_N (\frac{V_{room}}{k_b T_{room}} + \frac{V_{cell}}{k_b T}) + \frac{V_{cell}}{k_b T^2}}{1 + [\frac{\partial P}{\partial N}]_T (\frac{V_{room}}{k_b T_{room}} + \frac{V_{cell}}{k_b T})} \quad . \tag{5.3}$$

The value of $[\frac{\partial P}{\partial N}]_T$ can change wildly as the film goes through the sharp steps in the isotherm; could this cause the bumps in the rate of desorption?

To test this hypothesis, the desorption correction was calculated from the 95 K isotherm (figure 5.5). The heat of desorption, the pressure and the pressure derivatives at all temperatures were found by assuming equation B.6 is true, using the curve for the bulk vapor pressure, equation B.1. The desorption correction from 90 to 140 K for films with the same thickness as the actual data from figure

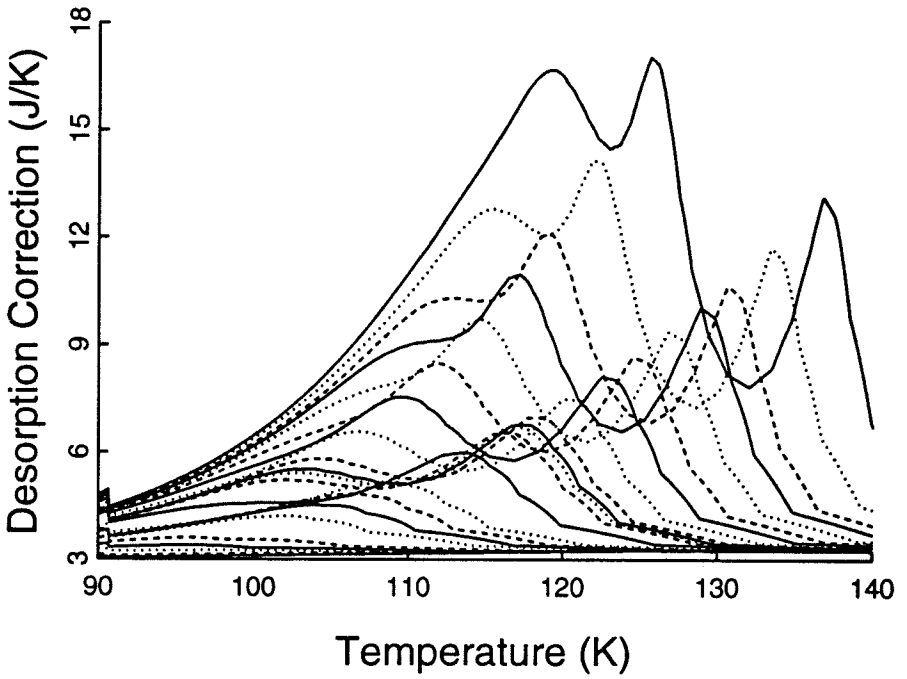

Figure 5.22: The desorption correction calculated using the data from the 95 K isotherm and assuming equation B.6 is true. The films have 0.87, 0.94, 1.03, 1.12, 1.25, 1.55, 1.70, 1.85, 2.06, 2.44, 2.67, 2,84, 3.00, 3.30, 3.66, 4.00, 4.43, 4.87, 6.0 nominal layers in the system (gas, film and capillary condensate).

5.10 (omitting the thickest film) are shown in figure 5.22. There are narrow bumps in the data from this calculation that are similar to those in the raw heat capacity (figure 5.10). These features are produced only from the isotherm data, and therefore can only be caused by changes in the rate of desorption caused by the variation in the isotherm slope. They are not expected to exactly coincide with the features in the data because equation B.6 is not strictly true, as shown by Hamilton [34, page 62,63].

The isotherm slope causes these features because as the temperature rises, the pressure rise is controlled by the two terms in equation 5.2. The first term is the vapor pressure increase if the film thickness were constant; but molecules must leave the film to increase the pressure in the 3-D gas. Desorption reduces the vapor pressure of the film (at constant temperature), and the second term accounts for this by reducing the pressure increase contributed by the first term.

However, when the system is passing through the vertical sections of the vapor pressure isotherm, the number of molecules in the film may decrease without a significant change in the pressure, so the pressure increase is larger. Because the vapor pressure isotherm slope varies greatly as the film goes through the steps in the isotherm, this effect can be very large at higher temperatures.

This analysis, combined with the evidence from figure 5.21, persuades us that the heat capacity features above 110 K are caused by the steps in the vapor pressure isotherm. However, since it is practically impossible to calculate the desorption correction at these temperatures exactly, this conclusion is not certain.

The desorption correction also affects the size of the first layer melting peaks and the peaks near the triple point. Subtracting the unapproximated desorption correction from the raw data makes the first layer melting peak in the 1.03 layer heat capacity run become a "valley" and dip below zero. The approximate desorption correction (equation B.6) corrects this problem, but the more proper solution is to use equation B.4, because the film is in two phase coexistence during melting. The first layer melting peak in the 1.03 layer run appears as expected when corrected for desorption with equation B.4. The data corrected for desorption assuming that $[\frac{\partial \mu}{\partial T}]_N$ equals $\frac{d\mu_\sigma}{dT}$ cannot be accurate when the film is in two phase coexistence, and likewise, the data corrected for desorption assuming that the film is in two phase coexistence cannot be accurate when there is no heat capacity peak. Thus there is no approximation to the desorption correction that will accurately treat heat capacity peaks from first order phase transitions. Therefore no analysis was performed to find the area under the first layer melting peaks.

The data with the approximate desorption correction subtracted (figure 5.21) show a discrete jump near the triple point caused by the sudden jump in $\frac{d\mu_\sigma}{dT}$. This prevents this data from being used to analyse the heat capacity peaks near T_3. Fortunately, the unapproximated desorption correction is accurate in this temperature range because $[\frac{dP}{dT}]_X$ is close enough to $[\frac{\partial P}{\partial T}]_N$.

5.3.4 Peaks Near T_3, The Melting of Capillary Condensate

As mentioned above, the cause of the hysteresis on the vapor pressure isotherm data was not known. Therefore, twelve heat capacity runs were performed on the desorption branch at coverages from one to seven layers adsorbed (figure 5.23). The most obvious difference between the adsorption and desorption branch data

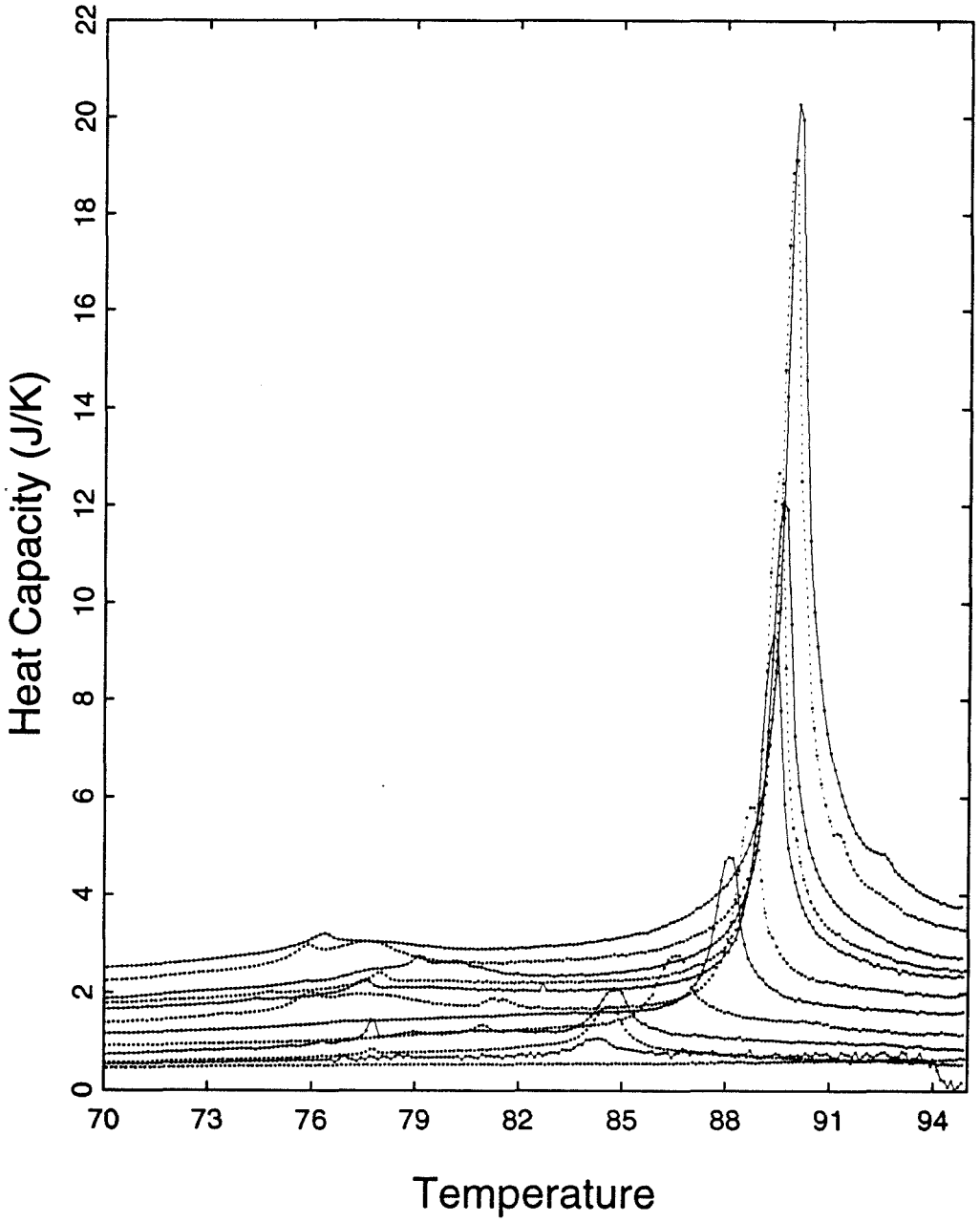

Figure 5.23: The heat capacity for films nearly on the desorption branch with the unapproximated desorption correction subtracted. The films have 1.16, 1.39, 1.74, 2.07, 2.47, 3.11, 3.81, 4.54, 4.84, 5.35, 6.29, 7.06 layers in the system (gas, film and capillary condensate). The 7.06 and 5.35 layer films were formed by desorption from a film that was initially 14 layers thick. The rest started with 11 layers adsorbed.

is that the triple point peaks in the desorption branch data are higher, narrower, at lower temperatures, and occur with much less gas adsorbed. In fact, in the desorption branch data, the peak disappears precisely when the amount adsorbed is less than the point where the hysteresis loop closes in figure 5.5 (1.1 layers adsorbed). This strongly suggests that these heat capacity peaks are due to the melting of bulk capillary condensate.

To demonstrate that the peak near T_3 is related to the vapor pressure hysteresis, three runs were made with the same amount of gas adsorbed on the substrate, two layers (figure 5.25).

The lowest curve in figure 5.25 was formed by increasing the amount adsorbed from zero to two effective layers while cooling from 120 to 108 K. The system state should therefore be on the lower boundary curve (adsorption branch) of figure 5.24. The film's heat capacity has two small, sharp peaks between 80 and 83 K in the temperature range shown, 75 to 92 K. The phase transitions causing these peaks will be discussed in section 5.3.5.

The central curve in figure 5.25 followed the central downward scanning curve in figure 5.24. The equivalent of 5.5 layers were condensed on the surface at low temperature (94 K). Then the film was warmed to 120 K, with the amount of gas in the vapor phase limited to 1/2 layer by closing the cryogenic valve at the mouth of the heat capacity cell. After cooling to 95 K, gas was removed from the system in 1/3 layer doses until two layers remained. The film is in the intermediate region, between the upper and lower boundary curves. The heat capacity for this film was radically different from the first case (on the adsorption branch). The two low temperature peaks present in the first case were translated to a lower temperature and a broad peak appeared, centered at 85 K.

The third case studied, the uppermost heat capacity curve in figure 5.25 was located on the uppermost isotherm in figure 5.24, very near to the upper boundary curve (desorption branch). The equivalent of 11 layers were condensed on the surface and the film was formed and annealed at 120 K, as in second case discussed above. After cooling to 95 K, gas was removed from the system in doses less than or equal to 1/3 layer until two layers remained. The position and size of the low temperature peaks is different from the other cases, and the high temperature peak is much larger.

The peak centered at 85 K in the two layer runs grows into the triple point peak at higher coverages. These data clearly show that the triple point peak is related to the vapor pressure hysteresis and therefore cannot be due to the melting of uniform

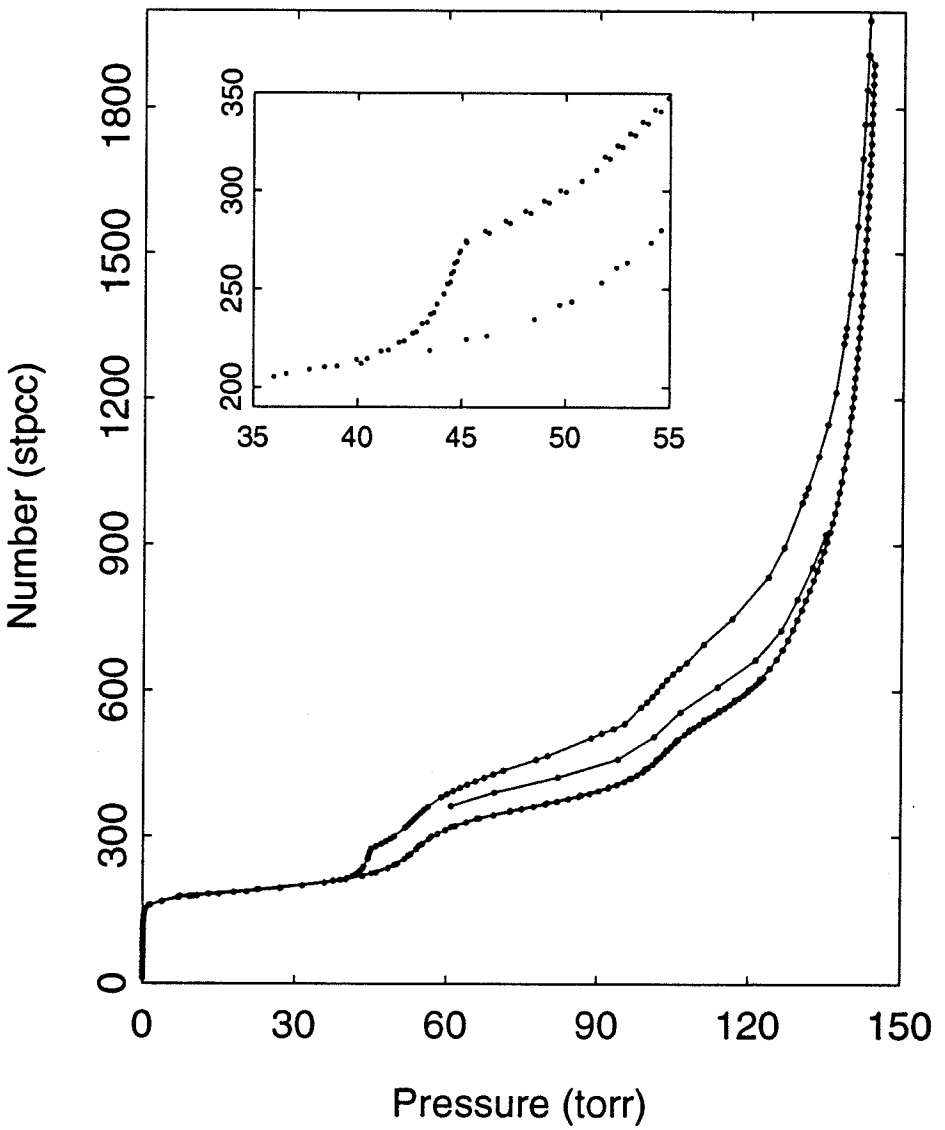

Figure 5.24: Vapor pressure isotherm for the adsorption branch with two downward scanning curves, starting at 11 (upper curve) and 5.5 (central curve) layers adsorbed.

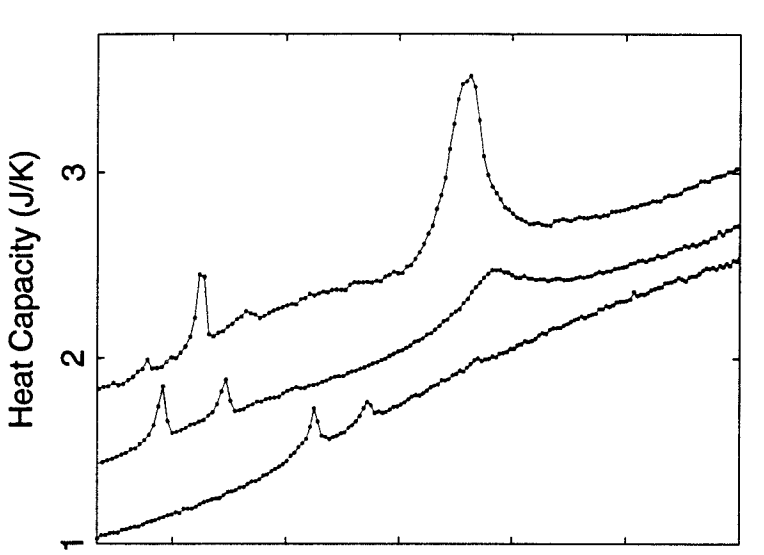

Figure 5.25: Heat capacity for three films with the same amount adsorbed (two layers), but at different locations on the hysteresis curve (figure 5.24). Upper curve: formed by withdrawing gas from the 11 layer film. Central curve: formed by withdrawing gas from the 5.5 layer film. Lower curve: formed by adding gas to an empty cell. Upper two curves displaced by .4 J/K and .8 J/K.

methane films[8], contradicting our previous publications [56, 57, 35, 74, 100], and those of others [48].

Furthermore, if a system has two states, the state present in true thermodynamic equilibrium is the one with the lowest chemical potential (pressure). Then the state on the desorption branch is the true equilibrium state, and all others are metastable. This has important implications, because there is only one true equilibrium state, but an infinite number of metastable states. There may also be many metastable states with the same chemical potential (pressure) but with different physical properties. This greatly affects the adsorption branch data because if a different film formation procedure is followed for two measurements, the resulting data may be different, even though the pressure is identical. To fully characterize the state of an adsorption branch system, the pressure and temperature must be known as functions of time since the substrate was bare (or above

[8]Except in the unusual case where the hysteresis is a property of the film itself. Later, evidence will be presented to the effect that the film is not affected by whatever causes the hysteresis, except for changing the vapor pressure and therefore the film's thickness.

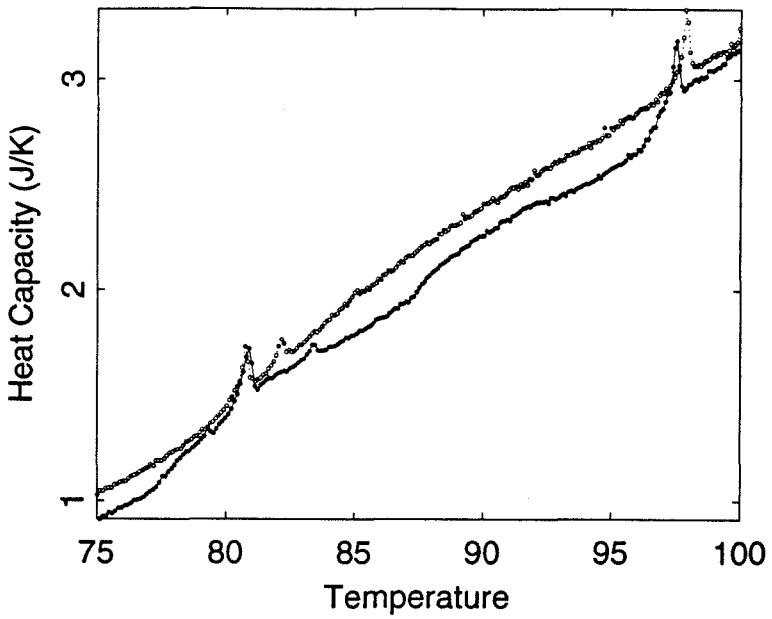

Figure 5.26: Heat capacity for two films with the same amount adsorbed (two layers), the same pressure, but with different heat capacities. The lower curve (nc22) was formed by a different procedure than the other films with the adsorption branch vapor pressure. The upper curve (nc08) was formed by the standard procedure.

the coverage where hysteresis begins). This result has a great effect on the current literature because virtually all of the published data on multilayer adsorbed films were on the adsorption branch (or in the intermediate region). Much of the current literature may need to be reevaluated.

In attempting to form a system on the desorption branch, a film was formed that had a vapor pressure corresponding to the adsorption branch, but a heat capacity much different from films formed by other methods. This film was prepared starting with a total system number equivalent to 5.5 layers adsorbed. With the calorimeter at 120 K, 3.5 layers worth of gas were rapidly removed from the system, leaving one layer worth of gas, and less than one layer adsorbed. (Note that the thickness of the uniform film is below the point at which hysteresis begins in figure 5.24.) The system was then cooled, causing nearly all the gas to condense. The resulting pressure at 95 K was equal to that on the adsorption branch. However, the heat capacity scan was not identical to the bottom curve in figure 5.24, even though these two films had the same pressure and amount ad-

sorbed. Figure 5.26 shows the heat capacity of this film (lower curve) compared with the another film on the adsorption branch, formed by gradually increasing the amount adsorbed while cooling down. Since the two films do not have the same heat capacity, they are in different physical states and therefore systems on the adsorption branch are in metastable states.

Does this mean that it is impossible to study adsorption branch films and get reproducible results? To test this, a pair of two layer films were prepared by identical methods. Figure 5.12 compares the heat capacity of these two runs near the low temperature features and the first layer melting heat capacity peak. The peaks are almost identical. Then, it is possible to obtain reproducible results from films on the adsorption branch if the same procedure is used to form all the films. However, it will be more difficult to compare results from different laboratories. Despite this, most of our study will concentrate on data on the adsorption branch. Since the original purpose of this study was to study the properties of uniform films, and not the complicated behavior of capillary condensate, the adsorption branch data are more useful because there is less capillary condensation to confuse the results, and the films are easier to form. To study films on the desorption branch, a very thick film (at least 14 layers) must be formed. Then this film's thickness must be reduced slowly to the desired coverage. Adsorption branch films are formed simply by condensing the desired amount of gas on a substrate, as long as the amount on the substrate increases.

Looking again at all the desorption branch heat capacity data (figure 5.23), it is apparent that the peak heights for the four thickest films are not in the proper order. The 5.35 layer peak is taller than the 6.29 layer peak. This happened because the 5.35 and 7.06 layer films were formed by desorption from a film that initially was 14 layers thick. The other films began at 11 layers. The state of the films that began at 14 layers were closer to the upper boundary curve than those that began at 11 layers. Therefore these films had more bulk matter capillary condensed. It is even likely that the films that began with 14 layers adsorbed were far from being on the desorption branch until most of the film was desorbed. As stated in section 5.2, the downward scanning curves do not necessarily join the upper boundary curves. Then, it is difficult to form films that are truly on the desorption branch.

To further analyse these peaks, they were fit to model curves in order to subtract a linear background and find the area under the curves. The peaks were fitted to nonlinear curves using the Levenberg-Marquardt method [101, page 542].

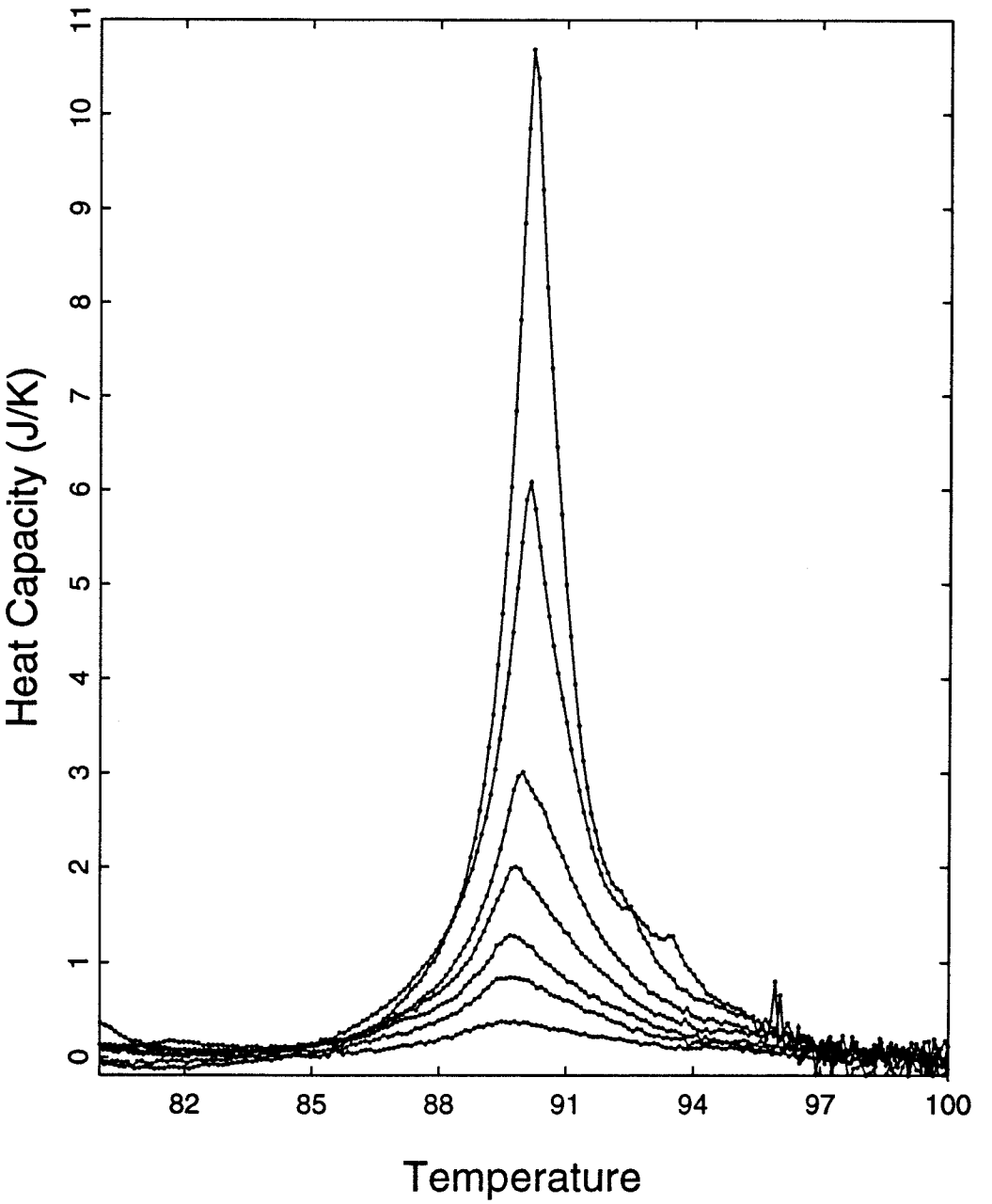

Figure 5.27: Heat capacity data from figure 5.20 (adsorption branch, with the unapproximated desorption correction subtracted), with a linear background subtracted to isolate the heat capacity of the peaks.

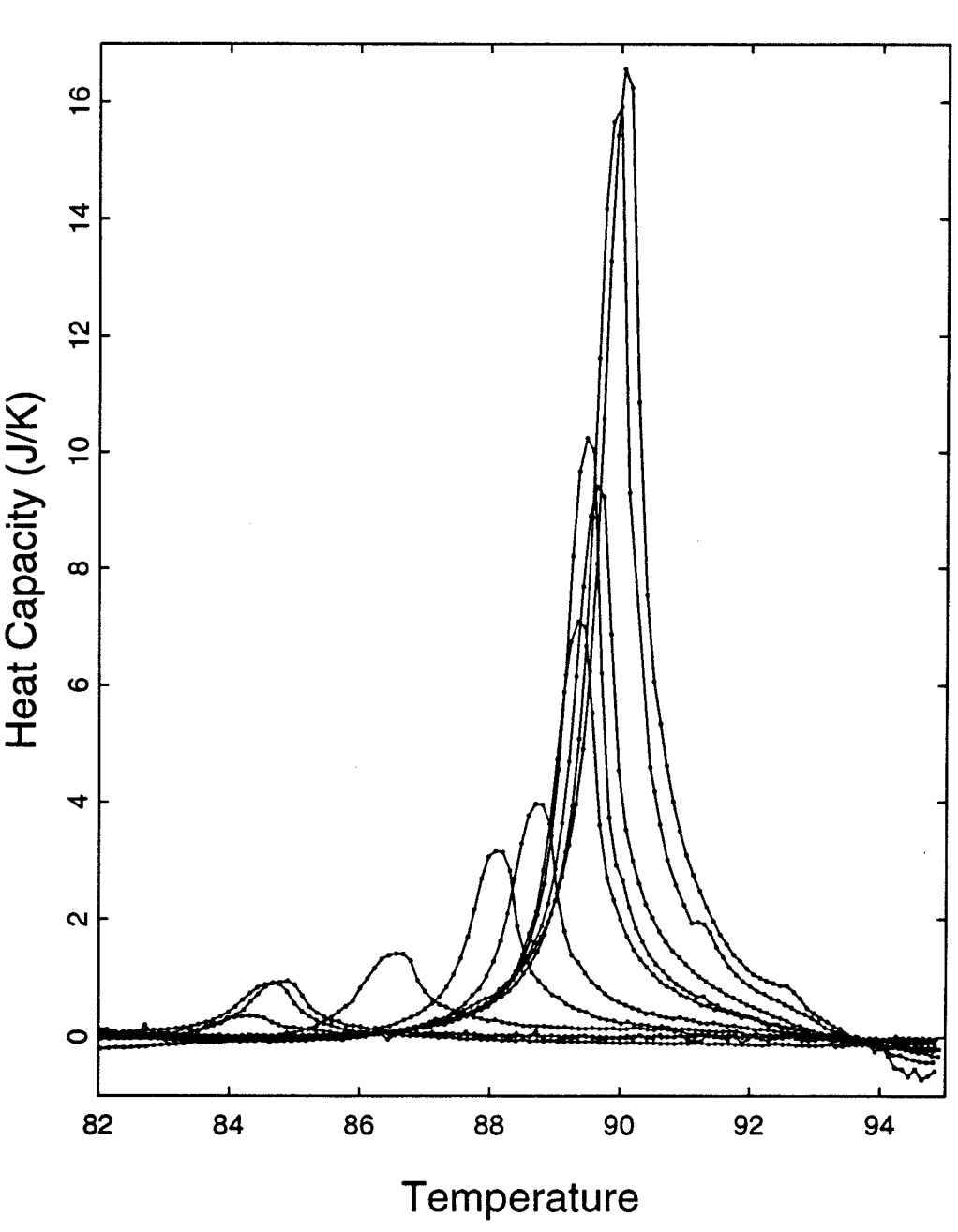

Figure 5.28: Heat capacity data from figure 5.23 (desorption branch, with the unapproximated desorption correction subtracted), with a linear background subtracted to isolate the heat capacity of the peaks.

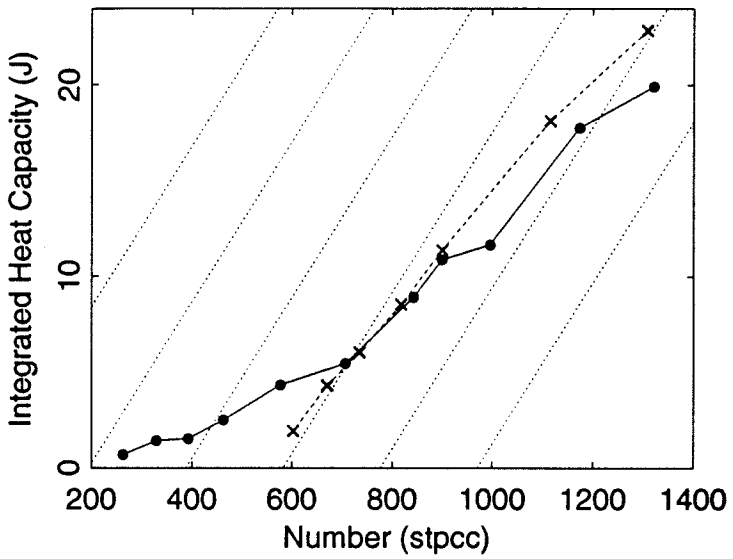

Figure 5.29: Integrated heat capacity vs. number adsorbed; circles are on desorption branch, crosses are on adsorption branch. Lines have the same slope as the bulk latent heat, each displaced by one layer adsorbed.

The adsorption branch peaks (corrected for desorption, with the cryogenic valve open) were found to fit well to the functional form:

$$\begin{aligned} A + BT + \frac{C}{1 + D(T - T_{pk})^2} \qquad & T < T_{pk} \\ A + BT + \frac{C}{1 + E(T - T_{pk})^2} \qquad & T > T_{pk} \end{aligned} \tag{5.4}$$

where A through E and T_{pk} are parameters in the least squares fit. Note that the left and right sides of the peak have different widths, set by parameters D and E. The desorption branch peaks were more asymmetric, so a different functional form was used for the right side of the peak:

$$\begin{aligned} A + BT + \frac{C}{1 + D(T - T_{pk})^2} \qquad & T < T_{pk} \\ A + BT + \frac{C}{1 + E(T - T_{pk})^{3/2}} \qquad & T > T_{pk} \end{aligned} \tag{5.5}$$

. Again, A through E and T_{pk} were chosen to minimize the sum of the squared errors. Several different simple fitting functions were tried, but these best matched the shapes of the peaks with the smallest number of adjustable parameters. Parameters A and B were then used to subtract the linear background from

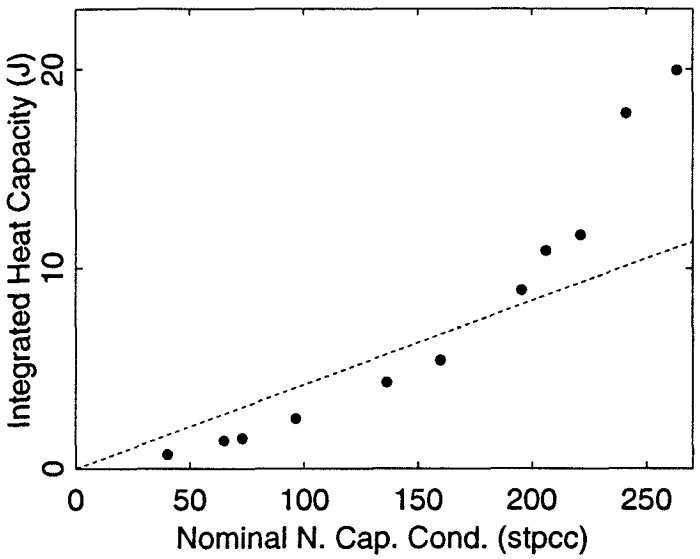

Figure 5.30: Integrated specific heat for films on the desorption branch plotted against the distance between the branches in the isotherm, approximately the amount capillary condensed.

the peaks, the results are plotted in figure 5.27 (adsorption branch) and figure 5.28 (desorption branch). Then, the area under these peaks was computed with a trapezoidal approximation. Figure 5.29 shows the integrated heat capacity for films both on the adsorption and desorption branches versus the total number adsorbed. Also shown are lines whose slope (0.042 J/STPCC) corresponds to the bulk latent heat, stepped one layer apart. The slope of the curves for the higher coverage data is near to the bulk value on both branches, indicating that the growth of the uniform film is virtually stopped when the capillary condensate begins to form. Two theoretical studies of adsorbed films coexisting with capillary condensate [96, 97] agree with this conclusion. At high coverages, the latent heat suggests that the system consists of three to 3.5 layers of uniform film coexisting with capillary condensate. Note that even though the desorption branch peaks are much taller and narrower than those on the adsorption branch, the area under the peaks are similar for the same amount adsorbed, at the higher coverages. The peak heights and widths are probably related to the size and geometry of the pores in which the capillary condensate resides. This is likely to be different for films on different branches, but the latent heat of the capillary condensate should be approximately the same.

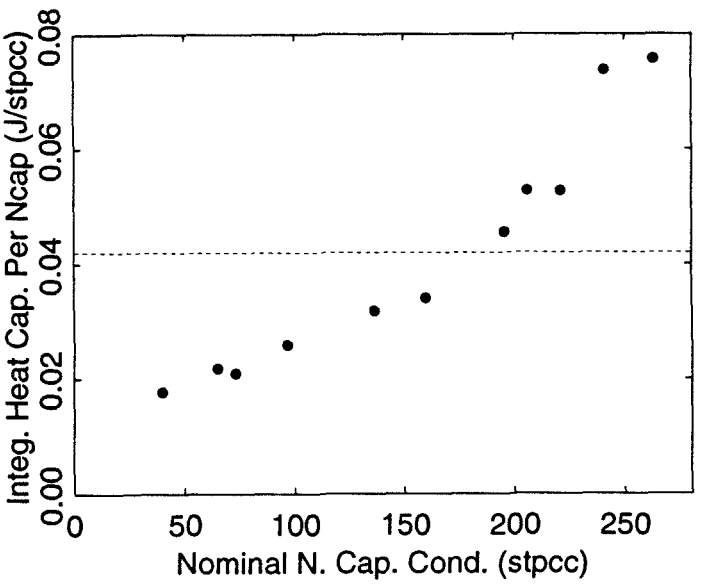

Figure 5.31: Integrated heat capacity divided by the distance between the branches in the isotherm at 95 K, plotted versus this distance. The vertical scale indicates the latent heat per molecule for films less than three layers thick.

Figure 5.30 shows the integrated heat capacity of the desorption branch plotted versus the difference in coverage between the two isotherms (shown in figure 5.8). The dashed line represents the bulk latent heat. The distance between the upper and lower branches of the hysteresis loop would indicate the amount capillary condensed if the only instance of capillary condensate were the excess matter on the desorption branch. This is likely to be true for about the first three layers adsorbed, since the triple point heat capacity peak appears at about three layers adsorbed on the adsorption branch. The fact that the points rise above that value proves that capillary condensation also occurs on the adsorption branch (since the latent heat of the capillary condensate is not likely to be above the bulk value). The points rise above the bulk value approximately at the coverage where the triple point peak appears on the adsorption branch. It was shown clearly that capillary condensation may be present on the adsorption branch of vapor pressure isotherms by the classic experiment by Carmen and Raal [29] in 1951. The low coverage portion of the desorption branch has a smaller slope and hence a lower latent heat, possibly because of size effects (it arises from condensate in small pores).

If it is assumed that the distance between the upper and lower branches of the

hysteresis curve indicates the amount capillary condensed, likely true for less than three layers adsorbed, then it is possible to compute the latent heat per molecule of the capillary condensate (figure 5.31). The latent heat per molecule is roughly half the bulk value and may or may not limit to zero when the amount capillary condensed goes to zero.

There was another study of the heat capacity of capillary condensed matter during melting by A.A. Antoniou [102], in 1964. This study of a porous glass substrate saturated with water found that the latent heat of the melting peak was consistent with approximately three monolayers of water of adsorbed films coexisting with capillary condensate. It is surprising that this agrees with our finding of three to 3.5 monolayers with capillary condensate, considering that the substrates, adsorbates and temperatures are so different. Along with heat capacity measurements, Antoniou also simultaneously measured the length change of the porous glass. From these measurements he concluded that the properties of the adsorbed water in the 30 Å pores are far different from those of bulk water. In this case, the latent heat of the capillary condensed water is likely to be far from the bulk value, especially when one considers that the pore size of the porous glass studied was so small. Calculations have shown that the surface tension of capillary condensed matter is significantly different from the bulk value for pores smaller than 100 Å [103, page 153].

Because our study varies the amount adsorbed (Antoniou only studied saturated systems), the latent heat per molecule of the capillary condensed matter can be measured with more certainty because the contribution from the adsorbed film can be subtracted off. For 30 Å pores, the latent heat of the capillary condensed methane would be noticeably smaller than the bulk. The pore size distribution of the samples used by Antoniou was peaked at about 30 Å, whereas the Grafoil pore size distribution is not well known, but should include pores from ten to several thousand angstroms. The cylindrical vapor-bulk interface radius of our thicker films is on the order of several hundred angstroms, so the capillary condensed methane is more likely to take on bulk values, as shown by the latent heat for the thicker films.

The previous discussion is almost overwhelming evidence in favor of naming capillary condensation as the cause of the vapor pressure hysteresis. The data in this work agree very well with the x-ray scattering data of capillary condensation of xenon on graphite foam and Grafoil [46], and the thermodynamic data from this study may help to determine the properties of capillary condensed matter, as

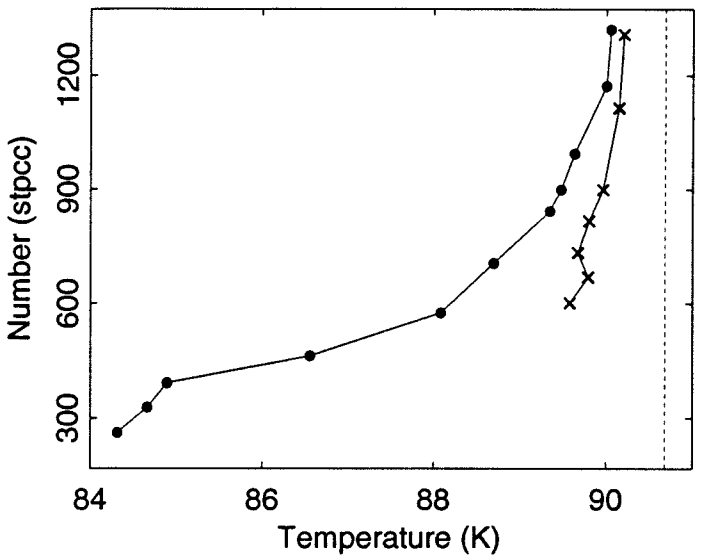

Figure 5.32: Peak temperature vs. number adsorbed; circles are on desorption branch, crosses are on adsorption branch.

will be seen in the following discussion.

When the number adsorbed versus temperature phase diagram (figure 5.15) is expanded to show only the triple point peaks (figure 5.32), it is clear that the curves for the data on the two branches do not overlay. But when the $\mu - \mu_o$ versus T phase diagram is expanded in figure 5.33, the curves for the data on both branches nearly overlap and form a straight line that intersects the bulk triple point. If the peak comes from the melting of capillary condensed bulk, then this line should extrapolate to the bulk triple point[9] as $\mu - \mu_o$ approaches zero (more support for the capillary condensation hypothesis). Prior to collecting the data, a model was created that predicted these results.

Melting Curve Model

A theoretical value for the melting temperature of capillary condensed matter was put forth by Defay and Prigogine [104, page 252], and rederived and extended to

[9]The highest coverage point on the adsorption branch in figure 5.32 was made to examine the triple point peak for very thick films. Other studies [37] have used the position of the triple point peak for very thick films (~20 layers) to calibrate thermometers to the bulk triple point, whereas in this study the thermometers were calibrated with a bulk methane sample. It is clear that an independent thermometer calibration is far superior since there is a measurable shift in the melting peak maximum temperature from the bulk triple point in even the thickest run.

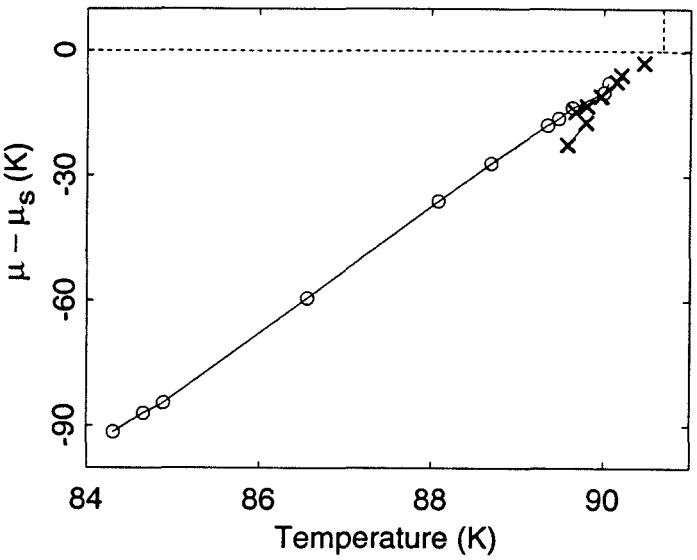

Figure 5.33: Peak temperature vs. $\mu - \mu_s$; circles are on desorption branch, crosses are on adsorption branch.

take into account partial wetting by Goodstein (see appendix C). The melting temperature shift from the bulk triple point is given as a function of the chemical potential in equation C.3. Figure 5.33 shows that T_m is linear over the range studied, in agreement with the theory.

The theory also explains why the data on both branches overlap. In the theory, there is no difference between the film on either branch, since the melting temperature is controlled by the chemical potential alone. Another way to look at this explanation is that the Kelvin equation (equation C.1) states that the radius of curvature of the condensate-vapor interface is related to the chemical potential of the film. Then the melting temperature of the condensate is controlled by the radius of curvature of the interface, and therefore set by the size of the pore that contains the condensate and the contact angle of the condensate with the pore wall. Then the melting temperature depression is the same for capillary condensate in a certain size pore independent of whether it is on the adsorption or desorption branch.

Despite its success, one questions whether the assumptions that lead to this theory are valid. Let us consider each assumption in turn:

- **The solid forms a perfect circular meniscus.**
  Crystalline solids form a faceted interface with the liquid or vapor unless

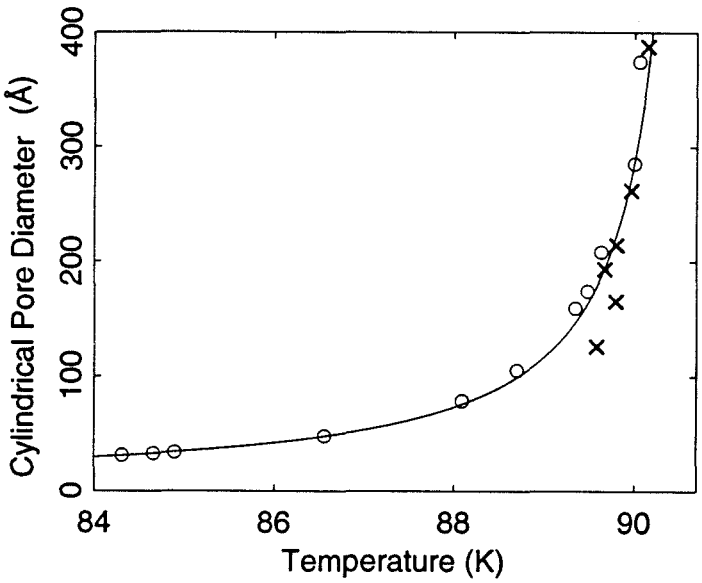

Figure 5.34: Cylindrical pore diameter as calculated with the Kelvin equation versus the heat capacity peak temperature for films on the desorption branch (circles) and adsorption branch (crosses). The line is the prediction of equation C.3.

the temperature is above the "roughening transition" temperature. The roughening transition is the temperature where an infinite number of steps on the surface occur [34, page 33]. The roughening transition was first predicted by Burton, Cabrera and Frank [105], and has been observed with a variety of experimental techniques [106, 107, 108, 109]. There is reason to believe that there is a roughening transition in bulk methane near 75 K from Hamilton's data [34] (as well as from the data from this study). At the roughening temperature, the sharp corners on the crystals become rounded, and as the temperature increases, the facets disappear completely. There is likely to be a different roughening temperature for each crystal face. It is uncertain whether all the crystal faces of methane that are exposed will be thoroughly rounded just below the triple point. If this assumption is not true, then the melting curve may still be a straight line, but instead of the solid surface tension, the melting curve will be a function of σ_s/r_s, where r_s is an effective radius [104, page 253]. The effective radius of curvature of the interface would depend on the contact angle and the exact geometry of the rounded facets that make up the interface. Since the solid interface may vary from pore to pore, each pore

may have a different melting curve. Also, the heat capacity peak may broaden.

- **The film has negligible thickness.**
  Figure 5.34 shows the cylindrical pore diameter as calculated from the Kelvin equation (equation C.1), using $v_s = 54.5$ Å^3 (specific volume of the solid)[110], and $\sigma_s \sim \sigma_l = 13$K/Å^2. The pore size for the slit-shaped pores (which are likely to be present in Grafoam) is twice that for cylinders for the same vapor pressure depression [96]. Then, the condensate-vapor interface diameter is from 50 to 200 Å, where the adsorption and desorption branch data overlap. The uniform film thickness is always less than four layers , or 14 Å, so it is reasonable to assume that the film has negligible thickness.

- **The Kelvin equation is valid for the pore size used and the solid and liquid surface tensions are independent of the pore size.**
  As stated by Gregg and Sing [103, page 153], for very small pores ($\sim$ 10 Å), the surface tension and molar volume deviate considerably from the bulk values, and the Kelvin equation becomes meaningless. When the meniscus is formed by only a few molecules, the continuum model that is used to derive the Kelvin equation breaks down. Calculations of size effects on the surface tension [111] find that the surface tension of matter with a (cylindrical) condensate-vapor interface radius of 100 Å is about 10% higher than the bulk value. Where the adsorption and desorption branch data overlap, the interfacial radius is between 50 and 200 Å (for slit shaped pores). Therefore, this effect is not likely to be very large. Also, the surface tensions of the solid and liquid phases should be shifted by roughly the same amount, so the melting curve is likely to be linear, especially in the larger pores. Then, the model will still predict the correct ratio of the surface tensions.

  As seen in figure 5.31 and 5.34, the latent heat of melting of the capillary condensate begins to reduce for pores less than 100 Å (cylindrical pore radius) or total amount adsorbed less than three layers on the desorption branch. For pores on the order of 20 Å, the latent heat is about half the bulk value. If the latent heat is so far below the bulk value, the other properties of the condensate are also likely to be different from the bulk.

It is surprising that the melting curve is linear when the condensate is in pores significantly smaller than 100 Å.

- **The value of $\mu_s - \mu_l$ can be approximated at the melting temperature with a linear extrapolation of the properties at the triple point.**
  This is equal to the approximation $\mu_s - \mu_l = L(T - T_3)/T_3$, which is just a linear extrapolation of the bulk phase boundaries in the μ – T plane using the slopes at the triple point. By examining the curvature of the bulk solid and liquid vapor pressure curves it can be seen that this approximation is at most in error by 6% at the lowest part of the melting curve (84 K).

- **The pores have parallel walls, for example, slits or cylinders.**
  The shape of the pores in Grafoam is not well known. There is some evidence to indicate that there may be some platlets that do not separate as far as others when the graphite crystals are exfoliated [46]. There must also be wedge shaped pores where the platelets meet. It is not obvious whether the pore geometry will alter the melting curve, and if the melting temperature for matter in a wedge-shaped pore depends on the wedge angle. Because there is pronounced hysteresis in the vapor pressure isotherm, there must be a significant number of pores that are parallel plates or bottle-shaped.

- **The matter in each pore is characterized by the vapor-condensate interface shape alone.**
  The shape of the interface between the condensate and its vapor determines the vapor pressure through the Kelvin equation (equation C.1). Then the shape of the pore governs the interface shape, but otherwise should not affect the melting temperature or other properties. However, for tapered pores (which are expected in the Grafoam), there must be finite size effects for matter that is deep inside the pores. The finite size effects could broaden the heat capacity peaks, and may explain why the latent heat is lower in the smaller pores while the melting curve is still a straight line. It is possible that the pore shape controls the orientation of the crystalline capillary condensate, and therefore sets which crystal faces are exposed if the interface has not completely roughened. It is very

difficult to determine how a certain pore shape can affect the properties of the condensate, and since the pore structure of the Grafoam is not well known, it is even harder to attempt to explain how these effects can change the data.

- **The contact angle between the condensate and the pore wall is constant with respect to changes in temperature and the adsorbed film thickness.** The presence of an adsorbed film can affect the contact angle of the solid or liquid condensate [112], and the surface tensions are expected to be changing slightly with temperature. For thin adsorbed films, this effect may change rapidly as a function of the density of the uppermost layer of the film, or if a phase transition occurs in the film (melting, for example). Most likely, the solid and liquid condensate contact angles are constant as the temperature changes, and the liquid wets the pore wall. There is evidence that methane films form at least eight uniform layers on the surface [5], but it is not certain if methane wets graphite macroscopically (equivalent to the contact angle being zero).

Besides explaining why the melting curve is a linear function of the chemical potential, and why the adsorption and desorption branch data have the same melting curve, the model could be used to predict the ratio of the liquid-gas surface tension to the solid-gas surface tension for methane if the contact angles were known. Since these are not known at this time, the possibilities will be examined. The slope of the melting curve in figure 5.33 indicates that

$$\frac{\sigma_{lg}\cos\theta_l}{\sigma_{sg}\cos\theta_s} = 1.01 \pm .01$$

if surface melting does not occur. This result has several consequences, depending on the values of θ_s and θ_l :

- If the liquid and solid capillary condensate both wet the pore wall, then $\theta_s = \theta_l = 0$ and $\sigma_{lg}/\sigma_{sg} = 1.01 \pm .01$. This result would be surprising because it is generally thought that the solid-vapor surface tension is slightly larger than the liquid-vapor surface tension.

- If the solid wets the pore wall but the liquid does not, then $\sigma_{lg}/\sigma_{sg} < 1.01 \pm .01$.

- Likewise if the liquid wets the pore wall but the solid does not, then $\sigma_{lg}/\sigma_{sg} > 1.01 \pm .01$.

- Nothing can be said about the surface tensions if neither solid nor liquid wet the pore wall and the contact angles are not known.

The phenomenon of surface melting is currently of great interest. A crystal that undergoes surface melting forms a liquid layer on the surface below the triple point temperature. As the temperature approaches the triple point, the liquid layer thickness increases until the entire crystal has melted. The condition for surface melting to occur is that $\sigma_{sl} + \sigma_{lg} \leq \sigma_{sg}$. Equation C.3 should hold true for surface melted capillary condensate when the liquid layer is thick, as discussed in appendix C, with σ_{sg} replaced by $\sigma_{sl} + \sigma_{lg}$. If methane capillary condensate undergoes surface melting, then our data suggest that

$$\frac{\sigma_{lg}\cos\theta_l}{(\sigma_{sl} + \sigma_{lg})\cos\theta_s} = 1.01 \pm .01.$$

Then, if surface melting does occur, several predictions are possible, depending on whether the solid and/or liquid wets the pore wall.

- If both the solid and liquid condensate wet the pore wall, then $\sigma_{lg}/((\sigma_{sl} + \sigma_{lg})) = 1.01 \pm .01$. Since surface tensions must be positive, nonzero numbers, this situation is not possible if surface melting occurs.

- If the solid wets the pore wall, but the liquid does not, then $\sigma_{lg}/(\sigma_{sl} + \sigma_{lg}) > 1.01 \pm .01$. Again, this is not possible.

- If the liquid wets the pore wall, but the solid does not, then $\sigma_{lg}/(\sigma_{sl} + \sigma_{lg}) < 1.01 \pm .01$, which is completely possible. It can be shown that this inequality simplifies to the trivial statement that the solid-liquid surface tension is greater than zero.

- If neither solid nor liquid wets the pore wall, then the contact angles determine whether surface melting is consistent with the data: $\cos\theta_l/\cos\theta_s \geq 1.01 \pm .01$.

It is expected that the liquid capillary condensate wets the pore wall, and there is some evidence to indicate that the solid does not wet. Inaba and Hess [5] indicate that the solid layer thickness may be limited to less than eight to

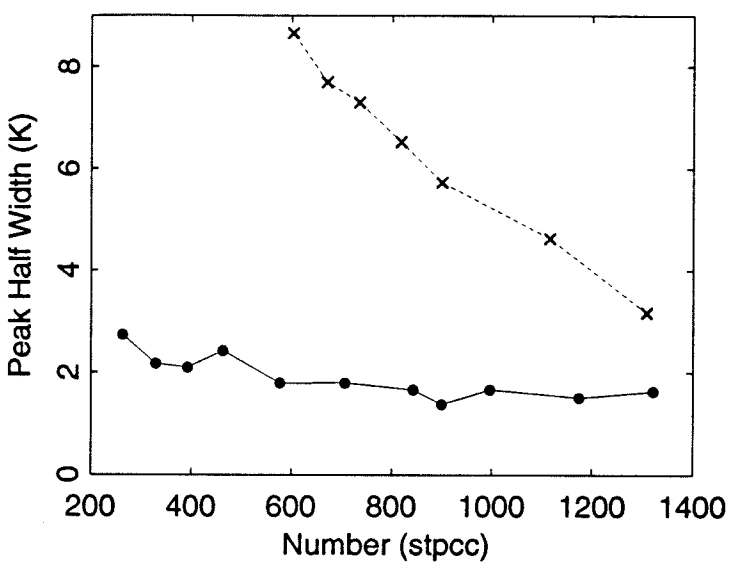

Figure 5.35: Full width at half maximum for the peaks on the adsorption branch (crosses) and on the desorption branch (circles) as a function of the total amount adsorbed.

11 layers for methane on flat graphite substrates, and also imply that the liquid forms very thick films. If their result is true, the data make two predictions:

- If bulk surface melting does not occur:
  The liquid-vapor surface tension is larger than the solid-vapor surface tension ($\sigma_{lg}/\sigma_{sg} > 1.01 \pm .01$).

- If bulk surface melting does occur:
  Then our data indicate that the solid-liquid surface tension is greater than or equal to zero (trivially).

Fortunately, there is more information in the heat capacity peaks near the triple point than just the peak locations.

Triple Point Peak Width

The capillary condensation melting peaks in figures 5.27 (adsorption branch) and 5.27 (desorption branch) are several degrees wide. If the capillary condensate is bulk matter whose vapor pressure is shifted by the curvature of the interface, and surface melting does not occur, then our model predicts that the heat capacity peaks should be very narrow. This is clearly not the case: these peaks are far

wider than the first layer melting peaks, for instance. Furthermore, the adsorption branch peaks are far wider than those on the desorption branch, and the adsorption branch peaks are far more asymmetric. Figure 5.35 shows the full width at half maximum for both branches. Note that the width of the desorption branch peaks remain relatively constant, while the adsorption branch peaks become narrower for thinner films. The width of the peaks on both branches is wider than the scatter in the peak temperature versus $\mu - \mu_o$ plot (figure 5.33).

Typical heat capacity peaks for first order phase transitions are delta functions, if taken at constant chemical potential, or mesa-shaped, if the path travels through the coexistence region over a finite temperature interval. In the latter case, while the peaks pass through the coexistence region, the system state travels along the melting curve in the $\mu - T$ plane. However, this cannot explain the broadness of the heat capacity peaks because the system state, as shown in figure 5.17, crosses the melting line at a finite angle. The path in the $\mu - T$ plane would need to follow the melting curve for several degrees in order to explain the width of the peaks. (However, there are weak features on the desorption branch pressure data that will be discussed below.) Two types of effects can cause the peaks to broaden. Some effects may shift the melting temperatures of each pore relative to the ideal melting curve, $T_m(\mu)$ (equation C.3), so that even if each pore melts at one temperature, the pores in the entire sample of Grafoam melt at different temperatures. Other effects may cause the capillary condensate in each pore to melt over a range of temperatures, so that the heat capacity peak from each pore is wide. In either case, it is surprising that there is a linear relationship between the temperature at the maxima of the wide heat capacity peaks and $\mu - \mu_o$.

Another unexpected feature that is common to all of the thick film studies is that the heat capacity is significantly greater than the film's background heat capacity above the triple point temperature. This means that some of the matter in the condensate melts above the triple point temperature. It is possible that the substrate causes the matter closest to it to melt above the triple point. The first layer melting discussed in section 5.3.2 occurs at 110 K, 20 K above the triple point. The layers close to the substrate in the capillary condensate may melt above T_3. This phenomenon is called "substrate freezing," and is analogous to surface melting [36]. Unfortunately, the formation of capillary condensate prevents us from forming thick enough films to study this effect in the uniform films. If substrate freezing occurs, there is a relationship between the surface tensions: $\sigma_{l\omega} \geq \sigma_{s\omega} + \sigma_{ls}$, where ω represents the substrate (wall). Likewise, if surface

freezing does not occur, then $\sigma_{l\omega} < \sigma_{s\omega} + \sigma_{ls}$.

Also, there exists a simple relationship between the contact angle of a condensed phase on a solid surface in equilibrium with vapor and the surface tensions (when the condensed phase does not wet the surface): $\sigma_{ig}\cos\theta_i = \sigma_{g\omega} - \sigma_{i\omega}$, or $\sigma_{ig} > \sigma_{g\omega} - \sigma_{i\omega}$ when phase i does not wet the surface [113, page 532], where i is l (liquid) or s (solid), g represents the vapor, and ω the solid surface (wall). When the condensed phase wets the surface, this equation becomes: $\sigma_{ig} \leq \sigma_{g\omega} - \sigma_{i\omega}$.

Then there are sixteen possible "states" that the system can have near the melting transition, depending on whether surface melting and/or substrate freezing occur, and whether the liquid and/or solid wet the pore walls. For each state, there are four equations that must be satisfied by the surface tensions:

- If substrate freezing occurs: $\sigma_{l\omega} \geq \sigma_{s\omega} + \sigma_{ls}$
  If substrate freezing does not occur: $\sigma_{l\omega} < \sigma_{s\omega} + \sigma_{ls}$

- If surface melting occurs: $\sigma_{sg} \geq \sigma_{ls} + \sigma_{lg}$
  If surface melting does not occur: $\sigma_{sg} < \sigma_{ls} + \sigma_{lg}$

- If the solid wets the pore wall: $\sigma_{sg} \leq \sigma_{g\omega} - \sigma_{s\omega}$
  If the solid does not wet the pore wall: $\sigma_{sg}\cos\theta_s = \sigma_{g\omega} - \sigma_{s\omega}$
  or $\sigma_{sg} > \sigma_{g\omega} - \sigma_{s\omega}$

- If the liquid wets the pore wall: $\sigma_{sg} \leq \sigma_{g\omega} - \sigma_{s\omega}$
  If the liquid does not wet the pore wall: $\sigma_{lg}\cos\theta_l = \sigma_{g\omega} - \sigma_{l\omega}$
  or $\sigma_{lg} > \sigma_{g\omega} - \sigma_{l\omega}$.

It can easily be shown that these inequalities cannot be satisfied simultaneously for two of the sixteen states, if the surface tensions are assumed to be constant over the entire temperature range of interest. When substrate freezing but not surface melting occurs while the liquid wets the pore wall and the solid does not, the inequalities cannot be satisfied. Likewise, when surface melting but not substrate freezing occurs while the solid wets the pore wall and the liquid does not, the inequalities cannot be satisfied.

Using the melting curve model, it was shown above that the slope of the melting curve gives us a relationship between the liquid-gas and solid-liquid surface tensions, when surface melting occurs and the solid wets the pore wall:

$$\frac{\sigma_{lg}}{\sigma_{sl} + \sigma_{lg}} > 1.01 \pm .01.$$

This equation states that the solid-liquid interface surface tension must be negative or zero. Since this surface tension must be greater than zero, four of the sixteen states are not allowed.

If it is assumed that both the solid and the liquid do not wet the substrate, and all the surface tensions are constant over our temperature range (84 to 92 K), then two equalities are true: $\sigma_{ig}\cos\theta_i = \sigma_{g\omega} - \sigma_{i\omega}$ with $i = l$ and s. It is possible to eliminate $\sigma_{g\omega}$ from the above equations: $\sigma_{lg}\cos\theta_l + \sigma_{l\omega} = \sigma_{sg}\cos\theta_s + \sigma_{s\omega}$. Including the above relationship in the condition for substrate freezing to eliminate $\sigma_{l\omega}$ gives: $\sigma_{lg}\cos\theta_l + \sigma_{ls} \leq \sigma_{sg}\cos\theta_s$. Dividing this relationship by $\sigma_{sg}\cos\theta_s$ gives

$$\frac{\sigma_{lg}\cos\theta_l}{\sigma_{sg}\cos\theta_s} + \sigma_{ls} \leq 1. \tag{5.6}$$

Using the melting curve model, it was shown above that the slope of the melting curve gives us a relationship between the liquid-gas and solid-gas surface tensions and contact angles, when surface melting does not occur and neither phase wets the pore wall: $\sigma_{lg}\cos\theta_l/(\sigma_{sg}\cos\theta_s) = 1.01 \pm .01$. Inserting this value into equation 5.6 yields:

$$(.01 \pm .01)\sigma_{sg}\cos\theta_s + \sigma_{ls} \leq 0.$$

Since σ_{ls} should be positive, the data indicate that the system cannot undergo substrate freezing without also surface melting when neither phase wets.

The above information is combined into table 5.1. This table shows that only certain possibilities agree with the relationships between the surface tensions and the melting curve when combined with the model.

The most significant feature of the table is that if substrate freezing occurs, as implied by the fact that the heat capacity is above the background when the temperature is above the triple point, and if the solid does not wet the pore wall (macroscopically) as implied by Inaba and Hess [5], then surface melting must also occur. Surface melting also would explain the broadness and asymmetry of the heat capacity peaks. If the bulk matter in the pore forms a thin layer of liquid at low temperature, then melts by increasing the thickness of this layer, then the heat capacity peaks would be broad, smoothly rising at low temperatures, but falling off sharply near the triple point.

The depth of the capillary condensate in the pore could control the peak width if surface melting was present. A certain amount of capillary condensed matter inside a porous substrate can exist at different locations within the pores. For

Substrate Freezing	Solid Wets	Liquid Wets	Surface Melting	Allowed?
Yes	Yes	Yes	No	Allowed
Yes	Yes	Yes	Yes	Prohibited
Yes	Yes	No	No	Allowed
Yes	Yes	No	Yes	Prohibited
Yes	No	Yes	No	Prohibited
Yes	No	Yes	Yes	Allowed
Yes	No	No	No	Prohibited
Yes	No	No	Yes	Allowed
No	Yes	Yes	No	Allowed
No	Yes	Yes	Yes	Prohibited
No	Yes	No	No	Allowed
No	Yes	No	Yes	Prohibited
No	No	Yes	No	Allowed
No	No	Yes	Yes	Allowed
No	No	No	No	Allowed
No	No	No	Yes	Allowed

Table 5.1: Possibilities for wetting, surface melting, and substrate freezing by the capillary condensate that are allowed by the relationships between the surface tensions and consistent with the slope of the melting curve and model.

example, for the same bulk-vapor interface radius, a certain amount of matter can be located in a small number of deep pores, or it can be situated in a larger number of shallow pores. Depending on the physical effect that explains the peak widths, the depth of the pore that encloses the capillary condensate could change the size and shape of the heat capacity peaks. For example, if surface melting is present, the matter in shallow pores will melt at lower temperatures because more matter is located close to the vapor-bulk interface. To test such a hypothesis, a theory of surface melting would need to be combined with a knowledge of the pores' sizes and shapes, and a model for the vapor pressure hysteresis.

The adsorption branch peaks become narrower with an increasing amount adsorbed (figure 5.35), but the peak width on the desorption branch is relatively constant. It is not clear how, but the geometry of the confined condensate on the desorption branch could change the nature of surface melting.

There may be other evidence to support the surface melting of capillary condensate. Bienfait et al. [48] have measured the mobility of methane films on graphite using quasi-elastic neutron diffraction. Their results were analysed with-

out including the possibility of capillary condensation. They concluded that the methane films undergo surface melting. Since the matter in their study was most likely capillary condensed, their study may indicate that the capillary condensate may undergo surface melting. Their result was dependent on the model used to fit the measured line-shapes, so it may be necessary for the data to be reanalysed to test this prediction.

Nenow and Trayanov consider the surface melting of curved interfaces, including a "positively" curved crystallite and a "negatively" curved spherical hole within a crystal [114]. They find that the quasi-liquid thickness is greater on a negative crystal, compared to the flat interface. Similarly, the quasi-liquid thickness is smaller on a positive crystal. Therefore, if our capillary condensed bulk undergoes surface melting, it should occur at lower temperatures than on flat surfaces. This may explain the broadness of the heat capacity peaks. Also, their model depends on the value of a quantity called the "disjoining pressure," a function of the quasi-liquid layer thickness that is very sensitive to the nature of the interatomic forces. Then, it is difficult to obtain a prediction about the width of the capillary condensate melting peaks, because it is not trivial to calculate the exact value of the disjoining pressure. However, no matter what the value is for the disjoining pressure, the the condition for surface melting to occur is still $\sigma_{sl} + \sigma_{lg} \leq \sigma_{sg}$.

If surface melting does not occur, there are still other possible causes for the heat capacity peak width. If the solid condensate is not far enough above the roughening temperature, or if the solid does not roughen, each pore will display a unique interface shape made of different crystal faces, each with its own surface tension. Each pore will melt according to equation C.3, but with a unique condensate-vapor interface shape, radius of curvature and surface tension. The melting curve of each pore will be different, but the sum of the heat capacities of all the pores may still follow equation C.3. However, all heat capacity measurements of the melting of matter in porous substrates have measured broad peaks [102, 115, 38, 116, 117]. Since the roughening transition temperature is universally about $.8T_3$, is it possible that there is still some remnant of the facets at the triple point for all the measurements? This explanation seems unlikely.

Another effect that could similarly broaden the heat capacity peak for each pore was suggested by D. Goodstein [118]. This idea explains that the pores may have large openings (> 100 Å), but the inner recesses of the tapered pores in Grafoam may be very small. If a considerable amount of solid matter was

"strained" by being confined within these small spaces, the free energy of the solid condensate could be increased, and the melting temperature of some of the matter in the pore would be decreased and the peaks broadened.

Along with the heat capacity features near the triple point, there are wiggles in the $\mu - \mu_o$ versus temperature data, but only on the desorption branch. As stated above, for a first order phase transition, if the chemical potential is not held constant, the system state in the $\mu - T$ phase diagram should pass along the melting curve as the system goes through the coexistence region. Figure 5.36 shows the system path in the $\mu - T$ plane for the thicker films, near the triple point. There are no visible features on the adsorption branch data, but on the desorption branch, there is a gentle rise in $\mu - \mu_o$ near where the peak in the heat capacity occurs. The path does not change slope enough to follow the melting curve, and the feature is about as broad as the heat capacity peaks. Even thought the adsorption branch heat capacity peaks are considerably wider than the desorption branch peaks, there is sufficient resolution in the pressure measurement to see similar features in $\mu - \mu_o$ for the adsorption branch data, if they were present. The wiggles in $\mu - \mu_o$ on the desorption branch may be broadened by any of the reasons given to explain the width of the heat capacity peaks, but there is no simple explanation for why the features are absent in the adsorption branch data or why the heat capacity peaks on the adsorption branch are much wider than those on the desorption branch.

Another unusual feature present in the data is an unusually large amount of noise on the heat capacity data from the run with coverage just above the closure of the hysteresis loop on the desorption branch. Could there be fluctuations in the heat capacity similar to those observed near the critical point of the liquid-gas coexistence region? Time was not available to repeat this heat capacity scan since it required reforming the film by desorbing gas from a very thick film. Future studies conducted with this apparatus may clarify this result.

Given the recent results of Larese et al. [45] of argon on graphite, and the more detailed study by Morishige et al. [46] of xenon on graphite, it is not surprising to find capillary condensation in the methane-graphite system. Furthermore, these results are in close agreement with those of Morishige et al. The capillary condensate appears at about three layers adsorbed on the adsorption branch, and remains down to coverages just above a monolayer on the desorption branch. The latent heats of melting of the condensate are in agreement with the formation of three to 3.5 layers of uniform film with bulk-like capillary condensate when more

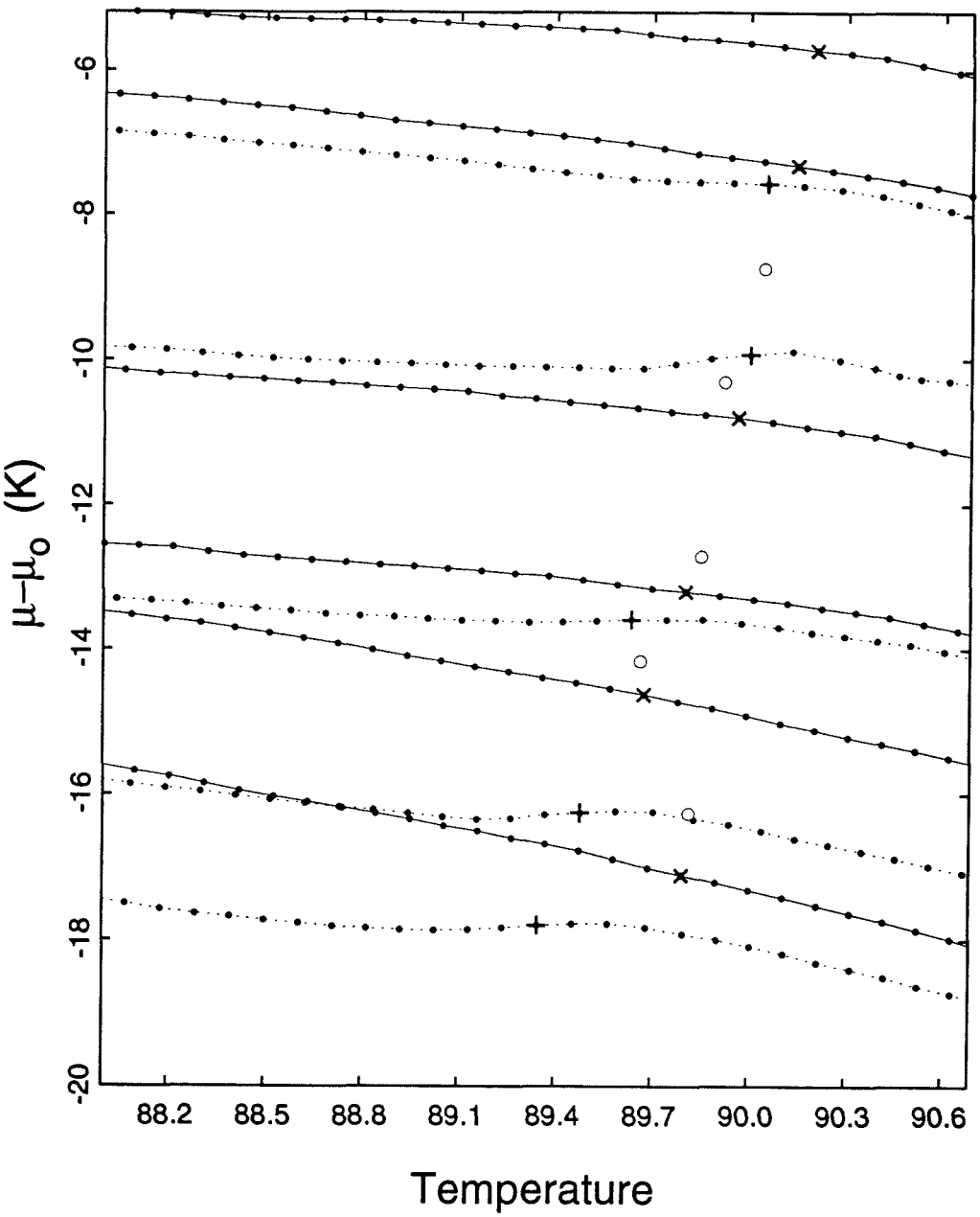

Figure 5.36: System state in the $(\mu - \mu_o)$ - T plane near the triple point for the thicker films. The solid curves are on the adsorption branch, the dashed curves are on the desorption branch. The symbols mark the maximum in the heat capacity. Crosses are on the desorption branch, "X" on the adsorption branch with the cryogenic cell valve open, circles on the adsorption branch with the cryogenic cell valve closed.

film is adsorbed. The heat capacity and vapor pressure data also reveal some interesting properties of the capillary condensate. For example, the latent heat of melting of the capillary condensate in very small pores is possibly as small as half the bulk value. The temperature of the maxima of the heat capacity curves are a linear function of $\mu - \mu_o$, in agreement with a simple model of melting in cylindrical pores. There is a noticeable contribution to the heat capacity peaks due to melting above the triple point, implying that substrate freezing occurs. If substrate freezing occurs, and the solid does not wet the substrate, then an analysis of the melting curve slope in the $(\mu - \mu_o) - T$ plane indicates that surface melting must also occur. Surface melting would explain the widths of the heat capacity peaks, but other explanations are possible if it does not occur.

Before discussing the low temperature peaks in the heat capacity data, it should be noted that when the locations of these peaks are plotted in the number adsorbed versus temperature plane, including the data on both the adsorption and desorption branch, the phase boundaries do not line up. These peaks must come from phase transitions in the uniform film, and the film thickness is modified by the presence of the capillary condensate. However, when the positions of both sets of the peaks were plotted in the μ - T plane (figure 5.37), the features line up together on the phase boundaries. The properties of the adsorbed film are clearly controlled by the chemical potential (pressure), independently of the amount capillary condensed. However, in the N vs. T phase diagram, the peaks on the adsorption branch occur at higher coverages, reflecting that the adsorbed film is thinner on the desorption branch because some of the methane is capillary condensed. When an N versus T phase diagram (figure 5.38) is made with N being the film thickness for points on the desorption branch reduced by the distance between the upper and lower boundary curves in figure 5.5 (N is unaltered on the adsorption branch), the phase boundaries again line up. There is no strong interaction between the capillary condensate and the adsorbed film. This may be our most important result regarding capillary condensation, because it says that it is still possible to study multilayer films, but the uniform film thickness may be changed by the amount capillary condensed. Accurate vapor pressure hysteresis curves at several temperatures are all that is needed to correct the coverage to find the thickness of the uniform film for coverages less than two or three layers. For thicker films, an independent measure of the amount capillary condensed on the adsorption branch is required.

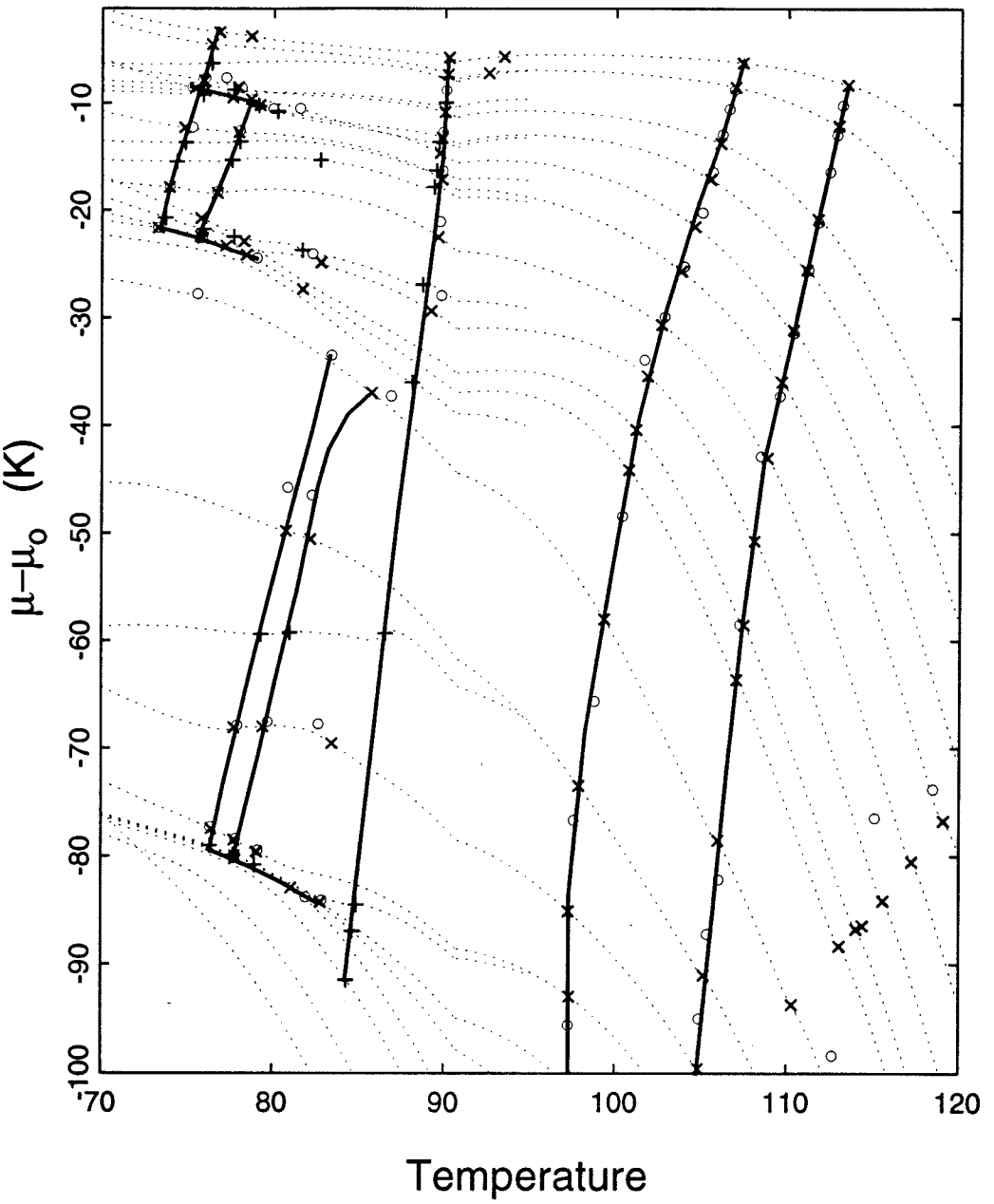

Figure 5.37: Locations of the peaks in the heat capacity in the $(\mu - \mu_o) - T$ plane for the higher coverages. Crosses are for data taken with the cryogenic valve open on the desorption branch, X on the adsorption branch with the valve open, and circles are for data taken with this valve closed. The dashed lines show the path travelled by the system as the system was warmed. Heavy lines connect similar peaks together to form phase boundaries.

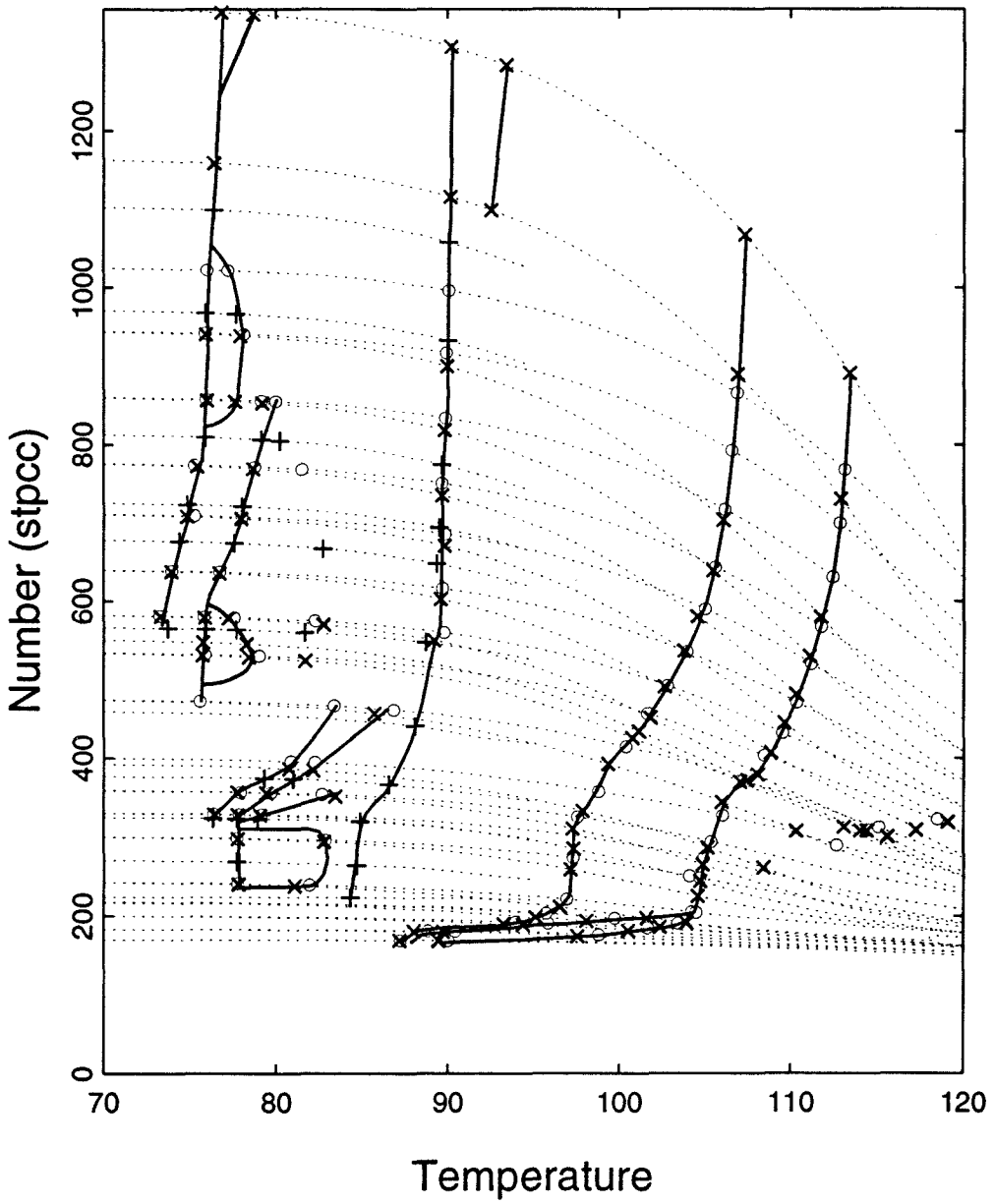

Figure 5.38: Locations of the peaks in the heat capacity in the number adsorbed versus temperature plane. The number for the points on the desorption branch (crosses) is reduced by the distance between the upper and lower boundary curves in figure 5.5. X denotes the location of peaks on the adsorption branch with the cryogenic valve open, and circles are for data taken with this valve closed.

5.3.5 Low Temperature Roughening/Layering Peaks

Hamilton [34] discovered a series of peaks in the heat capacity at temperatures between 75 and 80 K. These peaks were attributed to layer by layer condensation and the peaks' positions on an N vs. T phase diagram were presented [34, page 59]. Six blunt-nosed 2-D liquid-gas coexistence regions were shown, and the heat capacity peaks were thought to represent the experimental path passing out of these coexistence regions. In the limit of infinite film thickness, these phase transitions are said to become the bulk roughening transition. In thin films, the size of the steps in the roughened solid is limited by the substrate, but for very thick films, bulk behavior should be approximated.

The new data in the same coverage and temperature range show a much more detailed picture of these phase transitions. Figure 5.13 shows heat capacity peaks that locate at least seven distinct phase boundaries during second, third and fourth layer formation. In general, the phase diagram for each of these layers is very similar to the first layer phase diagram, and includes a 2-D liquid-gas coexistence region (as described by Hamilton) and a 2-D triple point.

Because the individual layers in a multilayer film interact with each other, it is not strictly correct to identify a phase boundary with a phase transition in any particular layer. But these phase transitions often occur only in a single layer, so it is convenient to associate the features with a layer in the film.

Heat capacity measurements are better than other techniques for locating phase boundaries, but not for identifying the phases before and after the transition. The tools we have at our disposal for identifying the nature of any particular phase transition are:

- The shape of the heat capacity peak. A very sharp peak may mark a first order phase transition such as melting, and a broad peak may come from passing through a liquid-vapor coexistence region or a higher order phase transition.

- The integrated area under the heat capacity curve (latent heat) indicates the change in entropy between the two phases. The change in the latent heat as a function of coverage can help identify the transition.

- The shape and size of each peak helps associate it with other peaks that appear similar but occur at different coverages.

- There are certain rules about how phase boundaries may connect with each other, or terminate. Melting, for example, is a first order phase transition that changes the symmetry of the solid, and therefore cannot end in a critical point [113, page 258].

These tools, combined with the experience gained from observations of other adsorbate/substrate systems, can help to identify phase transitions. However, it is important to remember that additional studies with different experimental techniques may be needed to completely describe the states of the film. Therefore most of our analysis is subject to revision. Theoretical and computational models of these multilayer films may also aid in solving the puzzle, especially where a phase transition may involve the interactions between layers.

It is certain that where these data see a heat capacity signal, a phase transition occurs, but at times the phase boundaries may be hidden because they are parallel to the experimental path, or because the heat capacity signals are too low and broad to be detected. Also, a first order phase transition is supposed to give a sharp heat capacity feature. If the experimental path is nearly tangent to a first order phase boundary, the heat capacity peak will be broad, and appear to be caused by a higher order phase transition.

The coverages mentioned in the discussion below are either the coverages on the adsorption branch, where there is less capillary condensation, or (for the desorption branch) the number adsorbed less the vertical distance between the branches on the vapor pressure isotherm. Therefore, all the coverages are relative to the total amount adsorbed on the adsorption branch, and not to the uniform film thickness, since there is a significant amount capillary condensed above three layers adsorbed on the adsorption branch. Unfortunately, we have no accurate way to measure the amount capillary condensed on the adsorption branch. Perhaps other experimental techniques (x-ray or neutron scattering) may be used to find this quantity in the future.

The amount adsorbed (layers) shown in figures 5.39, 5.41, and 5.42, below, is the total amount in the system during the heat capacity scan. Since the features in these figures occur at low temperature, when the vapor pressure is low, most of the gas in the system is adsorbed on the Grafoam. It is not possible to include the vapor pressure versus temperature data necessary to enable the reader to calculate the amount adsorbed on the curves in figures 5.39, 5.41, and 5.42. Figure 5.38 gives the amount adsorbed as a function of temperature for these curves, as well

as the locations of the peaks in the $N - T$ plane.

Second Layer Phase Diagram

Figure 5.39 shows the heat capacity signals associated with the second uniform layer. The scans are displayed with the lowest coverage at the bottom of the plot, so the topology of the N versus T phase diagram can be made by connecting the similar phase transitions to form the phase boundaries. Since, in the temperature range shown, the number in the first layer is relatively constant during second layer formation, the N versus T phase diagram is similar to the 2-D density versus temperature phase diagram for the second layer. However, figure 5.38 shows that the melting temperature of the first layer increases in the coverage range from about 200 to 500 STPCC. When the first layer is covered by the second (or more layers), the first layer melting temperature is a function of the first layer density, and a function of the energy necessary to promote a molecule into the other layers. Therefore the first layer density is increasing slightly in this coverage range. The first layer density can change the phase diagram of the second layer because the first layer is the "substrate" for the second layer.

Recall the N versus T phase diagram of the first layer of methane on graphite (figure 1.5) or the density versus temperature phase diagram for bulk matter (figure 1.4). There is a vapor-solid coexistence region at low temperatures that is separated from the vapor-liquid coexistence region by the triple point. At higher densities (coverages) there is no longer a vapor-bulk coexistence region, but there is a solid-liquid coexistence region. As the temperature increases, the heat capacity signals from passing through such a phase diagram at low coverage are first a sharp peak from the triple point, then a broad feature from passing through the liquid-vapor coexistence region. The end of the broad feature marks the boundary of the liquid-vapor coexistence region. If the scan passes exactly through the critical point of the liquid-vapor coexistence region, there should be a singularity in the heat capacity[10]. At the higher coverages, where the sample consists entirely of the condensed phase (not coexisting with gas), passing through the phase diagram at constant N should give a single mesa-shaped peak when the film goes through the solid-liquid coexistence region.

The second layer heat capacity peaks in figure 5.39 are labeled A through C.

[10]The singularity is very difficult to observe. It was not until 1963 that this signal was seen in bulk matter (by Voronel) [119, page 168].

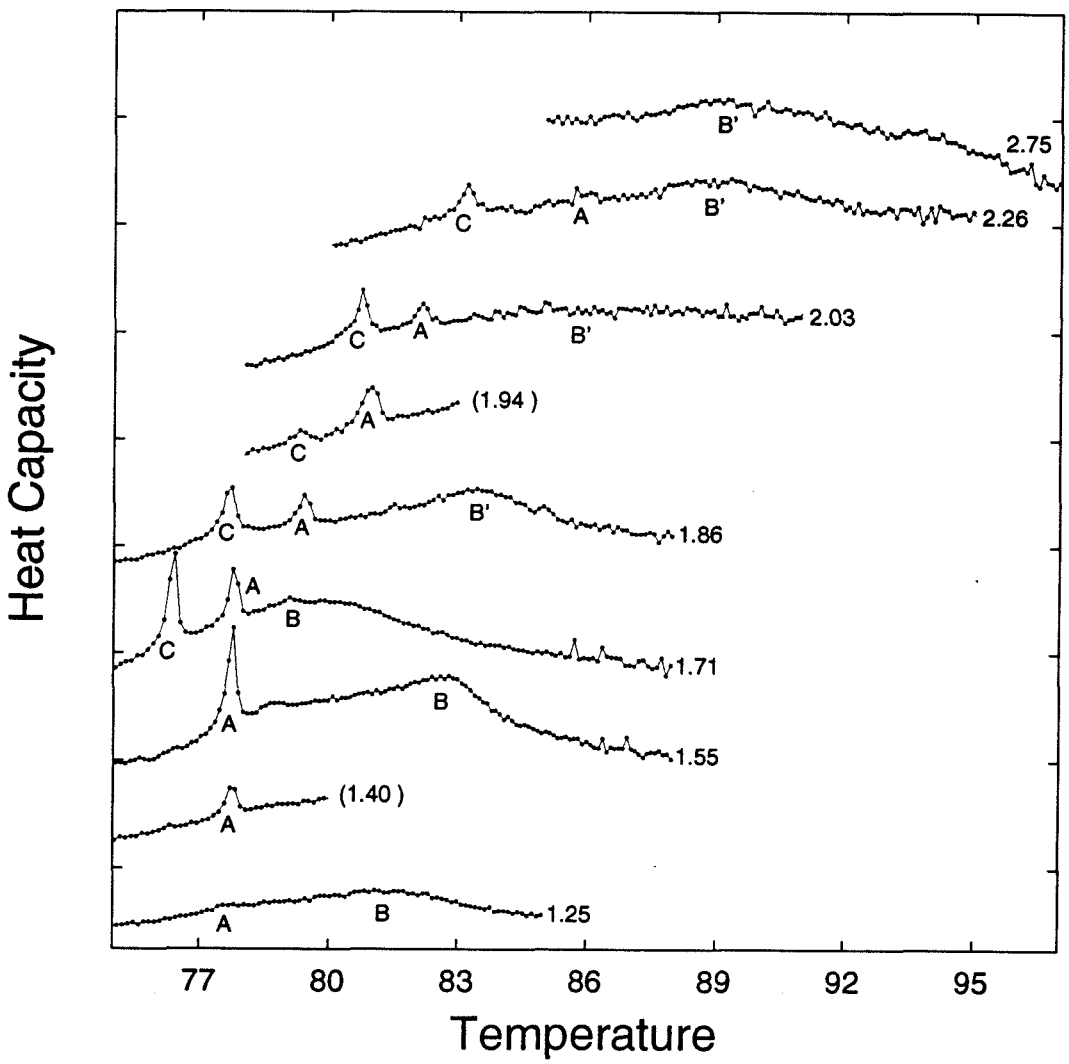

Figure 5.39: Heat capacity signals identified with the second layer. Numbers indicate the total amount (layers) in the system during the scan. Numbers enclosed in parentheses indicate desorption branch data whose coverage is reduced by the additional amount capillary condensed on that branch, relative to the adsorption branch. Letters identify heat capacity features for discussion in the text.

Heat capacity peak A is clearly identified as the second layer melting peak. In the three heat capacity runs, at 1.25, 1.40, 1.55 and 1.71 layers, this sharp peak rapidly increases in size, but appears at exactly the same temperature, the 2-D triple point for the second layer. This peak should increase in size at the same temperature as the coverage increases, until the 2-D condensed phase completes. Then there will be no more 2-D vapor phase and the melting peak should move to higher temperature. If there is a triple point, there should also be a liquid-vapor coexistence region and associated heat capacity peaks, labeled B in the figure. The location of peak B traces out a blunt-nosed phase boundary that seems to join with the melting peak near 1.71 layers. At this point another phase transition suddenly appears, peak C, below peak A in temperature. At higher coverages, peaks A and C move to higher temperatures at the same distance apart, about 2 K. Contrary to our expectation, at higher coverages (1.86), another peak (B') appears that is similar in shape to peak B, and at a temperature higher than peak A. At yet higher coverages, peaks A, B', and C move together to higher temperatures while peak B' broadens. Then peaks A and C seem to disappear suddenly at about 2.75 layers. Above this coverage, peak B' seems to disappear or become too low and broad to identify.

Examining the termination of peak B' on figure 5.13 shows that the capillary condensate triple point peak on the adsorption branch appears near where feature B' disappears. On the desorption branch, the triple point peak is very large and also near where peak B' terminates. It is unlikely that the phase boundary associated with peak B' ends on the capillary condensate melting curve, since the two systems (capillary condensate and uniform film) are likely to be decoupled. However, there is some evidence that there may be a slight difference between the uniform film heat capacity features on the adsorption branch and those on the desorption branch. The sizes and shapes of the peaks on the 1.94 layer run[11], on the desorption branch, in figure 5.39, are slightly different that those on the adsorption branch with coverages of 2.03 and 1.86 layers.

There are three unsolved problems in the second layer phase diagram.

- What is the phase transition causing peak C?

- What is the phase transition causing peak B'?

[11]Film thickness made approximately equal to that on the adsorption by subtracting the distance between the adsorption and desorption branch as a function of pressure.

- Why do peaks A, B', and C disappear at high temperature? What is the shape of the second layer phase diagram at higher coverages?

There have been two neutron scattering studies of multilayer methane on graphite done at the Brookhaven National Laboratory. All the data in the first study [47] were taken at low temperature, ($T \leq 50$ K), but the results are still interesting. They find that the monolayer lattice spacing is about 1% smaller than the bulk, in other words, the monolayer is more dense than the bulk. As the film is made thicker, the signal from a bilayer film that has the second layer incommensurate with the first appears. Thicker films have a trilayer structure (all the layers mutually commensurate) with nearly the bulk density. The results for thicker films are, unfortunately, questionable because the bulk signal was masked by the signal from the graphite, and therefore no bulk capillary condensate was observed (as noted by Morishige et al. [46]).

In a second study, Q. M. Zhang and J. Z. Larese [120] have recorded neutron scattering data for methane on graphite, and their data indicate a possible registry transition in the second layer. They state that the second layer is incommensurate with the first at low coverages, but as the coverage is increased there is a phase transition to a denser phase that has the second layer commensurate with the first. Feature B may be the heat capacity signal from this phase transition. At low temperature and high coverage, the layers are commensurate, and as the temperature is raised, the second layer becomes incommensurate with the first. This would explain why this phase transition appears near layer completion, when the 2-D vapor disappears. On the other hand, because the incommensurate-commensurate phase transition discovered by the neutron scattering study was supposed to have a nearly horizontal phase boundary in the N versus T plane, it may be invisible in the heat capacity data. Then, feature B would be caused by a different (unknown) phase transition.

Another (unpublished) plot from later data by Zhang and Larese examines the melting of the film at 2.2 layers. They show evidence of second layer melting beginning at 68 K, and finishing at 77 K. Our data in figure 5.39 show three features (A, B', and C) between 82 and 89 K at this coverage. Neutron scattering may show a much broader signal from melting because it is sensitive to the defects in the crystal structure of the 2-D solid that are likely to occur below the melting temperature. This is an example of how the data from several experimental methods must be carefully combined to map out these phase diagrams.

There are several possible explanations for the disappearance of each of the three peaks, A, B' and C.

1. A phase boundary may suddenly curve toward the horizontal in the N versus T plane and become invisible in the heat capacity data.

2. A phase boundary could end in a higher order phase transition that would be to hard to see with calorimetry.

3. Two or three of the phase boundaries may intersect to form closed regions of the phase diagram.

In the first case, the peaks would become too broad to distinguish from the noise in the data, but the peaks could reappear at a higher temperature at higher coverages, or end on another phase boundary (first layer melting, perhaps). This possibility is supported by the known example that the melting peak for the first layer of methane shoots upward thirty degrees in temperature just above layer completion. While it is shooting upward, the first layer melting peak becomes difficult to see with calorimetry, and was originally missed by several experimenters [8]. The location of the capillary condensate triple point peaks could easily mask peaks A and B. Note that a peak does appear in the highest coverage runs (6.0 and 7.0 layers) above the triple point peak, but its location on the phase diagram (figure 5.38) makes it unlikely to tie into either of the second layer peaks. This peak appears only a degree or so above the triple point, so the heat capacity signal from the second layer peaks should be measurable, because the phase boundary would not be horizontal in the N versus T plane. Therefore, there is no peak visible that is likely to connect with either A or C at higher coverages.

Could these phase boundaries simply end in a higher order phase transition? For example, if peak C is the signal from a phase transition between a second layer dense solid that is commensurate with the underlying first layer solid, to an expanded second layer solid that is incommensurate with the first layer, then the two phases on either side of peak C may have the same symmetry. In this case the phase boundary that causes peak C could end in a higher order (continuous) transition that would be very difficult to see in the heat capacity data. There are examples of first layer melting peaks disappearing at higher coverages, for example, CO on graphite [121].

Finally, the second layer N versus T phase diagram could include any of the three boundaries intersecting or crossing the others. Figure 5.40 shows six simple

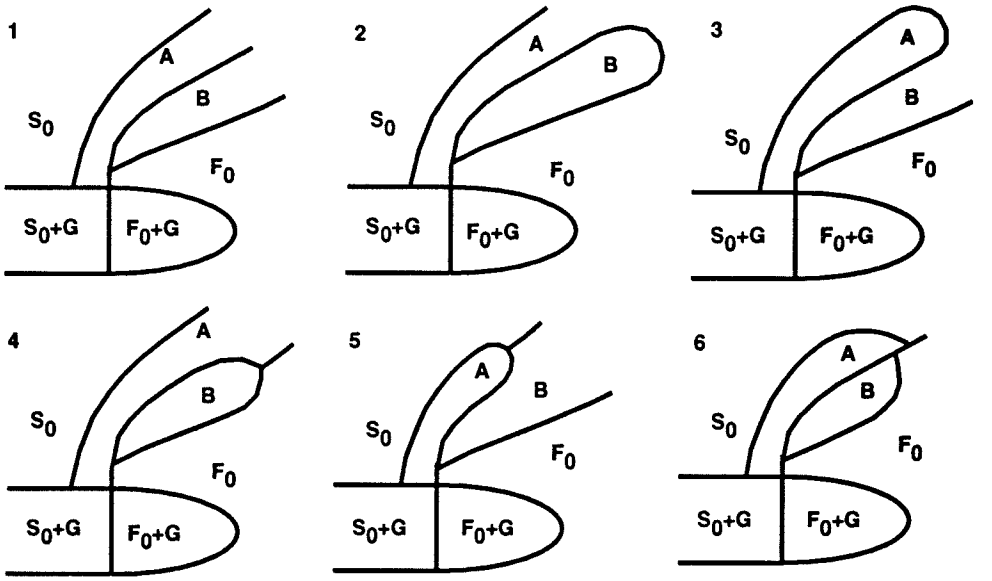

Figure 5.40: Six simple possibilities for the topology of the second, third and fourth layer phase diagrams. Note that the locations where the boundaries intersect may differ.

topologies[12] for the second layer phase diagram where at low temperature there exists a 2-D solid phase with long range order, and at high temperature there is a disordered 2-D fluid phase. The phase boundaries in this figure may be first or higher order. Where a phase boundary ends abruptly it may either change to a higher order phase transition, or curve toward the horizontal. Note that there must be at least one phase boundary (first or higher order) separating the high and low temperature phases, because the low temperature ordered solid phase cannot change into the disordered fluid phase without a phase transition occurring. The phases A and B in figure 5.40 can be anything as long as there is a phase boundary separating phases with different symmetry.

Monolayer phase diagrams with some of the topologies shown in figure 5.40 have been observed. As discussed above, the shape of the high coverage monolayer methane phase diagram is similar to number 4, with A being commensurate solid, and B as the expanded incommensurate solid phase (ES). The solid phase, S_0, is incommensurate with the substrate (DS). However, for the monolayer methane phase diagram, the A-B phase boundary does not join with the triple point melting

[12]It is possible to imagine even more complex phase diagrams, but the six shown are the simplest that could explain the data.

line, but continues downward through the solid-gas coexistence region.

The phase diagrams for krypton [122] and CO [121] both exhibit a phase diagram similar to number 2 in figure 5.40. Phase A corresponds to a reentrant fluid phase, and B corresponds with a commensurate solid phase. The solid phase, S_0, is incommensurate with the substrate. However, for these monolayer phase diagrams, (unlike figure 5.40) the A-S_0 phase boundary joins the S_0-(S_0 + G) boundary tangentially at a tricritical point. Curiously, the three features in the CO heat capacity data taken by Feng and Chan caused by passing through the S_0-A, A-B, and B-F_0 boundaries disappear at higher coverages and leave only a single broad feature. This is just like the second layer data in figure 5.39. However, our data show two sharp phase transitions, then a broad one, where Feng and Chan see two broad transitions, then a sharp one. But the second layer phases and phase diagram may still be similar to that of krypton or CO.

There are many phases that can be considered as candidates for A and B in the possible phase diagrams. In general, these phases fall into two categories, those with and without long range order. The phases are also categorized by the degree of epitaxy with the underlying first layer. There have been a wide array of adsorbed phases discovered for simple spherical molecules: commensurate solids, incommensurate solids, hexatic solids, domain wall fluids, modulated fluids, and rotationally oriented solids. Any phase can be inserted into figure 5.40 as long as there remain boundaries between phases that differ in symmetry. The possible phase diagrams that are *not* allowed are:

- Number 3, where B is a disordered phase, or one with different symmetry than S_0.
- Number 2, where A is an ordered phase, with different symmetry than the fluid phase, F_0.

Otherwise, A and B are not constrained.

Unfortunately, these data alone cannot determine which of these six topologies is correct for the second layer of methane. Therefore the phase boundaries in figure 5.38 are incomplete. Clearly, structural measurements are necessary to determine the exact phase in any region of the phase diagram. For example, the monolayer krypton phase diagram was initially studied with heat capacity [123] and a phase diagram was proposed. Since that time, there have been radical changes in the phase diagram due to vapor pressure and x-ray scattering data. Likewise, a careful

structural study of the phase diagram for the second, third and fourth layers of methane is required, with these heat capacity data as a guide to the locations of the phase transitions. The multilayer phases of methane are as interesting and complicated as the monolayer phases, and will require the same effort to understand.

Third and Fourth Layer Phase Diagrams

The third layer N versus T phase diagram is again similar to the standard liquid-solid-vapor density versus temperature phase diagram. Figure 5.41 shows the heat capacity scans for the coverages with peaks (labeled D-G') likely to be related to the third layer. The locations of these peaks are also shown in the N versus T phase diagram, figure 5.38. Peak D appears at nearly constant temperature[13] while the coverage is increased and therefore can be identified as the signal from the third layer triple point. Following peak D is a broad feature, E, that traces out the liquid-gas coexistence region. But, as with the second layer, there are surprises.

Peak F is far larger than the noise in the data, and is reproduced in three data runs at coverages between 2.9 and 3.0 layers. Two of the data runs are on the adsorption branch, taken from the same film, but the other was from a desorption branch film from a different cell filling. The peak appears at a similar position in the N versus T plane for the data from both branches, adsorption and desorption. However, this feature cannot be seen to connect with any phase boundary at either higher or lower coverages. The reasons why a phase boundary could become invisible to the heat capacity data have been outlined above. But in this case, the boundary disappears at both ends, over a short range of coverages. We have no simple explanation for this behavior.

Just as in the second layer, another peak appears in the third layer, G, a few degrees below the 2-D triple point peak (D), on the highest coverage run before the closure of the liquid-gas coexistence region. For higher coverages, the peak D moves to higher temperatures, just as melting does in the standard liquid-solid-

[13]Note that peak D on the 2.92 layer desorption branch run is at slightly higher temperature than peak D on the adsorption branch runs at 3.00 and 2.75 layers. Also, peak D on the 3.496 layer desorption branch run is slightly larger and peak G is slightly smaller than on the adsorption branch runs at 3.67 and 3.30 layers. This may indicate some small interaction between the capillary condensate and the film.

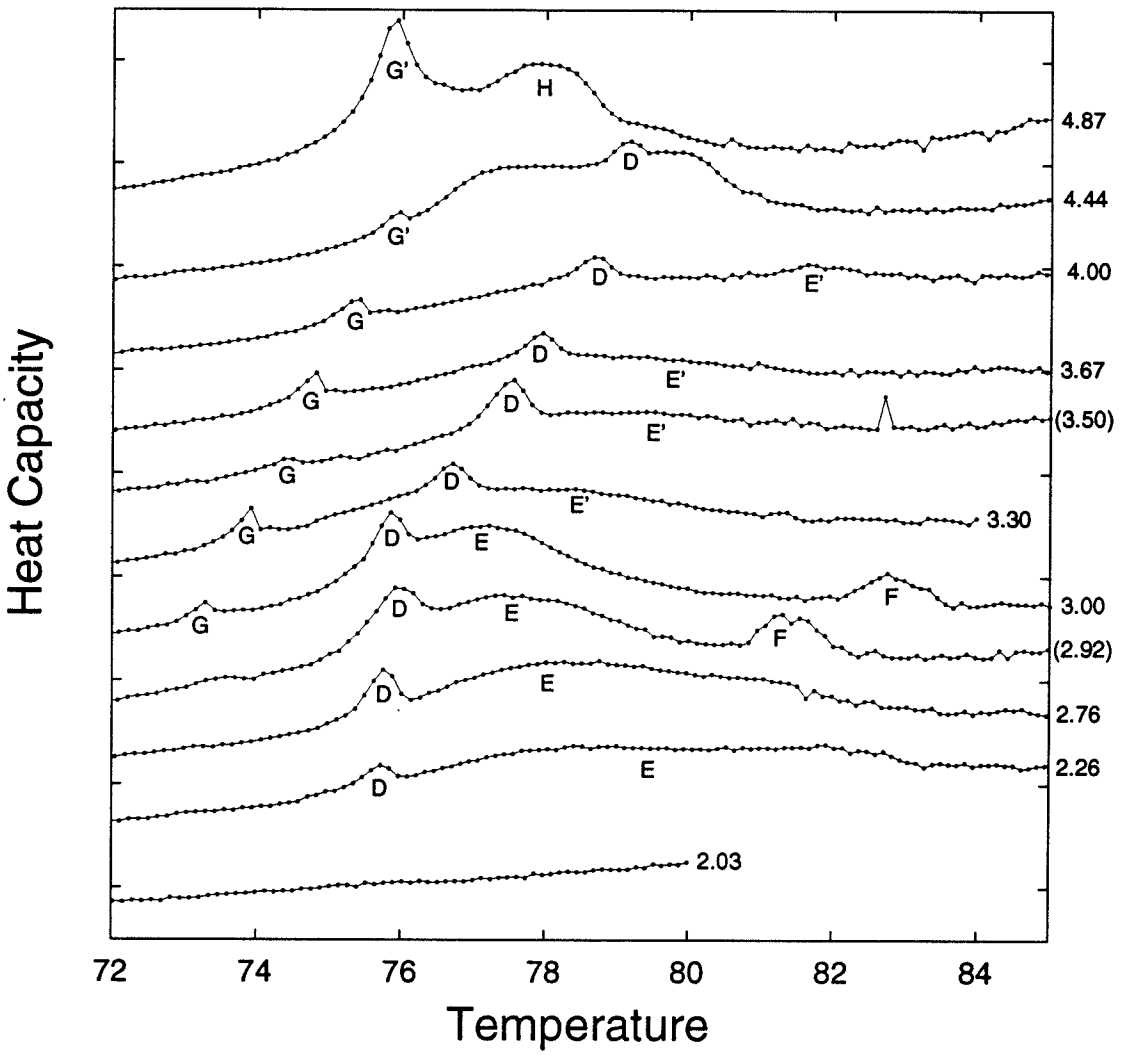

Figure 5.41: Heat capacity signals possibly identified with the third layer. Numbers indicate the total amount (layers) in the system during the scan. Numbers enclosed in parentheses indicate desorption branch data whose coverage is reduced by the additional amount capillary condensed on that branch, relative to the adsorption branch. Letters identify heat capacity features for discussion in the text.

vapor phase diagram. Also like the second layer, there is still a remnant[14] of peak E at coverages above the closure of the liquid-gas coexistence region (peak E'). Peaks D, E', and G move to higher temperature as the coverage is increased until features appear that mark the appearance of the fourth layer. Unlike the second layer, where peaks A, B' and C disappear at a temperature far above any peaks in the third layer, the third layer peaks seem to intertwine with the fourth layer peaks.

Peak G' can be identified as the fourth layer triple point peak in figure 5.42. Peak H appears to map out the fourth layer 2-D liquid-gas coexistence region, but it appears that a peak that is possibly associated with the third layer, G, connects with the fourth layer triple point peak, G'. At the coverage where peak G appears, 3.00 layers, the fourth layer is beginning to be filled with 2-D gas. There should be no fourth layer solid at this coverage, and peak G is very similar to peak C in the second layer. While it is comforting to find that peak G does not just disappear, like peaks A, B', and C in the second layer, it is surprising that it may join with a feature in the next (fourth) layer. It is possible that peak G may be the signal from incommensurate-commensurate solid or incommensurate solid-reentrant fluid phase transition in the third layer that drives the melting of the fourth layer.

Likewise, what is presumed to be the third layer triple point peak, D, in the extended third layer phase diagram, appears to intersect and end on the fourth layer coexistence region. The heat capacity data, with the cryogenic valve both open, and closed at 4.44 layers adsorbed on the adsorption branch, show three maxima in the fourth layer liquid-gas coexistence region. In the runs at the next higher coverage, 4.87 layers, only a single peak appears. Could the melting of the third layer interact with the fourth layer? Between 5.28 and 5.69 layers, the fourth layer 2-D melting increases in temperature and the signal from passing through the liquid-vapor coexistence region disappears. In the highest coverage run, however, a bump similar to H appears, H'. This peak is like peak E' in the second layer or peak B' in the first layer, but there is no sign of peaks at lower temperature than the 2-D triple point in the fourth layer like those seen in the second and third layers.

In the two highest coverage runs on figure 5.10, there is a peak that occurs above the capillary condensate melting peak. This peak may tie into one of the

[14]In the third layer, peak E' (like peak B' from the second layer, figure 5.39) is smaller and less convincing. It is possible that this peak is not really there.

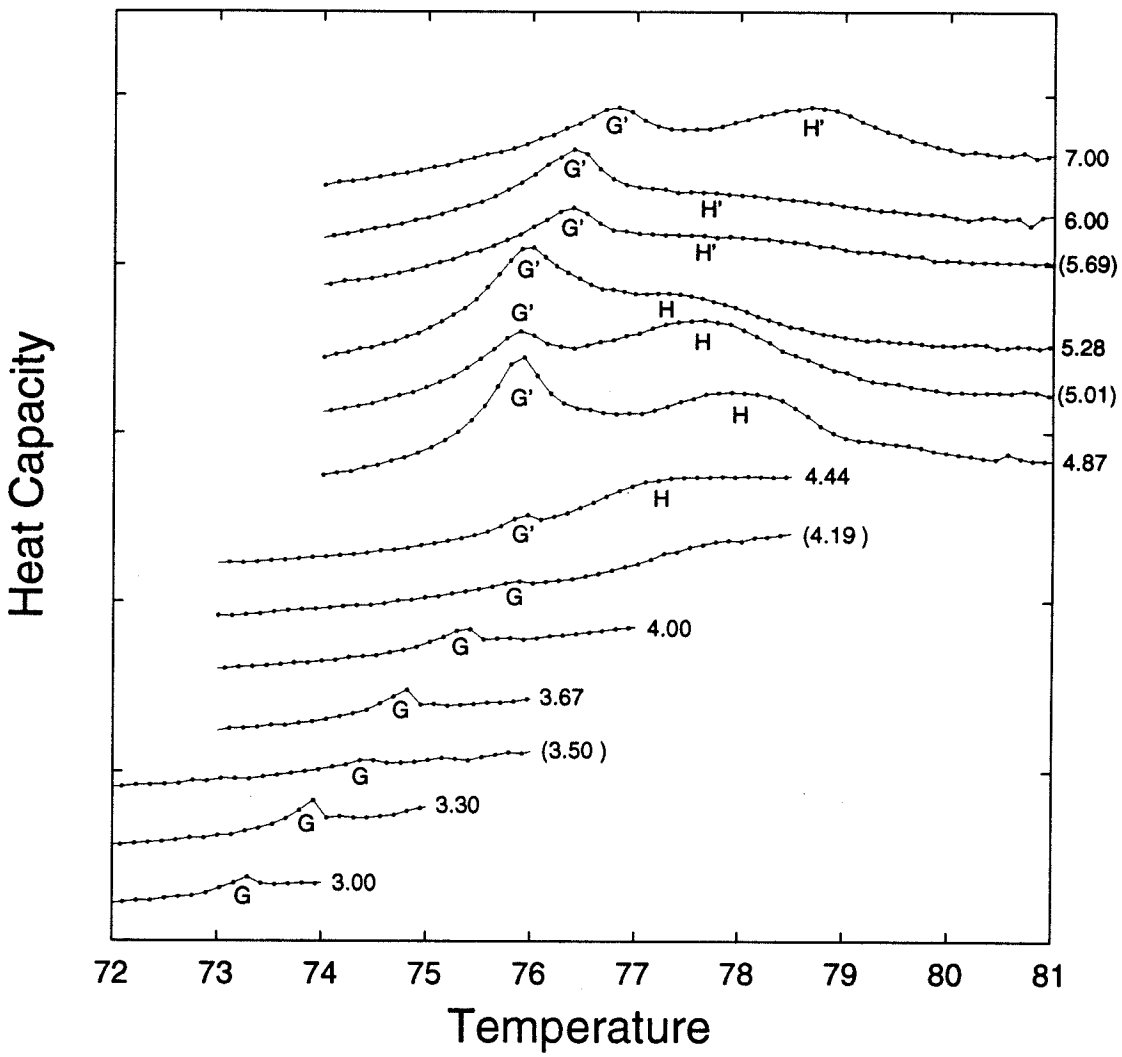

Figure 5.42: Heat capacity signals possibly identified with the fourth layer. Numbers indicate the total amount (layers) in the system during the scan. Numbers enclosed in parentheses indicate desorption branch data whose coverage is reduced by the additional amount capillary condensed on that branch, relative to the adsorption branch. Letters identify heat capacity features for discussion in the text.

peaks that disappeared at lower coverages, or may be caused by something else entirely.

There seems to be a remarkable similarity between the second, third and fourth layer phase diagrams. Each has a well defined liquid-gas coexistence region. The second, fourth, and possibly third layers have a heat capacity peak (B', E', and H') at higher temperatures than the melting peaks (A, D, and G) at coverages above that where the 2-D liquid-vapor coexistence regions end (1.86, 3.33, 5.69 layers). The second and third layers have a peak that appears at coverages just just above layer completion, at a lower temperature than the 2-D triple point (C and G). It is hoped that theoretical and computational simulations will explain some of the underlying physics causing these phenomena.

The possible interconnections between the third and fourth layer phase boundaries recall the statement made early in this work, that it is not strictly proper to consider the layers as noninteracting. It would be expected that the properties of the under-layers would strongly affect the phases of the upper layers. It could be argued that solid layers are unlikely to form on top of a liquid one, and that a layer is not likely to be more dense than the layers below it. For thick films, it is expected that the individual layers' phase diagrams should be so interconnected that the film should be thought of as a single system, not a collection of layers. As discussed above (include page number), layering transitions in thick films are best thought of as coexistence between films N and $N+1$ layers thick, instead of 2-D liquid-gas coexistence. But methane films that are four or less layers thick may be near the transition between these two types of behavior.

In fact, the initial purpose of this work was to examine the way these 2-D systems approached bulk behavior. The bulk properties of interest include the melting transition and surface roughening. Unfortunately, the films in this study seem not to be able to grow to sufficient thickness to enable a study of melting. Capillary condensation prevents the films from growing past about five layers thick, and the heat capacity signal from the melting of the capillary condensate obscures any signal from the film as it approaches bulk melting behavior. The connection between 2-D and 3-D melting is difficult to make from this work, since the individual layer melting signals from the second and third layers seem to tie into phase boundaries related to the 2-D nature of the films, or to drop off into nowhere. Presumably, thicker films could be formed[15] on single crystal substrates,

[15] At least to ten layers or so [5].

in which bulk melting would have to appear.

In the limit of thick films, the upper layers may mimic the bulk roughening transition as outlined by Hamilton [34, page 35]. Here it may be possible to examine how the bulk surface is constructed from 2-D layers. For very thick adsorbed films, one usually assumes that there is a sandwich made of the upper surface (similar to the roughened or unroughened bulk surface), the central region (similar to 3-D bulk matter), and a lower surface (which may have its own unique properties, e.g. substrate freezing). Is the possible interconnection of our third and fourth layer phase a sign that the film-vapor interface is approaching the behavior of the bulk-vapor interface? Unfortunately, this is not necessarily true.

There is a fundamental difference between the thick film-vapor interface and the bulk-vapor interface. If a certain amount of matter is added to a bulk crystal face in thermodynamic equilibrium at constant temperature, the thermodynamic properties of the interface are not changed. Microscopically, if the interface is below the roughening transition temperature for that facet, a terrace is made wider to accommodate the additional matter. If the film is above the roughening temperature, the mean height of the interface increases. In either case, the surface tension of the interface is not changed. However, if the number of molecules in a finite thickness adsorbed film is increased, the thermodynamic properties may be altered. For example, the uppermost layers of our film might solidify, and the surface tension may change.

The difference between the films and the bulk is the film's ability to support a fractional coverage in the uppermost layer. The bulk-vapor surface tension is defined as the energy cost of creating a bulk-vapor interface. The surface of the crystal includes the molecules in several uppermost layers, those with different properties than the underlying bulk. The surface layers of the crystal can be imagined as separated from the bulk matter by a dividing plane: a fixed number of molecules above this plane are in the surface, and those below it are in the bulk sample. The surface tension can be thought of as the difference (per unit area) between the total energy of these layers and the energy of the same number of bulk molecules. It is sufficient to locate this plane deep enough within the crystal so that moving the plane away from the surface to include more molecules in the surface layer does not change the value of the surface tension. The location of this dividing plane is somewhat arbitrary, but it is still a useful construction. When molecules are added to this bulk crystal face in thermodynamic equilibrium, the dividing plane moves so that the number of molecules in the surface is constant.

The energy of the molecules in the surface layers is then unchanged, as are all the properties of the bulk-vapor interface.

Likewise, the thick film on a solid substrate can be divided in two by a plane. Above this plane are the surface layers, but, unlike the bulk, below this plane each layer of the film is distinct from the others. However, the film has no well defined surface because the plane does not separate the surface from homogeneous matter below it. This construction was useful for the bulk, because if the dividing plane is positioned deep enough inside the crystal, its exact position is irrelevant; but for the film, since all the layers are unique, the upper interface cannot be isolated from the rest. For example, the value of the film's surface tension will depend on the location of the plane, unless the film is so thick that the middle layers are all alike. If such a plane is defined with a constant number of molecules, the film may still be separated into two systems, the surface layers lying on top of a substrate that is the rest of the film. When molecules are added to the film, the dividing plane moves upward, but the properties of the surface layers are not constant (as in the bulk surface). The surface layers change because the substrate for the surface layers changes, since the central layers of the film are unique. For the bulk, the properties of a layer of molecules depend on the distance of the layer from the bulk-vapor interface. But for thin films, the properties of each layer depend on the distance from the substrate. It is also possible for the uppermost layer of the film to contain a variable number of molecules, but the number of molecules of the uppermost layer of the bulk interface is constant since, when molecules are added, the interface rearranges itself and finds the equilibrium state. It has been said by den Nijs [124] that bulk-like surface roughening should not occur for films thinner than ten layers. It is presumed that the substrate will no longer control the position of the interface for films that are very thick. Similar processes are thought to drive an interesting phenomena called pre-roughening, where the fractional coverage of the uppermost layer on bulk interface changes to roughly one-half at the pre-roughening temperature [125].

This study cannot investigate the evolution of the 2-D film into bulk properties. But it does demonstrate some interesting physics and may lead to a greater understanding of bulk surfaces, especially if future work can determine the exact phases and phase diagram for a multilayer film such as methane.

Other heat capacity studies have found multilayer phase diagrams with some similar features, but none have seen the 2-D layering coexistence region along with the 2-D triple point and melting peaks extending to higher coverages. Some

Layer :	1	2	3	4	5
2-D Triple point	56 (Ref. [2])	77.7	75.9	76.0	—
$T_c(N)$ (this work)	69 (Ref. [2])	83	83	81	—
$T_c(N)$ (from [7])	—	82.5	82.5	86.7	87.5

Table 5.2: Layering critical point and 2-D triple point temperatures (in Kelvins).

studies have seen pieces of the second or higher layer phase diagrams:

- Ethylene: Heat capacity peaks due to layering but not due to melting for the second, third, fourth, and fifth layers [126].
- Carbon Monoxide: Second layer peaks that map out the layering coexistence region and the 2-D triple point melting; but the melting was either not seen or not examined at higher coverages [121].
- Argon and Neon: Melting peaks are traced out to higher coverages, but the study does not have sufficient resolution to see the coexistence regions and triple points. Peaks were seen for the second, third, and fourth layers of argon and neon [127, 45].

It is not clear whether these studies are limited due to noise in the data, or because the systems studied are different than methane-graphite.

The second and higher layer phase diagrams of methane may be significantly different than those for argon and neon. The monolayer heat capacity results for various adsorbates can be separated into two classes, those that have a narrow, tall first layer melting peak that extends to coverages far past monolayer completion (CH_4, Xe, Kr, among others) and those with rounded first layer melting peaks that seem to disappear at higher coverages (Ar). The individual layer phase diagrams for the second and higher layers may also fall into these two classes. It would be interesting to see the heat capacity measurements for argon, for example, made with a sensitive calorimeter.

The 2-D triple points and layering critical points for the second, third, and fourth layers of methane are listed in table 5.2. There have been recent vapor pressure measurements that found the layering critical temperatures, $T_c(n)$, for methane and other gases [7]. The values of $T_c(n)$ found by the location of the heat capacity peaks that mark out the coexistence region are very similar to those measured with vapor pressure isotherms for the second and third layers, but Larher and Angerand find a very different result for the fourth layer. Both

techniques are subject to errors. Our data may be in error because there may not be a measurement close enough to the critical point (our value would be too low), and it is difficult to locate the end of the rounded bumps in the heat capacity. The vapor pressure measurements rely on judging the steepness of the steps of the vapor pressure isotherms, and are even more difficult to interpret because the steps are also altered by substrate imperfections and capillary condensation. Capillary condensation could cause especially large errors in the fourth and fifth layer vapor pressure measurements, but should not greatly affect our measurements of the layering critical temperature. The value of the layering critical point for the thicker films is of particular interest because it may be close to the bulk roughening temperature for the analogous crystal face of the bulk solid[16].

One could argue, on general principles, that the monolayer phase diagrams on corrugated substrates differ from the bulk mainly in that there are several new solid phases that complicate the extended layer phase diagram (phase diagram above layer completion). These solid phases are created by the difference between the "natural" film lattice, which changes as a function of temperature, and the substrate periodicity. The fluid phases are not greatly affected by the order in the substrate. Therefore, each phase diagram for the second and higher layers should also have similar complications that are driven by the order of the (solid) layer underneath each layer as it forms. The data presented in this study are the first observation of complicated extended layer phase diagrams for thicker films that we are aware of. This study has recorded the signals of the phase transitions between the different phases in each layer because the apparatus was more sensitive to small heat capacity features than any previous instrument. Future studies of other adsorbates on graphite may find similar phase diagrams, and other experimental techniques may be used to help explain the structure of the adsorbed films.

Capillary Condensation: Revisited

Another piece of evidence about capillary condensation comes from the coverage where the second layer 2-D vapor-liquid coexistence region is completed, between 1.71 and 1.86 layers. Kim, Zhang and Chan [2] find that the dense incommensurate first layer solid phase first appears at about .85 layers adsorbed[17]. The

[16] As mentioned below, it should be possible to measure the properties of the fifth layer of methane. This may better locate the bulk roughening temperature.

[17] One layer is defined as the inflection point of the first step in the isotherm at 77 K. This does not necessarily correspond to a location of a phase boundary on the phase diagram and the

second layer solid should cover the surface at roughly twice that, or about 1.7 layers. This agrees well with the location of the endpoint of the second layer liquid-gas coexistence region, between the point where peak B is closest to peak A (1.71 layers), and where peak A moves up in temperature (1.86 layers). Unfortunately, such evidence cannot be used to predict the locations of the third and fourth layer coexistence regions because of capillary condensation. The third layer coexistence region ends between 3.0 and 3.3 layers, but three times the monolayer incommensurate solid coverage is only 2.6 layers. The fourth layer coexistence region ends between 5.3 and 5.7 layers adsorbed, compared to 3.4 layers (four times the monolayer incommensurate solid coverage). These data allow us to make a crude estimate of the amount of matter that is condensed in capillaries on the adsorption branch: there are between .4 and .7 layers capillary condensed when the uniform film is three layers thick, and between 1.9 and 2.3 layers capillary condensed at the point where the fourth layer liquid-gas coexistence region ends.

Cheng and Cole [96] give an estimate for the excess amount adsorbed in corners between flat plates in the thick film limit,

$$\delta N \sim z^6 \tag{5.7}$$

where δN is the amount capillary condensed, and z is the thickness of the uniform film. The uncertainty in our estimates of the amount capillary condensed is large, but our numbers seem to agree with Cheng and Cole's model. A curve following equation 5.7 can be made to pass within the uncertainties for the two data points. It is then interesting to estimate the amount capillary condensed when there are thicker films on the substrate. There would be 8.8, 26 and 66 layers worth of capillary condensate coexisting with uniform films five, six, and seven layers thick, respectively. This indicates that it is extremely difficult to study uniform films thicker than about five layers.

It is interesting to use the above estimate for the amount capillary condensed on the adsorption branch to correct the 95 K vapor pressure isotherm to give the uniform film thickness as a function of the chemical potential. Recall that figure 5.9 presented indirect evidence that capillary condensation occurs, in that the curve is not linear at higher coverages. In the limit of thick films, the Frenkel-

subsequent steps in the isotherms are not necessarily at integer multiples of this "monolayer" coverage. A layer is defined in this way because it allows different laboratories to compare results, because all must perform at least one vapor pressure isotherm in order to calibrate the substrate surface area.

Halsey-Hill isotherm (equation B.5) should be obeyed and the plot should be linear. Figure 5.9 also shows the 95 K isotherm with the estimated amount capillary condensed removed. The predicted amount adsorbed according to the Frenkel-Halsey-Hill equation is also shown. $\Delta C_3^{l\omega}$ was calculated independently from theory [36, page 94]. The slope of the corrected data and the model are surprisingly close, considering the crudeness of the estimates.

Capillary condensation hysteresis has been observed to disappear near the bulk critical point [128], and some authors have reported that it disappears at a temperature below the triple point temperature [129]. The termination of capillary condensation hysteresis may somehow be related to bulk surface roughening, because the vapor-solid interface for an unroughened crystal is faceted. If capillary condensation is prohibited or restricted below the roughening temperature, the observation of a wetting transition in the methane-graphite system at 75.5 K, by Inaba and Morrison [40], may be explained. Above the roughening temperature (presumably near 83 K) the films appear to wet the substrate because matter is drawn into the capillaries. Below this temperature, the amount of capillary condensation may be reduced, giving the appearance that the uniform film does not wet the substrate.

However, our data seem to indicate that the excess amount of capillary condensation on the desorption branch, relative to the amount on the adsorption branch, is approximately constant from 75 to 95 K. The phase boundaries from the data on both branches line up, in figure 5.38, even at 75 K, when the coverages on the desorption branch are corrected to equal those on the adsorption branch using the 95 K hysteresis curve. Therefore it is unlikely that there is a large change in the amount of capillary condensation at low temperatures. It is likely that the rate of growth of the capillary condensate is greatly altered below the roughening transition, since the bulk solid grows from the vapor much more slowly below the roughening transition temperature[18]. Therefore, our annealed films may differ from those formed by condensation from the vapor at low temperature (as in vapor pressure isotherms).

[18]This effect was what lead Burton, Cabrera and Frank [105] to predict the roughening transition.

Chapter 6

Conclusion

This work can clearly be divided into two parts, the creation of a new, more sensitive calorimeter, and the data from methane films on graphite. The former required nearly five years to design and construct, while the data were collected in seven months. Therefore, this work outlines two contributions. Obviously the data and the conclusions reached from them are valuable, but the construction of the instrument is an investment that will yield benefits in the future as different adsorbates or even different physical systems are studied with it.

On examining the data, it is apparent that many of the smaller features would be missed by a less sensitive calorimeter. The precision of the instrument, .02%, is nearly as good as any other, and it collects data much more rapidly than the other methods. Computer control adds to the reproducibility, enables new modes of operation, and relieves the operator of many long tedious hours of work.

Although the casual reader may be put off by the many details presented about the instrument, it is necessary to document the workings of the hardware and software both for the purpose of describing our work to the scientific community at large, and for passing on this knowledge within our own laboratory. The instrument is a straightforward application of already existing ideas, constructed with tape and rubber bands. However, it is more than simply the sum of its parts, however uncooperative they may be. I hope that the ideas and hard work that went into this creation will be useful in the future, and that I have left a useful tool for future research. Likewise, I have added only a small contribution to the total knowledge acquired by the the previous students in our laboratory in trying to understand the properties of these films.

Methane films on Grafoam have demonstrated a wealth of intricate details caused by the films' two dimensional nature, the periodicity of the substrate that

lies below each layer, and the cracks and corners in the porous substrate.

In the course of this work, it was discovered that the cracks in the adsorbate cause the formation of bulk capillary condensate for films thicker than three layers on the adsorption branch or 1.1 layers on the desorption branch. The heat capacity bumps near the bulk triple point are caused by the melting of this capillary condensate. This result contradicts the previous interpretations of prior data from our laboratory, as well as those by others, and prevents us from studying how bulk melting begins in these films. On the adsorption branch, the films are metastable, and therefore their states depend on the precise procedures used to form them. Films with different heat capacity signatures but the same vapor pressure were found, demonstrating that the adsorption branch films are metastable. However, true desorption branch films are difficult to create because the downward scanning curves in the hysteresis loop do not intersect the upper boundary curve until a large fraction of the film is desorbed. The amount of capillary condensation at two coverages on the adsorption branch can be crudely estimated from the positions of the features in the uniform film. When these data are combined with a simple model, the 95 K vapor pressure isotherm can be corrected for the effect of capillary condensation. Then, it agrees with the Frenkel-Halsey-Hill equation, where the constant in this equation is calculated independently.

The melting of the capillary condensate can provide some new information. The latent heat of melting of the confined bulk matter is half of the bulk value, or less, when it is in extremely small pores. When the amount capillary condensed is greater, the latent heat of melting is near the bulk value and the melting temperature tends toward the bulk triple point, as would be expected. The melting temperature of the capillary condensate, when defined at the maximum of the broad heat capacity features, seems to confirm a simple model for the melting of capillary condensate in cylindrical pores. This model says that, for both the adsorption and desorption branch, the melting temperature is controlled by the chemical potential of the film, and therefore also controlled by the size of the pore that confines the condensate. The model also depends on the contact angle between the condensate and the pore wall, and several different behaviors are possible depending on the values of the contact angle of the solid and liquid capillary condensate. The data imply that substrate freezing occurs. If substrate freezing occurs and the solid does not wet the pore wall, then it can be shown that surface melting must also occur from analysing the slope of the melting curve. Surface melting would explain the widths of the heat capacity peaks, but other explana-

tions are possible if it does not occur. The most important conclusion regarding capillary condensation may be that there is no strong interaction between the uniform film and the capillary condensate. Therefore, films up to five layers thick can be studied on this porous substrate.

These data contribute to the understanding of the phase diagram for the layer closest to the substrate. The first layer of methane melts far above the bulk triple point temperature when it is under a thick film, as seen in other systems. But the extended monolayer phase diagram proposed by Kim et al. must be modified. The commensurate solid to expanded incommensurate solid phase transition ends on the first layer melting curve. At high temperature, the film melts from the commensurate phase, instead of from the expanded incommensurate phase, as previously thought. This can be explained as due to the compression of the upper layers preventing the film from forming the expanded phase above about one layer adsorbed.

This is the first report of complicated phase diagrams (similar to that for the first layer) in the second, third and fourth layers of an adsorbed film. There is a clear 2-D triple point and liquid vapor coexistence region for each of these layers. The 2-D liquid-gas critical point for the second and third layers agree with data from an independent vapor pressure isotherm study, but the fourth layer disagrees. If the layering critical temperatures approach the roughening transition temperature in the bulk, as expected, our data indicate that bulk methane is roughened above about 81 K. There are also a number of more complicated phases that probably occur because of the periodicity of the underlying substrate for each new layer (the layer below it). The extended layer phases in the diagram for the second, third and fourth layers are likely commensurate and incommensurate phases, but these data do not clearly determine which are present at a certain location in the phase diagram, or even find where the phase boundaries connect or end. Curiously, the third and fourth layer phase diagrams may be connected together and this may be an indication that the film-vapor interface in thicker films approaches bulk behavior.

After a total of fifteen or more years of studying methane films on graphite in this laboratory, the multilayer phase diagram is still incomplete. It is certain that not much more can be gained by additional heat capacity studies of methane on graphite. Other methods must be utilized for a real understanding of the system. With these data as a map of the possible locations of phase transitions, these other techniques may complete the picture.

Appendix A

Example RPN Control Program

Reproduced below is the version of the experiment control program that was used to take heat capacity data with the cell cryogenic valve open. Space does not allow a full description of the RPN intrepeted language or all the macros and subroutines called by this program. It is meant to give an idea of the function of the intrepreter and the steps used to take the data. The language is not case sensitive. As is standard 'C' language programming practice, macro names are written in uppercase and internal language commands are in lowercase.

```
/* ###################### File name pres02.exp ##################
This can be started after aneal00.exp, which warms up to 120, that
'anneals' the film.

This file takes 3 arguments on the stack top:
TOP     minimum temperature to start calorimetry.
TOP-1   temperature to stop calorimetry.
TOP-2   base file/path name to record data to, without last two
        digits.
TOP-3   first file number to try.

The data is concatinated to each other in sucessive data files with a
number in the last two digits of the file name incremented by one each
time. For example if the base name was tst, then the program would
check to see if tst00,tst01 tst.. existed until it found a name that
didn't exist as a file in the specified directory.

It is binned on 3 points. This starts from high temperature, as high
as room temperature, and cools down to 65K or so. This file was
entered from start.exp, fstcool.exp or another program. It assumes
```

```
that we have most of the instruments calibrated and started.

Apon startup, the channels are arranged as follows. The cell and CTM
heaters are in series mode from start.exp:

          DIODE
          CHANNEL CHEB PID HTR_RES HTR_MAX  GAIN  Tint
CELL        ---     0   0   294.1   .045    -.1   600
CTM         ---     1   1   437.2   .227     10   300
ITM          E      2   2   208.    1.92     10   0
UTP          F      3   3   127.    3.15     10    0
INNER SH     G      4   4   244.    1.63     10    0
OUTER SH     H      5   5    81.    4.93     10    0
RTOR PRT            6
CTM PRT             7
FILL TUBE                  108      3.7
*/

base                          /* set the base for the subroutine args */
/* Define a macro file */
[C:/mark/interp/calor/calhelp2.exp] [MYMACS] set

[timer sleep clrevents] [WAIT] macro

/* ################## ADJUST THE CELL HEATER POWER RANGE ##############
higher power */
1 DTOA_RECAL SET_DATA
3.0 WAIT
/* set the modes, both heaters in series modes. Resistances are to
be set to cell=2219.3 or 294.1, ctm=437.2 by the user. */
294.1  DTOA_RESA SET_DATA
437.2 DTOA_RESB SET_DATA
6 DTOA_MODEA SET_DATA
1 DTOA_MODEB SET_DATA
/* start it off */
1 DTOA_RECAL SET_DATA

/* ########## MANUALLY START UP THE RELATIVE BRIDGE ##################
and set its ratio to ***.49920 ***
This may have to be done with the ht. exch. gas pumped out, otherwise
the resistances drift too much to startup the rel. bridge. */
```

```
/* ######################## BEGIN TEMPERATURE CONTROL ##################
Begin regulating all the bodies to maintain the proper gradients.
This will be done by heating the cell from the relative bridge output.
Call a subroutine file to set up the PID control parameters */
[CTL_SETUP] MYMACS fcall
[CTL_START] MYMACS fcall
10 0 [PID_DERNUM] MACFILE fcall

/* Switch the diode bridge to mode 1, compare slave diode voltages
against the CTM diode */
1 DIOD_RECAL SET_DATA

/* ############## INITIALIZE CRYOGENIC BATH FILLING ################ */
{ BATH_OUTMODE GET_DATA 0 == TRAP_MODE GET_DATA 0 == ||
     if
     0 BATH_INMODE SET_DATA        /* turn off filling */
     0 BATH_PMODE SET_DATA
     0 BATH_OUTMODE SET_DATA
     0 TRAP_MODE SET_DATA
     1. WAIT
     7200 BATH_OUTMODE SET_DATA         /* 2 hour fill time */
     10800 TRAP_MODE SET_DATA           /* 3 hour fill time */
     1. WAIT
     3 BATH_OUTMODE SET_DATA
     3 TRAP_MODE SET_DATA
}

/* ################## RESET THE VALVES ################################*/
CRYO_CELL VALVE_ON                     /* close cryo cell valve */
FILL_TUBE VALVE_ON                     /* close valve at probe top */
4 [PID_OFF] MACFILE FCALL              /* turn off shield heaters */
5 [PID_OFF] MACFILE FCALL
SWITCH_VAC VALVE_ON                    /* pump out heat switch */
0.0 DTOA_POWB SET_DATA                 /* turn off ctm heater */
0.0 BAR_ZERO SET_DATA                  /* disable barocell zero */
HI_VAC VALVE_ON                        /* remove probe ht exch gas */

/* ################### PUMP OUT FILL TUBE ###################### */
/* Dont run this section if we are restarting from a crash */
{
     1 if

     /* Prepare for pressure measurement, first pump out the fill
     tube. This must be done now because later the gas would freeze in
```

```
the fill tube. First, open the fill tube to the barocell to
measure the amount of gas removed. */

/* VCAL_VALVE VALVE_OFF Don't always open vcal */
FILL_TUBE VALVE_OFF
120.0 wait          /* wait for pressure equilibrium */

/* Record the pressure in the system before it is pumped out,
subroutine averages over 4 seconds. Set a variable to the
pressure */
[baro_ave] MYMACS fcall [bar_pre_pres] set

/* Average the pressure over 4 seconds */
ROOMT_TEMP GET_DATA
1.0 WAIT ROOMT_TEMP GET_DATA +
1.0 WAIT ROOMT_TEMP GET_DATA +
1.0 WAIT ROOMT_TEMP GET_DATA +
4.0 / [bar_pre_temp] set

/* Close the calibrate volume valve and pump out the manifold
and fill tube. */
VCAL_VALVE VALVE_ON
10.0 WAIT
MANI_VAC VALVE_ON

600. WAIT                          /* WAIT 10 MINUTES */

/* Measure the pressure over 4 seconds */
[baro_ave] MYMACS fcall [bar_vac_zero] set

/* Record all the relavent data to the sample gas filling log
file, write two copies of the file */
[c:/mark/interp/calor/fills.doc] namelog
[Pressure in manifold before pumping out is ]
bar_pre_pres tostr cat
writelog
[room temperature is ] bar_pre_temp tostr cat [ centigrade] cat
writelog
[barocell zero is is ] bar_vac_zero tostr cat
writelog
[ ] writelog

[c:/mark/interp/calor/fills2.doc] namelog
[Pressure in manifold before pumping out is ]
```

```
     bar_pre_pres tostr cat writelog
     [room temperature is ] bar_pre_temp tostr cat [ centigrade] cat
     writelog
     [barocell zero is is ] bar_vac_zero tostr cat
     writelog
     [ ] writelog

     /* Check to see if the pressure zero after pumping too high, if
     so close the valve and wait */
     {
     bar_vac_zero abs .1 >
          if
          MANI_VAC VALVE_OFF
          sleep
     }
}
/* ################### FILL TUBE PUMPED OUT ###################### */

/* ########### SETUP THE VALVES FOR COOLING DOWN ################## */
VCAL_VALVE VALVE_ON                /* close off the calibrated vol */
MANI_VAC VALVE_ON                  /* but pump on the manifold */
FILL_TUBE VALVE_ON                 /* Seal off the fill tube */
100.0 FVOUT_V2OUT4 SET_DATA        /* Heat the fill tube */

/* ######### INTRODUCE HEAT EXCHANGE GAS INTO THE PROBE #############
Leak a controlled amount of gas into the isolation vacuum
while pumping to introduce heat exchange gas for cooling the cell */
EXCH_GAS VALVE_OFF
VEECO_LEAK VALVE_ON
HI_VAC VALVE_ON

/* ############## SETUP COMPARISON THERMAL MASS CONTROL ##############
Control the comparison thermal mass so that it does not cool below the
setpoint. Subroutine sets up permanent PID control parameters from
values on the stack. The other bodies are regulated relative to the
CTM. */
CHEB_OUT1 MAKPTR          /* PID input from ctm diode temperature */
-1000.0                   /* Invalid temperature value */
0.0                       /* Minimum input temperature */
999.0                     /* Maximum input temperature */
0                         /* Ptr. to variable setpoint, not used. */
0.0                       /* Invalid value for var. setpt. not used */
DTOA_POWB MAKPTR          /* Where to send output, heater ch. ptr. */
1                         /* Output to float or double type */
```

```
1.0                         /* Heater resistance, not used */
.89                         /* Maximum power output */
1                           /* PID channel number */
[PID_SETUP] MACFILE fcall

/* ############ SET THE PARAMETERS FOR THE COOL-DOWN ############## */
4.0       [cpow] set                /* cool as T^-4 */
12.0  [cool_hours] set          /* cool 120 to 65 in 12 hours */
65.0      [end_temp] set
120.0 [beg_temp] set

/* ############ CALCULATE CONSTANTS FOR THE COOL DOWN ############# */
beg_temp cpow 1.0 - neg pow         /* Calculate internal constants */
[beg_temp] set

/* Cool down 'constant'. Time in this is kept by the experiment clock
units
    T1^-(n-1) - T0^-(n-1)
   ---------------------- = C
      ( t1 - t0 )
*/
end_temp cpow 1.0 - neg pow
beg_temp
 -
cool_hours 3600.0 * 2.0 *
/
[cool_const] set

/* Initialize the last time and temperature settings. Get an in-range
temperature value */
{
cheb_out1 get_data dup dup 0.0 < swap 999.0 > ||
while
     dump
}
[last_set] set
exp_timer get_data [last_time] set

/* ################### COOLDOWN LOOP ###################### */
{
/* Test to see if we are cold enough yet */
cheb_out1 get_data dup -1 nbase > swap 0.0 <= ||
while
     10.0 WAIT
```

```
/* ################ DECREASE THE CTM SETPOINT ################
so that it cools as
dT
--  =  - K T^3
dt

in stepwise changes every 10 seconds.

First get a valid CTM temperature value. */
{
cheb_out1 get_data dup dup 0.0 < swap 999.0 > ||
while
     dump
}

/* Compute the new temperature setpoint */
last_set
max
dup cpow pow
cpow 1.0 - /
neg
cool_const *
exp_timer get_data dup last_time -
swap [last_time] set
todoub *
+
dup [last_set] set

/* Reset the ctm setpoint, call subroutine to change PID
parameters */
2.              /* Gain, in watts per ohm */
0.              /* Derivative time constant */
300.            /* Integral time constant */
4 nover         /* Temperature control setpoint */
1               /* Channel number */
[PID_SET] MACFILE FCALL
dump
/*############## FINISHED SETTING THE CTM SETPOINT ############ */

/* ############ FILL THE HEAT SWITCH WHEN BELOW 75K ############
First see if it's already filled, check to see if it is being
evacuated. */
{
```

```
      SWITCH_VAC
      /* little routine to see if any valve is on */
      {
      dup 0x0100 & if
           DC_OUT GET_DATA 0x0FF & &
      } else {
           AC_OUT GET_DATA &
      }
      CHEB_OUT1 GET_DATA dup 75.0 < swap 0.0 > && && if
           /* Fill it */
           SWITCH_VAC VALVE_OFF
           SWITCH_GAS VALVE_ON
           3.0 WAIT
           SWITCH_GAS VALVE_OFF
      }

      /* ####### CHANGE TO MAXIMUM HT EXCH GAS PRESSRE BELOW 80K ######
      Turn off the veeco leak valve and use regular exch gas
      below 80K. First check to see if this has already been done. */
      {
      VEECO_LEAK
      /* little routine to see if any valve is on */
      { dup 0x0100 & if
           DC_OUT GET_DATA 0x0FF & &
      } else {
           AC_OUT GET_DATA &
      }
      CHEB_OUT1 GET_DATA dup 120.0 < swap 0.0 > && && if
           /* Put in the heat exhange gas. */
           VEECO_LEAK VALVE_OFF
           EXCH_GAS VALVE_ON
           45.0 WAIT
           HI_VAC VALVE_OFF
           EXCH_GAS VALVE_OFF
      }

}
/* ################### END OF COOLDOWN LOOP ###################### */

[cpow] purge                    /* Delete cooldown variables */
[cool_hours] purge
[end_temp] purge
[beg_temp] purge
[cool_const] purge
```

```
[last_time] purge
[last_set] purge

/* ########## PUMP OUT THE FILL TUBE AGAIN BEFORE RUNNING ############
and open up to the barocell, record the barocell zero. Set the zero in
the data recording and report it to log files */

0.0 BAR_ZERO SET_DATA
[baro_ave] MYMACS fcall [bar_pre_zero] set    /* Average over 4 sec. */

/* Check to see if the 'zero' is too high, if so close the valve
and wait */
{
bar_pre_zero abs .1 >
     if
     MANI_VAC VALVE_OFF
     SLEEP
}

/* Fill tube valve should be closed after pumping out the fill tube
above (before cooling down. (then if the valve leaks a little, we
won't loose lots of gas. reopen the manifold vacuum valve again,
recording the pressure in the system first. close the manifold vac
valve */

/* Set barocell zero for the data collection */
bar_pre_zero neg bar_zero set_data

MANI_VAC VALVE_OFF                  /* Stop pumping on manifold */
10.0 WAIT
FILL_TUBE VALVE_OFF                 /* Open fill tube to manifold */
120.0 WAIT

/* Measure pressure over 4 second average, set variable */
[baro_ave] MYMACS fcall [bar_pre_pres] set

/* Measure room temperature over 4 second average */
ROOMT_TEMP GET_DATA
1.0 wait ROOMT_TEMP GET_DATA +
1.0 wait ROOMT_TEMP GET_DATA +
1.0 wait ROOMT_TEMP GET_DATA +
4.0 / [bar_pre_temp] set

MANI_VAC VALVE_ON              /* Pump out fill tube and manifold */
```

```
600. WAIT                        /* Pump 10 MINUTES */

/* Record all the relavent data to the file. Record two copies of the
file */
[c:/mark/interp/calor/fills.doc] namelog
[barocell zero before run is ]
bar_pre_zero tostr cat writelog
[Pressure in manifold before pumping out when cold is (WITH ZERO
CORRECTED)= ]
bar_pre_pres tostr cat
writelog
[room temperature is ] bar_pre_temp tostr cat [ centigrade] cat
writelog
[ ] writelog

[c:/mark/interp/calor/fills2.doc] namelog
[barocell zero before run is ]
bar_pre_zero tostr cat writelog
[Pressure in manifold before pumping out when cold is (WITH ZERO
CORRECTED)= ]
bar_pre_pres tostr cat
writelog
[room temperature is ] bar_pre_temp tostr cat [ centigrade] cat
writelog
[ ] writelog

MANI_VAC VALVE_OFF       /* Stop pumping on manifold and fill tube */
10.0 WAIT
CRYO_CELL VALVE_OFF      /* Open the cryo cell valve */

/* ############ FINISHED PUMPING OUT THE FILL TUBE ################## */

/* ############ REMOVE THE HEAT EXCHANGE GAS ####################### */
VEECO_LEAK VALVE_OFF          /* Insure that we remove exch gas */
1 [PID_OFF] MACFILE FCALL     /* Remove CTM control */
0.0 FVOUT_V2OUT4 SET_DATA     /* Remove fill tube heater power */
HI_VAC VALVE_ON               /* Open prove pump valve */

/* ############ CONTROL RADIATION SHIELD TEMPERATURE ###############
wait until the shields' temperatures are within range. Shield
setpoints are relative to the CTM temperature. */
/* INNER SHIELD */
2.        /* Gain, in watts per ohm */
5.        /* Derivative time constant */
```

```
0.        /* Integral time constant */
-1.0      /* Temperature control setpoint, relative to CTM temp */
4         /* Channel number */
[PID_SET] MACFILE FCALL

/* OUTER SHIELD */
5.0       /* Gain, in watts per ohm */
5.        /* Derivative time constant */
0.        /* Integral time constant */
-1.5      /* Temperature control setpoint, relative to CTM temp */
5         /* Channel number */
[PID_SET] MACFILE FCALL

/* wait until the shields' temperatures are within range */
{
cheb_out1 get_data
dup 1.5 - cheb_out4 get_data >
over 2.0 - cheb_out5 get_data > ||
swap 0.0 < ||
while
     10.0 wait
}

/* ################ EVACUATE OR REFILL THE HEAT SWITCH ###############
if we are cooled to below 80K. */
{ -1 nbase 80. > if
     /* evacuate */
     SWITCH_GAS VALVE_OFF
     SWITCH_VAC VALVE_ON
} else {
     /* refill heat switch */
     SWITCH_VAC VALVE_OFF
     SWITCH_GAS VALVE_ON
     3.0 TIMER SLEEP CLREVENTS
     SWITCH_GAS VALVE_OFF
}

/* ############## REFILL THE LN2 TRAPS AND OUTER BATH ##################
3 BATH_OUTMODE SET_DATA
3 TRAP_MODE SET_DATA

/* ############ RESET THE INTEGRAL TERM FOR THE CELL PID CTL #########
this prevents overshoot */
0 [PID_INT_TOG] MACFILE FCALL
```

```
5.0 WAIT
0 [PID_INT_TOG] MACFILE FCALL

/* ################## SLOWLY RAMP UP THE CTM POWER ###################
Slowly ramp up the ctm power linearly over 20 minutes. And
ramp the shields to the setpoint slowly also */
1                                   /* initialize stack variable */
{
dup 300 <=                          /* run for 300 iterations */
     while

     /* ############### INCREASE THE CTM POWER ###################### */
     dup todoub 300.0 / .045 * DTOA_POWB SET_DATA

     /* ############### INCREASE THE SHIELDS' SETPOINTS ############ */
     dup todoub 300.0 / 1.0 * -1.0 +
     /* INNER SHIELD */
     2.             /* Gain, in watts per ohm */
     0.             /* Derivative time constant */
     0.             /* Integral time constant */
     4 nover        /* Temperature control setpoint */
     4              /* Channel number */
     [PID_SET] MACFILE FCALL

     /* OUTER SHIELD */
     5.0            /* Gain, in watts per ohm */
     0.             /* Derivative time constant */
     0.             /* Integral time constant */
     4 nover        /* Temperature control setpoint */
     5              /* Channel number */
     [PID_SET] MACFILE FCALL
     dump

     1 +            /* Increment stack variable */
}
dump                /* remove stack variable */

/* ############ SET CTM POWER TO FINAL VALUE ######################## */
.045 DTOA_POWB SET_DATA

/* ############ CONTROL THE SHIELD TEMPERATURES, AT SETPOINT ####### */
0.0 [CTL_NSHIELDS] MYMACS fcall
[CTL_NSTART] MYMACS fcall           /* Remove derivative control */
```

```
/* ########### EVACUATE THE HEAT SWITH ############################ */
/* first turn off utp PID integral term */
3 [PID_INT_TOG] MACFILE FCALL
SWITCH_GAS VALVE_OFF                /* turn off gas to ht sw. */
SWITCH_VAC VALVE_ON                 /* turn on pumping of ht sw. */
200.0 WAIT
/* restore utp PID integral term */
3 [PID_INT_TOG] MACFILE FCALL

/* ############ WAIT UNTIL CELL TEMPERATURE STABILIZES ##############
to within 1e-4 ohms of ballance on rel bridge output */
{
rel_drbal get_data abs 2.e-4 >
while
     2.0 TIMER SLEEP CLREVENTS
}

/* ################ FINAL CELL CONTROL PARAMETERS ################## */
-.1     /* gain IN WATTS PER OHM, must be negative */
2.0     /* derivative time constant */
600.    /* LONG integral time constant */
0.      /* setpoint */
0       /* channel number */
[PID_SET] MACFILE FCALL

/* Average the cell pid derivative over a LONG time to prevent noise */
10 0 [PID_DERNUM] MACFILE FCALL

/* Tweak the ratio to forget the old relative bridge sensitivity data */
.49930 REL_RATIO SET_DATA
2.0 WAIT
.49920 REL_RATIO SET_DATA

/* ################## SETUP THE OUTPUT FILE ########################
Define the variables that we want to save to the data file.
The global varaible dbase defines the data output basename, also the
number of bins (on stk top).
Find the lowest unused filename/number */

-4 nbase
{
/* make the file name */
dup -3 nbase swap
     { dup 9 <= if
```

```
          tostr
          0 tostr swap cat
     } else {
          tostr
     }
     cat
     /* check for access */
     {
     dup [.dat] cat access 0 ==
          if
          swap dump 0
     } else {
          dump 1 + 1
     }
while
}

/* Use 3 point binning and set this is the output file name */
3 MY_INIT_FS

/* Define the individual data items (ignoring the subroutine error
return.) */
EXP_TIMER      MY_ITEM_FS dump      /* time */
LATENCY        MY_ITEM_FS dump      /* time between interrupt and
                                    activation */
END_TIMER      MY_ITEM_FS dump      /* time at end of interrupt service
                                    half seconds */
END_CLK        MY_ITEM_FS dump      /* time at end of interrupt service
                                    1/256 of a 1/2 second units */
ABS_BALRES     MY_ITEM_FS dump      /* Cell plat. therm. resistance */
REL_DRBAL      MY_ITEM_FS dump      /* Rel Bridge Imballance */
DIOD_VOUT0     MY_ITEM_FS dump    /* CTM diode voltage */
DIOD_VOUT1     MY_ITEM_FS dump    /* ITM diode voltage */
DIOD_VOUT2     MY_ITEM_FS dump    /* UTP diode voltage */
DIOD_VOUT3     MY_ITEM_FS dump    /* I. Shield diode voltage */
DIOD_VOUT4     MY_ITEM_FS dump    /* O. Shield diode voltage */
/* REL_INSENS MY_ITEM_FS dump       Relative bridge sensitivity */
REL_IPH        MY_ITEM_FS dump    /* Raw in phase rel. br. output,
                                                    unaveraged */
REL_QPH        MY_ITEM_FS dump    /* Raw quad phase rel. br. output,
                                                    unaveraged */
REL_RELAY      MY_ITEM_FS dump    /* Whether relay is on */
DTOA_REPA      MY_ITEM_FS dump    /* Power delivered to cell */
BAR_PRES       MY_ITEM_FS dump    /* Barocell pressure, zero shifted */
```

```
ROOMT_TEMP     MY_ITEM_FS dump     /* Room Temp C */
[MY_START_FS] MACFILE FCALL        /* ### Start writing data file ### */

/* ###################### REPORT DATA TO THE LOG FILE ################
make a macro to simplify the code */
[GET_DATA TOSTR CAT WRITELOG] [tmacro] macro

[START_TEMP=] CHEB_OUT0 tmacro          /* cell temp at start */
[REL_RATIO=] REL_RATIO tmacro           /* rel. br. ratio setting */
[REL_RATIO_RL=] REL_RATIO_RL tmacro     /* rel. br. ratio compensated
                                           for lead resistance */
[REL_RATIO_IM=] REL_RATIO_IM tmacro     /* ditto, immag. part */
[REL_DR=] REL_DR tmacro                 /* dr resistor resistance */
[REL_IZERO=] REL_IPH_ZR tmacro          /* relative bridge ch. zero */
[REL_QZERO=] REL_QPH_ZR tmacro          /* ditto for quad phase */
[REL_SENRAT=] REL_SENRAT tmacro         /* rel br. ch. sens. ratio */
[DTOA_POWB=] DTOA_REPB tmacro           /* power to CTM */
[BAR_ZERO=] BAR_ZERO tmacro             /* Barocell zero reading */
[tmacro] purge                          /* delete macro */

/* ############## MAIN LOOP, TAKING HEAT CAPACITY DATA ################

Initialize a stack variable the rel br. in phase raw output */
0.0
{
cheb_out0 get_data -2 nbase <                /* check if T > Tmax */
     while
     20.0 WAIT

     /* ##### ADJUST CELL PID PARAMETERS WHEN WE GO THRU BUMPS #######
     turn down the integral time constant if we are going thru
     a peak. turn up the gain to max of -.6
     (Proportional .max output about 9mW) */
     {
     /* Test if rel br. is in range */
     rel_drbal get_data abs 10. <
          if
          {
          /* compute how far |output| is over 5000 */
          rel_iph get_data todoub 32768. - abs
          5000. max 32000. min 5000. -

          /* change if more than 500 different from last time thru
          this loop */
```

```
          2 ndup - abs 500. >
               if

               /* reset the cell control parameters to make the output
               nonlinear */
               dup 27000. / dup -500. * 600. + swap
               -.5 * -.1 +

               /* Call subroutine to reset the cell control
               parameters.
               new gain on stack top */
               2.0             /* Derivative time constant */
               3 nover         /* Integral time constant */
               0.              /* Temperature control setpoint */
               0               /* Channel number */
               [PID_SET] MACFILE FCALL

               dump swap dump      /* setup for next iteration */

          } else {
               dump           /* if the output is not changed much
                              do nothing */
          }
     }
}
dump                          /* clean up stack variable */

/* ##################### END OF HEAT CAPACITY LOOP ################### */

FLUSH_FS     /* Stop taking data and flush out the data buffer */
DUMP

0. DTOA_POWB SET_DATA    /* Turn off the power to the ctm */

0.0 BAR_ZERO SET_DATA    /* unzero the barocell output */

4 [PID_OFF] MACFILE FCALL     /* turn off the shields' control */
5 [PID_OFF] MACFILE FCALL

EXIT                     /* return to the calling program */
/* ##################### END OF PRES02 ############################ */
```

Appendix B

Experimental Procedures and Data Reduction

This chapter will describe the thermometer calibration and data collection procedures and show how the final results were calculated. In short, to make a heat capacity run the calorimeter was first cooled down to below 65 K. Then, the standard heat capacity heater was set to a constant power input. All of the temperature control circuits were started. The sample cell drift rate settled down to about 2 K/hour. Data were recorded to the disk every 1.5 seconds until the sample cell reached 120 K. This procedure was under the total control of the computer, so no time was lost waiting for the operator to initialize the next mode of operation. In the sections below we will describe the procedures used to take the isotherm and heat capacity data, and how the film heat capacity was calculated.

B.1 Thermometer and Methane Vapor Pressure Calibration

The accuracy of the calorimeter relies on the total thermal isolation of the sample cell and the standard heat capacity. The isolation is provided by surrounding these bodies with temperature regulated shields and supports. The temperature of the shields and supports are reported by diode thermometers. These thermometers must be accurately calibrated in order to maintain thermal isolation. It was far too expensive to purchase a set of calibrated diode thermometers, so our homemade thermometers were calibrated against the calibrated platinum thermometer. The thermometer calibration also served three other purposes: calibrating the

two additional platinum thermometers with the calibrated platinum thermometer, measuring the triple point temperature of methane to provide a primary temperature calibration, and measuring the vapor pressure of methane as a function of temperature[1]. Measuring the methane triple point, T_3, was important because there was a question of whether the melting peaks in the thick films were near T_3. Also, the platinum resistor thermometer calibration was not guaranteed to be more accurate than $\pm.05\ K$. The vapor pressure of methane, P_o, was needed to improve the measurement of $(P - P_o)$, which is small for thick films. It was also possible to compare the normal boiling temperature against tabulated values [130] to give another temperature calibration point. The pressure gauge accuracy was confirmed by recording the vapor pressure of methane at T_3.

For the calibration, a special lower assembly was attached to the vacuum joint below the upper thermal platform. This assembly was identical to that used for calorimetry, except that the sample cell was replaced with a heavy copper triple point cell. The triple point cell was a four inch long by 1.25 inch diameter copper bar mounted to the fill tube with a miniature stainless steel indium o-ring flange. The methane was contained inside twelve 3/16 inch diameter blind holes drilled inside the block. The cell held about 13 ml of methane. Space for eight diode thermometers and several platinum thermometers was provided on the bottom of the block. The thermometer leads were thermally tempered by gluing several turns of wire around the copper block. An evanohm wire heater was wound around the center of the body. There was no platinum thermometer on the body directly above the triple point cell (standard heat capacity), and thermal isolation was provided by feedback temperature control derived from the diode thermometer outputs.

There is a puzzling problem in attaining a stable thermal environment for the thermometer calibrations. To calibrate the thermometers, the triple point cell must be thermally isolated to prevent any temperature gradients between the thermometers, or between the methane and the thermometers. The only way to provide adequate thermal isolation is to have a set of calibrated thermometers on the radiation shields and supports. Which comes first, the calibrated thermometers (chicken), or the calibration (egg)? Fortunately, the thermometers required for providing isolation during the calibration do not need to be calibrated very accurately because the thermal conductivity of the massive copper triple point

[1]There is no accurate, published methane vapor pressure data below the triple point that was made since the adoption of the revised temperature scale, IPTS-68.

cell prevented large temperature gradients. These thermometers were calibrated by filling the vacuum can with liquid nitrogen and measuring the normal boiling point and the triple point temperatures. The temperature scale was taken from a simple linear fit to these two points[2]. The sensitivity to the isolation temperature was assessed by altering the isolation environment temperature and noting the relative temperature changes between the thermometers to be calibrated.

The diode and platinum thermometer calibration was performed from 63 K to 120 K. The eight diode thermometers were compared against the calibrated platinum thermometer by using three spare interface channels and three data runs. The platinum thermometers were calibrated against each other by multiplexing the thermometers with a tree-switched, computer controlled relay box. One of the eight diode thermometers on the triple point cell was used to provide feedback to maintain the triple point cell at constant temperature. Once the cell was at constant temperature, the calibrated thermometer resistance was recorded for five minutes. Then an unknown thermometer resistance was recorded for ten minutes, followed by another five minute measurement of the calibrated thermometer resistance. The resistance of the unknown thermometer averaged over the ten minute period was calibrated by the average of the calibrated thermometer resistance from the five minutes of data taken before and after the unknown thermometer data. Thus, any linear drift in the temperature would be cancelled out.

The triple point temperature and the methane vapor pressure were recorded by first filling the cell with 5 ml of high purity liquid methane. The pressure was recorded every other degree from 65 to 120 K. While drifting from 90 to 92 K, a very small heat input was applied to the cell (.01 W). The temperature was constant to within $\pm.0015$ K for three hours while the methane melted. The calibrated platinum thermometer temperature scale was in error by -48 mK at T_3 and -53 mK at the normal boiling point, so the temperature scale was shifted +50 mK. The triple point pressure was within .06% of the tabulated value (87.727 torr). This is close to the rated accuracy of the barocell, so the pressure calibration was not changed. Note that other studies of multilayer films have calibrated the thermometers against the triple point found from the maximum of the heat capacity for the melting of a very thick film (50 layers) [37]. These calibrations are possibly inaccurate because the melting temperature may be shifted because the methane is confined in the spaces between the Grafoam platelets (capillary

[2]Future calibrations can take advantage of the calibrated thermometers to achieve a higher accuracy.

condensation). The bulk saturated vapor pressure of methane was found to agree with the function:

$$\ln P = \frac{A_0}{T} + A_1 + A_2 T + A_3 T^2 \tag{B.1}$$

with separate constants[3] above and below the triple point, 90.685 K.

The AD-590J temperature sensor on the gas handling system was calibrated against the calibrated platinum thermometer while both were held within a copper block. The room temperature readings should be accurate to better than .1 K.

B.2 Vapor Pressure Isotherms and Data Reduction

Because the first step in qualifying a new calorimeter is to measure the area of the substrate with vapor pressure isotherms, these measurements will be described first.

As described above, Hamilton [34] found the area of his Grafoam substrate by finding the number of atoms in a registered monolayer of helium. Since the substrate used for this experiment (28.87 g of Grafoam (Mat) in a 105.3 ml sample cell) was identical to Hamilton's substrate (13 g of Grafoam, 326 ± 1.4 m^2), but about twice as large, to measure the area of the substrate for this experiment, it was only necessary to compare a vapor pressure isotherm with one at the same temperature measured by Hamilton. The isotherms were performed at 95 K, where the vapor pressure is high enough to reduce the time required for the gas to permeate through the Grafoam and to increase the pressure measurement accuracy. Vapor pressure isotherms may be made by either adding or removing gas from the system. Since it was suspected that hysteresis is present in the methane isotherms, data were taken for both upward and downward isotherms. An upward isotherm was used to calibrate the surface area because capillary condensation would not be present (in the first monolayer), and because the error in

[3]The constants were found to be (for T in Kelvins, and P in torr)

	$T < T_3$	$T > T_3$
A_0	−1302.974	−1252.889
A_1	21.95361	21.53245
A_2	−.0534394	−.0479023
A_3	.0002110157	.0001340099

the amount of gas in the system would be reduced.

B.2.1 Upward Vapor Pressure Isotherms

The procedure for making the upward vapor pressure isotherms was totally automated by the computer. Gas was admitted into the system by opening a pneumatically actuated leak valve. The computer stabilized the temperature by controlling the pressure of the heat exchange gas that thermally coupled the sample cell to the cold inner bath, and by manipulating the parameters to the temperature control algorithms. Then the data were recorded for ten minutes and the dosing procedure was repeated until enough doses had been made. The procedure for taking a vapor pressure isotherm was coded in a reverse polish notation (RPN) language experiment control file, similar to that in appendix A.

The program to take the isotherms was started with all the instruments initialized and running, and the system containing a known number of methane molecules. The 2015 ml volume was filled with about an atmosphere of high purity methane gas. The manifold valves are set to isolate the manifold from all the ports except the barocell, and the heat capacity cell. The reference side of the barocell is constantly pumped by the turbopump. The steps used to take the data were as follows (refer to figure 4.10 for the plumbing details and figure 4.6 to identify the calorimeter bodies):

1. Initialize the outer bath and vapor trap filling tasks.
2. Setup the valves :
   - Close valve from manifold to turbo pump.
   - Close valve from 2015 ml volume to manifold (leak valve).
   - Close valve from 350 ml volume to manifold.
   - Close leak valve that supplies heat exchange gas to the probe vacuum can.
   - Open valve from the probe gas fill tube to the manifold.
   - Open cryogenic valve just above the sample cell.
   - Open valve from roughing pump to the heat switch.
   - Open the high vacuum valve to evacuate the probe vacuum can.

3. Turn off the probe fill tube heater.

4. Set up the parameters for the proportional-integral-derivative (PID) controls to prevent the fill tube from becoming colder than the sample cell. Control the temperature of the standard to equal the sample temperature. Control the isolation thermal mass (ITM) and the upper thermal platform (UTM) at .1 K above the standard temperature by comparison with the standard diode thermometer. Apply no heat input to the sample cell.

5. Warm up or cool down to the chosen isotherm temperature. If cooling down:

   - Turn on probe fill tube heater to 1 W.
   - Open the helium heat exchange gas leak valve to introduce gas into the probe vacuum space to begin cooling down. Close probe vacuum can high vacuum valve after introducing gas.
   - Turn on probe fill tube heater to 1 W to prevent cold spots on the fill tube that would condense gas while there is heat exchange gas in the probe vacuum can.
   - Close the cryogenic valve just above the sample cell to prevent the extra gas in the fill tube and manifold from condensing on the Grafoam.
   - Wait until the sample cell is below the chosen isotherm temperature.
   - Set the sample cell temperature control to maintain the temperature at .3 K below the isotherm temperature.
   - Wait for the standard to cool to near the sample temperature.

6. If warming up:

   - Set the cell temperature control to .5 K below the chosen isotherm temperature.
   - Wait until the temperature is within 1 K of the set-point.

7. Set the radiation shield temperature control to 3 K below the standard temperature.

8. Ready the data file recording by naming the data items that are to be saved.

9. MAIN DOSING LOOP: Check to see if there have been enough doses of gas added to the system. If so, proceed with the next task.

10. Precool the cell to .4 K below the isotherm temperature to prepare for heat pulse when new gas adsorbs on the Grafoam. Set cell temperature set-point to .4 K below isotherm temperature and inject heat exchange gas (1 μmHg) into probe vacuum can. Turn on fill tube heater to prevent cold spots.

11. Close probe to manifold valve on top plate of probe to prepare for dosing.

12. Wait one minute, then measure the pressure in the manifold. Calculate the pressure increase needed for minimum dose (should not be much above the saturated bulk vapor pressure at the sample cell temperature).

13. OPTIONAL: Zero the barocell pressure sensor.

14. Open the leak valve on the 2015 ml volume. Close it when the pressure is high enough.

15. Record the new and old pressure in the manifold, and the room temperature to a "log" file for later processing.

16. Open the valve at the probe top and the cell cryogenic valve to admit the gas into the sample cell. The cell temperature will jump up about .5 K for a 1/20 of a layer dose.

17. Wait until the cell is cooled to below the isotherm temperature.

18. Reestablish sample cell temperature control at the present temperature. Wait until the standard cools to no warmer than .1 K above the sample cell temperature.

19. Remove integral control from the sample cell to prevent overshooting the desired temperature.

20. Remove the probe vacuum can heat exchange gas and wait until the standard and cell are near the desired set-points. While waiting, if either is above the set-point temperature, add heat exchange gas to the probe vacuum can.

21. Exponentially ramp the cell temperature to the set-point over a ten minute period. Then replace all the integral time constants now that it is not possible to overshoot.

22. Wait for the sample gas pressure to come to equilibrium. Compare the pressure every ten minutes until two successive readings are equal to within the barocell pressure gauge error.

23. Wait another five minutes, then record 10 minutes of data to a binary (not ASCII) data file. Ten minutes is long enough to judge the pressure equilibrium.

24. Repeat the dosing procedure by restarting at step 9 above.

B.2.2 Downward Vapor Pressure Isotherms

The downward isotherms are similar to the upward isotherms except that a known quantity of gas is taken from the system by removing all the gas from the manifold while it is closed off from the sample cell. Because it was necessary to make heat capacity runs at specific total system number values on the desorption branch, the experiment program for the downward isotherms kept track of the total system number and removed gas until the desired amount was withdrawn.

Prior to running the downward isotherm program, all the instruments were initialized and the system contained a known number of methane molecules. The 350 ml volume was evacuated and the manifold valves set isolate the manifold from all the ports except the barocell and the heat capacity cell. The reference side of the barocell is constantly pumped by the turbopump. The arguments to the program are the initial number in the system, the maximum amount of gas allowed for a single withdrawal, and the amount of gas desired in the system at the end of the program. The following steps were used to take the data:

1. Include steps 1 through 9 in the upward isotherm above to stabilize the calorimeter at the isotherm temperature.

2. Check to see if the next minimum sized gas withdrawal will undershoot the target system number. If so, exit loop and program.

3. MAIN DOSING LOOP: Determine whether including the 350 ml volume in the withdrawal will remove more than the maximum amount of gas per dose. If not, open the valve between the 350 ml volume and the manifold to withdraw gas from the sample cell and turn off the cell temperature control to allow the temperature to stabilize before recontrolling.

4. Withdraw gas from the system. Close the probe to manifold valve on the top plate of the probe. Wait one minute and record the pressure in the manifold. Open the manifold to turbopump valve and pump out the manifold and 350 ml volume (if used) with the turbopump for ten minutes. After five minutes of pumping, recontrol the cell temperature at .1 K below the chosen isotherm temperature.

5. Rezero the barocell pressure gauge.

6. Record the pressure in the manifold before and after the withdrawal and the room temperature in a "log" file for later calculations. Keep track of the total number in the system.

7. Turn off the integral temperature control term on the standard, isolation thermal mass, and the inner shield. Turn off the sample cell temperature control.

8. Close the small calibrated volume, then open the probe to manifold valve and the cryogenic cell valve to measure the pressure in the system.

9. Wait one minute, then recontrol the cell temperature control without integral control.

10. Wait for the cell to come to within 2 mK of the isotherm temperature. While waiting, if either the sample cell or the standard is above the set-point temperature, add heat exchange gas to the probe vacuum can to cool down.

11. Include the integral control term on the cell temperature control.

12. Wait for the sample gas pressure to come to equilibrium. Compare the pressure every ten minutes until two successive readings are equal to within the barocell pressure gauge error. While waiting, if the sample cell temperature drifts above the set-point by more than 1 mK, send a short burst of heat exchange gas into the probe vacuum can to cool the cell slightly. Record the pressure, temperature, and time to an ASCII "log" file every ten minutes in order to monitor the time it takes to reach equilibrium.

13. Wait another five minutes, then record 10 minutes of data to a binary (not ASCII) data file. Ten minutes is long enough to judge the pressure equilibrium. While taking data, if the sample cell temperature drifts above the set-point by more than 1 mK, send a short burst of heat exchange gas into the probe vacuum can to cool the cell slightly.

14. Repeat the dosing procedure by restarting at step 2 above.

B.2.3 Vapor Pressure Isotherm Data Reduction

The data from the upward and downward vapor pressure isotherms are stored in two files. The first is a binary file that records the pressure, temperature, and time for ten minutes for each dose, after the pressure has come to equilibrium. The second file holds the pressure in the manifold and the room temperature before and after each dose of gas.

MS-DOS batch files run compiled 'C' programs that calculate the number in the film and the pressure for each isotherm point. The data for each ten minute period are averaged, and the standard deviation is computed by a 'C' program that manipulates the binary data using a library of functions that read and buffer the data file. The pressure and temperature stability for each isotherm point can be assessed by examining the standard deviations. The number in the manifold before and after each dose is calculated from the second file by a 'C' program that includes the second virial correction. This program finds the value of the fourth dependent variable given the values of the three independent variables out of P, V, T, and N. The second virial coefficient was calculated using experimental data from M.A. Byrne et al. [131] using an 18-6 Lennard-Jones potential and the methods outlined by J.O. Hirshfelder et al. [132, page 162 and 1119]. The total number in the system during each isotherm point is calculated by a 'C'

program that is compiled by the batch file. The volumes of the various parts of the plumbing are known by expanding gas to or from the 2015 ml calibrated volume, and monitoring the pressure before and after the expansion. The 2015 ml volume was measured by Hamilton [34] by filling it completely with water and noting the weight change.

B.3 Heat Capacity Measurements and Data Reduction

Two types of heat capacity data were taken. The first had the cryogenic cell valve closed to reduce the 3-D gas volume. This reduces the number of gas molecules needed to raise the pressure as the cell warms, thereby reducing the size of the desorption correction to the heat capacity data. The second type of data had the cryogenic cell valve open in order to monitor the vapor pressure with the barocell pressure sensor at room temperature. The procedures used by the two versions are the same except for a few additional steps used in the second type. The RPN experiment control program used to collect the data with the cell cryogenic valve open is in appendix A.

B.3.1 Experimental Procedure

Prior to the heat capacity run, all the instruments were initialized and the system contained a known number of methane molecules. It is assumed that the calorimeter is above the desired starting temperature for calorimetry and will need to cool down to take data. The manifold valves are set to isolate the manifold from all the ports except the barocell and the heat capacity cell in order to monitor the pressure in the cell. The reference side of the barocell is constantly pumped by the turbopump. The arguments to the program are the starting and ending temperatures for calorimetry, the file name (and number) to record the binary data to. The steps used to take the data were split into a film formation program and a heat capacity program. Films on the adsorption branch were made using the film formation program. Films on the desorption branch were made by running the downward isotherm program, shown above.

Film Formation Program

Starting with the entire gas handling system and sample cell pumped out, the 2015 ml calibrated volume was filled with gas at a certain pressure. Gas was transferred from the calibrated volume to the sample cell by cooling the sample cell to condense the gas on the Grafoam surfaces. While cooling, the pressure in the system was monitored, and the number of molecules in the sample cell, fill tube, and calibrated volume were periodically computed by the computer. When the proper amount of gas was drawn into the cell, the cryogenic sample cell valve was automatically closed. Then the cell was warmed rapidly until it reached 118 K. After waiting ten minutes, the pressure in the calibrated volume, manifold and fill tube were recorded in a "log" file. From the data in this file, the total number in the cell was calculated by finding the amount of gas that remained in the calibrated volume, manifold and fill tube and subtracting the total of these from the initial number of molecules in the calibrated volume. Successive heat capacity scans for thicker films on the adsorption branch were done by forming a thicker film using the film forming program to draw more gas out of the calibrated volume and into the sample cell.

The number of gas molecules in the fill tube is difficult to estimate because it is impossible to measure the fill tube's temperature profile accurately. An experiment was performed to determine the amount of gas in the fill tube as a function of the upper thermal platform temperature, assuming that the number was proportional to the pressure (ideal gas law). A known amount of gas was filled into the fill tube and the manifold. The temperature was allowed to drift from 90 to 120 K and the number in the fill tube was monitored. It was found than the amount of gas in the fill tube more strongly correlated with the temperature of the probe pump line than with the upper thermal platform temperature. The number in the fill tube varied from .119 STPCC/Torr to .127 STPCC/Torr. The number in the fill tube was approximated by a simple constant (.123 STPCC/Torr) times the pressure. The error in the number in the fill tube introduced by this simplification is very small, at most $\pm$.003 STPCC/Torr or $\pm$.02 layers of methane gas on the Grafoil surface when the pressure is 1000 Torr [4].

[4]Since the fill tube constant was first determined, the method of cooling the probe had changed so that the inner bath is not filled but holds a constant amount of liquid nitrogen. The fill tube temperature should be much more stable and it is possible that a better calibration could be made.

Heat Capacity Procedure

1. Set up the parameters for the proportional, integral, and derivative (PID) control to prevent the fill tube from becoming colder than the sample cell. Control the temperature of the sample to equal the standard temperature. Control the isolation thermal mass (ITM) and the upper thermal platform (UTP) at .1 K above the standard temperature by direct electrical comparison with the standard diode thermometer. Apply no heat input to the standard heat capacity or the radiation shields.

2. Initialize the outer bath and vapor trap filling tasks.

3. Set-up the valves to close off the cell prior to cooldown:

   - Close the cryogenic sample cell valve.
   - Close valve from the probe gas fill tube to the manifold.
   - Close valve from manifold to turbo pump.
   - Close valve from 2015 ml volume to manifold (leak valve).
   - Close valve from 350 ml volume to manifold.
   - Close leak valve that supplies heat exchange gas to the probe vacuum can.
   - Open the high vacuum valve to evacuate the probe vacuum can.
   - Open valve from roughing pump to the heat switch.

4. [5] Pump out the fill tube and manifold to prepare for eventually opening the cell cryogenic valve to measure the pressure during the heat capacity run. Pump out the fill tube when it is warm to prevent condensing the gas in the fill tube while cooling down.

   - Open valve from the probe gas fill tube to the manifold.
   - Wait two minutes, then record the gas pressure and room temperature.
   - Pump out the manifold with the turbopump for 10 minutes.
   - Record the pressure before and after pumping out the manifold and the room temperature to a "log" file.

[5] Step only used for runs with the cryogenic valve open to read the pressure.

- Close valve from the probe gas fill tube to the manifold to prevent losing the slight amount of gas that leaks through the cryogenic valve while cooling down.

5. Turn on the fill tube heater to prevent the gas that leaks past the cryogenic valve from condensing.

6. Introduce heat exchange gas into the probe vacuum can to cool down. Close the probe high vacuum valve after the gas is admitted.

7. Set up PID control for the standard heat capacity from a simple fixed set-point.

8. Cool-down loop: repeat until the sample cell is below the heat capacity temperature starting point. Every ten seconds, reduce the standard temperature control set-point gradually to allow the standard to cool at the rate of twelve hours from 120 to 65 K, with the temperature always greater that a curve proportional to T^4. Each loop iteration, the temperature set-point reduction will be equal to KT^3 where K is chosen to cool from 120 to 65 K in 12 hours. When cooled below 75 K, fill the heat switch with helium gas to allow the upper thermal platform to cool to a lower temperature.

9. [6] Pump out the fill tube again.

   - Set the barocell zero; the manifold has been pumped on while the calorimeter was cooling down.
   - Stop pumping on the manifold by closing the valve to the turbopump.
   - Open the probe to manifold valve, wait two minutes. then record the pressure in the manifold to measure the amount of gas that leaked past the cryogenic cell valve. Record the pressure and temperatures to the "log" file for future calculations.
   - Pump out the fill tube with the turbopump for ten minutes.

10. Remove the helium heat exchange gas from the probe, open the probe high vacuum valve, and turn off the fill tube heater.

[6] Step only used for runs with the cryogenic valve open to read the pressure.

11. Turn off the PID temperature control for the standard heat capacity and turn on the control for the radiation shields. Wait until the radiation shields are near to the standard temperature.

12. Refill the liquid nitrogen vapor traps and the probe outer bath.

13. Linearly ramp the standard heater power from zero to .045 W over a 15 minute period.

14. Evacuate the heat switch to isolate the upper thermal platform from the inner bath. This reduces the heat leak when the calorimeter is at higher temperatures, and also reduces the temperature noise on the UTP.

15. Wait until the cell temperature control stabilizes within about .5 mK. Then set the final cell control parameters, .1 Watts/Ohm integral term, two second derivative time constant, 600 second integral time constant.

16. Specify the names of the data variables to be reported to the binary data file. Begin recording data to the file as an average over the data from three clock cycles (1.5 seconds) to reduce the data file size.

17. Report the value of certain variables that will be used by the data reduction programs to the ASCII "log" file.

18. Take calorimetry data until the heat capacity scan is finished. During calorimetry, if passing through a phase transition has caused the cell temperature control error to become a large fraction of the relative resistance bridge dynamic range, increase the gain of the PID control channel and reduce the integral time constant. For large temperature control errors the temperature control is nonlinear. If the relative resistance bridge were to overload, data points would be lost.

19. Stop recording data to the binary data file.

20. Turn off the standard heat capacity heater power.

B.3.2 Optimum Sample Cell Temperature Control Parameters

During early testing of the instrument, it was determined that the parameters for the sample cell temperature regulation during calorimetry were not the same as the

parameters tuned for optimum temperature control. The reported heat capacity for the sample cell is proportional to the sample cell heater power, determined by the PID control algorithm [91]:

$$W_0(t) = G(T_{std} - T_{cell}) + \frac{G}{t_{integral}} \int_0^t (T_{std}(t') - T_{cell}(t'))dt' + G t_{derivative} \frac{d(T_{std} - T_{cell})}{dt}$$

where G is the proportional gain term[7] in Watts per K, $t_{integral}$ is the integral control term time constant in seconds, $t_{derivative}$ is the derivative control term time constant in seconds. If the temperature control error is to be minimized, the gain is set to about half the value at which the control system oscillates. The integral or "reset" term aids the control by eliminating the steady temperature control error that would be present in a purely proportional control circuit, but this term tends to make the control unstable. Temperature oscillations with a period longer than $t_{integral}$ are corrected by the integral control. The integral time constant is set to several times the longest system thermal time constant to prevent this term from destabilizing the control. The smaller the size of this time constant, the greater the effect of this term. The derivative time constant helps the system to respond to high frequency perturbations of the system by changing the heater power to damp out any sudden changes in the temperature. This term tends to stabilize the system, but since the derivative of noisy data is difficult to compute using digital electronics, this term is difficult to use. This term is typically set to the thermal time constant of the thermometer[8].

The magnitude of the sample cell temperature control error only affects the data through the heat leaks to the sample cell and the standard heat capacity. The derivative of the sample cell temperature control error with respect to time corrects the sample cell heat capacity for the errors in the temperature control. If there is a large amount of noise in the sample cell heater power, there will be noise in the data, because the sample heat capacity is found from equation 3.1. The amount of noise on the sample cell heater power is set by the noise in the relative resistance bridge and the values for the temperature control parameters. If the proportional term is higher, the noise will be larger. The derivative of noisy data tends to be very noisy, so $t_{derivative}$ cannot be very large. The noise on the

[7]This coefficient ideally should be divided by the sample cell heat capacity to make the units 1/seconds, and make the control parameters independent of the heat capacity.

[8]Analog temperature control is much better for computing the derivative term. This apparatus does not usually need to respond to high frequency temperature noise, so a digital control circuit is more convenient.

integral of the temperature error tends to be small compared to the noise in the data. To reduce the noise in the calorimetry data, the control was dominated by the integral control term. To find the correction for the sample heat capacity to compensate for the imperfections in the temperature control, the derivative of the temperature control term is computed by fitting a least squares cubic polynomial to the data over a three minute time period. Then if there were significant spectral components in the temperature control error with a period much less than three minutes, the computed derivative would be incorrect and a higher order fit would be required. More parameters in the fit increase the noise in the correction. Using primarily integral control reduces the high frequency variations in the heater power, which reduces the rapid fluctuations in the temperature control error and therefore improves the accuracy of the correction term to the heat capacity.

Setting the temperature control parameters far from the values that are optimum for minimizing the temperature control error can backfire when scanning through a large peak in the heat capacity. If the temperature control error becomes larger than the dynamic range of the relative bridge, the derivative of the error cannot be computed, the correction term to the heat capacity cannot be found, and a data point is lost. Since the purpose of the experiment is to measure the heat capacity of the peaks with high resolution, missing data points cannot be tolerated. Therefore, the gain term and integral terms for the temperature control are increased whenever the relative bridge output is a large fraction of the full scale output. The control is nonlinear when the temperature control error is large. When passing through a sharp, high peak, the parameters are adjusted to prevent loosing data points, but the rate change of the temperature control error can be so rapid that the computed temperature control derivative used to compute the heat capacity correction can be in error. In this case the reported data curves show strange oscillations just at the trailing edge of the heat capacity spike. These can be corrected by running the apparatus at a lower drift rate. Most of the data were collected without enabling nonlinear control, and only the thickest films required its use.

B.3.3 Data Reduction

Heat Capacity Data

The raw data from the heat capacity measurements are recorded in two files: a binary data file that holds the values of certain variables averaged over 1.5 seconds,

and an ASCII file (log file) that identifies the binary data file structure and the values of certain initial parameters for the experiment.

Since the experiment ran for as long as 28 hours, the interrupt rate for the software was 2 Hz, and as many as 85 bytes of data need to be recorded at every tick of the clock, the data files would be very large, (17 megabytes). Because the time for thermal equilibrium within the heat capacity cell was a minute or so, there was no need to record the data more often than every several seconds. To reduce the size of the data files, the data acquisition software could average any of the variables over a certain (odd) number of clock ticks, N. The variables that are not averaged are reported as a vector in the output file. All the data in this report were reported every three clock ticks and the data files were about six megabytes long. The data could have been averaged over a longer time without changing the results.

The variables reported to the output file were identified by symbolic names in the log file. A 'C' subroutine library allowed the data reduction programs to access the data items by the symbolic names, to hide the structure of the binary data file. The library also buffered the data file to allow the efficient use of data files that are longer than the computer memory. The variables typically reported during each data run were:

EXP_TIMER, LATENCY, END_TIMER, and END_CLK Variables that keep track of the time for each particular record in the output file.

ABS_BALRES Holds the resistance of the sample cell platinum thermometer as calculated by the absolute resistance bridge.

REL_DRBAL Resistance imbalance for the relative resistance bridge. Approximately proportional to the temperature difference between the sample and the standard.

DIOD_VOUT0 through DIOD_VOUT4 The voltages of the diode thermometers that provide isolation for the sample and standard as measured by the diode interface.

REL_IPH, REL_QPH, and REL_RELAY Raw data output from the relative bridge so that the data can be totally recalculated later.

DTOA_REPA Sample cell heater power.

BAR_PRES Autoranging barocell pressure gauge output, only reported for data runs with the cryogenic valve open.

ROOMT_TEMP Temperature of the gas handling system as measured by a calibrated AD-590[9] thermometer, only reported for data runs with the cryogenic valve open.

After each run was completed and during the film formation and cooldown for the next run, the data files were split into several smaller files and copied to floppy disks. The data were loaded on another computer, and the results were calculated by MS-DOS batch files in two stages. The first stage took the binary data files and output the intermediate results averaged over three minute time segments in ASCII format. The second stage found the film heat capacity from the intermediate results. The first stage required about 1/2 hour of computations on a 25 mHz Intel i486 computer and the second stage required only a few minutes. The raw data and first stage results were copied to a UNIX[10] computer over the campus network and backed up on 60 Mb tape cartridges. The steps used to compute the data for the first stage are (the numbers used to refer to the thermometers are found in figure 3.1):

1. Find the resistance of the platinum thermometer on the sample cell that is part of the differential thermometer, T1, by using a calibration curve and the resistance of the absolute thermometer on the sample cell, T0. A simple filter program evaluates the third order Chebyshev polynomial calibration function that finds the value of one platinum thermometer given the value of the other at the same temperature. The two thermometers resistances are related by:

$$R_1(T) = R_0(T)(1 + Ch_3(R_0(T))$$

where Ch_3 is a third order Chebyshev polynomial, $R_1(T)$ is the unknown thermometer resistance, and $R_0(T)$ is the known thermometer resistance. The value is computed for every input record and output to a new data file.

2. Find the value of the thermometer resistance on the standard heat capacity that is part of the differential thermometer, T2, by analysing the raw

[9] Analog Devices Inc.
[10] ATT Bell Labs.

data from the relative resistance bridge and the resistance of thermometer T1 (calculated in step 1 above). This allows the calculation of the standard heat capacity platinum thermometer resistance and the relative resistance bridge imbalance resistance. The relative bridge output and sensitivity is found from equations 4.1 and 4.2 :

$$V_o = (rR_1 - (1-r)R_0)\frac{A}{1+BR_1}$$

where A and B are complex constants, R_1 is a platinum thermometer on the standard (T2), and R_0 is the platinum thermometer on the sample cell (T1). A and B come from a least squares fit to the bridge sensitivity as a function of R_1, as described on page 79.

3. Find the sample cell temperature from the resistance of the sample cell platinum thermometer, T0, and the standard temperature from the thermometer resistance, T2 (found in step 2). A simple filter program evaluates the 20th order Chebyshev polynomial to give the sample temperature, and a 4th order Chebyshev polynomial to give the standard temperature.

4. Compute the integral of the sample cell heater power since the data was started. This value may be useful for finding the latent heat of phase transitions.

5. Find the average over a three minute time period of the all the items in the raw data and the results from the computations above. The average is computed by fitting a least squares cubic polynomial to a three minute segment of data. Report the average every three minutes so that each average is statistically independent. Store these in a separate binary data file.

6. Find the derivative with respect to time of the resistance of the platinum thermometer on the cell that is part of the differential thermometer, the relative resistance bridge resistance imbalance, and the standard and sample cell temperatures. The derivatives are computed by fitting the data to a cubic polynomial over a three minute segment of data. Report the derivatives every three minutes so that each output points are statistically independent.

7. Convert the averaged diode thermometer voltages to temperatures using a third order Chebyshev polynomial function. The results are used for diagnostic purposes.

8. If the cryogenic valve was open during the data run and the pressure was recorded, compute the derivative with respect to time of the pressure and the room temperature using the method described above. Convert the binary data to ASCII format and make a file containing the data needed to compute the desorption correction for this run.

9. Convert some of the data items to ASCII format and make a file that contains the information necessary for the next stage of the data reduction programs to compute the heat capacity of the cell.

The second stage of the data reduction uses another MS-DOS batch file to calculate the sample cell heat capacity. Some of the calculations are made by 'C' programs compiled by the batch file. The batch file calls a program that in turn calls the compiler to compile a subroutine that does the desired computations. The subroutine is linked to a precompiled main program to make the new data reduction program. When the batch file calls the new data reduction program, the main program loops through the input data files, calling the subroutine once for each line in the input files to compute the results. The 'C' code for the short subroutine is entered into a text file directly by the batch program so that the batch file contains all the computer code for the computations. This prevents the proliferation of small single purpose 'C' programs that are hard to maintain and document. The data reduction program can access any column from any number of input files, and output lines of data containing any number of output columns. This technique is more flexible than standard spreadsheet programs because any feature in the 'C' language library can be used and the batch file can take advantage of many different compiled programs.

There are two types of data runs. The first type of data run measures the heat capacity of the sample cell without a film, and the heat capacity of the standard. The second type of data run finds the heat capacity of the film using the data from the background run. The steps used to compute the film heat capacity and the sample cell heat capacity from the intermediate data produced by stage one are:

1. If this is a background run, compute the standard heat capacity for every point using equation 3.2. Then, the standard heat capacity is smoothed by fitting a least squares third order Chebyshev polynomial to the data. This polynomial will be used for the calculations of the standard cell heat capacity and to reduce other data runs with gas in the sample cell.

2. If this is a run with gas in the cell, use the background run polynomial fit to compute the standard heat capacity at every temperature point in the input data file (that was averaged over three minute segments by the first stage of data reduction).

3. Find the derivatives of the differential thermometer platinum resistance thermometers calibration curves, dT/dR for use in evaluating equation 4.3 to find the derivative of the temperature control error with respect to time. These are computed by differentiating the fourth order Chebyshev polynomial function.

4. Compute k in equation 4.3 from the data saved in the "log" file when the data run was started. This value depends on the relative resistance bridge ratiotransformer setting, and the ratiotransformer lead wire resistance correction that was computed when the bridge was initialized.

5. Calculate the heat capacity of the sample cell from the data computed in stage one and in the steps above. Evaluate equation 4.3 to find the derivative of the temperature control error with respect to time. Use this value to compute the heat capacity assuming no stray heat flow by evaluating equation 3.1.

6. If this is a background run, fit a least squares third order Chebyshev polynomial to the sample cell heat capacity to use for subtracting the background from the data from runs with a film.

7. If this is a run with a film in the sample cell, subtract the sample cell background heat capacity specified by the Chebyshev polynomial function from the specified background run to compute the film heat capacity.

Gas Desorption Correction

The desorption correction corrects for the energy required to expel the methane molecules from the film against the van der Waals force. The molecules leave the film to increase the vapor pressure of the 3-D gas as the temperature of the film increases. This correction can be calculated exactly using thermodynamics if

$$P, T, \left[\frac{\partial P}{\partial T}\right]_N, \left[\frac{dN_{film}}{dT}\right]_X$$

are known exactly at every point where the correction is desired. N represents the number of molecules in the film and does not equal the total number in the system. X represents the experimental path, $N(P(T(time)), T(time))$ traveled by the system as it is warmed. The total number of molecules in the gas plus film are constant.

The total heat capacity of the calorimeter with a film is equal to:

$$C_{tot} = C_{cell} + C_N + C_{Vg} - q_d\left[\frac{dN}{dT}\right]_X \tag{B.2}$$

after Elgin [55, page 49], Hamilton[34, page 29], and Dash [133, page 77]. N refers to the number of molecules in the film[11], C_{Vg} is the heat capacity of the gas in the sample cell at constant volume, C_N is the heat capacity of the film at constant N, and C_{cell} is the bare sample cell heat capacity. Note that this equation defines q_d implicitly. If the pressure is measured during the heat capacity run and the cell background heat capacity is known, all the quantities can easily be calculated to find C_N except for q_d. The desorption correction, q_d, is found by a complicated thermodynamic analysis to be equal to:

$$q_d = \frac{3}{2}k_bT + T\left[\frac{\partial \mu}{\partial T}\right]_N - \mu - 2PT\frac{dB}{dT} + e_{rot}(T) \tag{B.3}$$

after Elgin [55, page 51], Hamilton [34, page 29], and Dash [133, page 77]. The chemical potential of the system, μ, is known from the pressure and temperature of the 3-D gas, see equation 2.1. B is the second virial correction. The rotational energy per molecule (in Joules), $e_{rot}(T)$, can be calculated as described by Hamilton [34, page 76]. $[\frac{\partial \mu}{\partial T}]_N$ is found from equation 2.1 and the value of $[\frac{\partial P}{\partial T}]_N$.

[11]The precise location where the film starts and the gas begins has been a point of dispute for quite a while. For all practical purposes, the film takes up no volume in the system, so the number of molecules in the film can be easily found by subtraction. For a discussion of this point see Elgin [55, page 44].

There is no easy way to find the value of $[\frac{\partial P}{\partial T}]_N$, because during the heat capacity run, only $[\frac{dP}{dT}]_X$ is recorded. Any change in temperature will decrease N, so it is impossible to keep N constant. The pressure change due to the loss of the molecules in the film can be subtracted off if $[\frac{\partial P}{\partial N}]_T$ is known:

$$\left[\frac{\partial P}{\partial T}\right]_N = \left[\frac{dP}{dT}\right]_X - \left[\frac{\partial P}{\partial N}\right]_T \left[\frac{dN}{dT}\right]_X$$

(or from a similar equation in μ). $[\frac{\partial P}{\partial N}]_T$ is best found from careful vapor pressure isotherms. But differentiation of numerical data is difficult even under ideal circumstances, and the collection of vapor pressure isotherm data is very time consuming[12]. As mentioned by Hamilton [34, page 29], $[\frac{\partial P}{\partial T}]_N$ is very nearly equal to $[\frac{dP}{dT}]_X$ when the pressure is low (< 100 torr), because the amount of desorption is small. Hamilton made separate vapor pressure isotherms at one degree intervals in order to calculate the desorption correction for the heat capacity data (also taken every degree). In this study, the data are reported every .1 K, are much more accurate, and include measurements at much higher temperatures and pressures. It would take a considerable time to make vapor pressure isotherms every .1 K that would be accurate enough to correct these data for desorption without introducing large scatter.

Furthermore, it is not possible to use more widely spaced isotherms to calculate $[\frac{\partial P}{\partial N}]_T$ because when there is a sharp phase transition in the data, there is a sharp feature in $[\frac{\partial P}{\partial N}]_T$, as mentioned on page 21. Whenever the film is in a coexistence region, $[\frac{\partial P}{\partial N}]_T$ must be zero. In the real data, the phase transitions are very sharp, and interpolating the desorption correction between widely spaced vapor pressure isotherms would be inaccurate. The film heat capacity error caused by inaccurate values of $[\frac{\partial \mu}{\partial N}]_T$ at high temperatures is much larger because it will be proportional to the amount of gas desorption squared:

$$\Delta C_N = T\left[\frac{dN}{dT}\right]_X^2 \Delta\left[\frac{\partial \mu}{\partial N}\right]_T$$

and the amount of gas desorption increases rapidly as the film vapor pressure increases.

[12] A continuous method of collecting vapor pressure isotherm data may be more accurate for computing the derivative. Another barocell pressure gauge could be mounted on the calibrated volume and then gas could be leaked slowly into the system. Then the number in the system and the pressure would be known as a function of time. Similar techniques have been mentioned in the literature, although usually with (inaccurate) gas flow meters.

The data in this study were analysed without taking vapor pressure isotherms by using the pressure measurements taken during the data runs to make a two dimensional grid in T and N of pressure measurements. This grid is very finely spaced in T, but coarsely spaced in N, but was sufficient to calculate the desorption correction when T and P were low. At higher pressures and temperatures two approximations were used.

When the film is known to be passing through a first order phase transition and in a two phase region, $[\frac{\partial P}{\partial N}]_T$ must be zero, and the desorption correction can be computed because

$$\left[\frac{\partial P}{\partial T}\right]_N = \left[\frac{dP}{dT}\right]_X. \tag{B.4}$$

First order heat capacity peaks at high temperature and pressure were badly distorted when the coarse grid was used to calculate the desorption correction. C_N would even be found to be negative occasionally! But using this approximation, the peaks appeared as would be expected.

When the film is not clearly going through a first order phase transition, a model exists that allows a crude approximation to the desorption correction, the Frenkel-Halsey-Hill isotherm [134, 135, 136]

$$\mu - \mu_o = -\frac{\Delta C_3^{i\omega}}{d^3} \tag{B.5}$$

where i = l (liquid) or s (solid), d is the film thickness (usually in Å), and $\Delta C_3^{i\omega}$ is defined by Pettersen [36, page 93]. Equation B.5 can be used to estimate the desorption correction because according to this approximation

$$\left[\frac{\partial(\mu - \mu_o)}{\partial T}\right]_N = 0 \tag{B.6}$$

so that

$$\left[\frac{\partial \mu}{\partial T}\right]_N = \left[\frac{\partial \mu_o}{\partial T}\right]_N.$$

However, Hamilton [34, page 62,63] has clearly shown that the vapor pressure isotherms for methane on Grafoil do not fall exactly on a universal curve, and equation B.6 is not true everywhere. But it will be seen from the data that this approximation is much better than using the coarse grid at high temperatures and pressures. The nature of this approximation can be found by a simple manipulation of equation B.3. Equation 2.1 gives the chemical potential of methane gas as a function of the pressure and temperature. The value of $[\frac{\partial \mu}{\partial T}]_N$ as a function of

T, P, and $[\frac{\partial P}{\partial T}]_N$ is

$$\left[\frac{\partial \mu}{\partial T}\right]_N = k_b \log\left(\frac{1}{k_b}\left(\frac{2\pi\hbar^2}{mk_b}\right)^{3/2}\frac{P}{T^{5/2}}\right) - \frac{5}{2}k_b + P\frac{dB(T)}{dT} + \frac{d\mu_{rot}(T)}{dT} + \left[\frac{\partial P}{\partial T}\right]_N\left(\frac{k_bT}{P} + B(T)\right). \quad \text{(B.7)}$$

Eliminating the logarithmic term from equation B.7 using equation 2.1 and multiplying by T gives:

$$0 = \mu - T\left[\frac{\partial \mu}{\partial T}\right]_N - \frac{5}{2}k_bT + \left[\frac{\partial P}{\partial T}\right]_N\left(\frac{k_bT^2}{P} + TB(T)\right) + \left(T\frac{d\mu_{rot}(T)}{dT} - \mu_{rot}\right) + P\left(T\frac{dB(T)}{dT} - B(T)\right)$$

This equation is true for any P and T where methane exists as a gas, therefore it is also true along the coexistence lines between gas and solid or liquid:

$$0 = \mu_o - T\frac{d\mu_o}{dT} - \frac{5}{2}k_bT + \frac{dP_o}{dT}\left(\frac{k_bT^2}{P_o} + TB(T)\right) + \left(T\frac{d\mu_{rot}(T)}{dT} - \mu_{rot}\right) + P_o\left(T\frac{dB(T)}{dT} - B(T)\right)$$

Adding this complicated form of zero to the equation B.3 for q_d, realizing that $e_{rot} = \mu_{rot} - T\frac{d\mu_{rot}}{dt}$ [34, page 79] and rearranging gives:

$$q_d = \frac{dP_o}{dT}\left(\frac{k_bT^2}{P_o} + TB(T)\right) - k_bT - (\mu - \mu_o) + T\left[\frac{\partial(\mu - \mu_o)}{\partial T}\right]_N + P_o\left(3T\frac{dB(T)}{dT} - B(T)\right).$$

But $(k_bT^2/P_o + TB(T))$ equals the virial approximation of Tv, where v is the specific volume of the gas. Then the Clausius-Clapyeron [113, page 256] equation shows that the first term in the expression for q_d is equal to the latent heat of fusion of methane gas, assuming that the specific volume of the condensed phase is zero. The latent heat of fusion minus k_bT is a good first approximation to q_d, since

$$q_d = q_{st} - k_bT = Tv\left[\frac{\partial P}{\partial T}\right]_N - k_bT$$

from reference [55, page 50,51], ignoring the virial terms, and where q_{st} is the isosteric heat of adsorption defined by $[\frac{\partial P}{\partial T}]_N = N_g q_{st}/(TV)$. There are two significant correction terms to this approximation to q_d, ignoring $B(T)$. The first,

$-(\mu - \mu_o)$, is simply the difference in the free energy per particle between the film and the condensed bulk phase, a sensible contribution to the approximation. The second term, $T[\frac{\partial(\mu-\mu_o)}{\partial T}]_N$, is zero in any model where $\mu - \mu_o = f(N)$, for example the Frenkel-Halsey-Hill approximation, equation B.5. Hamilton [34, equation 8, page 63] discusses the significance of such a model, but it is not clear what the derivative of $(\mu - \mu_o)$ with respect to temperature would contribute to this approximation for q_d.

This approximation for q_d works much better than computing the derivatives from the coarse pressure grid at high temperature (T > 100 K), but it is especially bad when passing through the triple point temperature, where there is a discontinuity in $d\mu_o/dT$. Then, there is a discontinuity in the calculated desorption correction, as will be seen in the next chapter.

Appendix C

Capillary Condensate Melting Curve Model

During the progress of this experiment, Professor David Goodstein conceived a model for the melting temperature (as a function of the 3-D vapor pressure) for capillary condensate inside a porous solid. This model is closely related to an argument given by Defay and Prigogine [104, page 252], but it can be extended further to consider the case where the solid or liquid capillary condensate does not wet the uniform film. The derivation of this model depends on the exact geometry of the pore, and only pores with straight walls will be considered here (cylinders and channels).

The chemical potential of the capillary condensate is shifted from that of bulk matter, as stated by the Kelvin equation [25, 3]:

$$\mu - \mu_i = -\frac{v_i \sigma_{ig}}{D} \tag{C.1}$$

i is l or s (bulk liquid or solid), v is the specific volume of the bulk phase in the capillary, and D is given by $1/D = 1/R_1 + 1/R_2$. R_1 and R_2 are the Gaussian radii of curvature of the interface between the condensate and its vapor (concave when D is positive). Figure C.1 (upper left) shows a cylindrical pore that is partially filled with capillary condensate. Then $D = R/2$, where R is the condensate-vapor radius. The pore radius can be related to the interface radius through the contact angle, θ_i, $R_p = R\cos\theta_i$. Then, equation C.1 can be written as

$$\mu = \mu_i(T, R_p) = \mu_i(T) - \frac{2 v_i \sigma_{ig}}{R_p} cos\,\theta_i \tag{C.2}$$

for cylindrical pores. Note that θ is zero when the capillary condensate wets the pore wall. The liquid and/or solid may or may not wet the pore wall.

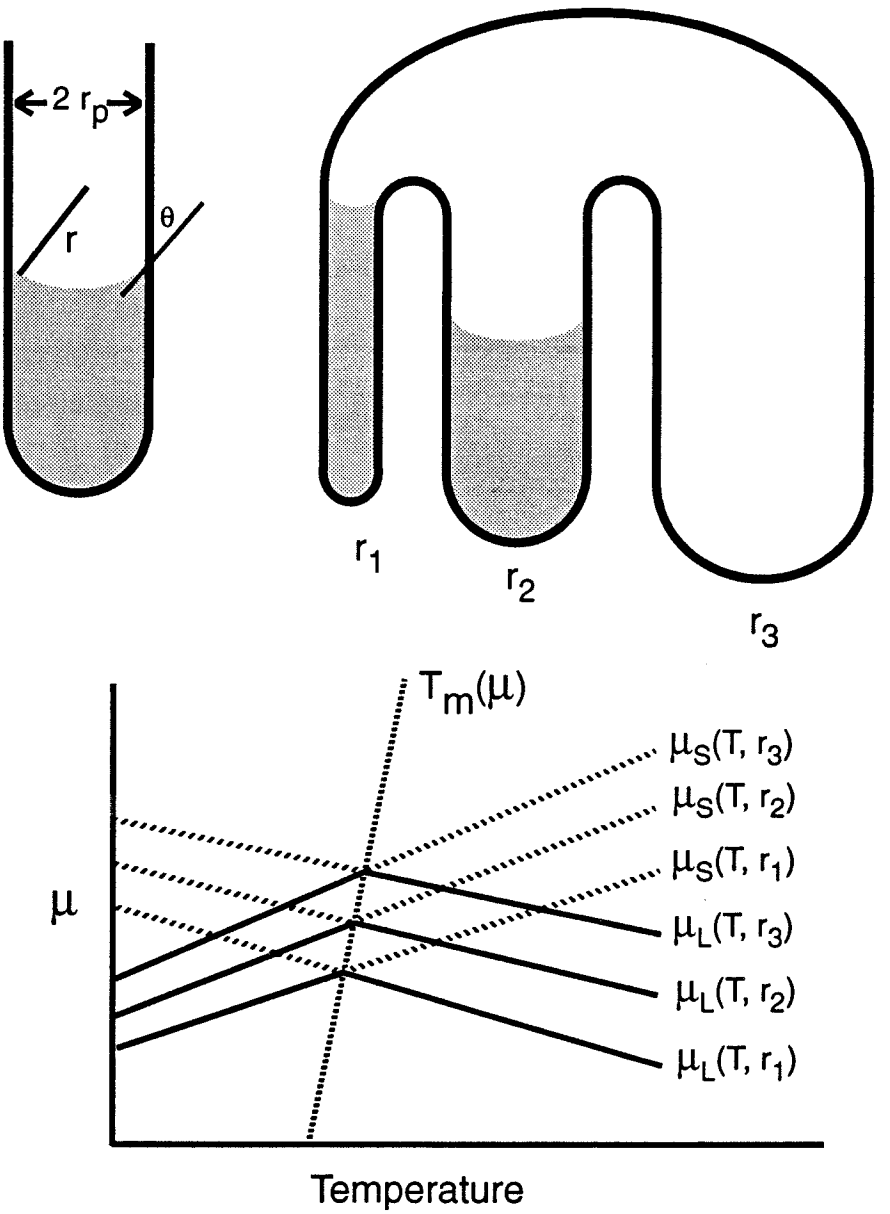

Figure C.1: Upper Left: capillary condensate in cylindrical pore of radius r_p, vapor-condensate radius r, and contact angle θ. Upper Right: hypothetical system with three cylindrical pores with radii $r_1 < r_2 < r_3$. The number in the system is fixed and pore 2 is shown partially filled. Lower: Chemical potential versus temperature diagram with curves for three cases, pores 1, 2, and 3 partially filled with solid or liquid.

The upper right part of figure C.1 shows a closed system consisting of three cylindrical pores with different radii. If matter is slowly added to this system with the temperature far below the bulk triple point temperature, the chemical potential increases and eventually reaches $\mu = \mu_s(T, r_1) = \mu_{os}(T) - 2v_s\sigma_{sg}cos\theta_s/r_1$. At this point the smallest pore begins to fill. Then, if more matter is added to the system, the pore fills at constant chemical potential, until the vapor-interface surface reaches the mouth of the pore. When the pore becomes "overfilled", the vapor-interface radius increases and the chemical potential rises above $\mu_s(T, r_1)$. Adding more matter will increase the chemical potential until it reaches $\mu_s(T, r_2)$, where the second pore fills at constant chemical potential. Note that the condensate-vapor radius of the first pore continues to increase in order to match the higher chemical potential. Throughout this discussion, the solid-vapor interface is considered to be fully roughened and therefore able to form a cylindrical meniscus. Figure C.1 shows the system with the second pore partially filled.

If the temperature rises, with the number of molecules held fixed, the solid capillary condensate in the second pore will melt. The stable phase at a given value of temperature and pressure is the one with the lowest chemical potential[1]. The bottom of figure C.1 shows the chemical potential as a function of temperature for the system with solid or liquid partially filling either the first, second or third pores. When, for example, the second pore is filled, the first (smaller) pore is overfilled and the third (larger) pore is empty. As the temperature rises, the system will exist in the lowest chemical potential state that is accessible. The chemical potential of the system equals $\mu_s(T, r_2)$ until $\mu_s(T, r_2) = \mu_l(T, r_2)$, when the solid capillary condensate will melt. This defines the melting temperature, $T_m(\mu)$, at the chemical potential where melting occurs inside a pore with radius r_2. Notice that the chemical potential for liquid in the smaller pore, $\mu_l(T, r_1)$, intersects the chemical potential path of the system when the second pore is filled with solid, $\mu_s(T, r_2)$. However, the smaller pore does not melt at the point of intersection because it is overfilled with solid that acts as if the pore was wider.

By examining the melting temperature of the entire range of pore sizes, the melting curve, $T_m(\mu)$ can be traced out. $T_m(\mu)$ can be found from equation C.2:

$$\mu = \mu_s(T) - \frac{2v_s\sigma_{sg}}{R_p}cos\theta_s = \mu_l(T) - \frac{2v_l\sigma_{lg}}{R_p}cos\theta_l.$$

Then, using a well known relationship between the slopes of the bulk sublimation

[1]Equivalent to the phase with the lowest Gibbs free energy per particle.

and evaporation curves,

$$\mu_s(T) - \mu_l(T) = L\frac{(T_m - T_3)}{T_3} = \frac{2v_s\sigma_{sg}}{R_p}cos\,\theta_s - \frac{2v_l\sigma_{lg}}{R_p}cos\,\theta_l$$

where L is the bulk latent heat per molecule. Since the melting occurs in a partially filled pore, the pore radius, R_p, can be found from the chemical potential using equation C.2: $1/R_p = (\mu - \mu_s)/(-2v_s\sigma_{sg}cos\theta_s)$. Then, the melting temperature can be written as a function of the chemical potential

$$T_m = T_3 + T_3\frac{\mu - \mu_s(T)}{L}\left(1 - \frac{v_s\sigma_{sg}cos\,\theta_s}{v_l\sigma_{lg}cos\,\theta_l}\right). \tag{C.3}$$

It is clear that T_m is a linear function of μ that limits toward T_3 as μ approaches μ_s.

The assumptions made in solving this model are:

- The solid forms a perfect circular meniscus rather than flat facets.
- The uniform film has a negligible thickness compared with the pore size.
- The Kelvin equation is valid for the pore size used, the solid and liquid surface tensions and the molar volume of solid and liquid capillary condensate are constant, and independent of the pore size and temperature. In other words, the matter in each pore is characterized by a single number, the radius of curvature of the condensate-vapor interface, $1/D = 1/R_1 + 1/R_2$, whatever the pore shape or size is.
- The chemical potential difference between the bulk solid and liquid ($\mu_s - \mu_l$) can be approximated at the melting temperature with a linear extrapolation of the properties at the triple point.
- The contact angle between the condensate and the pore wall must be constant with regard to changes in temperature and the adsorbed film thickness.
- The pores have parallel walls, for example, slits or cylinders.

Depending on the specific application of this model, each of these assumptions may or may not be valid.

Note that this theory is valid even if the condensate melts by first forming a liquid layer on top of the solid inside the pore [104, page 254-255]. In this

case, σ_{sg}, in equation C.3, should be replaced by $\sigma_{lg} + \sigma_{ls}$. The modified melting curve will be true only if a liquid layer is thick enough that the condensate-vapor surface interface surface tension and the liquid layer-solid condensate interface surface tension are equal to the bulk values (when the liquid layer thickness is greater than about 100 Å). The melting curve then predicts the temperature at which the majority of the capillary condensate melts. Before reaching the melting temperature, $T_m(\mu)$, a fraction of the solid capillary condensate will melt to form the liquid layer.

Bibliography

[1] Hyung Kook Kim. *Thermodynamic Study of Ethylene and Methane Adsorbed on Graphite.* PhD thesis, Pennsylvania State University, State College, Pennsylvania, December 1985.

[2] H.K. Kim, Q.M. Zhang, and M.H.W. Chan. Thermodynamic study of monolayer methane on graphite. *Phys. Rev. B*, 34(7):4699–4709, October 1986.

[3] Stephen Brunauer and L.E. Copeland. Surface tension, adsorption. In E. U. Condon and Hugh Odishaw, editors, *Handbook of Physics*, pages 5–90. McGraw-Hill, New York, second edition, 1967.

[4] G. Zimmerli and M.H.W. Chan. Complete wetting of helium on graphite. *Phys. Rev. B*, 38(13):8760–8766, November 1988.

[5] H.S. Nham and G.B. Hess. Ellipsometric study of krypton, methane, and argon films on graphite: How complete is wetting? *Langmuir*, 5(3):575–582, 1989. Presented at the symposium on "Adsorption on Solid Surfaces", 62nd Colloid and Surface Science Symposium.

[6] Stephen Brunauer, P.H. Emmett, and Edward Teller. Adsorption of gases in multimolecular layers. *J. Am. Chem. Soc.*, 60:309–319, February 1938.

[7] Y. Larher and F. Angerand. The roughening temperature of the densest crystal face of Ar, Kr, CO, CH_4 derived from multilayer adsorption studies. *Europhysics Letters*, 7(5):447–451, November 1988.

[8] R. Marx and E.F. Wassermann. Heat capacity study of the first monolayer of adsorbed methane on Grafoil. *Solid State Comm. (USA)*, 40(10):959–961, December 1981.

[9] A. Thomy and X. Duval. Adsorption of simple molecules on graphite I Homogeniety of the surface of exfoliated graphite, originality and complexity of adsorption isotherms. *J. Chim. Phys.*, 66(11-12):1960–1973, November 1969. In French.

[10] A. Thomy and X. Duval. Adsorption of simple molecules on graphite II Variation of the adsorption potential as a function of the number of adsorbed layers. *J. Chim. Phys.*, 67(2):286–290, February 1970. In French.

[11] A. Thomy and X. Duval. Adsorption of simple molecules on graphite III passage of the first layer through successive states. *J. Chim. Phys.*, 67(6):1101–1170, June 1970. In French.

[12] C. Bockel, A. Thomy, and X. Duval. Comparative study of the first adsorption layer of methane on boron nitride and graphite. *Surf. Sci.*, 90(1):109–120, December 1979.

[13] A. Thomy, X. Duval, and J. Regnier. Two-dimensional phase transitions displayed by adsorption isotherms on graphite and other lamellar solids. *Surf, Sci. Rep.*, 1:1–38, June 1981.

[14] P. Vora, S K. Sinha, and R.K. Crawford. Neutron-diffraction study of phases of CD_4 monolayer films on graphite. *Phys. Rev. Lett.*, 43(10):704–708, September 1979.

[15] J.P. Coulomb, R. Kahn, and M. Bienfait. Study of the mobility of a two-dimensional hypercritical fluid by cold neutron quasi-elastic scattering. *Surf. Sci.*, 61(1):291–293, January 1976.

[16] J.P. Coulomb, M. Bienfait, and P. Thorel. Study of the mobility of a hypercritical two-dimensional fluid by quasi-elastic neutron scattering. *J. de Physique Colloq.*, 38(C-4):31–37, October 1977.

[17] M. Bienfait. Two-dimensional melting and polymorphism in adsorbed phases. *Surf. Sci.*, 89:13, 1979.

[18] A. Glachant, J.P. Coulomb, M. Bienfait, and J.G. Dash. A first order two-dimensional melting transition: methane adsorbed on (0001) graphite. *J. de Physique Lett.*, 40L(20):543–545, October 1979.

[19] J.P. Coulomb, M. Bienfait, and P. Thorel. Mobility measurements of two kinds of two-dimensional fluids adsorbed on graphite. *J. de Physique*, 42(2):293–306, February 1981.

[20] I. Marlow, R.K. Thomas, T.D. Trewern, and J.W. White. Neutron scattering and physisorption. *J. de Physique Colloq.*, 38(C-4):19–25, October 1977.

[21] M.W. Newberry, T. Rayment, M.V. Smalley, and R.K. Thomas. Rotational tunneling of methane on the surface of graphitized carbon blacks studied by neutron scattering spectroscopy. *Chem. Phys. Lett.*, 59(3):461–466, December 1978.

[22] G. Bomchil, A. Hüller, T. Rayment, S.J. Roser, M.V. Smalley, R.K. Thomas, and T.K. White. The structure and dynamics of methane adsorbed on graphite. *Phil. Trans. R. Soc. Lond. B*, 290:537–552, 1980.

[23] Robert L. Elgin and David L. Goodstein. ^{4}He on Grafoil: The melting transition. In John G. Daunt and E. Lerner, editors, *Monolayer and Submonolayer Helium Films*, pages 35–52, New York and London, 1973. Cryogenics Center, Stevens Institute of Technology, Plenum Press.

[24] Michael Bretz. Specific heat of 2nd layer He^4 films. In John G. Daunt and E. Lerner, editors, *Monolayer and Submonolayer Helium Films*, pages 11–18, New York and London, 1973. Cryogenics Center, Stevens Institute of Technology, Plenum Press.

[25] W. Thomson. *Phil. Mag.*, 42(4):448, 1871.

[26] Kittur Subba Rao. Scanning of the hysteresis loop. Titania gel-water system. *J. Phys. Chem.*, 45:500, 506, 513, 517, 1941.

[27] A. Graham Foster. Sorption hysteresis. Part II The rôle of the cylindrical meniscus effect. *J. Chem. Soc.*, pages 1806–1812, 1952.

[28] Leonard H. Cohan. Sorption hysteresis and the vapor pressure of concave surfaces. *J. Amer. Chem. Soc.*, 60:433–435, February 1938.

[29] P.C. Carman and F.A. Raal. Physical adsorption of gases on porous solids. i. comparison of loose powders and porous plugs. *Proc. Royal Soc.*, 209A:59–69, 1951.

[30] D.H. Everett. Adsorption hysteresis. In E. Alison Flood, editor, *The Gas Solid Interface.* Marcel Decker Inc., New York, 1967. Chapter 36.

[31] S.J. Gregg and K.S.W. Sing. *Adsorption, Surface Area and Porosity.* Academic Press Inc., London and New York, first edition, 1967.

[32] J.W. Sutherland. The usefulness of measurements of the physical adsorption of gases in characterizing carbons. In R.L. Bond, editor, *Porous Carbon Solids.* Academic Press, London and New York, 1967. Chapter 1.

[33] D.H. Everett and F.S. Stone, editors. *The Structure and Properties of Porous Materials.* Academic Press Inc. and Butterworth's Scientific Publications, New York and London, 1958.

[34] Jeffrey John Hamilton. *A Thermodynamic Study of Methane Multilayers Adsorbed on Graphite.* PhD thesis, California Institute of Technology, Pasadena, California, May 1983.

[35] M.S. Pettersen, Mark J. Lysek, and D.L. Goodstein. The multilayer melting transition in methane adsorbed on graphite. *Surf. Sci.*, 175:141–156, 1986.

[36] Michael S. Pettersen. *Melting of Methane Adsorbed on Graphite Studied by Nuclear Magnetic Resonance.* PhD thesis, California Institute of Technology, Pasadena, California, May 1988.

[37] D.M. Zhu and J.G. Dash. Surface melting and roughening of adsorbed argon films. *Phys. Rev. Lett.*, 57(23):2959–2962, December 1986.

[38] J.A. Morrison and L.E. Drain. The heat capacity of multimolecular layers of adsorbed argon. *J. Chem. Phys.*, 19(8):1063, August 1951.

[39] J. Piper and J.A. Morrison. Heats of adsorption of methane multilayers on graphite. *Phys. Rev. B*, 30(6):3486–3489, September 1984.

[40] A. Inaba and J.A. Morrison. The wetting transition and adsorption/desorption hysteresis for the CH_4/graphite system. *Chem. Phys. Lett.*, 124(4):361–364, February 1986.

[41] A. Inaba, Y. Koga, and J.A. Morrison. Multilayers of methane adsorbed on graphite. *J. Chem. Soc., Faraday Trans. II*, 82(10):1635–1646, October 1986. Also see discussion on pages 1820-1826.

[42] A. Inaba, J.A. Morrison, and J.M. Telfer. Critical wetting of graphite by krypton and xenon. *Molecular Physics*, 62(4):961–969, November 1987.

[43] F. Ser, Y. Larher, and B. Gilquin. Multilayer adsorption of xenon and argon on graphite, Wetting behavior. *Molecular Physics*, 67(5):1077–1084, August 1989.

[44] T. Meichel, P.T. Dawson, J.A. Morrison, D.E. Sullivan, and Y. Koga. Adsorption of ethylene on graphite near saturation: Wetting transition/capillary condensation. *Langmuir*, 6(10):1579–1584, October 1990.

[45] J.Z. Larese and Q.M. Zhang. Layer-by-layer melting of argon films on graphite: A neutron diffraction study. *Phys. Rev. Lett.*, 64(8):922–925, February 1990.

[46] K. Morishige, K. Kawamura, M. Yamamoto, and I. Ohfuji. Capillary condensation of Xe on exfoliated graphite. *Langmuir*, 6(8):1417–1421, August 1990.

[47] J.Z. Larese, M. Harada, L. Passell, J. Krim, and S. Satija. Neutron-scatttering study of methane bilayer and trilayer films on graphite. *Phys. Rev. B*, 37(9):4735–4742, March 1988.

[48] M. Bienfait, P. Zeppenfeld, J.M. Gay, and J.P. Palmari. Surface melting on the close-packed (111) face of methane thin films condensed on graphite. *Surf. Sci.*, 226(3):327–338, March 1990.

[49] David L. Goodstein, J.G. Dash, and W.D. McCormick. Phase change in adsorbed helium at low temperature. *Phys. Rev. Lett.*, 15(10):447–449, September 1965.

[50] David L. Goodstein, W.D. McCormick, and J.G. Dash. Sintered copper sponges for use at low temperatures. *Cryogenics*, 6(3):167–168, June 1966.

[51] Andre Thomy and Xavier Duval. Isotherms d'adsorption de krypton sur differents graphites exfolies. *Comptes Rendus*, 259(22):4007–4009, November 1964.

[52] Grafoam is a registered trademark of the Union Carbide Corporation for expanded graphite products.

[53] R.J. Bergeneau, P.A. Heiney, and J.P. Pelz. High resolution x-ray studies of monolayer krypton on varied forms of graphite. *Physica (Utrecht)*, 109/110B:1785–1795, 1982.

[54] C. Uher. Thermal conductivity of several exfoliated graphites from 2 K to 300 K. *Cryogenics*, 20(8):445–447, August 1980.

[55] Robert Lawrence Elgin. *The Thermodynamics of the ^{4}He Submonolayer Film Adsorbed on Grafoil.* PhD thesis, California Institute of Technology, Pasadena, California, May 1973.

[56] Jeffrey J. Hamilton and David L. Goodstein. Thermodynamic study of methane multilayers adsorbed on graphite. *Phys. Rev. B*, 28(7):3838–3848, October 1983.

[57] David L. Goodstein, Jeffrey J. Hamilton, Mark J. Lysek, and G. Vidali. Phase diagrams of multilayer adsorbed methane. *Surf. Sci.*, 148:187–199, 1984.

[58] H.S. Nham and G.B. Hess. Layer critical points of multilayer ethane adsorbed on graphite. *Phys. Rev. B*, 38(7):5166–5169, September 1988.

[59] J.H. Campbell, M. Bretz, and M.H.W. Chan. A micro-calorimeter for monolayer films. In U. Eckern, A. Schmid, W. Weber, and H. Wühl, editors, *Proceedings of the 17th International Conference on Low Temperature Physics, LT-17*, pages 1165–1166, Amsterdam-Oxford-New York-Tokyo, August 1984. The International Union of Pure and Applied Physics, North-Holland.

[60] P. Taborek and D.L. Goodstein. Control of ultralow pressures: an absolute thermodynamic manometer. *Rev. Sci. Instrum.*, 50(2):227–230, February 1979.

[61] David L. Goodstein. *States of Matter.* Prentice-Hall, Englewood Cliffs, New Jersey, 1975.

[62] Rudolf Marx. Calorimetric studies of phase transitions in two-dimensional physisorbed films. *Physics Reports*, 125(1):1–67, August 1985.

[63] J.W. Riehl and K. Koch. NMR relaxation of adsorbed gases: Methane on graphite. *J. Chem. Phys.*, 57(5):2199–2208, September 1972.

[64] Jeffrey H. Quateman and Michael Bretz. Dynamics of methane monolayers adsorbed on graphite. *Phys. Rev. Lett.*, 49(20):1503–1507, November 1982.

[65] Jeffrey H. Quateman and Michael Bretz. Nuclear-magnetic-resonance study of methane adsorbed on graphite. *Phys. Rev. B*, 29(3):1159–1175, February 1984.

[66] Peter W. Stephens, Paul A. Heiney, Robert J. Birgeneau, Paul M. Horn, David E. Moncton, and George S. Brown. High-resolution x-ray scattering study of the commensurate-incommensurate transition of monolayer Kr on graphite. *Phys. Rev. B*, 29(6):3512–3532, March 1984.

[67] T.L. Hill. Physical adsorption and the free volume model for liquids. *J. Chem. Phys.*, 17(6):590, June 1949.

[68] Comité International des Ponds et Mesures. The international practial temperature scale of 1968. *Metrologia*, 5(2):35–44, April 1969. Also see pages 45-49.

[69] Guy K. White. *Experimental techniques in low-temperature physics.* Oxford University Press: London, Clarendon Press: New York, third edition, 1979.

[70] P. Sullivan and G. Seidel. Steady state ac-temperature calorimetry. *Phys, Rev.*, 173(3):679–685, September 1968.

[71] M.J. Buckingham, C. Edwards, and J.A. Lipa. A high precision scanning ration calorimeter for use near phase transitions. *Rev. Sci. Instrum.*, 44(9):1167–1172, September 1973.

[72] J.W. Loram. A new high-precision continuous-heating differential calorimeter for the temperature range 1.5 K to 300 K. *J. Phys. E*, 16:367–376, 1983.

[73] W.V. Johnson and G.W. Lindberg. Stability and calibration of miniature platinum resistance thermometers. *Rev. Sci. Instrum.*, 39(12):1925–1928, December 1968.

[74] M.S. Pettersen, M.J. Lysek, and D.L. Goodstein. Melting in multilayer adsorbed films. *Phys. Rev. B*, 40(7):4938–4946, September 1989.

[75] H.R. Meck. A survey of methods of stability analysis of ring-stiffened cylinders under hydrostatic pressure. *J. of Engineering for Industry ASME Ser. B*, 87(3):385–390, August 1965.

[76] M.E. Lunchick. Plastic general instability pressure of submarine pressure hulls. Technical Report paper 62 WA 262, ASME.

[77] M.E. Lunchick. Plastic general-instability pressure of ring stiffened cylindrical shells. Technical Report 1587, U.S. Navy DTMB, September 1963.

[78] M.H. Jawad. Design of conical shells under external loads. *J. Pressure. Vessel Tech., Trans. ASME*, 102:230–239, May 1980.

[79] V.J. Johnson ed. a compendium of the properties of materials at low temperature (phase 1), Part II. Properties of solids. Technical Report WADD Technical Report 60-56, NBS Cryogenice Engineering Laboratory, Wright-Patterson Air Force Base, Ohio, October 1960.

[80] A. Bellatreccia, P. Cardoni, L. Martinis, L. Mori, and F. Scaramuzzi. Superleak tight aluminum to stainless steel bond. *Cryogenics*, 23(9):556–557, October 1983.

[81] C. Boyd, D. Juanarena, and M.G. Rao. Cryogenic pressure sensor calibration facility. In R. W. Fast, editor, *Advances in Cryogenic Engineering, Proceedings of the 1989 Cryogenic engineering conference*, pages 1573–1581, New York and London, 1990. Plenum Press.

[82] G. Krafft, H.J. Spiegel, and G. Zahn. Suitability of commercial strain gauge pressure transducers for low temperature application. *Cryogenics*, 20(11):625–628, November 1980.

[83] A. Roth. *Vacuum Technology.* North-Holland Physics Publishing, Amsterdam, second edition, 1982.

[84] Paul Horowitz and Winfield Hill. *The Art of Electronics.* Cambridge University Press, London and New York, first edition, 1980.

[85] A.C. Anderson. Low-noise AC bridge for resistance thermometry at low temperatures. *Rev. Sci. Instrum.*, 44(10):1475–1477, October 1973.

[86] M.A. Logan. An AC bridge for semiconductor resistivity measurements using a four-point probe. *Bell System Tech Journal*, 40(3):885–920, May 1961.

[87] Henry P. Hall. Chapter 9, Impedance measurement. In Benard M. Oliver and John M. Cage, editors, *Electronic Measurements and Instrumentation.* McGraw Hill Book Company, New York, 1971.

[88] Ralph Morrison. *Grounding and Shielding Techniques in Instrumentation.* John Wiley and sons, New York, London, Sidney, 1967.

[89] C.A. Gearhart, Jr., J.A. McLinn, and W. Zimmermann, Jr. Simple high-stability potentiometric AC bridge circuits for high-resolution low-temperature resistance thermometry. *Rev. Sci. Instrum.*, 46(11):1493–1499, November 1975.

[90] A.C. Anderson. Erratum: Low-noise AC bridge for resistance thermometry at low temperatures. *Rev. Sci. Instrum.*, 47(5):642–643, May 1976.

[91] E.M. Forgan. On the use of temperature controllers in cryogenics. *Cryogenics*, 14(4):207–214, April 1974.

[92] Richard M. Foard. Multitasking methods. *P.C. Tech Journal*, pages 53–60, March 1986.

[93] Michael Hyman. *Memory Resident Utilities, Interrupts, and Disk Management with MS and PC DOS.* Managment Information Source Inc., Portland, Oregon, 1987.

[94] John Angermeyer, Kevin Jaeger, Raj Kumar Bapna, Nabajyota Barkakati, Rajagopalan Dhesikan, Walter Dixon, Andrew Dumke, Jon Fleig, and Michael Goldman. *The Waite Group's MS-DOS Developer's Guide, Second Edition.* Howard W. Sams and Co., Indianapolis, Indiana, 1989.

[95] J.H. de Boer. The shapes of capillaries. In D.H. Everett and F.S. Stone, editors, *The Structure and Properties of Porous Materials.* Academic Press Inc. and Butterworth's Scientific Publications, New York and London, 1958. pages 68-94.

[96] E. Cheng and M.W. Cole. Physical adsorption near an oblique corner. *Phys. Rev. B*, 41(14):9650–9653, May 1990.

[97] P.C. Ball and R. Evans. Structure and adsorption at gas-solid interfaces : Layering transitions from a continuum theory. *J. Chem. Phys.*, 89(7):4412–4423, October 1988.

[98] A.J. Jin, M.R. Bjurstrom, and M.H.W. Chan. Thermodynamic evidence of first order melting of Xe on graphite. *Phys. Rev. Lett.*, 62(12):1372–1375, March 1989.

[99] R.D. Etters, M.W. Roth, and B. Kuchta. Calculated melting behavior of partial and complete N_2 monolayers deposited on graphite. *Phys. Rev. Lett.*, 65(25):3140–3143, December 1990.

[100] M.J. Lysek, M.S. Pettersen, and D.L. Goodstein. Observation of a first order triple-point dewetting transition in methane adsorbed on graphite. *Phys. Lett. A*, 115(7):340–342, April 1986.

[101] William H. Press, Brian P. Flannery, Saul A. Teukolsky, and William T. Vetterling. *Numerical Recipies in C.* Cambridge University Press, Cambridge, 1988.

[102] A.A. Antoniou. Phase transformations of water in porous glass. *J. Phys. Chem.*, 68(10):2754–2764, October 1964.

[103] S.J. Gregg and K.S.W. Sing. *Adsorption, Surface Area and Porosity.* Academic Press Inc., London and New York, second edition, 1982.

[104] R. Defay and I. Prigogine. *Surface Tension and Adsorption.* John Wiley and Sons, Inc., New York, 1966.

[105] W.K. Burton, N. Cabrera, and F.C. Frank. The growth of crystals and the equilibrium structure of their surfaces. *Philos. Trans. R. Soc. London Ser. A*, 243:299–358, 1951.

[106] Edward H. Conrad, Ralph M. Aten, Donald S. Kaufman, Lynn R. Allen, Thomas Engel adn Marcel den Nijs, and Eberhard K. Riedel. Observation of surface routhening on Ni(115). *J. Chem. Phys.*, 84(2):1015–1028, January 1986.

[107] Edward H. Conrad, Ralph M. Aten, Donald S. Kaufman, Lynn R. Allen, Thomas Engel adn Marcel den Nijs, and Eberhard K. Riedel. Erratum: Observation of surface routhening on Ni(115) [j. chem. phys. 84 1015 (1986). *J. Chem. Phys.*, 85(8):4756–4757, October 1986.

[108] J.W.M. Frenken, R.J. Hamers, and J.E. Demuth. Thermal roughening studied by scanning tunneling microscopy. *J. Vac. Sci. Technol. A*, 8(1):293–296, January/February 1990.

[109] Minoru Maruyama. Growth and roughening transition of rare gas crystals. *J. Cryst. Growth*, 89:415–422, 1988.

[110] V.G. Manzhelii and A.M. Tolkachev. Densities of ammonia and methane in the solid state. *Soviet Physics-Solid State*, 5(12):2605–2510, June 1964.

[111] J.C. Melrose. *Amer. Inst. Chem. Eng. J.*, 12:986, 1966.

[112] B. Legait and P.G. de Gennes. Capillary rise between closely spaced plates: effect of van der Waals forces. *J. Physique Lett.*, 45(13):L–647 – L–652, July 1984.

[113] L.D. Landau and E.M. Lifshitz. *Statistical Physics, Part 1.* Pergamon Press, Oxford, third edition, 1980.

[114] D. Nenow and A. Trayanov. Surface melting of small crystals. *J. Cryst. Growth*, 99(1-4):102–105, 1990.

[115] J.L. Tell and H.J. Maris. Specific heats of hydrogen, duterium, and neon in porous Vycor glass. *Phys. Rev. B*, 28(9):5122 – 5125, Novermber 1983.

[116] D.M. Zhu and J.G. Dash. Evolution of multilayer Ar and Ne films from two-dimensional to bulk behavior. *Phys. Rev. B*, 38(16):11673–11687, December 1988.

[117] D.B. Pengra, Da-Ming Zhu, and J.G. Dash. Surface melting of strained and unstrained layers: Kr , Ar, and Ne. *Surf. Sci.*, 245(1/2):125–131, April 1991.

[118] D.L. Goodstein. Private communication.

[119] C. Tessier and Y. Larher. 2-D melting in physadsorbed monolayers of Ar, Kr, Xe, and CH_4. In S. K. Sinha, editor, *Ordering in Two Dimensions.* Elsevier North Holland Inc., Amsterdam, 1980. Pages 163-168.

[120] J.Z. Larese and Q.M. Zhang. Private communication.

[121] Y.P. Feng and M.H.W. Chan. Tricritical and critical melting transitions on commensurate co on graphite. *Phys. Rev. Lett.*, 62(18):2148–2151, April 1990.

[122] E.D. Specht, A. Mak, C. Peters, M. Sutton, R.J. Birgeneau, K.L. D'Amico, D.E. Moncton, S.E. Nagler, and P.M. Horn. Phase diagram and phase transitions of krypon on graphite in the extended monlolayer regime. *Z. Phys. B*, 69(2/3):347–377, December 1987.

[123] D.M. Butler, J.A. Litzinger, and G.A. Stewart. *Phys. Rev. Lett.*, 44(7):466–468, Feburary 1980.

[124] Marcel den Nijs. Private Communication.

[125] Koos Rommelese and Marcel den Nijs. Preroughening transitions in surfaces. *Phys. Rev. Lett.*, 59(22):2578–2581, November 1987.

[126] H.K. Kim, Y.P. Feng, Q.M. Zhang, and M.H.W. Chan. Phase transitions of ethylene on graphite. *Phys. Rev. B*, 37(7):3511–3523, March 1988.

[127] D.M. Zhu. *A Thermodynamic Study of Surface Roughening and Surface Melting in Multilayer Ar and Ne Films.* PhD thesis, University of Washington, Seatle, Washington, August 1988.

[128] Thomas Michalski, Anke Benini, and Gerhard H. Findenegg. A study of multilayer adsorption and pore condensation of pore fluids in graphite substrates on approaching the bulk critical point. *Langmuir*, 7(1):185–190, January 1991.

[129] C. Hodgson and R. McIntosh. The freezing of water and benzene in porous vycor glass. *Canadian J. Chem.*, 38(6):958–971, June 1960.

[130] R. Kleinrahm and W. Wagner. Measurement and correlation of the equilibrium liquid and vapor densities and the vapor pressure along the coexistence

curve of methane. *Chem. Thermo.*, 18(8):739–760, 1986. Also see reference 16 in this paper.

[131] M.A. Byrne, M.R. Jones, and L.A.K. Stavely. Second virial coefficients of argon, krypton, and methane and their binary mixtures at low temperatures. *Trans. Faraday Soc.*, 64:1747–1756, 1968.

[132] J.O. Hirschfelder, C.F. Curtiss, and R. Byron Bird. *Molecular Theory of Gases and Liquids.* Wiley and sons, New York, 1954, 1964.

[133] J.G. Dash. *Films on Solid Surfaces.* Academic Press, New York, San Francisco, London, 1975.

[134] J. Frenkel. *Kinetic Theory of Liquids.* Oxford University, London, 1949.

[135] G.D. Halsey. Physical adsorption on non-uniform surfaces. *J. Chem. Phys.*, 16(10):931–937, October 1948.

[136] T.L. Hill. Statistical mechanics of adsorption. V. Thermodynamics and heat of adsorption. *J. Chem. Phys.*, 17(6):520–535, June 1949.